From Slow to Ultra-fast MAS: Structural Determination of Type-Three Secretion System Bacterial Needles and Inorganic Materials by Solid-State NMR

Dissertation

zur Erlangung des mathematisch-naturwissenschaftlichen Doktorgrades

"Doctor rerum naturalium"

der Georg-August-Universität Göttingen

-

im Promotionsprogramm ProPhys

der Georg-August University School of Science (GAUSS) program

vorgelegt von

Jean-Philippe Demers

aus Saint-Jean-sur-Richelieu, QC, Canada

Göttingen, 2014

From Slow to Ultra-fast MAS: Structural Determination of Type-Three Secretion System Bacterial Needles and Inorganic Materials by Solid-State NMR

Dissertation

zur Erlangung des mathematisch-naturwissenschaftlichen Doktorgrades

"Doctor rerum naturalium"

der Georg-August-Universität Göttingen

-

im Promotionsprogramm ProPhys

der Georg-August University School of Science (GAUSS) program

vorgelegt von

Jean-Philippe Demers

aus Saint-Jean-sur-Richelieu, QC, Canada

Göttingen, 2014

Members of the Thesis defense Committee

Professor Dr. Konrad Samwer (1st reviewer)

I. Institute of Physics, Georg-August-Universität Göttingen

Professor Dr. Christian Griesinger (2nd reviewer)

Department of NMR-based Structural Biology, Max Planck Institute for Biophysical Chemistry, Göttingen

Dr. Adam Lange

Department of NMR-based Structural Biology, Solid-State NMR Spectroscopy, Max Planck Institute for Biophysical Chemistry, Göttingen

Professor Dr. Helmut Grubmüller

Department of Theoretical and Computational Biophysics, Max Planck Institute for Biophysical Chemistry, Göttingen

Professor Dr. Hans Hofsäss

II. Institute of Physics, Georg-August-Universität Göttingen

Professor Dr. Markus Zweckstetter

German Center for Neurodegenerative Diseases (DZNE), Göttingen

Date of the oral examination: April 23rd 2014

Affidavit

I hereby declare that this thesis has been written independently and with no other sources and aids than quoted.

Furthermore I confirm that this thesis has not been submitted as part of another examination process neither in identical nor in similar form.

Jean-Philippe Demers	Place, Date

"I have not yet lost a feeling of wonder, and of delight, that this delicate motion should reside in all the ordinary things around us, revealing itself only to him who looks for it. I remember, in the winter of our first experiments, just seven years ago, looking on snow with new eyes. There the snow lay around my doorstep - great heaps of protons quietly precessing in the earth's magnetic field. To see the world for a moment as something rich and strange is the private reward of many a discovery."

— Edward M. Purcell, Research in nuclear magnetism,
Nobel lecture, Dec. 11th 1952

À mes parents,

Acknowledgements

I would like to specially thank my supervisor Adam Lange for his support throughout my Ph.D., by being a constant source of motivation and new interesting ideas and by being a nice supervisor with many human qualities: tolerance, openness and patience.

I had the opportunity to work in an environment of exceptional scientific richness at the Max-Planck Institute for Biophysical Chemistry in the NMR-based Structural Biology department and I want to thank Christian Griesinger for creating and organizing this environment.

I am extremely grateful to the members of my research group in Solid-State NMR: Vinesh Vijayan, Robert Schneider, Karsten Seidel and Antoine Loquet had the patience and the generosity to teach me the practical aspects of solid-state NMR directly at the instrument. I also want to thank all my colleagues of the group over the years for their friendship and their conversations: Ashutosh, Zrinka, Guohua, Veniamin, Pascal, Sheng-Qi, Venita, Hannes, Nils, Chaowei, Songhwan, Birgit, Benni, Suresh, Ann-Christin. I am very grateful to Ann-Christin Poeppler for the proofreading of my thesis. I have special thanks for Venita for helping me improve my spoken German, and for Antoine and Hannes for many interesting discussions on solid-state NMR. I want to thank Vinesh, Zrinka, Gitta, Birgit and Hannes for their help in the maintenance of the 800 MHz ssNMR spectrometer.

Many interesting projects were possible due to the help of our collaborators. I want to thank Rajendra S. Ghadwal, Shaban Khan, Sakya S. Sen, Amit Pratap Singh, Prinson Samuel and Herbert W. Roesky of the Institute of Inorganic Chemistry at the Georg-August-Universität Göttingen for providing us many interesting inorganic

compounds. I want to thank Jacek Biernat and Eckhard Mandelkow at the Max-Planck Unit for Structural Molecular Biology at DESY in Hamburg for providing us tau samples. I want to thank Yusuke Nishiyama and Michal Malon at JEOL RESONANCE Inc in Tokyo for carrying experiments at ultra-fast MAS.

For my research project on the study of the T3SS needle, I want to thank Birgit Habenstein for her great help on the project, Antoine Loquet and Suresh Kumar Vasa for technical assistance and discussion on this topic, Christian Griesinger and Arturo Zychlinsky for the initial support of the project, and Brigitta Angerstein for expert technical assistance. I want to thank Nikolas G. Sgourakis at the Laboratory of Chemical Physics, NIDDK/NIH, Bethesda MD and David Baker at the University of Washington in Seattle, WA for a very active collaboration concerning the modelling of structural data, Rashmi Gupta, Michael Kolbe and Britta Laube at the Max Planck Institute for Infection Biology in Berlin for carrying *in vivo* experiments on bacteria, Dietmar Riedel at the MPIbpc in Göttingen for recording electron microscopic images of polymerized needles, Gregory Bubnis and Helmut Grubmüller for discussions on computational simulations of T3SS needle functions. Foremost, I want to thank and highlight the work of Karin Giller and Stefan Becker in our department at the MPIbpc in producing biological samples of unsurpassed quality for our solid-state NMR studies. I also want to thank Stefan Becker for keen and crucial discussions of our structural studies.

I want to thank the Defense committee and the support of Konrad Samwer over the course of my Ph.D. I want to acknowledge the financial support of the Natural Sciences and Engineering Research Council of Canada (NSERC/CRSNG) of Canada and the Max Planck Society.

Finally, on the personal side, I want to thank the support and friendship of the members of the NMR-based Structural Biology Department: Davood, David, Hari, Adam, Sibelle, Rakhi, Pablo, Luigi, Hessam, Marta, Han, Guohua and many others.

My interest in science has always been highly supported and nurtured in my school, college and university time. For this I want to thank my science teachers and mentors Martin Bisaillon, Gilles Dumas and Linda Brunet at École secondaire Marcellin-Champagnat, Céline Dupont at Collège Édouard-Montpetit, Éric Rassart at UQÀM, Hugh Clark, Moshe Szyf and Anthony Mittermaier at McGill University. I had the chance to develop my interest for science through science fair competitions. I want to thank those who provide teenagers this wonderful opportunity: I especially want to thank the work of Marie-Hélène Deneault, Jean Verville, Carole Charlebois and Marthe Poirier at the Conseil de développement du loisir scientifique (CDLS) and Conseil du Loisir Scientifique de la région Métropolitaine (CLSM) who had a positive impact on my interest in a scientific research life.

Je souhaite remercier mes parents Diane et Roland Pierre, ma soeur Karoline et son copain Xavier, ainsi que mes amis Jasmin, Veronik et Willy pour leur essentiel soutien moral. My friends Tatiane, Peipei and Chuli have been encouraging me and for this I am grateful. I want to thank the support, listening and companionship of Xueqin Zeng.

Contents

Part I: Introduction to Solid-State NMR

1. Introduction to Solid-State NMR

In this section, some nuclear spin interactions and experimental techniques of interest to solid-state NMR are presented. For interactions due to local magnetic fields, we also describe the structural information gained by measurement of the interaction, with a particular emphasis on the application to protein studies.

The nuclear spin interactions can be summarized by the total Hamiltonian $\hat{\mathcal{H}}$ [Joules]:

[Eq. 1] $$\hat{\mathcal{H}} = \overbrace{\hat{\mathcal{H}}_0 + \hat{\mathcal{H}}_{RF(t)}}^{\text{External spin interactions}} + \overbrace{\hat{\mathcal{H}}_{CS} + \hat{\mathcal{H}}_D + \hat{\mathcal{H}}_J + \hat{\mathcal{H}}_Q + \hat{\mathcal{H}}_{stoc(t)}}^{\text{Local interactions}}$$

The individual terms are:

- Static magnetic field $\hat{\mathcal{H}}_0$ (1.1.2.) and applied field $\hat{\mathcal{H}}_{RF(t)} = -\gamma \cdot \hat{\vec{I}} \cdot \vec{B}_{1(t)}$
- Chemical shift $\hat{\mathcal{H}}_{CS}$ (1.1.3)
- Dipolar couplings $\hat{\mathcal{H}}_D$ (1.1.4)
- Scalar *J*-coupling: $\hat{\mathcal{H}}_J = 2\pi \cdot J_{ij} \cdot 2\hat{I}_{zi}\hat{I}_{zj}$
- Electric quadrupolar coupling: $\hat{\mathcal{H}}_Q = \frac{eQ}{2I(2I-1)}\hat{I}\hat{V}\hat{I}$

The last term $\hat{\mathcal{H}}_{stoc(t)}$ represents stochastic time-fluctuation of local fields, for example due to molecular motions, leading to relaxation.

1.1. Nuclear spin

In order to be NMR-active, a nuclide must possess a nuclear magnetic moment and the concomitant nuclear spin. For an isotope ${}^{A}_{Z}E$, where A is the mass number $(A = N + Z)$, Z is the number of protons and N the number of neutrons, the nucleus will

possess a magnetic moment only in the presence of one or more unpaired nucleons. This occurs when either N or Z is an odd number.

To calculate the spin of a nucleus, the nuclear shell model can be used in the simple case of a single unpaired nucleon (proton or neutron). In this model, the nuclear orbitals for protons and neutrons are filled up independently from lowest to highest energy following the Aufbau principle (Figure 1). Each nuclear orbital is characterized by a total angular momentum quantum number 'I' and orbital angular momentum quantum number 's'.

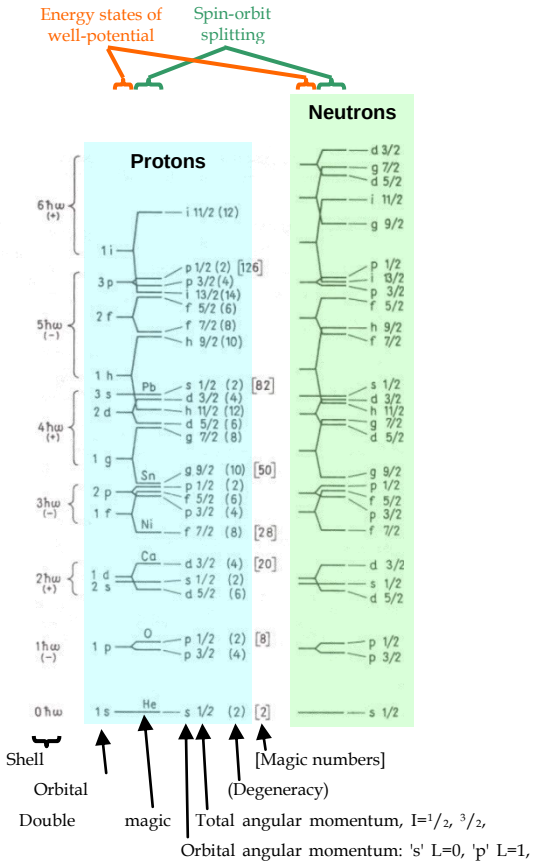

Figure 1: Nuclear energy levels in the shell model. Adapted from Kernphysik[1].

The current thesis focuses on the study of spin-$^1/_2$ nuclides by solid-state NMR: ^{1}H, ^{13}C, ^{15}N, ^{29}Si, ^{31}P and ^{119}Sn. Spin-$^1/_2$ nuclides have advantageous properties for NMR spectroscopy: they often have high gyromagnetic ratios which leads to high sensitivity, they do not possess an electrical quadrupolar coupling which leads to simplified spectra and longer coherence lifetimes, and most of their nuclear spin interactions are represented as tensors of rank two or zero. The last point has important implications for the technique of Magic-Angle Spinning (MAS) presented in Section 1.2.1. A few nuclides are presented in Table 1.

Isotope		Spin	N.A.	Freq. at 18.8T
^{1}H	Proton	$^1/_2$	99.99%	800.1 MHz
^{2}H	Deuterium	1	0.01%	122.8 MHz
^{13}C	Carbon	$^1/_2$	1.07%	201.2 MHz
^{15}N	Nitrogen	$^1/_2$	0.36%	81.1 MHz
^{17}O	Oxygen	$^5/_2$	0.04%	108.5 MHz
^{19}F	Fluor	$^1/_2$	100 %	752.9 MHz
^{27}Al	Aluminium	$^5/_2$	100 %	208.5 MHz
^{29}Si	Silicium	$^1/_2$	4.67 %	159.0 MHz
^{31}P	Phosphorus	$^1/_2$	100 %	323.9 MHz
^{119}Sn	Tin	$^1/_2$	8.59 %	191.5 MHz

Table 1: Properties of some common nuclides

1.2. Interaction with external magnetic fields

The splitting of nuclear energy levels due to the interaction with an external magnetic field is described by the Zeeman splitting Hamiltonian:

[Eq. 2] $$\hat{\mathcal{H}}_Z = -\sum_i \gamma_i \cdot \hat{\vec{I}}_i \cdot \vec{B}$$

where $\gamma_i = \frac{g \cdot \mu_N}{\hbar}$ is the gyromagnetic ratio (g: g-factor, μ_N: nuclear magneton)

$\hat{\vec{I}}_i = \hat{I}_{ix}\vec{e}_x + \hat{I}_{iy}\vec{e}_y + \hat{I}_{iz}\vec{e}_z = \left(\hat{I}_{ix}, \hat{I}_{iy}, \hat{I}_{iz}\right)$ is the total angular moment operator ,

$\vec{B} = B_x\vec{e}_x + B_y\vec{e}_y + B_z\vec{e}_z = \begin{pmatrix} B_x \\ B_y \\ B_z \end{pmatrix}$ is the magnetic induction vector.

The magnetic induction $\vec{B}$ [Telsa, $\frac{N}{A \cdot m}$] is related to the magnetic field $\vec{H}$ [A/m]: $\vec{B} = \mu_0\left(\hat{1} + \hat{\chi}\right)\left(\vec{H} + \vec{h}\right)$, with μ_0 as the vacuum permeability (4π N/A^2), $\hat{\chi}$ as the magnetic susceptibility tensor, a dimensionless second-rank tensor, and $\vec{h}$ as the demagnetization field, or stray field, usually small for modern spectrometers $\left\|\vec{H}\right\| >> \left\|\vec{h}\right\| \approx 0$. The laboratory frame axes (LAB) are usually defined using the right-hand convention with the magnetic field $\vec{H}_0$ along the *z* axis. In an anisotropic medium, the susceptibility can be considered scalar, with $\chi > 0$ for paramagnetic materials and $\chi < 0$ for diamagnetic materials, and hence $\vec{B}_0 = \begin{pmatrix} 0 \\ 0 \\ B_0 \end{pmatrix}$

The size of the spin operators represented as matrices, such as the angular moment operators $\hat{I}_{ix}$, $\hat{I}_{iy}$, $\hat{I}_{iz}$, depends on the number of involved spins and on the multiplicity of their spin $(2I_i + 1)$. The product operator formalism employed here is introduced formally in monographs[2,3].

The total external Hamiltonian is $\hat{\mathcal{H}}_{ext} = \overbrace{\hat{\mathcal{H}}_0 + \hat{\mathcal{H}}_{RF(t)}}^{\text{External spin interactions}}$. The interaction with the static field is described by:

[Eq. 3] $$\hat{\mathcal{H}}_0 = \hbar\sum_i \omega_{0,i}\hat{I}_{iz}$$

with the Larmor angular frequency $\omega_{0,i} = -\gamma_i B_0$ [MHz rad] or linear frequency $\nu_{0,i} = \omega_{0,i}/2\pi$ [MHz]. The interaction with time-dependent radio-frequency (RF) fields is described in Section 1.2.1.

1.2.1. Spin-lock RF pulse

A ubiquitous building block in solid-state NMR pulse sequences is the spin-lock RF pulse. Magnetization is preserved along a given axis in the rotating frame by the application of an external field $\vec{B}_1$ parallel to this axis. If the RF field is sufficiently strong, then dephasing due to dipolar couplings and chemical shifts is small or negligible. Magnetization can thus be stored for relatively long periods, limited only by the spin-lattice relaxation in the rotating frame with a time constant $T_{1\rho}$.

When used in combination with MAS, some spin interactions can be reintroduced at some specific amplitudes of the RF field because of the interference between RF irradiation and MAS. The recoupling conditions can lead to magnetization transfer, as in the case of Hartmann-Hahn cross-polarization, or can lead to dephasing and loss of stored magnetization which usually have to be avoided.

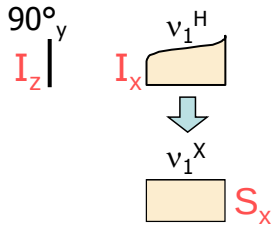

- H and X nuclei are *locked* in the rotating frame by the spin-lock RF field
- At the **Hartmann-Hahn** condition, $\left(\nu_1^{H} - \nu_1^{X}\right) = \pm\frac{1}{2}\nu_{MAS}$ HX dipolar couplings are re-introduced.

$^{1}H \Rightarrow {}^{13}C$, $^{1}H \Rightarrow {}^{15}N$, $^{15}N \Rightarrow {}^{13}C$

Figure 2: Mechanism of cross-polarization

1.3. Chemical shielding

Due to the electronic environment surrounding the nucleus, the resonance frequency deviates from the bare Larmor frequency presented in Eq. 3. The contribution can be separated into two contributions: closed-shell electrons contribute the chemical shift (Eq. 4) and open-shell electrons, e.g. occurring in metallic systems, contribute the Knight shift (Eq. 5).

[Eq. 4] $$\hat{\mathcal{H}}_{\mathrm{CS}} = \sum_i \gamma_i \cdot \hat{\vec{I}}_i \cdot \hat{\sigma}_i \cdot \vec{B}$$

[Eq. 5] $$\hat{\mathcal{H}}_{\mathrm{KS}} = -\sum_i \gamma_i \cdot \hat{\vec{I}}_i \cdot \hat{K}_i \cdot \vec{B}$$

The chemical shift shielding tensor $\hat{\sigma}_i$ is a 3×3 second-rank tensor; its elements σ_{jk} represent the magnetic field induced in direction *j* when an external field is applied in direction *k* (Eq. 6)[3].

[Eq. 6] $$\hat{\sigma} = \begin{pmatrix} \sigma_{xx} & \sigma_{xy} & \sigma_{xz} \\ \sigma_{yx} & \sigma_{yy} & \sigma_{yz} \\ \sigma_{zx} & \sigma_{zy} & \sigma_{zz} \end{pmatrix}$$

As the variation in the value of the σ_{jk} elements ranges typically on the order of 10^{-6} to 10^{-4}, values are presented in parts per million (ppm). The chemical shift is commonly expressed in reference to a standard compound by a deshielding tensor $\hat{\delta}$, also called Chemical Shift Anisotropy (CSA) tensor, with elements δ_{jk} (Eq. 7).

[Eq. 7] $$\delta_{jk} = \frac{\sigma_{\mathrm{ref}} - \sigma_{jk}}{1 - \sigma_{\mathrm{ref}} - \chi}$$, or approximately $\delta_{jk} \approx \sigma_{\mathrm{ref}} - \sigma_{jk}$

Second-rank tensors can be decomposed into components which are purely of rank zero, one and two. For instance, the CSA tensor is expressed as the three

components (Eq. 8), with $\delta_{iso} = \frac{1}{3}\left(\delta_{xx} + \delta_{yy} + \delta_{zz}\right)$, $\delta^{a}_{jk} = \frac{1}{2}\left(\delta_{jk} - \delta_{iso}\right)$, $\delta^{s}_{jk} = \frac{1}{2}\left(\delta_{jk} + \delta_{iso}\right)$ and $\Delta\delta_j = \delta_{jj} - \delta_{iso}$.

[Eq. 8] $$\hat{\mathcal{H}}_{CS} = \sum_i \gamma_i \cdot \hat{\hat{I}}_i \cdot \left(\hat{1} + \hat{\delta}_i\right) \cdot \vec{B}$$

[Eq. 9] $$\hat{\delta} = \delta_{iso} \cdot \underbrace{\begin{pmatrix} 1 & 0 & 0 \\ 0 & 1 & 0 \\ 0 & 0 & 1 \end{pmatrix}}_{\text{Purely rank zero}} + \underbrace{\begin{pmatrix} 0 & \delta^{a}_{xy} & \delta^{a}_{xz} \\ -\delta^{a}_{yx} & 0 & \delta^{a}_{yz} \\ -\delta^{a}_{zx} & -\delta^{a}_{yz} & 0 \end{pmatrix}}_{\text{Purely rank one}} + \underbrace{\begin{pmatrix} \Delta\delta_x & \delta^{s}_{xy} & \delta^{s}_{xz} \\ \delta^{s}_{yx} & \Delta\delta_y & \delta^{s}_{yz} \\ \delta^{s}_{zx} & \delta^{s}_{zy} & \Delta\delta_z \end{pmatrix}}_{\text{Purely rank two}}$$

Those three components behave differently under rotation and are called respectively the isotropic, anti-symmetric and symmetric part of the tensor. The isotropic part (rank zero) is invariant under rotation, meaning that it will lead to the same frequency shift regardless of the orientation of the external field. Because of symmetry considerations, the off-diagonal elements of the anti-symmetric component (rank one) will not affect the principal values under the diagonalization transformation associated with matrix rotation. As a result, the anti-symmetric component does not affect NMR resonance frequencies, but it can affect relaxation. In contrast, as the rank-two component is symmetric, its off-diagonal components can contribute to the principal values. The frequency shift imparted by the symmetric part of the tensor depends on its orientation relative to the external field.

The CSA tensor provides a description of the electronic environment at the site of the nucleus: the isotropic value δ_{iso} relates to the average local electron density, the anisotropy parameter δ_{aniso} reflects the magnitude of the difference between the most and least shielded direction, and the asymmetry parameter η_{asym} indicates the deviation of the tensor from axial symmetry. The orientation of the Principal Axis Frame (PAF) of the CSA tensor relative to the molecular frame is not directly accessible from simple

MAS experiments but can be determined by experiments carried on single crystal[4], or by determining vector angle (VEAN) restraints[5].

1.4. Prediction of Chemical Shift Anisotropy (CSA) tensor values

Currently, knowledge of the isotropic chemical shifts or CSA tensors for NMR-active nuclei does not lead to a direct determination of the atomic structure of a compound, and does not even guarantee the correct identification of its chemical composition or configuration. However, the reverse problem, i.e. prediction of chemical shifts and CSA values knowing the chemical composition and molecular structure, is less convoluted and has seen recent progress. Two main approaches are employed: 1) devising empirical rules from the study of systematic trends in experimental data, 2) prediction of CSA tensors from theoretical considerations, for example by using density functional theory (DFT).

Examples of empirical rules for ^{13}C chemical shifts include the Grant-Paul rules for alkanes[6] and the Lendeman-Adams rules for methylalkanes[7]. Such rules aim at identifying the functional groups, the chemical substituants, the diastereomeric conformation, the protonation status of an atom.

In proteins and peptides, the backbone dihedral angles φ and ψ have an influence on the local electron density and affect the chemical shift of H_N, C', C_α, C_β and N[8]. As the secondary structure of proteins is strongly related to backbone dihedral angles through the Ramachandran plot, the secondary structure propensity of proteins can be estimated from backbone isotropic chemical shifts[9]. The chemical shift of valine methyl carbons has also been linked to the sidechain dihedral angle χ_1[10].

On the other hand, predictions of chemical shifts can be computed from first principles using quantum mechanical principles. One successful approach which can reproduce solution-state NMR chemical shifts employs Gauge-including atomic orbitals (GIAO)[11]. However, this method has two disadvantages for the interpretation of solid-state NMR chemical shifts. First, the local chemical environment present in solid samples depends not only on the properties of isolated molecular systems but also on the characteristics of the assembly, for example including translational symmetries present in crystalline systems[12]. Secondly, the repercussion of using multiple copies of an isolated molecule with the GIAO method is an increase in computational time. In order to compute predictions for periodic systems, an alternative description of the system based on plane-wave pseudopotentials was introduced in the Gauge-including projector augmented-wave (GIPAW) method[13]. Similarly to the Projector Augmented-Wave (PAW) method[14], this method does not misrepresent the form of electronic wave functions in the vicinity of the nucleus and employs periodic boundary conditions to represent finite and infinite periodic systems. The GIPAW method is implemented notably in the CASTEP[15,16] and Quantum Espresso[17] programs.

1.5. Dipolar couplings

[Eq. 10]
$$\hat{\mathcal{H}}_D = \frac{\mu_0}{4\pi}\frac{\gamma_i\gamma_j}{r_{ij}^3}\frac{1-3\cos^2\theta}{2}2\hat{I}_{zi}\hat{I}_{zj}$$

As dipolar coupling tensors are traceless, dipolar couplings are averaged out to a first-order under Magic-Angle Spinning. Heteronuclear and homonuclear couplings behave differently in this respect since homonuclear couplings are time-dependent[18].

On the other hand, higher-order cross-terms involving dipolar couplings are not averaged by Magic-Angle Spinning. For example, some terms containing the heteronuclear dipolar coupling D_{HX} can lead to severe broadening of the X resonance

during acquisition. To be removed, manipulation of the I spin by r.f. irradiation must be carried out, a technique called heteronuclear decoupling (Section 1.2.6).

1.5.1. Measurement of inter-nuclear distances

Dipolar couplings allow the precise determination of inter-nuclear distances due to the dependence on r_{ij}^3. In solid-state NMR, dipolar couplings can be experimentally determined from the build-up curve (or decay curve) during a dipolar recoupling pulse sequence element.

The dipolar coupling d_{HX} between proton and a low-gamma nucleus X (^{13}C, ^{15}N) can be determined using a Lee-Goldburg cross-polarization build-up. Heteronuclear dipolar, e.g. ^{13}C-^{15}N, can be measured by TEDOR experiments. Homonuclear ^{13}C-^{13}C dipolar couplings can be measured by REDOR and double quantum-single quantum (DQ-SQ) experiments.

An alternative technique to detect proximities between like spins is to allow transfer of magnetization through the incoherent process of spin diffusion, for example proton spin diffusion in ChhC and NhhC experiments[19,20] or facilitated spin diffusion such as Proton-Driven Spin Diffusion (PDSD) [21] and RAD/DARR[22,23].

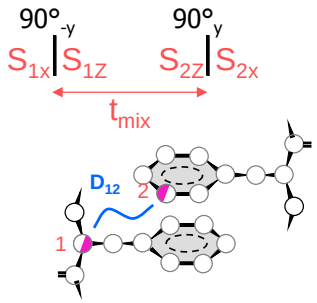

- ^{13}C magnetization is placed along the *z* axis
- CC dipolar couplings allow **flip-flop transfer** between spin 1 and 2 during mixing

In **PDSD**: HH and HC dipolar couplings accelerate the transfer
In **DARR**: ^1H irradiation at the $\nu_1^H = \nu_{MAS}$ condition recouples HH and HC couplings

Figure 3: Mechanism of facilitated spin diffusion

1.5.2. Measurement of molecular motions

For measurement of dipolar couplings over large distances, the effect of molecular motion is usually neglected. However, when the distance is known, for instance in the case of a chemically-bonded i-j nuclei pair, an effective dipolar coupling d_{ij}^{eff} can be measured and compared to the dipolar strength for a completely rigid inter-nuclear vector d_{IJ} (calculated using Eq. 4). An order parameter[24] S_{ij} for the inter-nuclear vector can then be defined:

[Eq. 11] $$S_{ij} = d_{ij}^{eff} / d_{ij}$$

We employed this approach, first demonstrated on ubiquitin[25], for the determination of the flexibility of the N-terminal helix of the VDAC beta-barrel protein[26]. Experiments are recorded in a DQ-SQ fashion, with the evolution of DQ coherences in the indirect dimension and SQ in the direct dimension. The SPC5[27] composite pulse element for SQ→DQ excitation and DQ→SQ re-conversion. The build-up is recorded by acquiring a series of spectra, incrementing the excitation and re-conversion times. SPC5 build-up curves were recorded for the uniformly-labeled Type-Three Secretion System needle of *Shigella flexneri*.

Similarly, order parameters for bonded ^{1}H-^{13}C atom pairs can be determined by recording a Lee-Goldburg cross-polarization build-up to measure the effective dipolar coupling d_{HC}^{eff} and comparing the obtained value to the rigid calculated value. Such measurements were carried on dry valine powder, a dry polymer, tyrosine-ethylester (TEE) and methyl ^{13}C-labeled MxiH needles.

1.6. Magic-Angle Spinning

As introduced in section 1.1.3, only the rank-two tensor part has to be considered for the orientation-dependent contribution to the resonance frequency. For an arbitrary

tensor, there exists a frame, called the Principal Axis Frame (PAF) where the symmetric part of the tensor is diagonal, with all off-diagonal elements $\delta^{s}_{jk} = 0$ (Eq. 12).

[Eq. 12]
$$\hat{\delta}^{s,PAS} = \begin{pmatrix} \Delta\delta_x^{PAS} & 0 & 0 \\ 0 & \Delta\delta_y^{PAS} & 0 \\ 0 & 0 & \Delta\delta_z^{PAS} \end{pmatrix}$$

Purely rank two

In the case of a static sample, the tensor in the laboratory frame (LAB) is found by rotation of the PAF tensor around the Euler angles α, β, γ. For a periodic mechanical rotation as in Variable-Angle Spinning[28] and Magic-Angle Spinning, the PAF tensor is first transformed to a rotor-fixed frame (ROT) by Euler rotation (Eq. 13). The time-dependent LAB tensor is then obtained by Euler rotation of the ROT tensor around the mechanical rotation axis.

[Eq. 13]
$$\hat{\delta}^{s,ROT} = \hat{R}_{(\alpha,\beta,\gamma)} \hat{\delta}^{s,PAF} \hat{R}^{-1}_{(\alpha,\beta,\gamma)}$$

Here, the rotation matrix $\hat{R}_{(\alpha,\beta,\gamma)}$ is an operation defined as three successive rotations following the convention of Brink and Satchler:

- First, a rotation of angle γ around the *z*-axis,
- Second, a rotation of angle β around the new *y'*-axis
- Last, a rotation of angle α around the new *z''*-axis

[Eq. 14]
$$\hat{R}_{(\alpha,\beta,\gamma)} = \hat{R}_{z''(\alpha)} \hat{R}_{y'(\beta)} \hat{R}_{z(\gamma)} = \begin{pmatrix} (c_\alpha c_\beta c_\gamma - s_\alpha s_\gamma) & (-c_\alpha c_\beta s_\gamma - s_\alpha c_\gamma) & c_\alpha s_\beta \\ (s_\alpha c_\beta c_\gamma + c_\alpha s_\gamma) & (-s_\alpha c_\beta s_\gamma + c_\alpha c_\gamma) & s_\alpha s_\beta \\ -s_\beta c_\gamma & s_\alpha s_\gamma & c_\beta \end{pmatrix},$$

$$\hat{R}^{-1}_{(\alpha,\beta,\gamma)} = \hat{R}_{(-\gamma,-\beta,-\alpha)} = \hat{R}_{z''(-\gamma)} \hat{R}_{y'(-\beta)} \hat{R}_{z(-\alpha)}$$

[Eq. 15]
$$\hat{\delta}^{s,LAB} = \hat{R}_{(\omega_r t, \theta_r, 0)} \hat{\delta}^{s,ROT} \hat{R}^{-1}_{(\omega_r t, \theta_r, 0)}$$

When ω_r is large compared to the breadth of the chemical shift anisotropy interaction $\Delta\delta_z^{PAS} - \Delta\delta_x^{PAS}$, the contribution of the anisotropic part of the chemical shift tensor becomes time-independent to a first-order approximation.

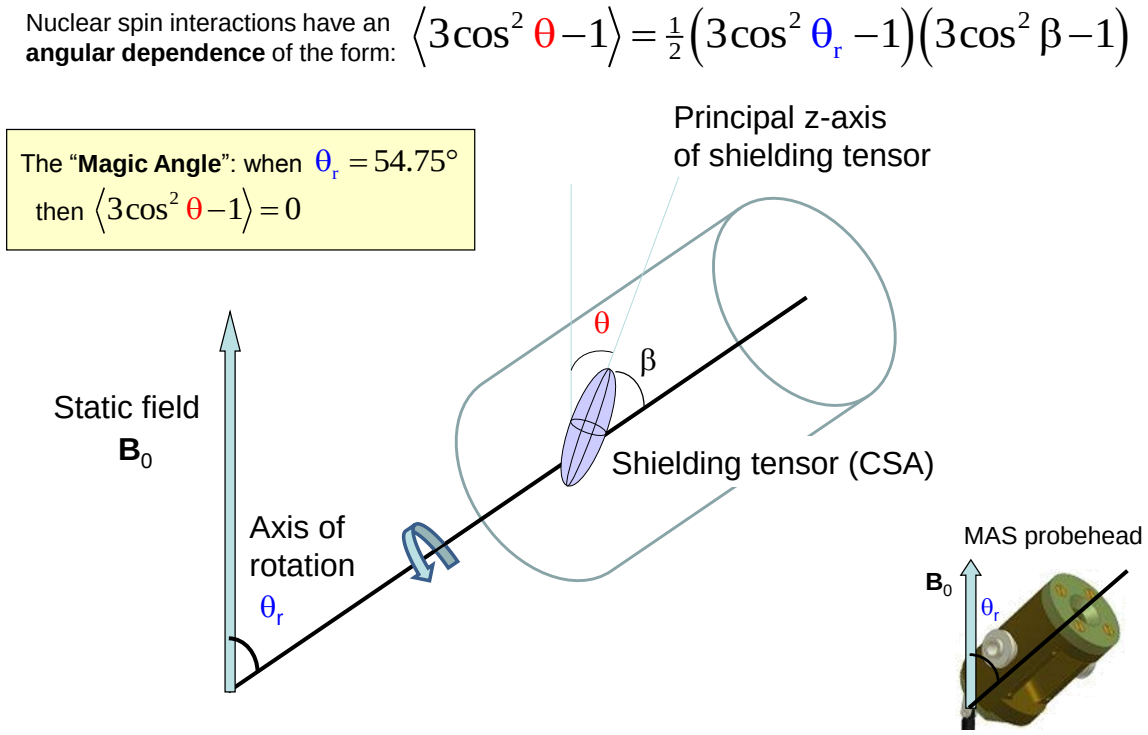

Figure 4: Magic Angle Spinning. Melinda Duer „Solid-State NMR Spectroscopy, Principles and Applications", 2002, Blackwell Science Ltd.

For the average $\langle 3\cos^2\theta - 1\rangle$ to be suppressed, the term $(3\cos^2\theta_r - 1)$ should go to zero: $3\cos^2\theta_r = 1$, $\cos^2\theta_r = \frac{1}{3}$, $\theta_r = \arccos\sqrt{\frac{1}{3}} \approx 54.74°$.

This angle of 54.74° is called the "magic" angle since the angular term has an average frequency contribution of zero. The part of a nuclear Hamiltonian which depends on the angle θ with respect to the magnetic field is called the anisotropic

component, or the second-rank component, of the Hamiltonian. For any time-independent nuclear interaction, the anisotropic component will average to zero when rotated around the magic angle.

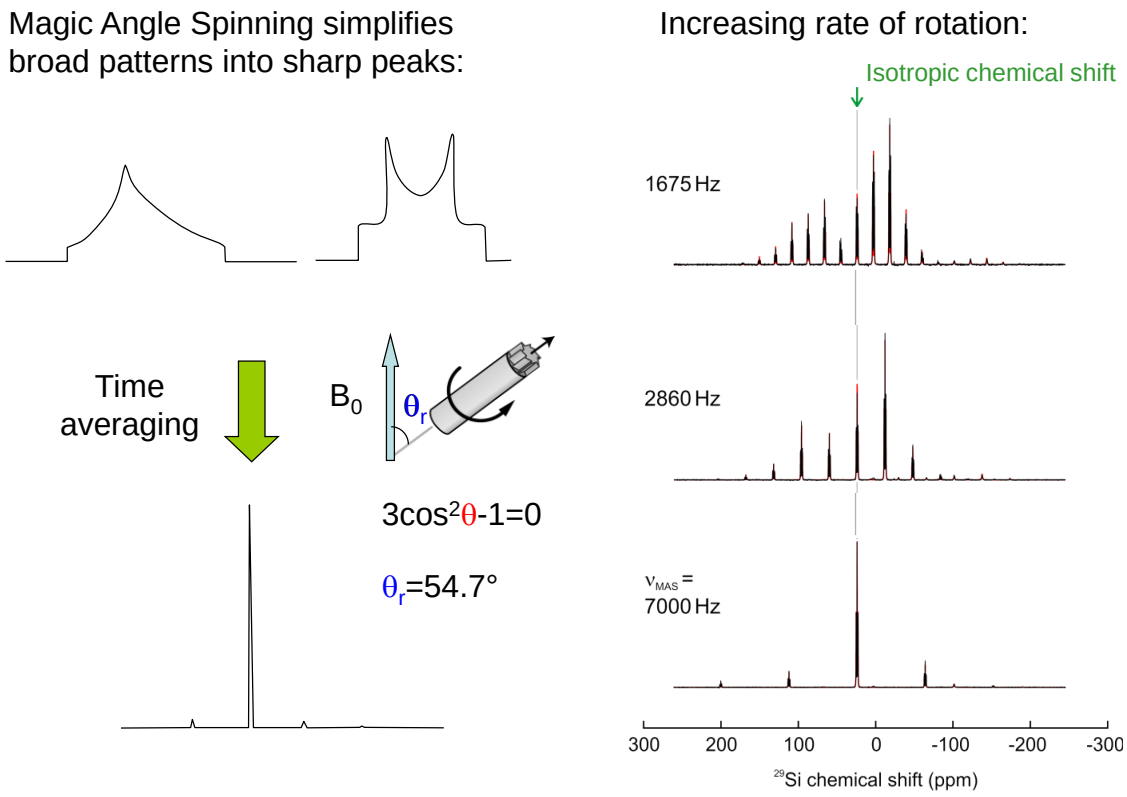

Figure 5: Effect of magic-angle spinning on anisotropic interactions.

1.7. Isotopic labeling

A desired objective in solid-state NMR spectroscopy is to have the capability to selectively activate and deactivate any arbitrary nuclear interactions. Although efforts have been devoted to the development of new RF pulse sequence techniques, important improvements in the study of proteins by solid-state NMR have been obtained in the past decade by the introduction of selective isotopic labeling of the NMR sample.

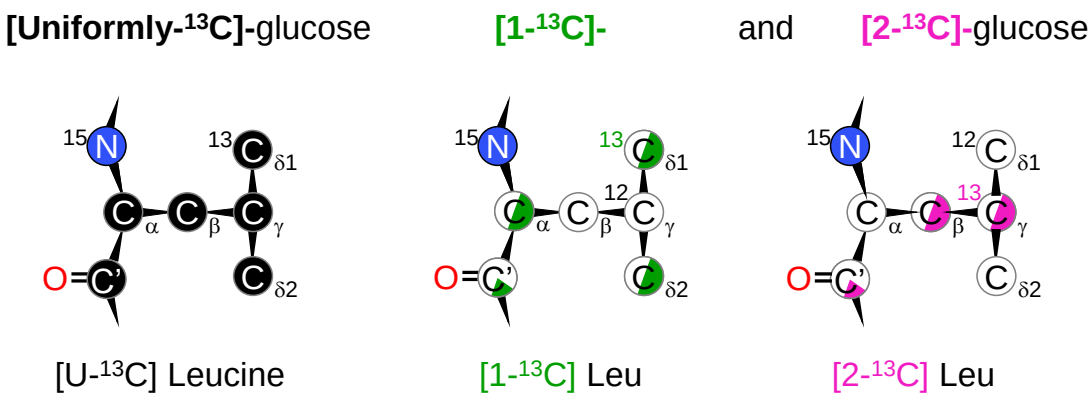

Figure 6: Labeling pattern of leucine residues.

The desired patterns are formed by introducing isotopically labeled compounds in the culture medium during over-expression of the protein of interest. The commonly-used uniform [^{1}H, ^{13}C, ^{15}N] labeling is produced by employing uniformly-[^{13}C]-labelled glucose and [^{15}N]-ammonium chloride. Prominently, some newly introduced labeling schemes employ [1,3-^{13}C]-glycerol[29], [1-^{13}C]-glucose[30], or [2-^{13}C]-glucose[31,32] as carbon source.

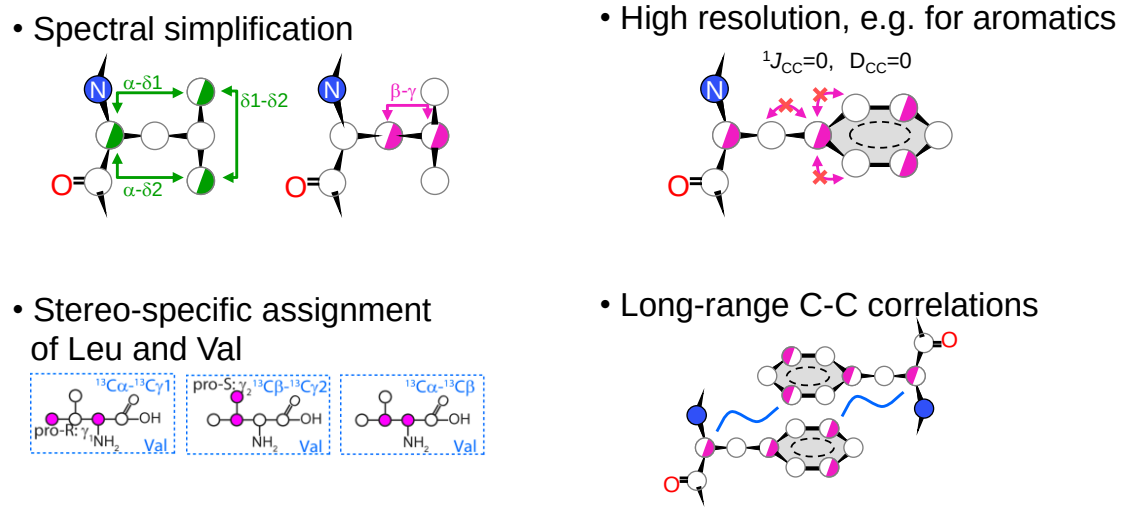

Figure 7: Advantages of sparse labeling patterns

The dilution of ^{13}C spins results in an improved ^{13}C resolution due to the removal of one-bond ^{13}C-^{13}C dipolar and J_{CC} couplings[33]. This greatly facilitates the chemical shift assignment process. Another advantage of sparse labeling schemes relative to uniform labeling is the the simplification of spectra: even though the number of NMR-active carbons is much sparser in glucose labeling (1 in 6 carbons is ^{13}C labeled), the number of detectable correlations is reduced, allowing gaining back a large sensitivity in multi-dimensional spectra. Because of the alternating pattern of glucose labeling schemes, where two labeled carbons rarely occur next to each other, the transfer efficiency is enhanced because of the reduction in dipolar truncation and longer distance correlations can be observed.

1.8. References

1. Mayer-Kuckuk, T. in *Kernphysik* Ch. 6, 185-231 (Vieweg+Teubner Verlag, 1994).
2. Ernst, R. R., Bodenhausen, G., Wokaun, A. *Principles of nuclear magnetic resonance in one and two dimensions*. 148-157 (Clarendon Press, 1994).
3. Levitt, M. H. *Spin Dynamics: Basics of Nuclear Magnetic Resonance*. (Wiley, 2008).
4. Griffin, R. G., Bullitt, J. G., Ellett, J. D., Waugh, J. S., Mehring, M. Single-Crystal Study of F-19 Shielding Tensors of a Trifluoromethyl Group. *Journal of Chemical Physics* **57**, 2147-& (1972).
5. Franks, W. T., Wylie, B. J., Schmidt, H. L. F., Nieuwkoop, A. J., Mayrhofer, R.-M., Shah, G. J., Graesser, D. T., Rienstra, C. M. Dipole tensor-based atomic-resolution structure determination of a nanocrystalline protein by solid-state NMR. *Proceedings of the National Academy of Sciences of the United States of America* **105**, 4621-6 (2008).
6. Grant, D. M., Paul, E. G. Carbon-13 Magnetic Resonance. II. Chemical Shift Data for Alkanes. *Journal of the American Chemical Society* **86**, 2984-90 (1964).
7. Lindeman, L. P., Adams, J. Q. Carbon-13 Nuclear Magnetic Resonance Spectrometry - Chemical Shifts for Paraffins Through C9. *Analytical Chemistry* **43**, 1245-& (1971).
8. Shen, Y., Bax, A. SPARTA plus : a modest improvement in empirical NMR chemical shift prediction by means of an artificial neural network. *Journal of Biomolecular NMR* **48**, 13-22 (2010).
9. Wang, Y. J., Jardetzky, O. Probability-based protein secondary structure identification using combined NMR chemical-shift data. *Protein Sci* **11**, 852-61 (2002).
10. Hansen, D. F., Kay, L. E. Determining Valine Side-Chain Rotamer Conformations in Proteins from Methyl C-13 Chemical Shifts: Application to the 360 kDa Half-Proteasome. *Journal of the American Chemical Society* **133**, 8272-81 (2011).
11. Wolff, S. K., Ziegler, T. Calculation of DFT-GIAO NMR shifts with the inclusion of spin-orbit coupling. *Journal of Chemical Physics* **109**, 895-905 (1998).
12. Harris, R. K. NMR crystallography: the use of chemical shifts. *Solid State Sciences* **6**, 1025-37 (2004).
13. Pickard, C. J., Mauri, F. All-electron magnetic response with pseudopotentials: NMR chemical shifts. *Physical Review B* **63** (2001).
14. Blochl, P. E. Projector Augmented-Wave Method. *Physical Review B* **50**, 17953-79 (1994).

15. Clark, S. J., Segall, M. D., Pickard, C. J., Hasnip, P. J., Probert, M. J., Refson, K., Payne, M. C. First principles methods using CASTEP. *Zeitschrift Fur Kristallographie* **220**, 567-70 (2005).
16. Segall, M. D., Lindan, P. J. D., Probert, M. J., Pickard, C. J., Hasnip, P. J., Clark, S. J., Payne, M. C. First-principles simulation: ideas, illustrations and the CASTEP code. *Journal of Physics-Condensed Matter* **14**, 2717-44 (2002).
17. Giannozzi, P., Baroni, S., Bonini, N., Calandra, M., Car, R., Cavazzoni, C., Ceresoli, D., Chiarotti, G. L., Cococcioni, M., Dabo, I., Dal Corso, A., de Gironcoli, S., Fabris, S., Fratesi, G., Gebauer, R., Gerstmann, U., Gougoussis, C., Kokalj, A., Lazzeri, M., Martin-Samos, L., Marzari, N., Mauri, F., Mazzarello, R., Paolini, S., Pasquarello, A., Paulatto, L., Sbraccia, C., Scandolo, S., Sclauzero, G., Seitsonen, A. P., Smogunov, A., Umari, P., Wentzcovitch, R. M. QUANTUM ESPRESSO: a modular and open-source software project for quantum simulations of materials. *Journal of Physics-Condensed Matter* **21** (2009).
18. Duer, M. J. *Solid State NMR Spectroscopy: Principles and Applications*. (Wiley, 2008).
19. Lange, A., Seidel, K., Verdier, L., Luca, S., Baldus, M. Analysis of proton-proton transfer dynamics in rotating solids and their use for 3D structure determination. *Journal of the American Chemical Society* **125**, 12640-8 (2003).
20. Lange, A., Becker, S., Seidel, K., Giller, K., Pongs, O., Baldus, M. A concept for rapid protein-structure determination by solid-state NMR spectroscopy. *Angewandte Chemie-International Edition* **44**, 2089-92 (2005).
21. Szeverenyi, N. M., Sullivan, M. J., Maciel, G. E. Observation of spin exchange by two-dimensional fourier-transform ^{13}C cross-polarization magic-angle spinning. *Journal of Magnetic Resonance* **47**, 462-75 (1982).
22. Takegoshi, K., Nakamura, S., Terao, T. ^{13}C–^{1}H dipolar-assisted rotational resonance in magic-angle spinning NMR. *Chemical Physics Letters* **344**, 631-7 (2001).
23. Morcombe, C. R., Gaponenko, V., Byrd, R. A., Zilm, K. W. Diluting abundant spins by isotope edited radio frequency field assisted diffusion. *Journal of the American Chemical Society* **126**, 7196-7 (2004).
24. Torchia, D. A., Szabo, A. The Information-Content of Powder Lineshapes in the Fast Motion Limit. *Journal of Magnetic Resonance* **64**, 135-41 (1985).
25. Schneider, R., Seidel, K., Etzkorn, M., Lange, A., Becker, S., Baldus, M. Probing Molecular Motion by Double-Quantum (C-13,C-13) Solid-State NMR Spectroscopy: Application to Ubiquitin. *Journal of the American Chemical Society* **132**, 223-33 (2010).
26. Zachariae, U., Schneider, R., Briones, R., Gattin, Z., Demers, J.-P., Giller, K., Maier, E., Zweckstetter, M., Griesinger, C., Becker, S., Benz, R., de Groot, B. L., Lange, A. beta-Barrel Mobility Underlies Closure of the Voltage-Dependent Anion Channel. *Structure* **20**, 1540-9 (2012).
27. Hohwy, M., Rienstra, C. M., Jaroniec, C. P., Griffin, R. G. Fivefold symmetric homonuclear dipolar recoupling in rotating solids: Application to double quantum spectroscopy. *Journal of Chemical Physics* **110**, 7983-92 (1999).
28. Laws, D. D., Bitter, H. M. L., Jerschow, A. Solid-state NMR spectroscopic methods in chemistry. *Angewandte Chemie-International Edition* **41**, 3096-129 (2002).
29. LeMaster, D. M., Kushlan, D. M. Dynamical mapping of E-coli thioredoxin via C-13 NMR relaxation analysis. *Journal of the American Chemical Society* **118**, 9255-64 (1996).
30. Hong, M. Determination of multiple phi-torsion angles in proteins by selective and extensive ^{13}C labeling and two-dimensional solid-state NMR. *Journal of Magnetic Resonance* **139**, 389-401 (1999).
31. Lundström, P., Vallurupalli, P., Hansen, D. F., Kay, L. E. Isotope labeling methods for studies of excited protein states by relaxation dispersion NMR spectroscopy. *Nature Protocols* **4**, 1641-8 (2009).
32. Lundström, P., Teilum, K., Carstensen, T., Bezsonova, I., Wiesner, S., Hansen, D. F., Religa, T. L., Akke, M., Kay, L. E. Fractional C-13 enrichment of isolated carbons using [1-C-13]- or [2-C-13]-glucose facilitates the accurate measurement of dynamics at backbone C-alpha and side-chain methyl positions in proteins. *Journal of Biomolecular NMR* **38**, 199-212 (2007).
33. Loquet, A., Lv, G., Giller, K., Becker, S., Lange, A. ^{13}C spin dilution for simplified and complete solid-state NMR resonance assignment of insoluble biological assemblies. *Journal of the American Chemical Society* **133**, 4722-5 (2011).

Part II: Ultrafast Magic-Angle Spinning and Low-Power Sequences

2. Introduction to ultra-fast MAS spinning solid-state NMR

2.1. Summary

Recent progresses in multi-dimensional solid-state NMR correlation spectroscopy at high static magnetic fields and ultra-fast magic-angle spinning are discussed in this chapter. The chapter will focus on applications to protein resonance assignment and structure determination as well as on the characterization of protein dynamics in the solid state. First, the consequences of ultra-fast spinning on sensitivity and sample heating are considered. Recoupling and decoupling techniques at ultra-fast MAS are then presented, as well as more complex experiments assembled from these basic building blocks. Furthermore, we discuss new avenues in biomolecular solid-state NMR spectroscopy that become feasible in the ultra-fast spinning regime such as sensitivity enhancement based on paramagnetic doping.

Contribution statement

The present chapter is part of an invited review in the following Trends article:

"Progress in correlation spectroscopy at ultra-fast magic-angle spinning: Basic building blocks and complex experiments for the study of protein structure and dynamics", *Jean-Philippe Demers, Veniamin Chevelkov, Adam Lange,* **Solid State Nuclear Magnetic Resonance**, vol. 40(3), pp. 101–13 (2011)

Two additional sections on proton NMR and protein dynamics at ultra-fast MAS have been omitted in the present chapter and can be found in the original publication.

2.2. Introduction

The last decade has seen tremendous technological and methodological developments in the field of magic-angle spinning (MAS) solid-state NMR (ssNMR)[1,2]. These developments have allowed for the structural characterization of many samples of high biological interest: microcrystalline proteins, amyloid fibrils, oligomeric assemblies, and membrane proteins in a native-like environment. Part of those

developments can be attributed to the widespread adoption of high static magnetic fields.

At the same time, fast spinning MAS probe-heads of a new generation have been developed and are now commercially available. This promises to further improve the resolution and sensitivity of biological solid-state NMR. Additionally in the ultra-fast spinning regime, fundamentally new applications have become feasible. In this chapter, we will discuss these recent improvements: the study of paramagnetic metal binding centers, new methods for resonance assignment and collection of long-range distance restraints.

It should be noted that complementary information to the current article is available. In a review by Anne Lesage[1], the advantages of fast MAS are presented in the context of organic solid materials along with recent advances in structural investigations. The mechanical aspect of fast rotation and the impact of coil dimension on radio-frequencies (RF) are discussed in a recent chapter of the Encyclopedia of Magnetic Resonance by Ago Samoson and coworkers[3]. Another chapter of the Encyclopedia of Magnetic Resonance by Donghua H. Zhou[4] introduces fast MAS in combination with proton detection and paramagnetic doping.

In this chapter, we will distinguish between three regimes of spinning frequencies: low MAS below 20 kHz, fast MAS between 20–40 kHz, and ultra-fast MAS above 40 kHz. So far, ultra-fast MAS can be attained with rotors of reduced size: 40–50 kHz MAS for rotors of outer diameter (o.d.) 1.8 mm and 1.6 mm, and 60–70 kHz MAS for rotors of o.d. 1.3 mm and 1.2 mm. More recently, MAS frequencies of up to 80 kHz have been reached by rotors with an o.d. of 1.0 mm (JEOL, Japan)[5]. For comparison purposes, the characteristics of some commercially available rotors (Fig. 1a) are

summarized in Table 1. The reduction in rotor dimensions has important repercussions with respect to sensitivity, RF performance, and sample heating.

The effects of high spinning rates are decisive in preserving a competitive sensitivity compared to larger rotors. For resonances with large chemical shift anisotropies, the very fast rotation has the consequence of moving spinning sidebands out of the spectral window, increasing the intensity of the center band[6,7]. Homonuclear dipolar couplings are as well greatly reduced[5], resulting in narrower and more intense lines[8]. Pulse sequences developed for ultra-fast MAS promise further improvements in sensitivity and resolution by employing four complementing strategies: 1) increased transfer to cross-peaks during magnetization mixing steps, 2) reduced decay of spin-locked and transverse magnetization, 3) low-power sequences which enable fast recycling and long acquisition times, 4) proton detection. The application of ultra-fast MAS techniques to the study of proteins and other biomolecules is discussed in the following sections.

2.3. Influence of rotor diameter on NMR sensitivity

In NMR, sensitivity per unit square root time $(S/N)_t$, or more simply *sensitivity*, is generally defined as the signal to noise ratio (S/N) in the frequency domain per unit square root time (Eq. 1)[9]. It is closely related to the time-domain S/N directly following a 90° pulse, which has been described in a closed-form expression by Hoult and Richards[10]. The signal part (Eq. 2) depends notably on the sample volume V_{sample} and on the coil sensitivity $(B_1)_{xy}$, defined as the magnitude of the transverse magnetic field induced in the sample by a current of 1 ampere flowing in the RF coil[11]. In ultra-fast MAS rotors, the large reduction in active volume expectedly results in a reduction of the

absolute signal. Contrarily, for a solenoid coil, the coil sensitivity $(B_1)_{xy}$ is improved with smaller diameters (Eq. 3), reflecting an improvement of the filling factor. The noise amplitude σ_{noise} (Eq. 4) depends on the spectral bandwidth Δf, and resistance losses R_{noise} (conductive, magnetic, and dielectric losses) which are mostly dictated by the wire geometry of the receiver coil. If we make the fair assumption that the height to radius ratio is conserved among the different coils, then noise amplitude is unaffected by the rotor diameter. The outcome is that the absolute S/N is roughly proportional to the rotor diameter, as described in Ref. [7,11]. The S/N relative to the amount of material is improved in rotors of smaller diameter, which is advantageous for mass-limited samples (Fig. 1b).

[Eq. 1] $$(S/N)_t \equiv \frac{S}{\sigma_{noise}\sqrt{T_{tot}}}$$

S: Frequency domain signal peak amplitude
σ_{noise}: Frequency domain R.M.S. noise amplitude
T_{tot}: Total experimental time

[Eq. 2] $$(S/N)_t \propto V_{sample} \cdot (B_1)_{xy} \cdot M_0 \cdot \omega_0 \cdot K$$

$(B_1)_{xy}$: Sensitivity of the RF coil
V_{sample}: Sample volume
K: RF inhomogeneity factor
M_0: Initial magnetization
ω_0: Larmor frequency

[Eq. 3] $$(B_1)_{xy} = \frac{\mu_0 \cdot n}{2} \frac{1}{\sqrt{r_{coil}^{\,2} + \left(\frac{1}{2} h_{coil}\right)^2}}$$

μ_0: Vacuum permeability ($4\pi \cdot 10^{-7}$ N·A^{-2})
n: Number of wire turns in solenoid
r_{coil} and h_{coil}: Radius and height of the solenoid coil

[Eq. 4] $\sigma_{noise} = \sqrt{4 \cdot k_B \cdot T_c \cdot R_{noise} \cdot \Delta f}$

k_B: Boltzmann constant
T_c: Coil temperature
R_{noise}: Resistance losses
Δf : Bandwidth of the receiver

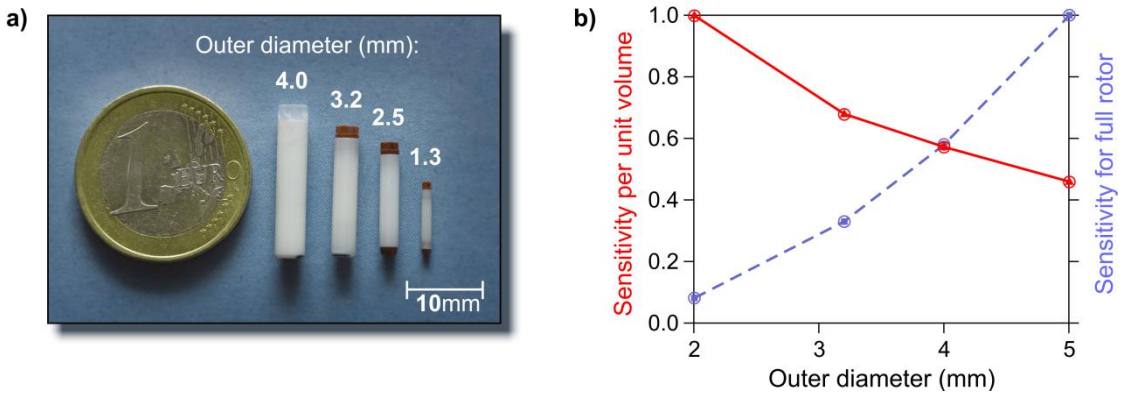

Figure 1: **a)** MAS rotors of different sizes. For ultra-fast MAS, rotors of 1.3 mm o.d. have an active volume of 1.7 µL and can spin up to 67 kHz. **b)** While larger rotors are more sensitive, (total sensitivity $(S/N)_t$, blue) small rotor sizes exhibit a higher sensitivity per unit volume ($(S/N)_t/V_{sample}$, red). Figure adapted from Ref. [12].

2.4. Influence of ultra-fast MAS on sample heating

The high coil sensitivity $(B_1)_{xy}$ also entails high RF performance for ultra-fast MAS probe-heads, meaning that large RF fields can be generated by the coil without requiring a large input power from the amplifiers[4]. However, such strong RF irradiation has the drawback of depositing a high amount of energy in the sample. For instance, rapidly-oscillating electric fields will bring free charge carriers in motion and will induce the realignment of molecular dipoles[13]. The resistance of the environment to such motion draws energy from the electric field; a sample with high resistance is termed "lossy". The situation is particularly critical in the study of biological samples[14,15], which are fragile and often preserved in ionic buffers or in a lipid environment. Eventually, the

heat contributed can lead to irremediable alteration of the sample, for instance degradation, denaturation, or aggregation. Another cause of concern is the effect of heating on experimental results. RF absorption and heat dissipation depend on numerous factors, crippling reproducibility of results if different pulse sequences, sample conditions, or instruments are used. The heterogeneity of spectroscopic observables due to spatial temperature gradients is exacerbated at strong RF fields and can persist for several hundreds of milliseconds after the heating pulse[15]. Small rotors are beneficial in this respect, as temperature gradients due to irradiation increase as the fourth power of the coil diameter[16].

To overcome the transient heat deposition by RF, one strategy is the development of pulse sequences requiring minimal amounts of irradiation power. Another strategy is to change the design of the RF coil in order to reduce the generation of time-varying electric fields during irradiation. Multiple designs have been introduced to replace or improve the typically employed solenoidal coils and are discussed in a review by Christopher V. Grant and coworkers[17]. Designs which have been combined with MAS include the scroll coil[18], the cross coil/solenoid[16], the Z coil[19], the loop-gap loaded coil[15], and "low-E" coils[20]. Both of those strategies directly improve spectral resolution since they allow longer acquisition times to be tolerated.

An additional cause of heating in MAS solid-state NMR is the power loss due to friction between the pressured gas and the bearings. The power loss is proportional to the square of the spinning frequency[21] and can lead to temperature increases of 40–60°C at 60 kHz MAS in comparison with the static case[4]. In contrast to RF heating, frictional heating remains uniform over time, although non-uniform spatially. It is likely that cooling gas remedies frictional heating more effectively than it does RF heating[16]. Because of the large temperature difference, the flow and temperature of the cooling gas have to be gradually adapted during spinning-up and spinning-down of the rotor. For

biological samples, a facile temperature calibration can be done on the water ^{1}H signal in combination with internal DSS chemical shift referencing[22].

Experiments for gathering distance restraints at ultra-fast MAS are still scarce. Since approaches based on PDSD will fail under ultra-fast MAS conditions, other strategies have to be pursued. One successful approach has been presented by Lewandowski et al.[23]. In this study, the authors demonstrated that the PAR experiment works even at an MAS frequency of 65 kHz. Application to GB1 yielded highly-resolved 2D spectra which allow for the extraction of long-range ^{13}C–^{13}C proximities.

Another promising approach for the detection of long-range restraints has recently been reported by Huber et al.[24]. This approach relies on the measurement of long-range proton-proton distances in extensively deuterated samples with proton-detected 3D and 4D correlation experiments. The method utilizes DREAM mixing for efficient proton-proton transfer and was applied to a sparsely methyl- and amide-labeled ubiquitin sample. Simultaneously, a very similar approach has also been presented by Linser et al.[25].

Meier and co-workers also demonstrated that $^{3h}J_{NC'}$ hydrogen-bond scalar couplings can be directly detected at ultra-fast MAS (55–57 kHz) using extensively deuterated samples[26]. The measurement of these sub-Hertz scalar couplings currently remains challenging but the approach is potentially very useful for structural biology applications and could further research on β-sheet-rich amyloid fibrils.

2.5. Protein resonance assignment and structural characterization

Achieving a complete assignment of the NMR signals constitutes the first step in structural studies using solid-state NMR and still stands as a major obstacle in obtaining

site-specific structural information. Usually, a combination of two-dimensional correlation spectra is required for the sequential resonance assignment of uniformly [^{13}C, ^{15}N]-labeled proteins. For larger systems, often assignment ambiguities remain and 3D or even 4D solid-state NMR experiments need to be performed[27-30].

At low MAS frequencies (~ 7–13 kHz), the standard repertoire of experiments for protein resonance assignment consists of homonuclear ^{13}C–^{13}C correlation experiments such as proton-driven spin-diffusion (PDSD)[31] or alternatively RAD/DARR[32,33] as well as heteronuclear ^{15}N–^{13}C correlation experiments such as NCACX or NCOCX. In the latter case, the transfer from C_α or C' to CX often relies on PDSD or DARR. However, PDSD and DARR become ineffective at high spinning frequencies and at high static magnetic fields. In the case of ultra-fast MAS, the MIRROR[34], RESORT[35], and PARIS[36,37] experiments can be used analogously to PDSD and DARR (see Section 4 on Dipolar recoupling at ultra-fast MAS). As well, Hou and coworkers reported homonuclear ^{13}C–^{13}C spin-diffusion experiments based on R-symmetry sequences[38]. They found that such experiments work well at fast MAS frequencies of 40 kHz where conventional PDSD or DARR experiments already fail.

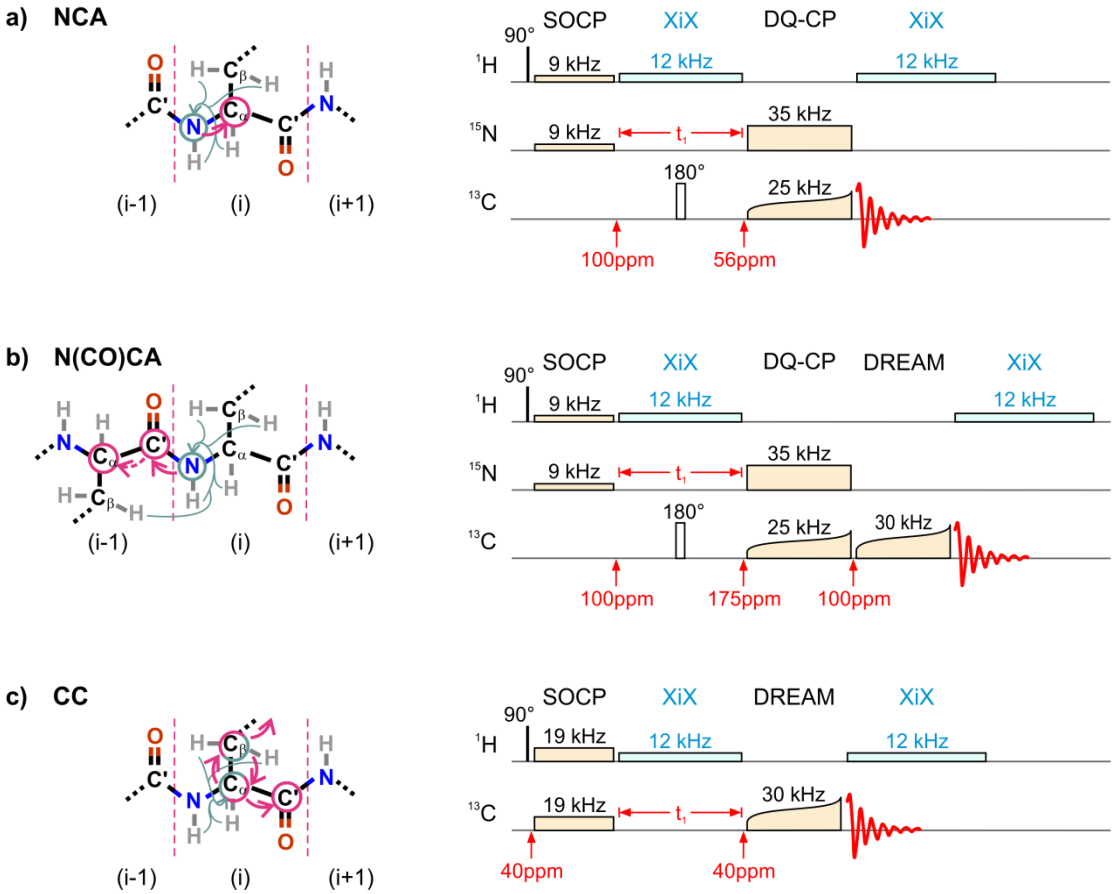

Figure 2: Complete set of low-power experiments for assignment of uniformly [^{13}C, ^{15}N]-labeled proteins. *(Left panels)* Assignment of backbone N-C correlation proceeds through **a)** NCA for intra-residue correlations and **b)** N(CO)CA for correlation to carbons of the preceding residue. **c)** Intra-residue side-chain ^{13}C correlations are obtained from the CC spectrum. *(Right panels)* Corresponding pulse schemes. Initial ^{1}H to ^{15}N transfer is carried through low-power SOCP at 9 kHz. The RF strength of SOCP is increased to 19 kHz in the CC experiment as in Ref. [39] in order to excite the full ^{13}C aliphatic region. For N–C experiments, J_{NC}-couplings are removed in the indirect dimension by application of a 180° pulse midway through t_1 evolution. Adiabatic shaped pulses are employed on the ^{13}C channel for SPECIFIC-CP and DREAM recoupling elements; the indicated frequency corresponds to the average RF strength. Low-power XiX decoupling is applied during t_1 evolution and acquisition. The ^{13}C carrier position is changed during experiments, indicated by red arrows. Figure adapted from Ref. [40].

Several first-order recoupling sequences for ^{13}C–^{13}C transfer have been introduced which work well at ultra-fast spinning, for example DREAM[41] providing double-quantum transfer, or RFDR[42,43] providing zero-quantum transfer. A general difference between PDSD which is a second-order process and first-order dipolar recoupling experiments such as DREAM and RFDR is that the latter ones are strongly influenced by dipolar truncation[44]. Here, transfer is restricted to the strongest dipolar couplings present, usually between directly bonded nuclei, e.g. C_α and C_β. Relying only on first-order sequences therefore restricts the number of observed correlations. The detection of sequential transfer, for instance between C_α nuclei of adjacent residues, feasible with PDSD[45], is therefore difficult to achieve with first-order recoupling sequences.

Nevertheless, it is in principle possible to compile a set of experiments suitable for the complete resonance assignment of uniformly labeled proteins at ultra-fast MAS. For instance, such a complete set of experiments was introduced by Vijayan et al. and is depicted in Fig. 2[40]. The set comprises CC, NCA, and N(CO)CA two-dimensional correlation experiments. Applications to ubiquitin and tau paired helical filaments are described in Ref. [40]. After resonance assignments have been obtained, ^{13}C and ^{15}N chemical shifts can be readily analyzed in terms of secondary structure using secondary chemical shifts[46] or statistical database approaches such as TALOS[47].

2.6. Paramagnetic doping and paramagnetic proteins

As previously mentioned, the ultra-fast spinning regime has the advantage that entirely low-power sequences can be applied[40,48]. While low-MAS heteronuclear decoupling sequences are *a priori* viable at faster MAS, an important realization from the beginning of the last decade was that commensurate or improved decoupling

performances are realized at low RF powers in the ultra-fast MAS regime[49]. The sequences which are currently considered to offer the best decoupling are low-power XiX[50], low-power TPPM[51], swept low-power TPPM[52], and low-amplitude PISSARRO[53]. In practice, more than one decoupling sequence should be tested, as the relative performance can fluctuate depending on the MAS frequency, static magnetic field B_0, and on the molecular system, similar to what was investigated at low MAS[54,55].

Since only weak RF fields in the order of 10–20 kHz are used for heteronuclear ^{1}H decoupling, the strain on the instrumentation and the heat deposition are mitigated. Multi-dimensional spectra can be recorded with longer acquisition times and faster repetition rates compared with experiments at low spinning frequencies and high power decoupling. For instance, an extremely well-resolved band-selective INADEQUATE-S^{3}E spectrum of microcrystalline GB1 is reported in Ref. [56], recorded with maximum acquisition times of 37 ms in t_1 and 50 ms in t_2 at 60 kHz MAS on a 1 GHz (23.5 T) spectrometer.

Such low-power approaches for resonance assignment and detection of structural restraints can be combined with paramagnetic optimized relaxation times[57,58]. The recycle delay can then be reduced and the resulting sensitivity enhancement compensates for the loss of sensitivity due the small sample volume of fast-spinning MAS rotors. For this purpose, paramagnetic dopants such as Cu-EDTA are added in concentrations of 10–250 mM. This shortens the ^{1}H T_1 relaxation times down to 50–100 ms[59]. Reif and co-workers have proposed to combine ultra-fast MAS, paramagnetic doping, and deuteration[14]. Nadaud and coworkers have demonstrated that a similar approach comprising 2D and 3D correlation spectra can also be applied to proteins with covalently bound paramagnetic tags[60].

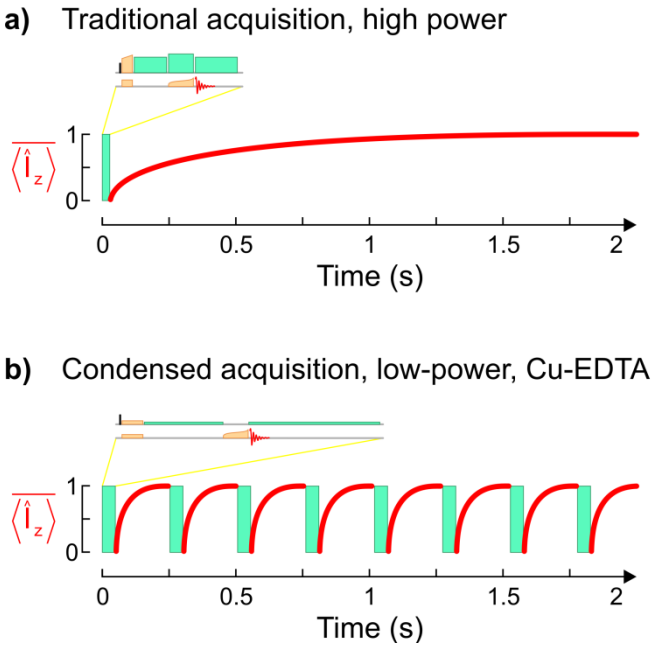

Figure 3: Fast repetition rates and paramagnetic doping. In traditional acquisition, the duration of the inter-scan delay is dictated by the delay necessary for heat dissipation, and by the recovery rate of proton longitudinal magnetization, as depicted by the red curve. **b)** In condensed acquisition, the experiment can be repeated at a faster rate, approximately an order of magnitude faster, owing to the acceleration of ^{1}H longitudinal relaxation rate by paramagnetic dopants. The use of entirely low-power sequences prevents excessive deposition of heat and allows for longer acquisition times, therefore increasing resolution.

Furthermore, fast recycling experiments can be readily applied to paramagnetic metalloproteins. For example, a 2D ^{13}C–^{13}C correlation spectrum of the oxidized, paramagnetic form of human copper zinc superoxide dismutase (SOD) could be acquired with a shortened recycle delay of 500 ms[61]. Bertini et al. reported the application of ultra-fast MAS and fast recycling protocols to detect residues as close as 5.6 Å from the Co^{II} in MMP-12[62]. This opens the way to characterize the metal coordination environment of metalloproteins by ssNMR which was previously unobservable at lower spinning frequencies due to large and highly anisotropic paramagnetic chemical shifts.

2.7. Dipolar recoupling at ultra-fast MAS

The standard building units for multi-dimensional ssNMR experiments are homonuclear and heteronuclear recoupling sequences, along with periods of evolution where decoupling is often required. Magnetization transfer can be mediated by a choice of mechanisms: through space via dipolar couplings, or through chemical bonds via *J*-couplings. The progress made in *J*-based sequences, see Ref. [56,63] for instance, has been recently discussed[1,64,65] and will not be considered here in detail. As previously mentioned, in many cases the homonuclear dipolar recoupling sequences that are employed at low MAS must be adapted as either they are not efficient anymore at ultra-fast MAS or their RF requirements are too elevated for the current instruments and samples. For example, symmetry-based pulse sequences such as SPC5[66] or C7 and POST–C7[67,68] require an irradiation of respectively 5 and 7 times the MAS frequency on the low-frequency channel. An important advantage of ultra-fast MAS is that ^{1}H decoupling can be omitted in many recoupling sequences such as DREAM[48], RFDR[69], CMpRR[70], and ^{15}N–^{13}C SPECIFIC-CP[40,59]. Another important advance in recent years is the emergence and better understanding of second-order recoupling sequences. The present section will highlight the particularities of dipolar recoupling techniques at ultra-fast MAS. We will discuss separately first-order and second-order recoupling techniques. Here, first-order indicates that the effect occurs due to the first term of the Magnus expansion in the average Hamiltonian treatment of the pulse sequence[71], while second-order effects arise due to the second term (commutator terms) of the Magnus expansion.

2.7.1. First-order dipolar recoupling: homonuclear double-quantum

First-order dipolar recoupling experiments fall into two categories depending on whether their effective Hamiltonian is of double-quantum (DQ) or zero-quantum (ZQ) nature[72]. The important consequence is that the transferred magnetization will change

its sign for DQ transfer but not for ZQ. For DQ mixing, this makes it possible to distinguish between direct transfers, which have negative cross-peaks relative to the diagonal, and relay transfers (i.e. two subsequent transfers during the same mixing period) which have positive cross-peaks.

Because of its low RF requirements, the double-quantum homonuclear rotary resonance condition, DQ-HORROR[73], is frequently employed (Eq. 5). In this sequence, *cw* irradiation is applied on the X channel at approximately $\frac{1}{2}\nu_r$, such that the sum of effective fields on A and B equals the MAS frequency. Here, X represents the nucleus for which recoupling occurs (e.g. ^{13}C, ^{15}N). The recoupling is commonly realized with the adiabatic version of DQ-HORROR, namely the DREAM scheme[41], which was first presented as a DQ filter scheme[74]. The initial magnetization is spin-locked with an applied RF of amplitude far inferior or far superior to the HORROR condition. The RF strength is then gradually changed, effectively 'dragging' the spin-system adiabatically through the recoupling condition (Fig. 4a). This makes the sequence robust against RF mismatch and distribution of dipolar coupling frequencies due to crystallite orientation and isotropic chemical shift distribution.

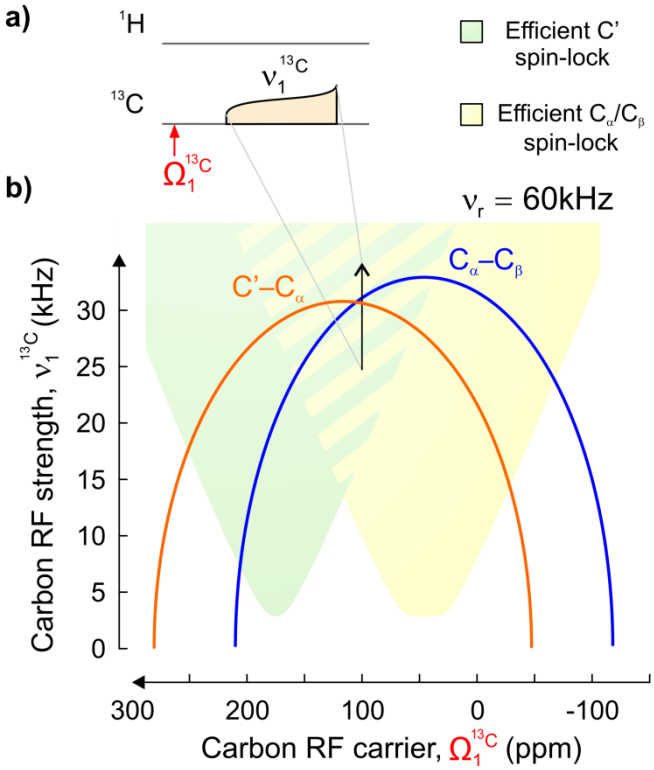

Figure 4: Figure 2.3: Optimization of 13C–13C DREAM transfer. **a)** The DREAM recoupling element is characterized by the carrier position $\Omega_1^{^{13}C}$ and the average RF strength ν_1^X. At ultra-fast MAS, no ^{1}H decoupling is applied during recoupling. **b)** Calculated transfer conditions for C'–C_α transfer (orange) and C_α–C_β transfer (blue). Transfer occurs at different RF strengths because of their different chemical shift separation, as calculated from Eq. 5. Typical ^{13}C isotropic chemical shifts are considered: C' (175.8 ppm), C_α (57.5 ppm) and C_β (34.6 ppm). The black arrow represents the amplitude of the RF field during a DREAM adiabatic sweep with carrier position at 100 ppm. Recoupling can be achieved off-resonance but the spin-lock is inefficient, leading to magnetization loss. Approximate regions of efficient spin-lock, as observed in ubiquitin at 18.8 T, are highlighted in green for C' and in yellow for C_α/C_β. The mixing duration for DREAM is optimized between 2–10 ms.

[Eq. 5] $$\nu_r = \underbrace{\sqrt{\nu_1^2 + \left(\Omega_{iso}^A\right)^2}}_{\text{effective field on spin A}} + \underbrace{\sqrt{\nu_1^2 + \left(\Omega_{iso}^B\right)^2}}_{\text{effective field on spin B}}$$

ν_r: MAS frequency
ν_1: RF nutation frequency
Ω_{iso}: Chemical shift offset relative to carrier

DREAM is narrow-banded at low MAS and broadband at ultra-fast MAS, as it can recouple two spins with an isotropic chemical shift separation of up to $\frac{1}{2}\nu_r$. This

feature is nicely illustrated in the work of Ernst et al.[48], where ^{13}C–^{13}C cross-peaks with increasing chemical shift separation appear as the spinning rate is increased from 30 to 60 kHz. This work also demonstrates that above a given spinning rate ($\geq$50 kHz MAS), cross-peak intensities are unaffected by the presence or absence of ^{1}H decoupling. The RF field strength employed for the DREAM shaped pulse depends on both the carrier position Ω_1^X and the chemical shift separation of the recoupled spin pair. Fig. 4b illustrates the different RF fields required for C_α–C' and C_α–C_β, transfers. Practically, the best transfer conditions are obtained with the carrier frequency set to the middle of the range of resonances to be recoupled and the average irradiation frequency slightly below $\frac{1}{2}\nu_r$ [41]. Due to the distribution of chemical shifts in proteins, different spin pairs cross the resonance condition at different times during the adiabatic sweep[75]. For example, as seen from the arrow depicted in Fig. 4b, the C'–C_α condition is traversed before the C_α–C_β condition. This leads to an intricate pattern of magnetization transfer and asymmetric cross-peak intensities in 2D spectra.

New DQ recoupling schemes have also been recently introduced for the study of ^{19}F–^{19}F proximities[76,77] or for ^{31}P recoupling[78]. Symmetry-based techniques are utilized in these schemes in order to be more robust against the broad range of ^{19}F chemical shifts, or against the large ^{31}P CSA.

2.7.2. First-order dipolar recoupling: homonuclear zero-quantum

The sign alternation is not encountered when using ZQ recoupling, of which the chief sequence at ultra-fast MAS is RFDR. In this sequence, a train of rotor-synchronized π (180°) pulses is applied on the X channel in the middle of every rotor period (Fig. 5b). RFDR has been firstly analyzed considering π pulses as delta functions[42,43], where dipolar couplings are restored only in an interaction frame which involves both RF and isotropic chemical shifts. However, it was then found that when finite pulse-width

effects are considered, an interaction frame involving the RF is sufficient to re-introduce the dipolar coupling, making RFDR largely insensitive to chemical shift offsets[79,80]. RFDR is versatile in the slow and fast MAS regimes (<40kHz), as it can be used in broadband or band-selective experiments. The band-specific implementation requires weaker-RF π pulses which occupy a larger fraction of the rotor period. In a study by Bayro and co-workers[81], this specificity has been combined with sparse labeling in order to reduce the number of actively recoupled nuclei and circumvent dipolar truncation. A large amount of aliphatic correlations, including long-range C_α–C_α contacts, could be obtained at 12.5 kHz MAS in [2-^{13}C]glycerol-labeled 2-PI3-SH3 amyloid fibrils. At ultra-fast MAS, RFDR is used as a broadband sequence and ^{1}H decoupling is generally omitted[61]. Proton irradiation can re-introduce depolarization conditions which are only avoided through a careful selection of ^{1}H RF strength, with independent levels chosen for the duration of the π pulse and for the window between pulses[69]. Proper phase cycling of the π pulses is critical to eliminate residual DQ dipolar terms or chemical shift terms. Usually, supercycles of the XY–4 scheme (XY–8, XY–16, XY–32) are employed[79-81]. These phase cycling schemes are beneficial in attenuating the imperfections introduced by the large number of consecutive π pulses.

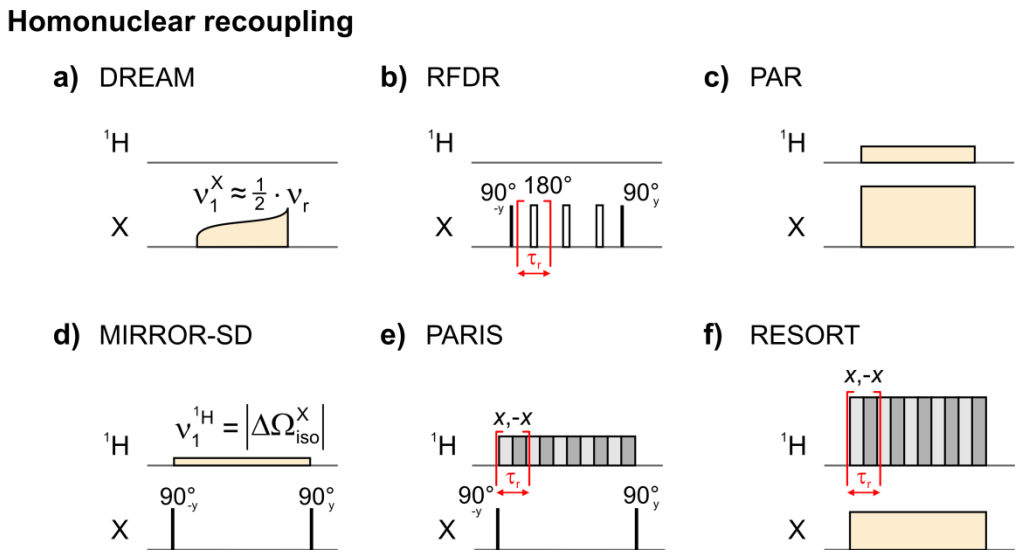

Figure 5: Building blocks for homonuclear recoupling. Representation of pulse sequence elements for homonuclear recoupling and spin diffusion at ultra-fast MAS: **a)–b)** first-order sequences and **c)–f)** second-order sequences. Initial magnetization on the *x*-axis of a first X-nuclei spin is transferred to *x*-axis magnetization of a second spin of the same isotope. Continuous-wave irradiation is denoted by yellow pulses and phase-alternated irradiation (*x*,-*x*) by light and dark grey blocks. For both channels, the carrier position is set in the mid-range $\Omega_1^X = \frac{1}{2}\left(\Omega_{min}^X + \Omega_{max}^X\right)$ of frequencies to be recoupled. **a)** In DREAM, ν_1^X is the average RF strength at midpoint during the sweep, as selected from Fig. 4b. Rotor-synchronized pulses are employed for **b)** RFDR, **e)** PARIS, and **f)** RESORT, with the period indicated in red (n.b. $\tau_r = \nu_r^{-1}$). For RFDR, the pulse is centered during one rotor period and $\tau_{pulse} << \tau_r$. For PARIS and RESORT, the duration for each pulse is half the rotor period. **c)** For ^{13}C–^{13}C PAR at 65 kHz MAS, a low-power condition of ($\nu_1^{^{13}C} \approx 1.12 \cdot \nu_r$, $\nu_1^{^1H} \approx 0.3 \cdot \nu_r$) can be exploited for biological samples. **d)** In MIRROR-SD, $\left|\Delta\Omega_{iso}^X\right|$ refers to the isotropic chemical shift separation between the two low-γ nuclei of interest. More information on pulse settings for PAR and RESORT is available in Ref. [23,82] and [35], respectively.

2.7.3. First-order dipolar recoupling: heteronuclear

For sensitivity reasons, the initial polarization in ssNMR experiments originates from protons. It is then transferred to low-γ nuclei (e.g. ^{13}C or ^{15}N). Hartmann-Hahn cross-polarization (CP) is the most common technique for this transfer[83,84]. The ZQ and

DQ recoupling conditions used in Hartmann-Hahn CP are described in Fig. 7a. The use of an adiabatic ramp is recommended to increase transfer efficiency[85-87], for reasons similar to those previously exposed for the DREAM scheme. While the RF strengths employed must be sufficiently strong to spin-lock the desired chemical shift ranges, a special attention must be paid to minimize the power deposition. The DQ n=1 condition constitutes the first-order recoupling condition with the lowest RF requirements. In a work by Laage et al.[88], this condition is used in a band-selective fashion in order to excite either the carbonyl or the aliphatic ^{13}C region of human SOD. RF field strengths of $\nu_1^{^{13}C} = 14$ kHz, $\nu_1^{^{1}H} = 46$ kHz are employed at 60 kHz MAS, as illustrated in Fig. 6a.

Hartmann-Hahn transfers between ^{15}N and ^{13}C are an important component of N–C, N–C–C, and C–N–C correlation experiments, sometimes referred to as double cross-polarization (DCP) experiments. Band-specific transfers are employed similarly to the SPECIFIC-CP technique introduced by Baldus and coworkers[89,90]. As any ZQ condition would require strong irradiation on at least one of the low-frequency channels, the DQ n=1 condition (Eq. 6) is the condition of choice at ultra-fast MAS (Fig. 6d).

[Eq. 6] $\nu_1^{^{13}C} + \nu_1^{^{15}N} = \nu_r$

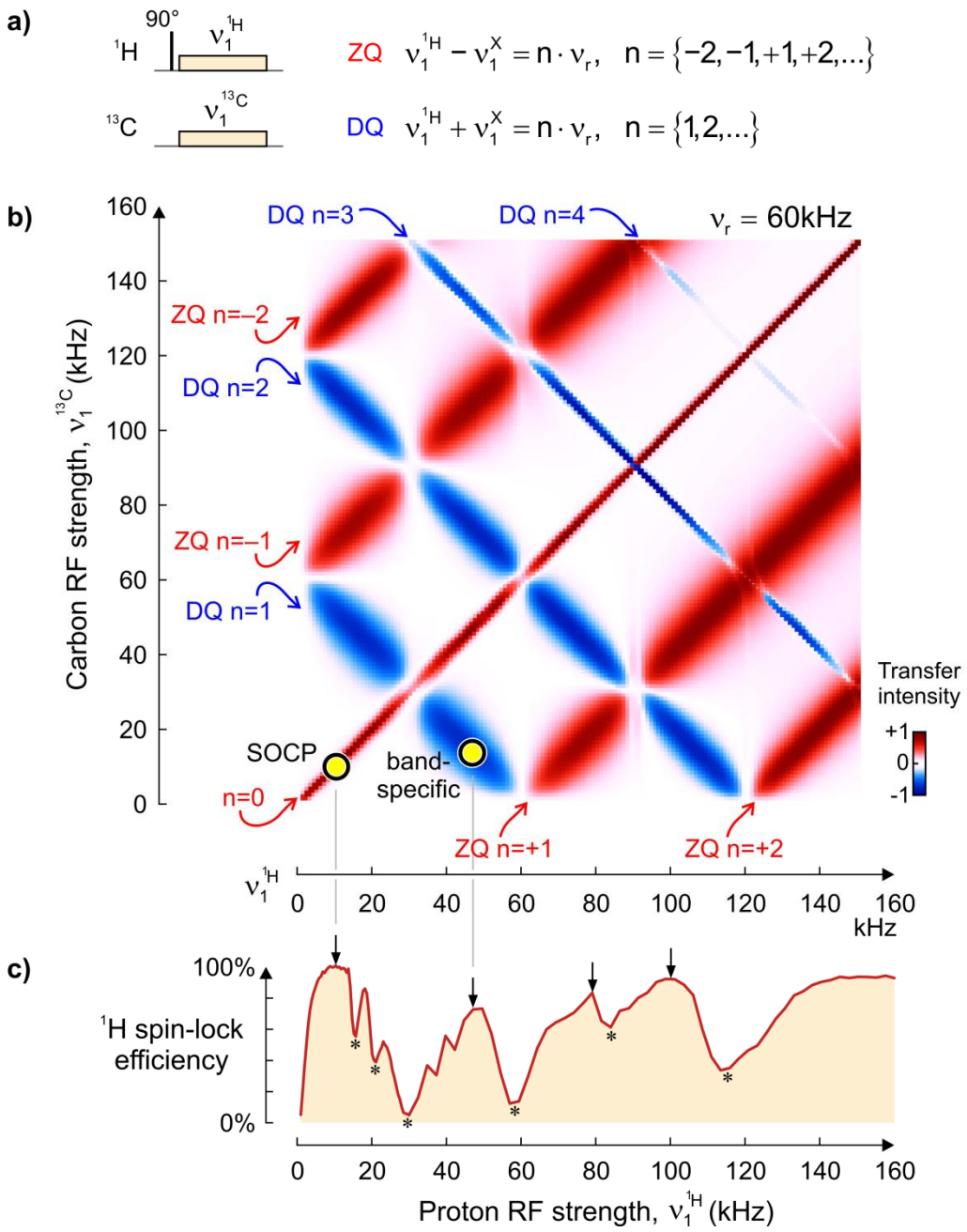
a)
90°
^{1}H
$\nu_1^{^1H}$
^{13}C
$\nu_1^{^{13}C}$
ZQ $\nu_1^{^1H} - \nu_1^X = n \cdot \nu_r, \quad n = \{-2,-1,+1,+2,...\}$
DQ $\nu_1^{^1H} + \nu_1^X = n \cdot \nu_r, \quad n = \{1,2,...\}$
b)
ν_r = 60kHz
DQ n=3
DQ n=4
ZQ n=–2
DQ n=2
ZQ n=–1
DQ n=1
SOCP
band-specific
n=0
ZQ n=+1
ZQ n=+2
Carbon RF strength, $\nu_1^{^{13}C}$ (kHz)
Transfer intensity
+1
0
-1
$\nu_1^{^1H}$
0 20 40 60 80 100 120 140 160
kHz
c)
100%
^{1}H spin-lock efficiency
0%
0 20 40 60 80 100 120 140 160
Proton RF strength, $\nu_1^{^1H}$ (kHz)

Figure 6: Selecting optimal ^{1}H–X cross-polarization conditions. **a)** Pulse scheme for ^{1}H–^{13}C CP. The ZQ (red) and DQ (blue) Hartmann-Hahn conditions lead respectively to positive and negative transfers. **b)** Map of magnetization transfer at 60 kHz MAS simulated for a CH_2 group, considering the ^{1}H–^{1}H and ^{1}H–^{13}C dipolar couplings. In addition to $n = \pm 1, \pm 2$ ZQ and n=1,2 DQ conditions, transfer conditions due to higher order terms appear: the n=0 condition used in SOCP, as well as the n=3 and n=4 DQ conditions. The RF settings for SOCP and band-specific CP are indicated. Intensities correspond to the average ^{13}C magnetization for time points between 6 and 8 ms. **c)** Efficiency of ^{1}H spin-lock as a function of RF strength, as measured after 2.5 ms of spin-lock in [^{15}N,^{13}C]-labeled glutamine. Conditions of least decay, indicated by arrows, should be employed for CP. Deleterious recoupling conditions at ratio of $\frac{1}{4}, \frac{1}{3}, \frac{1}{2}, 1, \frac{3}{2}$, and 2 times ν_r are indicated by asterisks.

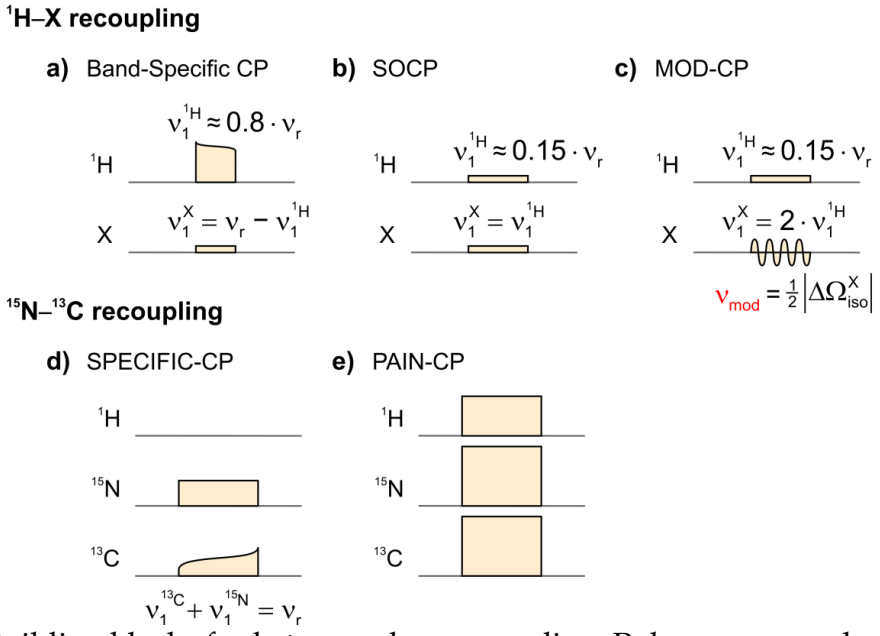

Figure 5: Building blocks for heteronuclear recoupling. Pulse sequence elements for ^{1}H–X and ^{15}N–^{13}C transfers. The initial state of the spin-system are **a)–c)** $\hat{I}_x^{^1H}$, and **d)–e)** $\hat{S}_x^{^{15}N}$; the desired final states are **a)–c)** $\hat{S}_x^{X}$, and **d)–e)** $\hat{S}_x^{^{13}C}$ For all channels, the carrier position is set to the mid-range of frequencies to be recoupled. RF field strength recommendations are indicated for **a)–d)**, see also Fig. 7b and 7c. For MOD-CP, a cosine amplitude modulation of frequency ν_{mod} is applied on the X channel. Adiabatic amplitude sweeps are applied for ^{1}H–X band-specific CP and ^{15}N–^{13}C SPECIFIC-CP. **e)** Pulse settings and durations for PAIN-CP are discussed in Ref. [91]

An adiabatic amplitude sweep is commonly employed on ^{13}C to increase the long-term stability of the experiment[27]. The RF fields on both channels must be chosen so as to prevent homonuclear recoupling conditions such as HORROR ($\nu_{RF} = \frac{1}{2}\nu_r$), or rotary resonance ($\nu_{RF} = \nu_r$). As ^{13}C has a large chemical shift range, RF frequencies between $\frac{1}{3}\nu_r$ and $\frac{2}{3}\nu_r$ should be avoided, especially at high fields or with a large adiabatic sweep. Alternatively, the adiabatic amplitude sweep can be done on the ^{15}N channel. Efficient transfers have been accomplished without proton decoupling at 40 kHz MAS and above[40,59]. Strong ^{1}H decoupling ($\nu_1^{^1H} >> 2.5 \cdot \nu_r$) is required in the fast MAS regime (20 kHz)[91,92], although efficient transfers might be possible in some conditions in the absence of ^{1}H decoupling[93].

2.7.4. Second-order recoupling

The previously mentioned first-order recoupling sequences are necessarily susceptible to the phenomenon of dipolar truncation[45,94]: in a multi-spin system, magnetization is preferentially transferred to a strongly coupled partner, extinguishing transfer to a weakly coupled partner. Sequences operating through a second-order mechanism, less prone to dipolar truncation, are appropriate for transfer to remote nuclei and collection of long-ranged distance restraints. Second-order recoupling sequences that work well in the ultra-fast MAS regime include PAR[23,82,95], MIRROR-SD[34], RESORT[35], and PARIS[36,37,96] in the homonuclear case; PAIN-CP[91,92], SOCP[97], MOD-CP[39], and MIRROR-CP[98] in the heteronuclear case.

The general designation of third spin assisted recoupling (TSAR) describes a mechanism B–[A]–C where two nuclei B and C are recoupled through their respective dipolar coupling with a third spin A (i.e. B–A and C–A couplings) rather than directly[92,95,99]. The first use of the TSAR mechanism for magnetization transfer has been

introduced in a work by Lewandowski and coworkers with Proton assisted insensitive nuclei cross polarization (PAIN-CP) where second-order N–C transfer was demonstrated at 20 kHz MAS[92]. The ^{15}N–[^{1}H]–^{13}C TSAR mechanism is obtained by applying *cw* irradiation simultaneously on three channels (Fig. 6e): ^{1}H, ^{13}C, and ^{15}N. A thorough theoretical description of PAIN was recently published[91]. The homonuclear analog of PAIN, Proton assisted recoupling (PAR), generates X–[^{1}H]–X transfer by concurrent *cw* irradiation on the proton and X channel (Fig. 5c). For ^{15}N–^{15}N PAR at 20 kHz MAS, ($\nu_1^{^1H} = \nu_1^{^{15}N} > 2\cdot\nu_r$) and ($\nu_1^{^{15}N} \approx 0.2\cdot\nu_r$, $\nu_1^{^1H} \approx 3\cdot\nu_r$) are suggested. Inter-nuclear proximities can be probed from the build-up of transferred intensity during the PAR element, as demonstrated with ^{13}C–^{13}C cross-peak build-ups in microcrystalline Crh[95]. The use of PAR at ultra-fast MAS (65 kHz MAS) was demonstrated on microcrystalline GB1[23] where ^{13}C–^{13}C correlations could be obtained with a low-power condition of ($\nu_1^{^{13}C} \approx 1.12\cdot\nu_r$, $\nu_1^{^1H} \approx 0.3\cdot\nu_r$). A condition at ($\nu_1^{^{13}C} \approx 1.75\cdot\nu_r$, $\nu_1^{^1H} \approx 1.3\cdot\nu_r$) has also been used. Possible optimization protocols for PAR are discussed in Ref. [23,82]. When setting up a PAR or a PAIN experiment, an important aspect is to avoid RF frequencies which lead to first-order recoupling conditions (e.g. HORROR, rotary resonance, and Hartmann-Hahn matching). First, the regions to be excluded from the optimization space are identified by simulating an interference map of the spin system. RF power levels are then optimized around regions of known high transfer, identified from a polarization transfer map. Scripts for generating such maps, including C_α–C_β, C_α–C', and C_α–C_γ transfers, are available[23].

Analogous to PAR, the RESORT experiment has been presented for homonuclear transfer[35]. The low-γ nuclei are spin-locked with *cw* irradiation; however in this case, phase-alternated irradiation is applied on ^{1}H (Fig. 5f). This generates an effective Hamiltonian with the same form as for PAR but with different transfer conditions. RESORT has been demonstrated at 40 kHz MAS on microcrystalline ubiquitin.

In contrast to previous sequences, second-order recoupling can also be accomplished with sequences where no irradiation is applied on the X channel. For example, proton spin diffusion (^{1}H–^{1}H) and proton-driven spin diffusion (^{13}C–^{13}C or ^{15}N–^{15}N) do not require any irradiation during mixing. However, as PDSD relies on energy-level broadening due to homonuclear ^{1}H–^{1}H and heteronuclear ^{1}H–X dipolar interactions to increase the spectral overlap between low-γ spin pairs, it only functions at low MAS. In the fast MAS range, the dipolar-assisted rotational resonance (DARR) method is used to accelerate the transfer[32,100]. According to Takegoshi and coworkers[100], the effect of irradiating the protons at the rotary resonance condition (Eq. 7) is to restore the spectral overlap between a sideband of an X spin and the ^{1}H–X dipolar pattern of another X spin. Spin-diffusion mediated by DARR is abolished at ultra-fast MAS. Indeed, in a study by Scholz and coworkers, it was found that irradiating at the n=1 or n=2 DARR condition could not induce C' to C_α transfer at 45 kHz MAS[34]. Instead, proton irradiation at the mixed rotational and rotary resonance (MIRROR) condition was found to mediate spin-diffusion (Fig. 5d). The strongest transfer occurs when the applied field on ^{1}H matches the ^{13}C chemical shift difference (Eq. 8, n=0). The recoupling can be carried using phase-alternated irradiation instead of *cw*, providing increased robustness against $\nu_1^{^1H}$ mismatch. Because of the dependence on ^{13}C chemical shift, MIRROR is an intrinsically band-selective sequence. This building block is particular in that it has a dual function and can promote both ^{13}C–^{13}C recoupling (MIRROR-SD) and ^{1}H–^{13}C transfer (MIRROR-CP)[98]. The PARIS scheme has also been proposed to promote ^{13}C–^{13}C recoupling[36] and it employs phase-alternated ^{1}H pulses which have a duration of either $\frac{1}{2}$ or 2 times the rotor period (Fig. 5e). PARIS-*xy*, a variant of PARIS with the *x*,-*x*,-*y*,*y* phase cycle[37], was recently used in the 39–52 kHz MAS range to record ^{13}C–^{13}C correlations in selectively-labeled amyloid-β peptides[96].

[Eq. 7] $\nu_1^{^1H} = n \cdot \nu_r, \quad n = \{1, 2\}$

[Eq. 8] $\nu_1^{^1H} = n \cdot \nu_r \pm \Delta\Omega_{iso}^{^{13}C}, \quad n = \{0, \pm1, \pm2, \pm3, \pm4\}$

Second-order processes can also accomplish the initial cross-polarization from ^{1}H to low-γ nuclei. Indeed, second-order cross-polarization (SOCP) was introduced in a study by Lange et al.[97]. An important observation is that decay during ^{1}H spin-lock is highly dependent on the applied RF strength. Efficient spin-locking of ^{1}H magnetization does not require strong RF fields, but can be accomplished with low-power irradiation, e.g. 9.4 kHz at 65 kHz MAS. The most efficient ^{1}H RF frequencies only appear at certain ratios of the MAS frequency, usually with $\nu_1^{^1H}$ equal to 0.15, 1.67, and 2.55 times ν_r (Fig. 7c). Those ratios are identified by monitoring the signal intensity as a function of ^{1}H spin-lock field. SOCP is achieved with the n=0 Hartman-Hahn condition: $\nu_1^{^1H} = \nu_1^X$ (Fig. 6b). The predominant transfer mechanism is due to second-order cross-terms between homonuclear and heteronuclear dipolar couplings, although transfer can in principle also occur through *J*-couplings. Notable advantages of SOCP are the higher sensitivity compared to first-order high-power CP, as initial magnetization can originate from protons not directly coupled to the S spin, and the robustness against RF field inhomogeneities, due to matching at the n=0 condition. SOCP is employed in a band-selective fashion in the construction of a complete set of experiments for protein assignment at ultra-fast MAS (Fig. 2). For the initial H–X transfer, band specificity is beneficial for N–C experiments; however, broadband excitation may be desired in the case of C–C spectra. The RF strength on both channels can then be slightly increased to 19 kHz at 60 kHz MAS, therefore avoiding the higher order $\nu_1 = \frac{1}{4}\nu_r$ and $\nu_1 = \frac{1}{3}\nu_r$ recoupling conditions. When two regions present a large chemical shift separation $\left|\Delta\Omega_{iso}^X\right|$, for instance C' and C_α in proteins, the simultaneous excitation of both regions is achievable at low-power through the amplitude-modulated second-order cross-

polarization scheme (MOD-CP)[39]. In the MOD-CP scheme, a cosine amplitude modulation with frequency $\nu_{mod} = \frac{1}{2}\left|\Delta\Omega^{X}_{iso}\right|$ is applied on the X channel (Fig. 6c). The ^{13}C RF strength is doubled, $\nu_1^X = 2 \cdot \nu_1^{^1H}$, creating the two distinct excitation regions. The simultaneous excitation of C' and C_α, or C' and C_β regions is demonstrated in microcrystalline ubiquitin at 60 kHz. MOD-CP restores the high information content per spectrum as found in high-power broadband excitation, while limiting the RF expenditure of the pulse sequence. MOD-CP can potentially be exploited for the study of organic materials, since several other spin–$^1/_2$ nuclei such as ^{31}P, ^{15}N, ^{29}Si, and ^{19}F cover a large range of isotropic chemical shifts.

2.8. Conclusions

A new generation of fast spinning MAS probe-heads has opened ways to improved resolution and sensitivity of biological solid-state NMR. Additionally, fundamentally new applications such as the study of paramagnetic metalloproteins have become feasible in the ultra-fast spinning regime. In this chapter, we have discussed those recent developments: the study of paramagnetic metal binding centers, and new methods for resonance assignment and detection of long-range distance restraints. Additionally, the topics of proton NMR at fast MAS and the study of protein dynamics are presented in our Trends article[101]. We expect that ongoing research from an increasing number of laboratories in this still largely unexplored area of solid-state NMR will lead to even more powerful methods and exciting new applications.

2.9. References

1. Lesage, A. Recent advances in solid-state NMR spectroscopy of spin I=$^1/_2$ nuclei. *Physical Chemistry Chemical Physics* **11**, 6876-91 (2009).
2. Renault, M., Cukkemane, A., Baldus, M. Solid-State NMR Spectroscopy on Complex Biomolecules. *Angewandte Chemie-International Edition* **49**, 8346-57 (2010).

3. Samoson, A., Tuherm, T., Past, J., Reinhold, A., Heinmaa, I., Anupõld, T., Smith, M. E., Pike, K. J. *Fast Magic-Angle Spinning: Implications*. 1-20 (John Wiley & Sons, Ltd, 2010).
4. Zhou, D. H. *Fast Magic Angle Spinning for Protein Solid-State NMR Spectroscopy*. 331-342 (John Wiley & Sons, Ltd, 2007).
5. Nishiyama, Y., Endo, Y., Nemoto, T., Utsumi, H., Yamauchi, K., Hioka, K., Asakura, T. Very fast magic angle spinning ^{1}H–^{14}N 2D solid-state NMR: Sub-micro-liter sample data collection in a few minutes. *Journal of Magnetic Resonance* **208**, 44-8 (2011).
6. Herzfeld, J., Berger, A. E. Sideband Intensities in NMR-Spectra of Samples Spinning at the Magic Angle. *Journal of Chemical Physics* **73**, 6021-30 (1980).
7. Ernst, M., Detken, A., Bockmann, A., Meier, B. H. NMR spectra of a microcrystalline protein at 30 kHz MAS. *Journal of the American Chemical Society* **125**, 15807-10 (2003).
8. Ernst, M., Samoson, A., Meier, B. H. Low-power decoupling in fast magic-angle spinning NMR. *Chemical Physics Letters* **348**, 293-302 (2001).
9. Ernst, R. R., Bodenhausen, G., Wokaun, A. *Principles of nuclear magnetic resonance in one and two dimensions*. 148-157 (Clarendon Press, 1994).
10. Hoult, D. I., Richards, R. E. Signal-to-Noise Ratio of Nuclear Magnetic-Resonance Experiment. *Journal of Magnetic Resonance* **24**, 71-85 (1976).
11. Peck, T. L., Magin, R. L., Lauterbur, P. C. Design and Analysis of Microcoils for NMR Microscopy. *Journal of Magnetic Resonance Series B* **108**, 114-24 (1995).
12. McNeill, S. A., Gor'kov, P. L., Struppe, J., Brey, W. W., Long, J. R. Optimizing ssNMR experiments for dilute proteins in heterogeneous mixtures at high magnetic fields. *Magn Reson Chem* **45**, S209-S20 (2007).
13. de Lacaillerie, J. B. D., Jarry, B., Pascui, O., Reichert, D. "Cooking the sample": Radiofrequency induced heating during solid-state NMR experiments. *Solid State Nuclear Magnetic Resonance* **28**, 225-32 (2005).
14. Linser, R., Chevelkov, V., Diehl, A., Reif, B. Sensitivity enhancement using paramagnetic relaxation in MAS solid-state NMR of perdeuterated proteins. *Journal of Magnetic Resonance* **189**, 209-16 (2007).
15. Krahn, A., Priller, U., Emsley, L., Engelke, F. Resonator with reduced sample heating and increased homogeneity for solid-state NMR. *Journal of Magnetic Resonance* **191**, 78-92 (2008).
16. Doty, F. D., Kulkarni, J., Turner, C., Entzminger, G., Bielecki, A. Using a cross-coil to reduce RF heating by an order of magnitude in triple-resonance multinuclear MAS at high fields. *Journal of Magnetic Resonance* **182**, 239-53 (2006).
17. Grant, C. V., Wu, C. H., Opella, S. J. Probes for high field solid-state NMR of lossy biological samples. *Journal of Magnetic Resonance* **204**, 180-8 (2010).
18. Stringer, J. A., Bronnimann, C. E., Mullen, C. G., Zhou, D. H. H., Stellfox, S. A., Li, Y., Williams, E. H., Rienstra, C. M. Reduction of RF-induced sample heating with a scroll coil resonator structure for solid-state NMR probes. *Journal of Magnetic Resonance* **173**, 40-8 (2005).
19. Dillmann, B., Elbayed, K., Zeiger, H., Weingertner, M. C., Plotto, M., Engelke, F. A novel low-E field coil to minimize heating of biological samples in solid-state multinuclear NMR experiments. *Journal of Magnetic Resonance* **187**, 10-8 (2007).
20. McNeill, S. A., Gor'kov, P. L., Shetty, K., Brey, W. W., Long, J. R. A low-E magic angle spinning probe for biological solid state NMR at 750 MHz. *Journal of Magnetic Resonance* **197**, 135-44 (2009).
21. Stachowiak, G. W., Batchelor, A. W. *Engineering tribology*. 266 (Elsevier Butterworth-Heinemann, 2005).
22. Bockmann, A., Gardiennet, C., Verel, R., Hunkeler, A., Loquet, A., Pintacuda, G., Emsley, L., Meier, B. H., Lesage, A. Characterization of different water pools in solid-state NMR protein samples. *Journal of Biomolecular NMR* **45**, 319-27 (2009).
23. Lewandowski, J. R., De Paepe, G., Eddy, M. T., Struppe, J., Maas, W., Griffin, R. G. Proton Assisted Recoupling at High Spinning Frequencies. *Journal of Physical Chemistry B* **113**, 9062-9 (2009).

24. Huber, M., Hiller, S., Schanda, P., Ernst, M., Boeckmann, A., Verel, R., Meier, B. H. A Proton-Detected 4D Solid-State NMR Experiment for Protein Structure Determination. *Chemphyschem : a European journal of chemical physics and physical chemistry* **12**, 915-8 (2011).
25. Linser, R., Bardiaux, B., Higman, V., Fink, U., Reif, B. Structure Calculation from Unambiguous Long-Range Amide and Methyl ^{1}H–^{1}H Distance Restraints for a Microcrystalline Protein with MAS Solid-State NMR Spectroscopy. *Journal of the American Chemical Society* **133**, 5905-12 (2011).
26. Schanda, P., Huber, M., Verel, R., Ernst, M., Meier, B. H. Direct Detection of $^{3h}J_{NC'}$ Hydrogen-Bond Scalar Couplings in Proteins by Solid-State NMR Spectroscopy. *Angewandte Chemie-International Edition* **48**, 9322-5 (2009).
27. Franks, W. T., Kloepper, K. D., Wylie, B. J., Rienstra, C. M. Four-dimensional heteronuclear correlation experiments for chemical shift assignment of solid proteins. *Journal of Biomolecular NMR* **39**, 107-31 (2007).
28. Franks, W. T., Atreya, H. S., Szyperski, T., Rienstra, C. M. GFT projection NMR spectroscopy for proteins in the solid state. *Journal of Biomolecular NMR* **48**, 213-23 (2010).
29. Schuetz, A., Wasmer, C., Habenstein, B., Verel, R., Greenwald, J., Riek, R., Bockmann, A., Meier, B. H. Protocols for the Sequential Solid-State NMR Spectroscopic Assignment of a Uniformly Labeled 25 kDa Protein: HET-s(1-227). *ChemBioChem* **11**, 1543-51 (2010).
30. Sperling, L. J., Berthold, D. A., Sasser, T. L., Jeisy-Scott, V., Rienstra, C. M. Assignment Strategies for Large Proteins by Magic-Angle Spinning NMR: The 21-kDa Disulfide-Bond-Forming Enzyme DsbA. *Journal of molecular biology* **399**, 268-82 (2010).
31. Szeverenyi, N. M., Sullivan, M. J., Maciel, G. E. Observation of spin exchange by two-dimensional fourier-transform ^{13}C cross-polarization magic-angle spinning. *Journal of Magnetic Resonance* **47**, 462-75 (1982).
32. Takegoshi, K., Nakamura, S., Terao, T. ^{13}C–^{1}H dipolar-assisted rotational resonance in magic-angle spinning NMR. *Chemical Physics Letters* **344**, 631-7 (2001).
33. Morcombe, C. R., Gaponenko, V., Byrd, R. A., Zilm, K. W. Diluting abundant spins by isotope edited radio frequency field assisted diffusion. *Journal of the American Chemical Society* **126**, 7196-7 (2004).
34. Scholz, I., Huber, M., Manolikas, T., Meier, B. H., Ernst, M. MIRROR recoupling and its application to spin diffusion under fast magic-angle spinning. *Chemical Physics Letters* **460**, 278-83 (2008).
35. Scholz, I., Meier, B. H., Ernst, M. NMR polarization transfer by second-order resonant recoupling: RESORT. *Chemical Physics Letters* **485**, 335-42 (2010).
36. Weingarth, M., Demco, D. E., Bodenhausen, G., Tekely, P. Improved magnetization transfer in solid-state NMR with fast magic angle spinning. *Chemical Physics Letters* **469**, 342-8 (2009).
37. Weingarth, M., Bodenhausen, G., Tekely, P. Broadband magnetization transfer using moderate radio-frequency fields for NMR with very high static fields and spinning speeds. *Chemical Physics Letters* **488**, 10-6 (2010).
38. Hou, G., Yan, S., Sun, S., Han, Y., Byeon, I. L., Ahn, J., Concel, J., Samoson, A., Gronenborn, A. M., Polenova, T. Spin diffusion driven by R-symmetry sequences: applications to homonuclear correlation spectroscopy in MAS NMR of biological and organic solids. *Journal of the American Chemical Society* **133**, 3943-53 (2011).
39. Demers, J.-P., Vijayan, V., Becker, S., Lange, A. Tailored low-power cross-polarization under fast magic-angle spinning. *Journal of Magnetic Resonance* **205**, 216-23 (2010).
40. Vijayan, V., Demers, J. P., Biernat, J., Mandelkow, E., Becker, S., Lange, A. Low-Power Solid-State NMR Experiments for Resonance Assignment under Fast Magic-Angle Spinning. *Chemphyschem : a European journal of chemical physics and physical chemistry* **10**, 2205-8 (2009).
41. Verel, R., Ernst, M., Meier, B. H. Adiabatic dipolar recoupling in solid-state NMR: The DREAM scheme. *Journal of Magnetic Resonance* **150**, 81-99 (2001).
42. Bennett, A. E., Griffin, R. G., Ok, J. H., Vega, S. Chemical shift correlation spectroscopy in rotating solids: Radio frequency-driven dipolar recoupling and longitudinal exchange. *Journal of Chemical Physics* **96**, 8624-7 (1992).

43. Sodickson, D. K., Levitt, M. H., Vega, S., Griffin, R. G. Broad-Band Dipolar Recoupling in the Nuclear-Magnetic-Resonance of Rotating Solids. *Journal of Chemical Physics* **98**, 6742-8 (1993).
44. Bayro, M. J., Huber, M., Ramachandran, R., Davenport, T. C., Meier, B. H., Ernst, M., Griffin, R. G. Dipolar truncation in magic-angle spinning NMR recoupling experiments. *Journal of Chemical Physics* **130** (2009).
45. Grommek, A., Meier, B. H., Ernst, M. Distance information from proton-driven spin diffusion under MAS. *Chemical Physics Letters* **427**, 404-9 (2006).
46. Luca, S., Filippov, D. V., van Boom, J. H., Oschkinat, H., de Groot, H. J. M., Baldus, M. Secondary chemical shifts in immobilized peptides and proteins: A qualitative basis for structure refinement under Magic Angle Spinning. *Journal of Biomolecular NMR* **20**, 325-31 (2001).
47. Cornilescu, G., Delaglio, F., Bax, A. Protein backbone angle restraints from searching a database for chemical shift and sequence homology. *Journal of Biomolecular NMR* **13**, 289-302 (1999).
48. Ernst, M., Meier, M. A., Tuherm, T., Samoson, A., Meier, B. H. Low-power high-resolution solid-state NMR of peptides and proteins. *Journal of the American Chemical Society* **126**, 4764-5 (2004).
49. Ernst, M. Heteronuclear spin decoupling in solid-state NMR under magic-angle sample spinning. *Journal of Magnetic Resonance* **162**, 1-34 (2003).
50. Ernst, M., Samoson, A., Meier, B. H. Low-power XiX decoupling in MAS NMR experiments. *Journal of Magnetic Resonance* **163**, 332-9 (2003).
51. Kotecha, M., Wickramasinghe, N. P., Ishii, Y. Efficient low-power heteronuclear decoupling in ^{13}C high-resolution solid-state NMR under fast magic angle spinning. *Magn Reson Chem* **45**, S221-S30 (2007).
52. Lewandowski, J. R., Sein, J., Sass, H. J., Grzesiek, S., Blackledge, M., Emsley, L. Measurement of Site-Specific ^{13}C Spin-Lattice Relaxation in a Crystalline Protein. *Journal of the American Chemical Society* **132**, 8252-4 (2010).
53. Weingarth, M., Bodenhausen, G., Tekely, P. Low-power decoupling at high spinning frequencies in high static fields. *Journal of Magnetic Resonance* **199**, 238-41 (2009).
54. Gerbaud, G., Caldarelli, S., Ziarelli, F., Gastaldi, S. The influence of the molecular system on the performance of heteronuclear decoupling in solid-state NMR. *Journal of Magnetic Resonance* **210**, 75-81 (2011).
55. Comellas, G., Lopez, J. J., Nieuwkoop, A. J., Lemkau, L. R., Rienstra, C. M. Straightforward, effective calibration of SPINAL-64 decoupling results in the enhancement of sensitivity and resolution of biomolecular solid-state NMR. *Journal of Magnetic Resonance* **209**, 131-5 (2011).
56. Bertini, I., Emsley, L., Felli, I. C., Laage, S., Lesage, A., Lewandowski, J. R., Marchetti, A., Pierattelli, R., Pintacuda, G. High-resolution and sensitivity through-bond correlations in ultra-fast magic angle spinning (MAS) solid-state NMR. *Chemical Science* **2**, 345-8 (2011).
57. Ganapathy, S., Naito, A., McDowell, C. A. Paramagnetic Doping as an Aid in Obtaining High-Resolution ^{13}C NMR Spectra of Biomolecules in the Solid State. *Journal of the American Chemical Society* **103**, 6011-5 (1981).
58. Wickramasinghe, N. P., Kotecha, M., Samoson, A., Past, J., Ishii, Y. Sensitivity enhancement in ^{13}C solid-state NMR of protein microcrystals by use of paramagnetic metal ions for optimizing ^{1}H T_1 relaxation. *Journal of Magnetic Resonance* **184**, 350-6 (2007).
59. Wickramasinghe, N. P., Parthasarathy, S., Jones, C. R., Bhardwaj, C., Long, F., Kotecha, M., Mehboob, S., Fung, L. W. M., Past, J., Samoson, A., Ishii, Y. Nanomole-scale protein solid-state NMR by breaking intrinsic ^{1}H T_1 boundaries. *Nature Methods* **6**, 215-8 (2009).
60. Nadaud, P. S., Helmus, J. J., Sengupta, I., Jaroniec, C. P. Rapid Acquisition of Multidimensional Solid-State NMR Spectra of Proteins Facilitated by Covalently Bound Paramagnetic Tags. *Journal of the American Chemical Society* **132**, 9561-3 (2010).
61. Laage, S., Sachleben, J. R., Steuernagel, S., Pierattelli, R., Pintacuda, G., Emsley, L. Fast acquisition of multi-dimensional spectra in solid-state NMR enabled by ultra-fast MAS. *Journal of Magnetic Resonance* **196**, 133-41 (2009).

62. Bertini, I., Emsley, L., Lelli, M., Luchinat, C., Mao, J. F., Pintacuda, G. Ultrafast MAS Solid-State NMR Permits Extensive ^{13}C and ^{1}H Detection in Paramagnetic Metalloproteins. *Journal of the American Chemical Society* **132**, 5558-9 (2010).
63. Tian, Y., Chen, L. L., Niks, D., Kaiser, J. M., Lai, J. F., Rienstra, C. M., Dunn, M. F., Mueller, L. J. J-Based 3D sidechain correlation in solid-state proteins. *Physical Chemistry Chemical Physics* **11**, 7078-86 (2009).
64. Lesage, A. *Indirect Coupling and Connectivity*. 317-330 (John Wiley & Sons, Ltd, 2007).
65. Mueller, L. J., Titman, J. J. *Correlation Spectroscopy for Resonance Assignments in Solid-State Proteins using J-Couplings*. 297-316 (John Wiley & Sons, Ltd, 2007).
66. Hohwy, M., Rienstra, C. M., Jaroniec, C. P., Griffin, R. G. Fivefold symmetric homonuclear dipolar recoupling in rotating solids: Application to double quantum spectroscopy. *Journal of Chemical Physics* **110**, 7983-92 (1999).
67. Lee, Y. K., Kurur, N. D., Helmle, M., Johannessen, O. G., Nielsen, N. C., Levitt, M. H. Efficient Dipolar Recoupling in the NMR of Rotating Solids - A Sevenfold Symmetrical Radiofrequency Pulse Sequence. *Chemical Physics Letters* **242**, 304-9 (1995).
68. Hohwy, M., Jakobsen, H. J., Eden, M., Levitt, M. H., Nielsen, N. C. Broadband dipolar recoupling in the nuclear magnetic resonance of rotating solids: A compensated C7 pulse sequence. *Journal of Chemical Physics* **108**, 2686-94 (1998).
69. Bayro, M. J., Ramachandran, R., Caporini, M. A., Eddy, M. T., Griffin, R. G. Radio frequency-driven recoupling at high magic-angle spinning frequencies: Homonuclear recoupling *sans* heteronuclear decoupling. *Journal of Chemical Physics* **128**, 11 (2008).
70. De Paepe, G., Bayro, M. J., Lewandowski, J., Griffin, R. G. Broadband homonuclear correlation spectroscopy at high magnetic fields and MAS frequencies. *Journal of the American Chemical Society* **128**, 1776-7 (2006).
71. Haeberlen, U., Waugh, J. S. Coherent averaging effects in magnetic resonance. *Phys Rev* **175**, 453-67 (1968).
72. Levitt, M. H., Raleigh, D. P., Creuzet, F., Griffin, R. G. Theory and Simulations of Homonuclear Spin Pair Systems in Rotating Solids. *Journal of Chemical Physics* **92**, 6347-64 (1990).
73. Nielsen, N. C., Bildsoe, H., Jakobsen, H. J., Levitt, M. H. Double-quantum homonuclear rotary resonance: Efficient dipolar recovery in magic-angle spinning nuclear magnetic resonance. *Journal of Chemical Physics* **101**, 1805-12 (1994).
74. Verel, R., Baldus, M., Ernst, M., Meier, B. H. A homonuclear spin-pair filter for solid-state NMR based on adiabatic-passage techniques. *Chemical Physics Letters* **287**, 421-8 (1998).
75. Verel, R., Meier, B. H. Polarization-Transfer Methods in Solid-State Magic-Angle-Spinning NMR: Adiabatic CN Pulse Sequences. *Chemphyschem : a European journal of chemical physics and physical chemistry* **5**, 851-62 (2004).
76. Wang, Q., Hu, B. W., Fayon, F., Trebosc, J., Legein, C., Lafon, O., Deng, F., Amoureux, J. P. Double-quantum ^{19}F–^{19}F dipolar recoupling at ultra-fast magic angle spinning NMR: application to the assignment of ^{19}F NMR spectra of inorganic fluorides. *Physical Chemistry Chemical Physics* **11**, 10391-5 (2009).
77. Wang, Q., Hu, B. W., Lafon, O., Trebosc, J., Deng, F., Amoureux, J. P. Homonuclear dipolar recoupling under ultra-fast magic-angle spinning: Probing ^{19}F–^{19}F proximities by solid-state NMR. *Journal of Magnetic Resonance* **203**, 113-28 (2010).
78. Hu, B., Delevoye, L., Lafon, O., Trebosc, J., Amoureux, J. P. Double-quantum NMR spectroscopy of ^{31}P species submitted to very large CSAs. *Journal of Magnetic Resonance* **200**, 178-88 (2009).
79. Bennett, A. E., Rienstra, C. M., Griffiths, J. M., Zhen, W. G., Lansbury, P. T., Griffin, R. G. Homonuclear radio frequency-driven recoupling in rotating solids. *Journal of Chemical Physics* **108**, 9463-79 (1998).
80. Ishii, Y. 13C–13C dipolar recoupling under very fast magic angle spinning in solid-state nuclear magnetic resonance: Applications to distance measurements, spectral assignments, and high-throughput secondary-structure determination. *Journal of Chemical Physics* **114**, 8473-83 (2001).

81. Bayro, M. J., Maly, T., Birkett, N. R., Dobson, C. M., Griffin, R. G. Long-Range Correlations between Aliphatic ^{13}C Nuclei in Protein MAS NMR Spectroscopy. *Angewandte Chemie-International Edition* **48**, 5708-10 (2009).
82. Lewandowski, J. R., De Paepe, G., Eddy, M. T., Griffin, R. G. ^{15}N–^{15}N Proton Assisted Recoupling in Magic Angle Spinning NMR. *Journal of the American Chemical Society* **131**, 5769-76 (2009).
83. Pines, A., Gibby, M. G., Waugh, J. S. Proton-Enhanced NMR of Dilute Spins in Solids. *Journal of Chemical Physics* **59**, 569-90 (1973).
84. Stejskal, E. O., Schaefer, J., Waugh, J. S. Magic-angle spinning and polarization transfer in proton-enhanced NMR. *Journal of Magnetic Resonance* **28**, 105-12 (1977).
85. Metz, G., Wu, X. L., Smith, S. O. Ramped-Amplitude Cross Polarization in Magic-Angle-Spinning NMR. *Journal of Magnetic Resonance Series A* **110**, 219-27 (1994).
86. Hediger, S., Meier, B. H., Kurur, N. D., Bodenhausen, G., Ernst, R. R. NMR Cross-Polarization by Adiabatic Passage through the Hartmann-Hahn Condition (APHH). *Chemical Physics Letters* **223**, 283-8 (1994).
87. Hediger, S., Meier, B. H., Ernst, R. R. Adiabatic Passage Hartmann-Hahn Cross-Polarization in NMR Under Magic-Angle Sample-Spinning. *Chemical Physics Letters* **240**, 449-56 (1995).
88. Laage, S., Marchetti, A., Sein, J., Pierattelli, R., Sass, H. J., Grzesiek, S., Lesage, A., Pintacuda, G., Emsley, L. Band-Selective ^{1}H–^{13}C Cross-Polarization in Fast Magic Angle Spinning Solid-State NMR Spectroscopy. *Journal of the American Chemical Society* **130**, 17216-7 (2008).
89. Baldus, M., Geurts, D. G., Hediger, S., Meier, B. H. Efficient ^{15}N–^{13}C polarization transfer by adiabatic-passage Hartmann-Hahn cross polarization. *Journal of Magnetic Resonance Series A* **118**, 140-4 (1996).
90. Baldus, M., Petkova, A. T., Herzfeld, J., Griffin, R. G. Cross polarization in the tilted frame: assignment and spectral simplification in heteronuclear spin systems. *Molecular Physics* **95**, 1197-207 (1998).
91. De Paepe, G., Lewandowski, J. R., Loquet, A., Eddy, M., Megy, S., Bockmann, A., Griffin, R. G. Heteronuclear proton assisted recoupling. *Journal of Chemical Physics* **134**, 095101-18 (2011).
92. Lewandowski, J. R., De Paepe, G., Griffin, R. G. Proton assisted insensitive nuclei cross polarization. *Journal of the American Chemical Society* **129**, 728-9 (2007).
93. Bjerring, M., Nielsen, A. B., Tosner, Z., Nielsen, N. C. Broadband heteronuclear dipolar recoupling without ^{1}H decoupling in solid-state NMR using simple cross-polarization methods. *Chemical Physics Letters* **494**, 326-30 (2010).
94. Hodgkinson, P., Emsley, L. The Accuracy of Distance Measurements in Solid-State NMR. *Journal of Magnetic Resonance* **139**, 46-59 (1999).
95. De Paepe, G., Lewandowski, J. R., Loquet, A., Bockmann, A., Griffin, R. G. Proton assisted recoupling and protein structure determination. *Journal of Chemical Physics* **129** (2008).
96. Weingarth, M., Masuda, Y., Takegoshi, K., Bodenhausen, G., Tekely, P. Sensitive ^{13}C–^{13}C correlation spectra of amyloid fibrils at very high spinning frequencies and magnetic fields. *Journal of Biomolecular NMR*, 1-8 (2011).
97. Lange, A., Scholz, I., Manolikas, T., Ernst, M., Meier, B. H. Low-power cross polarization in fast magic-angle spinning NMR experiments. *Chemical Physics Letters* **468**, 100-5 (2009).
98. Scholz, I., Meier, B. H., Ernst, M. MIRROR-CP: A proton-only experiment for the measurement of ^{13}C spin diffusion. *Chemical Physics Letters* **479**, 296-9 (2009).
99. De Paepe, G., Lewandowski, J. R., Griffin, R. G. Spin dynamics in the modulation frame: Application to homonuclear recoupling in magic angle spinning solid-state NMR. *Journal of Chemical Physics* **128**, 26 (2008).
100. Takegoshi, K., Nakamura, S., Terao, T. ^{13}C–^{1}H dipolar-driven ^{13}C–^{13}C recoupling without ^{13}C rf irradiation in nuclear magnetic resonance of rotating solids. *Journal of Chemical Physics* **118**, 2325-41 (2003).
101. Demers, J.-P., Chevelkov, V., Lange, A. Progress in correlation spectroscopy at ultra-fast magic-angle spinning: Basic building blocks and complex experiments for the study of protein structure and dynamics. *Solid State Nuclear Magnetic Resonance* **40**, 101-13 (2011).

3. Complete set of low-power experiments for protein assignments

3.1. Summary

In this study, we introduce a complete set of low-power solid-state NMR experiments sufficient for protein resonance assignment under fast MAS (> 60 kHz), including sequential ^{15}N-^{13}C correlation experiments. The low rf (radio frequency)-field requirements of our experiments prevent considerable heating of the sample, therefore avoiding protein degradation, making this approach well-suited for the investigation of temperature-sensitive biomolecules.

As an application, NCA, N(CO)CA, and ^{13}C-^{13}C correlation spectra were recorded at 60 kHz MAS on less than 1 mg of [^{13}C, ^{15}N] isotope-labeled sample. We also demonstrate that our approach can be readily performed on protein samples in which the ^{1}H T_1 relaxation times are shortened by means of paramagnetic doping[1,2]. Here, the reduced recycle delay enhances sensitivity but requires the use of NMR sequences with low-power deposition, as described in this communication.

Contribution statement

The results of this chapter are presented in the following publication:

"Low-Power Solid-State NMR Experiments for Resonance Assignment under Fast Magic-Angle Spinning", *Vinesh Vijayan, Jean-Philippe Demers, Jacek Biernat, Eckhard Mandelkow, Stefan Becker, Adam Lange,* **Solid State Nuclear Magnetic Resonance**, vol. 40(3), pp. 101–13 (2011)

The tau sample was prepared by J.B. and E.M. The ubiquitin sale was prepared by S.B and Karin Giller. Brigitta Angerstein helped with the Cu-EDTA doping and filling of tau sample. V.V. and J.P.D. performed the solid-state NMR experiments.

3.2. Introduction

Solid-state NMR has evolved in the past decade into a powerful technique for the characterization of biomolecular structure and dynamics[3]. Micro-crystalline globular proteins[4,5], amyloid fibrils[6-9] and membrane proteins[10,11] can now be routinely studied using solid-state NMR techniques. This was made possible in part due to the development of 2D and 3D homonuclear and heteronuclear experiments that correlate ^{13}C and ^{15}N spins for resonance assignment as well as for obtaining long-range distance restraints in structure elucidation[12].

Remarkable developments in magic angle spinning (MAS) probe technology also contributed to this success. Now, a new generation of commercially available 1.3 mm probes can reach above 60 kHz of MAS. This allows for more efficient averaging of strong dipolar couplings, hence providing better resolution in highly crowded protein spectra[13,14].

On the other hand, fast spinning reduces the effectiveness of many of the routinely used NMR experiments for obtaining resonance assignments. For example, at low MAS (~15 kHz), ^{13}C-^{13}C correlations are often measured by proton driven spin diffusion (PDSD) [15]. Under very fast MAS, efficient averaging of dipolar couplings renders PDSD experiments ineffective. Instead, selective dipolar recoupling of spins becomes necessary to allow for efficient polarization transfer[14,16-18].

3.3. Hypotheses and Method Summary

Hypotheses:

It is possible to record a complete set of low-power solid-state NMR experiments sufficient for protein resonance assignment under ultra-fast MAS, including sequential ^{15}N-^{13}C correlation experiments.

The set of low-power experiments is readily amenable for protein samples of very low quantity and for samples where the ^{1}H T_1 relaxation times are shortened by means of paramagnetic doping.

Method summary:

The N-CA, N-CO-CA and C-C solid-state NMR experiments were composed by selecting low-power elements for magnetization transfer and heteronuclear decoupling.

The experiments were performed at 60 kHz MAS on mass-limited (ubiquitin) and Cu(II)-EDTA doped samples (tau-Paired Helical Filaments).

3.4. Materials and Methods

3.4.1. Sample preparation

Uniformly [^{13}C, ^{15}N]-labeled ubiquitin was recombinantly expressed in *E. coli* and purified as previously described[19,20]. Micro-crystals were obtained by precipitating the sample with polyethylene glycol[21]. Approximately 1 mg of micro-crystalline protein was filled into a rotor of o.d. 1.3 mm.

Tau–PHFs from the construct K19 were obtained using previously published procedures[22]. For paramagnetic doping, about 1 mg of PHFs were incubated in 150 mM Cu-EDTA solution for 2 days. After centrifugation, the pellet was subsequently transferred into a 1.3 mm rotor.

3.4.2. Solid-state NMR experiments

All spectra were recorded on a Bruker Avance III 800 MHz standard-bore spectrometer equipped with a 1.3 mm triple-resonance probe. MAS frequencies of 60 kHz were used in all experiments. The probe temperature was set to -30° C corresponding to a sample temperature of ~+30° C.

Initial polarization transfer to $^{15}N/^{13}C$ was achieved using SOCP with rf-field amplitudes of ~9 kHz on both channels (contact time = 4 ms for ^{1}H-^{15}N and 2.5 ms for ^{1}H-^{13}C, respectively). ^{15}N to ^{13}C transfers (mixing time = 5 ms) used a tangential amplitude sweep from ~23 to ~27 kHz on carbons (Δrf = 2 kHz) and an rf field amplitude of ~35 kHz applied on ^{15}N. Double-quantum ^{13}C-^{13}C mixing was accomplished by a linear amplitude ramp around ~30 kHz for the N(CO)CA (mixing time = 4.5 ms) and by a tangential amplitude sweep from ~25 to ~35 kHz (mixing time = 4 ms, Δrf = 5 kHz) for the DREAM ^{13}C-^{13}C experiment.

3.5. Results and Discussion

Figure 1 presents the different pulse schemes that were used to obtain ^{15}N-^{13}C and ^{13}C-^{13}C correlations. At low MAS, the initial cross-polarization (CP) transfer from protons to low-γ nuclei generally requires high power irradiation on both channels. In contrast, under fast MAS, efficient CP transfer is also possible at low rf-fields[23,24].

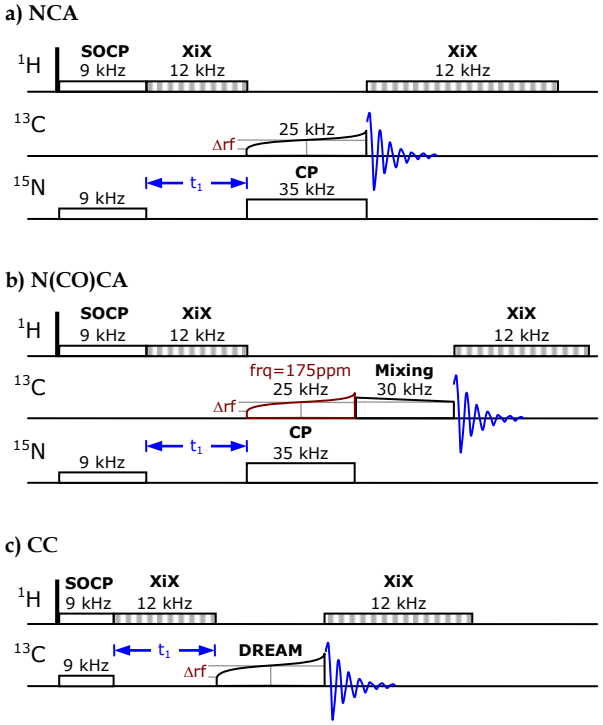

Figure 1: Pulse schemes for measuring ^{15}N-^{13}C and ^{13}C-^{13}C correlation spectra at high spinning speed. SOCP is used for the initial polarization transfer from ^{1}H to ^{13}C/^{15}N. (a,b) Double-quantum ^{15}N-^{13}C transfer makes use of a tangential amplitude sweep on the carbons. (b) An amplitude ramp around the HORROR condition is used for the CO-Cα transfer in the N(CO)CA experiment. (c) A DREAM mixing sequence was used to record the ^{13}C-^{13}C correlation spectrum.

Our pulse schemes use second order cross-polarization (SOCP)[24] for the initial magnetization transfer. SOCP at the n = 0 Hartman-Hahn condition relies on second-order cross-terms between homonuclear and heteronuclear couplings. SOCP works efficiently at low rf-fields if sufficient care is taken to avoid detrimental dipolar and/or CSA recoupling conditions at the used rf-field amplitudes. We employed rf-fields of 9 kHz, well below all resonance conditions. SOCP is intrinsically band selective as only weak rf-fields are applied. The rf-fields employed here are sufficient to excite all ^{15}N protein backbone resonances in ^{15}N-^{13}C correlation experiments but give rise to a band-selective transfer to Cα or CO in ^{13}C-^{13}C correlation experiments.

For the ^{15}N-^{13}C transfer, we make use of a SPECIFIC-CP[25] step. SPECIFIC zero quantum (ZQ) or double quantum (DQ) transfer is possible whenever one of the following conditions is fulfilled (Eq. 1), where + and – on the left hand side of the equation apply to DQ and ZQ transfer, respectively; Ω_I and Ω_S are chemical shift offsets, ω_{1I} and ω_{1S} are rf-field amplitudes for I and S spins, respectively, and ω_r is the spinning frequency.

$$\sqrt{\Omega_I^2 + \omega_{1I}^2} \pm \sqrt{\Omega_S^2 + \omega_{1S}^2} = n\omega_r \; ; \; n = \pm 1, \pm 2 \qquad (1)$$

In the absence of chemical shift offsets, the above equation is the familiar selection rule for DQ and ZQ transfer in normal CP experiments. At high MAS, DQ CP can be easily matched with low rf-fields. The DQ CP condition was first investigated by Meier[26] and more recently exploited by Emsley and co-workers[27] in the context of band-selective ^{1}H-^{13}C polarization transfer in the high MAS regime. We used the low rf-field capabilities of DQ CP for ^{15}N-^{13}C heteronuclear magnetization transfer similar to recent work by Ishii and coworkers[1].

For homonuclear polarization transfer from CO to Cα in the N(CO)CA experiment (see Figure 1b), a ramped pulse (100 to 80%) around the HORROR[28] dipolar recoupling condition – corresponding to 30 kHz rf-field at 60 kHz MAS - is utilized. On a 800 MHz spectrometer, the rf-field amplitude employed here is sufficient to cover both Cα and CO resonances and compensates for chemical shift offsets. In the DREAM[16] ^{13}C-^{13}C correlation experiment (see Figure 1c), a tangential amplitude sweep on ^{13}C is applied.

The experiments described here use low rf-fields for all the magnetization transfer periods. Accordingly, only low power proton XiX[29] (12 kHz) decoupling was used during the t_1 and t_2 periods. Note that no proton decoupling had to be employed

during DQ SPECIFIC-CP, ramped ^{13}C-^{13}C mixing, and DREAM dipolar recoupling periods.

3.5.1. Application to mass-limited protein samples

As a first application of our fast MAS approach to resonance assignment, NCA, N(CO)CA and ^{13}C-^{13}C correlation spectra of PEG-precipitated uniformly [^{13}C,^{15}N] labeled ubiquitin were recorded at 60 kHz MAS. The sample contained less than 1 mg of isotope-labeled protein packed in a 1.3 mm rotor. The resulting spectra are shown in Figure 2 and exhibit excellent S/N (signal to noise) and resolution. Sequential correlations can be easily obtained from a combination of all three spectra as exemplified for residues V26-K27 and I30-Q31 in sequential walks (indicated in Figure 2 with green lines).

The total experimental times for N(CO)CA and NCA spectra were 128 and 61 hours, respectively. The DREAM ^{13}C-^{13}C spectrum was recorded in 14 hours

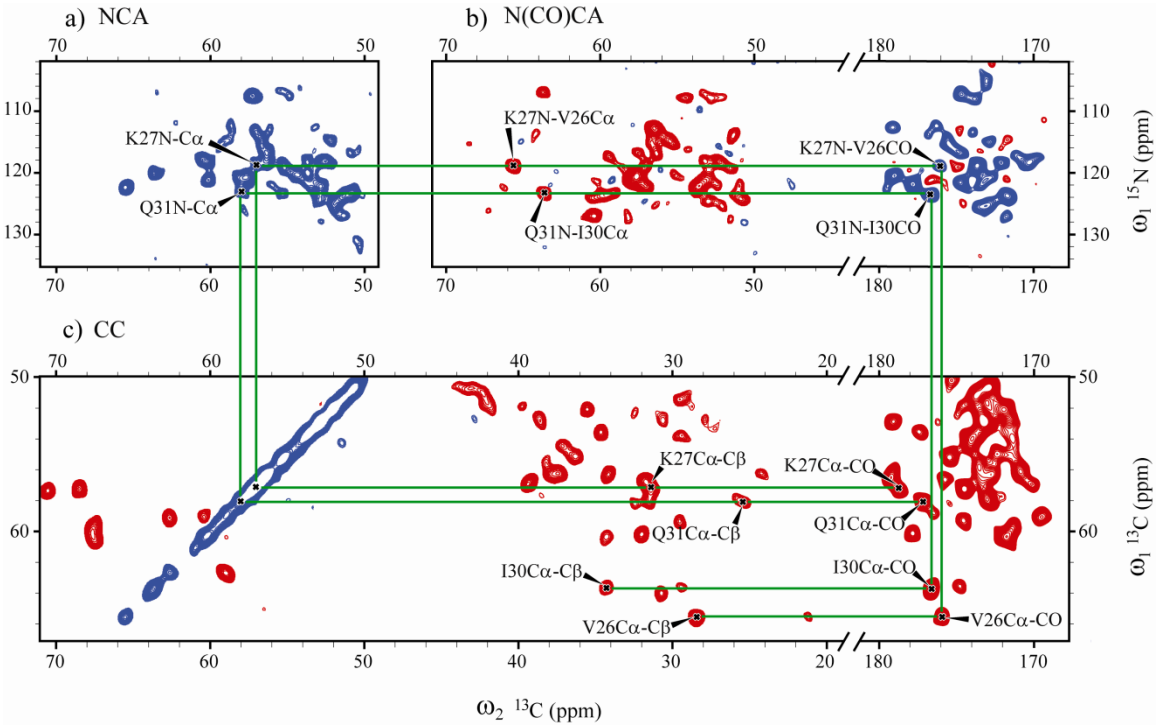

Figure 2: ^{15}N-^{13}C and ^{13}C-^{13}C correlation spectra of ubiquitin at 60 KHz MAS. (a) NCA spectrum. (b) Cα and CO regions of N(CO)CA spectrum. (c) Cα-Cβ and Cα-CO regions of ^{13}C-^{13}C DREAM spectrum. Carrier frequencies were 4.1 ppm on ^{1}H, 119 ppm on ^{15}N, 56 ppm on ^{13}C for NCA and ^{13}C-^{13}C, and 100 ppm on ^{13}C for N(CO)CA except for the tangential sweep where the carrier was set to 175 ppm. Negative contours are shown in red and positive contours in blue. Sequential correlations (indicated with green lines) can be easily obtained from these spectra as exemplified for residues V26-K27 and I30-Q31.

3.5.2. Application to paramagnetic protein samples

Our low-power approach for resonance assignment under fast MAS is ideally combined with paramagnetic optimized relaxation times for sensitivity enhancement. As an example we present data that was recorded on approximately 1 mg of Cu(II)-EDTA (Cu-EDTA) doped uniformly [^{13}C, ^{15}N] labeled paired helical filaments (PHFs) formed from the tau construct K19. The presence of tau aggregates in neurons is a pathological hallmark of Alzheimer's disease[22,30].

The reduced ^{1}H T_1 relaxation time in the Cu-EDTA doped sample enabled us to shorten the inter-scan delay in our experiments to 400 ms. The NCO spectrum of K19 PHFs is shown in Figure 3. This spectrum was recorded in 19 hours and compares favorably to results obtained at lower speed both in terms of S/N and resolution[22].

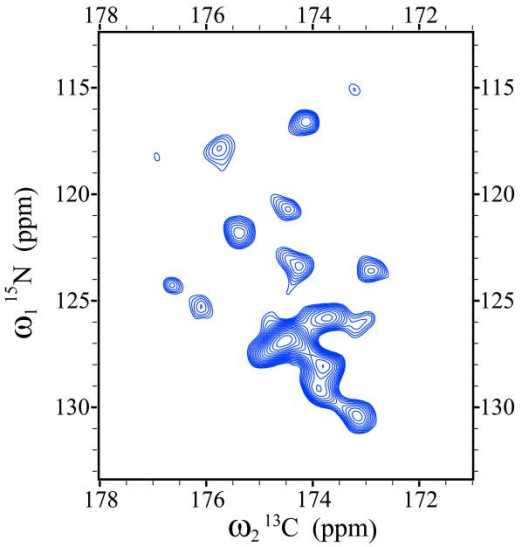

Figure 3. NCO spectrum of uniformly [^{13}C, ^{15}N] isotope-labeled paired helical filaments formed from the tau construct K19 doped with 150 mM Cu-EDTA. The spectrum was recorded at 60 kHz MAS on a standard-bore 800 MHz spectrometer.

3.6. Conclusion

We have shown that all experiments needed for sequential resonance assignment including ^{15}N-^{13}C correlation experiments can be measured at very high spinning speed and with low rf power deposition. With the full set of correlation experiments available, solid state NMR assignment of proteins is now possible at high spinning speeds. By exploiting the better resolution at higher spinning speed, the low power approach to resonance assignment under fast MAS as described here – possibly in combination with paramagnetic optimized relaxation times – promises to be of general use for the characterisation of protein structure and dynamics.

3.7. References

1. Wickramasinghe, N. P., Parthasarathy, S., Jones, C. R., Bhardwaj, C., Long, F., Kotecha, M., Mehboob, S., Fung, L. W. M., Past, J., Samoson, A., Ishii, Y. Nanomole-scale protein solid-state NMR by breaking intrinsic ^{1}H T_1 boundaries. *Nature Methods* **6**, 215-8 (2009).
2. Linser, R., Chevelkov, V., Diehl, A., Reif, B. Sensitivity enhancement using paramagnetic relaxation in MAS solid-state NMR of perdeuterated proteins. *Journal of Magnetic Resonance* **189**, 209-16 (2007).
3. McDermott, A. E. Structural and dynamic studies of proteins by solid-state NMR spectroscopy: rapid movement forward. *Current Opinion in Structural Biology* **14**, 554-61 (2004).
4. Loquet, A., Bardiaux, B., Gardiennet, C., Blanchet, C., Baldus, M., Nilges, M., Malliavin, T., Böckmann, A. 3D Structure Determination of the Crh Protein from Highly Ambiguous Solid-State NMR Restraints. *Journal of the American Chemical Society* **130**, 3579-89 (2008).
5. Castellani, F., van Rossum, B., Diehl, A., Schubert, M., Rehbein, K., Oschkinat, H. Structure of a protein determined by solid-state magic-angle-spinning NMR spectroscopy. *Nature* **420**, 98-102 (2002).
6. Wasmer, C., Lange, A., Van Melckebeke, H., Siemer, A. B., Riek, R., Meier, B. H. Amyloid fibrils of the HET-s(218-289) prion form a beta solenoid with a triangular hydrophobic core. *Science* **319**, 1523-6 (2008).
7. Helmus, J. J., Surewicz, K., Nadaud, P. S., Surewicz, W. K., Jaroniec, C. P. Molecular conformation and dynamics of the Y145Stop variant of human prion protein. *Proceedings of the National Academy of Sciences of the United States of America* **105**, 6284-9 (2008).
8. Heise, H., Hoyer, W., Becker, S., Andronesi, O. C., Riedel, D., Baldus, M. Molecular-level secondary structure, polymorphism, and dynamics of full-length alpha-synuclein fibrils studied by solid-state NMR. *Proceedings of the National Academy of Sciences of the United States of America* **102**, 15871-6 (2005).
9. Petkova, A. T., Yau, W. M., Tycko, R. Experimental constraints on quaternary structure in Alzheimer's beta-amyloid fibrils. *Biochemistry* **45**, 498-512 (2006).
10. Lange, A., Giller, K., Hornig, S., Martin-Eauclaire, M. F., Pongs, O., Becker, S., Baldus, M. Toxin-induced conformational changes in a potassium channel revealed by solid-state NMR. *Nature* **440**, 959-62 (2006).
11. Shi, L., Ahmed, M. A. M., Zhang, W., Whited, G., Brown, L. S., Ladizhansky, V. Three-Dimensional Solid-State NMR Study of a Seven-Helical Integral Membrane Proton Pump-Structural Insights. *Journal of molecular biology* **386**, 1078-93 (2009).
12. Luca, S., Heise, H., Baldus, M. High-resolution solid-state NMR applied to polypeptides and membrane proteins. *Accounts of Chemical Research* **36**, 858-65 (2003).
13. Zhou, D. H., Shah, G., Cormos, M., Mullen, C., Sandoz, D., Rienstra, C. M. Proton-detected solid-state NMR Spectroscopy of fully protonated proteins at 40 kHz magic-angle spinning. *Journal of the American Chemical Society* **129**, 11791-801 (2007).
14. Ernst, M., Meier, M. A., Tuherm, T., Samoson, A., Meier, B. H. Low-power high-resolution solid-state NMR of peptides and proteins. *Journal of the American Chemical Society* **126**, 4764-5 (2004).
15. Dusold, S., Sebald, A. Dipolar recoupling under magic-angle spinning conditions. *Annual Reports on Nmr Spectroscopy, Vol 41* **41**, 185-264 (2000).
16. Verel, R., Baldus, M., Nijman, M., van Os, J. W. M., Meier, B. H. Adiabatic homonuclear polarization transfer in magic-angle-spinning solid-state NMR. *Chemical Physics Letters* **280**, 31-9 (1997).
17. Bennett, A. E., Griffin, R. G., Ok, J. H., Vega, S. Chemical shift correlation spectroscopy in rotating solids: Radio frequency-driven dipolar recoupling and longitudinal exchange. *Journal of Chemical Physics* **96**, 8624-7 (1992).
18. Ishii, Y. 13C–13C dipolar recoupling under very fast magic angle spinning in solid-state nuclear magnetic resonance: Applications to distance measurements, spectral assignments, and high-throughput secondary-structure determination. *Journal of Chemical Physics* **114**, 8473-83 (2001).
19. Lazar, G. A., Desjarlais, J. R., Handel, T. M. De novo design of the hydrophobic core of ubiquitin. *Protein Sci* **6**, 1167-78 (1997).

20. Seidel, K., Etzkorn, M., Heise, H., Becker, S., Baldus, M. High-resolution solid-state NMR studies on uniformly [C-13,N-15]-labeled ubiquitin. *ChemBioChem* **6**, 1638-47 (2005).
21. Martin, R. W., Zilm, K. W. Preparation of protein nanocrystals and their characterization by solid state NMR. *Journal of Magnetic Resonance* **165**, 162-74 (2003).
22. Andronesi, O. C., von Bergen, M., Biernat, J., Seidel, K., Griesinger, C., Mandelkow, E., Baldus, M. Characterization of Alzheimer's-like paired helical filaments from the core domain of tau protein using solid-state NMR spectroscopy. *Journal of the American Chemical Society* **130**, 5922-8 (2008).
23. Laage, S., Sachleben, J. R., Steuernagel, S., Pierattelli, R., Pintacuda, G., Emsley, L. Fast acquisition of multi-dimensional spectra in solid-state NMR enabled by ultra-fast MAS. *Journal of Magnetic Resonance* **196**, 133-41 (2009).
24. Lange, A., Scholz, I., Manolikas, T., Ernst, M., Meier, B. H. Low-power cross polarization in fast magic-angle spinning NMR experiments. *Chemical Physics Letters* **468**, 100-5 (2009).
25. Baldus, M., Petkova, A. T., Herzfeld, J., Griffin, R. G. Cross polarization in the tilted frame: assignment and spectral simplification in heteronuclear spin systems. *Molecular Physics* **95**, 1197-207 (1998).
26. Meier, B. H. Cross polarization under fast magic angle spinning: thermodynamical considerations. *Chemical Physics Letters* **188**, 201-7 (1992).
27. Laage, S., Marchetti, A., Sein, J., Pierattelli, R., Sass, H. J., Grzesiek, S., Lesage, A., Pintacuda, G., Emsley, L. Band-Selective ^{1}H–^{13}C Cross-Polarization in Fast Magic Angle Spinning Solid-State NMR Spectroscopy. *Journal of the American Chemical Society* **130**, 17216-7 (2008).
28. Nielsen, N. C., Bildsoe, H., Jakobsen, H. J., Levitt, M. H. Double-quantum homonuclear rotary resonance: Efficient dipolar recovery in magic-angle spinning nuclear magnetic resonance. *Journal of Chemical Physics* **101**, 1805-12 (1994).
29. Ernst, M., Samoson, A., Meier, B. H. Low-power XiX decoupling in MAS NMR experiments. *Journal of Magnetic Resonance* **163**, 332-9 (2003).
30. Mandelkow, E., von Bergen, M., Biernat, J., Mandelkow, E.-M. Structural principles of tau and the paired helical filaments of Alzheimer's disease. *Brain Pathology* **17**, 83-90 (2007).

4. Tailored low-power cross-polarization under ultra-fast MAS

4.1. Summary

High static magnetic fields and very fast magic-angle spinning (MAS) promise to improve resolution and sensitivity of solid-state NMR experiments. The fast MAS regime has permitted the development of low-power cross-polarization schemes, such as second-order cross-polarization (SOCP), which prevent heat deposition in the sample. Those schemes are however limited in bandwidth, as weak radio-frequency (RF) fields only cover a small chemical shift range for rare nuclei (e.g. ^{13}C). Another consideration is that the efficiency of cross-polarization is very sensitive to magnetization decay that occurs during the spin-lock pulse on the abundant nuclei (e.g. ^{1}H). Having characterized this decay in glutamine at 60 kHz MAS, we propose two complementary strategies to tailor cross-polarization to desired spectral regions at low RF power. In the case of multiple sites with small chemical shift dispersion, a larger bandwidth for SOCP is obtained by slightly increasing the RF power while avoiding recoupling conditions that lead to fast spin-lock decay. In the case of two spectral regions with large chemical shift offset, an extension of the existing low-power schemes, called MOD-CP, is introduced. It consists of a spin-lock on ^{1}H and an amplitude modulated spin-lock on the rare nucleus. The range of excited chemical shifts is assessed by experimental excitation profiles and numerical simulation of an I_2S spin system. All SOCP-based schemes exhibit higher sensitivity than high-power CP schemes, as demonstrated on solid (glutamine) and semi-solid (hydrated, micro-crystalline ubiquitin) samples.

Contribution statement

The results of this chapter are contained in the following article:

"Tailored low-power cross-polarization under fast magic-angle spinning" *Jean-Philippe Demers, Vinesh Vijayan, Stefan Becker, Adam Lange,* **Solid State Nuclear Magnetic Resonance**, vol. 40(3), pp. 101–13 (2011)

The ubiquitin protein sample was prepared by S.B and Karin Giller. J.P.D. performed the solid-state NMR experiments and quantum mechanical simulations.

4.2. Background and Motivation

The past decade has seen a tremendous development in the field of solid-state NMR[1,2]. Part of this development can be attributed to the widespread adoption of high static magnetic fields. High fields provide better sensitivity, since the improvement in signal-to-noise ratio (S/N) is roughly proportional to $B_0^{3/2}$. Furthermore, chemical shift dispersion directly scales with the field strength, which is beneficial for the resolution of crowded spectra. Similar to the progress provided by high B_0 fields, a recent wave of improvement in resolution and sensitivity has been brought about by the development of very fast MAS probe heads and pulse techniques. MAS frequencies of up to 67 kHz are now reached by rotors with an o.d. of 1.3 mm. As a consequence of the very fast rotation, chemical shift anisotropies are efficiently averaged and dipolar couplings are greatly reduced[3], resulting in narrow line-widths. The large decrease in sample volume reduces the sensitivity; this effect is partially compensated since the S/N per unit volume follows the inverse of the RF coil diameter[4,5]. Therefore, at equal MAS speed, the absolute S/N is roughly proportional to the rotor diameter.

At high static field, large chemical shift dispersions entail the generation of larger applied B_1 fields in order to excite the full spectral width of nuclei such as ^{13}C and ^{15}N. Strong radio frequency (RF) irradiation can deposit a high amount of energy in the

sample. The heat contributed can lead to irremediable alteration of the sample. This situation is particularly critical for the study of biological samples, which are fragile and often preserved in ionic buffers[6]. In fast MAS experiments, additional heating is caused by the friction of the MAS rotor with the surrounding gas, which can increase the temperature by about 60 K at 60 kHz MAS. To overcome the heating problem, one strategy is to reduce electric fields through modifications of the RF coil design[7-13]. A concurrent and complementary strategy is the development of pulse sequences requiring minimal amounts of irradiation power. This additionally mitigates the strain that strong RF generation imposes on the instrumentation. Substantial gains in sensitivity can further be obtained by combining low-power pulse sequences and fast MAS with shortening of the recycling delay. For instance, in the presence of paramagnetic nuclei, the ^{1}H longitudinal relaxation times are reduced, thus allowing fast acquisition[14-18].

Low-power alternatives compatible with very fast magic-angle spinning of the rotor have been recently introduced for many of the fundamental building blocks of solid-state NMR pulse sequences. This comprises proton heteronuclear decoupling (e.g. XiX[19-21], TPPM[22-24], PISSARRO[25]), mixing schemes (e.g. HORROR[26], ocHORROR[27], DREAM[21,28,29], RFDR[30-32], MIRROR[33], PARIS[34], PAR[35,36]), and cross-polarization[37,38]. Low-power cross-polarization schemes, such as band-selective ^{1}H-^{13}C cross-polarization[37], and second-order cross-polarization (SOCP)[38], are easily incorporated into multidimensional experiments. The band-selective ^{1}H-^{13}C CP was included in the low-power pulse sequence for CC-RFDR[17]. We have recently presented a set of low-power solid-state NMR experiments assembled based on SOCP, NCA, N(CO)CX and CC, that are sufficient for protein resonance assignment under fast MAS, and which include sequential ^{15}N-^{13}C correlation[18]. SOCP is a second order recoupling experiment, part of the growing family that presently consists of PAIN-CP[39], PAR[35,36,40], MIRROR[33], RESORT[41] and SOCP.

4.2.1. Previous low-power cross-polarization schemes

An intrinsic limitation of the low-power CP schemes is their band-selective aspect, since a low-power irradiation cannot efficiently spin-lock the full range of chemical shifts for rare nuclei.

Thus far, two cross-polarization schemes at low RF power and high MAS have been proposed. Under magic-angle spinning, cross-polarization is obtained when the effective nutation frequencies of the rare and abundant spins match the Hartmann-Hahn condition (Eq. 1), see ref. [42-45]. The addition (+) and difference (–) conditions correspond to double-quantum (DQ) and zero-quantum (ZQ) transfer, respectively.

(Eq. 1) $\left|\nu_1^S \pm \nu_1^I\right| = n \cdot \nu_{MAS}, \qquad n = \{0,1,2\}$

The band-selective ^{1}H-^{13}C CP scheme[17,37] employs the n = 1 DQ condition. The proton spin-lock frequency is set between the $\kappa = \frac{1}{2}$ and $\kappa = 1$ ratio, at $\nu_1^H = \nu_{MAS} - \nu_1^C$, such that a low-power pulse can be used to spin-lock rare nuclei. In second-order cross-polarization (SOCP)[38], the I and S spin-lock frequencies are matched at the n = 0 Hartmann-Hahn condition, $\nu_1^I = \nu_1^S$. Magnetization transfer occurs predominantly through second-order cross-terms between homonuclear I-I and heteronuclear I-S dipolar couplings. SOCP allows the use of low-power RF for both nuclei, such that the proton spin-lock frequency is set below the $\kappa = \frac{1}{4}$ condition.

In the current study, we present two strategies to alleviate this limitation. In case of multiple sites with small chemical shift dispersion, we employ SOCP with increased RF frequency. In case of regions with large chemical shift dispersion, low-power CP is employed with an amplitude modulation on the rare nucleus spin-lock pulse (the "S"

spin, e.g. ^{13}C or ^{15}N). This constitutes an extension of the present schemes which restores the high information content per spectrum that is found in broadband excitation while conserving the benefits of low-power solid-state NMR pulse sequences.

In order to select optimal conditions, we first characterized the decay of ^{1}H spin-locked magnetization as a function of RF-field strength and MAS frequency.

4.3. Hypotheses and Method Summary

Hypotheses:

It is possible to excite multiple bandwidths during ^{1}H-^{13}C cross-polarization using an amplitude modulation on the ^{13}C channel.

Any arbitrary offset between the two bandwidths can be generated, making the amplitude-modulated cross-polarization a general tool for tailored magnetization transfer at ultra-fast MAS.

The cross-polarization schemes which avoid rapid ^{1}H magnetization decay during spin-lock have higher transfer efficiency.

Method summary:

The effect of amplitude modulation on cross-polarization was analyzed through experimental and simulated excitation profiles.

The decay of ^{1}H spin-locked magnetization was characterized as a function of RF-field strength and MAS frequency.

The efficiency of the cross-polarization schemes is demonstrated on solid (glutamine as a dry powder) and semi-solid (hydrated, micro-crystalline ubiquitin) samples.

4.4. Materials and Methods

4.4.1. Sample preparation

Uniformly [^{13}C, ^{15}N]-labeled ubiquitin was prepared as described in Section 3.4.1. Uniformly [^{13}C, ^{15}N]-labeled L-glutamine was purchased from Cambridge Isotope Laboratories (Cambridge, MA). A 1.3-mm rotor was packed with 2.91 mg of L-glutamine.

4.4.2. Solid-state NMR spectroscopy

Spectra were recorded at 18.8 T (800 MHz ^{1}H Larmor frequency) on a Bruker Avance III standard-bore spectrometer equipped with a 1.3-mm triple-resonance probe head (Bruker). Three MAS frequencies were used for the spin-lock experiments: 40.2, 49.9, and 60.0 kHz. All other experiments were performed at 60.0 kHz. The temperature of the ubiquitin sample was estimated to be +6.7 °C at a MAS frequency of 40 kHz, +17.0 °C at 50 kHz and +31.0 °C at 60 kHz. This estimate was obtained by comparison of the isotropic ^{1}H chemical shift of water at high-speed MAS to published chemical shifts[46]. For all experiments, the ^{1}H-^{13}C and ^{1}H-^{15}N dipolar couplings were decoupled during acquisition using 12 kHz of XiX decoupling on ^{1}H (ref. [19,20]). A recycling delay of 2 seconds was employed. Chemical shifts are reported in ppm from DSS, calibrated using adamantane as external reference[47]. CP-MAS spectra were acquired with 128 scans for ubiquitin (Figure 4 a,b,d) and 32 scans for glutamine (Figure 4 and 6). The 2D ^{13}C-^{13}C DREAM spectrum was recorded with 250 t_1 points and 288 scans, for a total experimental time of 40 hours. The maximum acquisition time was 6.2 ms in the t_1 and 14.4 ms in the t_2 dimension. Double-quantum ^{13}C-^{13}C mixing was accomplished by a tangential amplitude sweep[28,29] from ~25 to ~35 kHz during 5 ms.

4.4.3. Measurement of excitation profiles

Signal intensity was detected after a cross-polarization of 5 ms through a series of ^{1}H-^{15}N CP-MAS spectra in glutamine (Figure 2). To record a complete profile, the ^{15}N carrier was swept from 102 kHz upfield to 102 kHz downfield of the resonances in steps of 750 Hz. The glutamine ^{15}N spectrum has two resonances corresponding to the side-chain amide and to the backbone amine at 111.1 ppm and 38.16 ppm, respectively. The homonuclear dipolar couplings between ^{15}N are considered to be insignificant, based on the large distance separation between two nitrogen atoms in the crystal structure (ref. [48,49]). Hence, signals from both side-chain and backbone were combined in the analysis to increase S/N.

4.4.4. Quantum mechanical simulations

The simulated excitation profiles of ^{1}H-^{15}N CP in glutamine were obtained from a step-wise integration procedure of the Liouville-von Neumann equation within the numerical simulation routine GAMMA[50], see Appendix. Neglecting scalar through-bond couplings, the relevant internal system Hamiltonian in the Zeeman interaction frame contains ^{15}N isotropic chemical shift, dipolar couplings (^{1}H-^{1}H and ^{1}H-^{15}N) and RF irradiation on ^{1}H and ^{15}N (time-dependent in case of MOD-CP). Mimicking the situation in an NH_2 group, a proton-proton distance of 1.74 Å (corresponding dipolar coupling: 23.2 kHz) and proton-nitrogen distances of 1.05 Å (dipolar coupling: 10.5 kHz) were used. To obtain a complete excitation profile, simulations were carried out in steps of 375 Hz such that the ^{15}N isotropic chemical shift covered a range from –102 kHz to +102 kHz. The expectation value of spin-locked ^{15}N magnetization was averaged for all time points between 6 ms and 8 ms. Powder averaging involved 120 orientations. All simulated profiles were adjusted with a single, global scaling factor in order to be compared with experimental profiles. This global scaling factor was found by least-squares fitting of simulated to observed signal intensities.

4.5. Results

4.5.1. Characteristics of spin-locked magnetization

We studied the dependence of recoupling conditions on MAS frequency, performing the spin-lock experiments at three different MAS frequencies: 40 kHz, 50 kHz, and 60 kHz (Figure 1). The decay of ^{1}H (the "I" spin) magnetization was monitored by applying a spin-lock for 2.5 ms in glutamine, with nutation frequencies ν_1^H ranging from 0 to $3\times\nu_{MAS}$. The remaining magnetization was transferred for detection to the nearest ^{13}C nucleus through a high-power ZQ CP. The signal presented in Figure 1 represents the addition of intensities from all five ^{13}C resonances of glutamine. The three intensity curves at different MAS were individually normalized against a control experiment in which the ^{1}H spin-lock period was omitted (i.e. a normal ZQ CP experiment without a spin-lock between ^{1}H 90° pulse and CP).

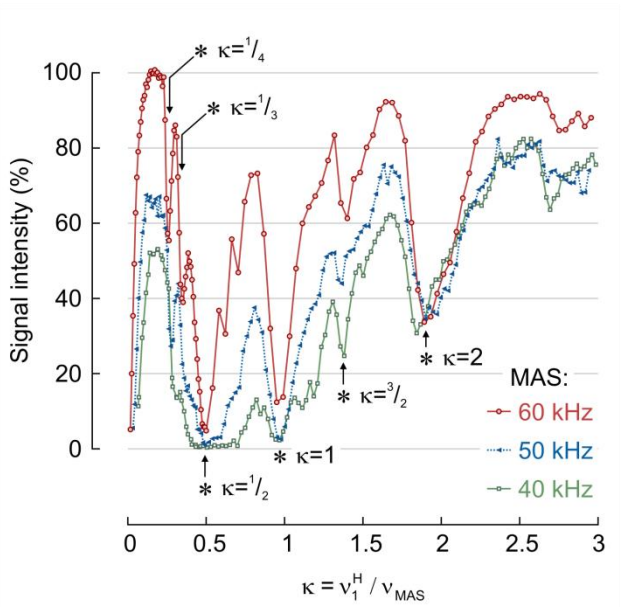

Figure 1: Proton spin-lock efficiency. The ^{1}H spin-lock efficiency was monitored as a function of RF-field strength ν_1^H and MAS frequency ν_{MAS}. Signal intensity is detected indirectly on ^{13}C after 2.5 ms of ^{1}H spin-lock. Spin-lock efficiency is measured at three different MAS frequencies: 40 kHz (green squares), 50 kHz (blue triangles), and 60 kHz (red circles). Asterisks indicate recoupling conditions that lead to rapid magnetization decay, near the ratios $\kappa = \left\{\frac{1}{4}, \frac{1}{3}, \frac{1}{2}, 1, \frac{3}{2}, 2\right\}$.

As previously described[38], spin-locked proton magnetization decays rapidly when the ratio of nutation frequency to MAS frequency, $\kappa = \nu_1^H / \nu_{MAS}$, is around $\kappa = \frac{1}{4}$, $\frac{1}{3}$, $\frac{1}{2}$, 1, $\frac{3}{2}$, or 2. Those conditions are indicated in Figure 1 by asterisks. At $\kappa = \frac{1}{2}$, the HORROR condition[26], homonuclear dipolar couplings are recoupled; at the $\kappa = 1$ rotary resonance condition, chemical shift anisotropies as well as homonuclear and heteronuclear dipolar couplings are recoupled; while the $\kappa = 2$ rotary resonance condition recouples chemical shift anisotropies and heteronuclear dipolar couplings. The $\kappa = \frac{1}{4}$, $\frac{1}{3}$, and $\frac{3}{2}$ conditions can be understood in terms of higher-order perturbation theory[38,51].

Two inferences can be made as the MAS frequency increases. First, the overall magnetization decay is slower at high MAS, for all nutation frequencies with ratio $\kappa < 2$. Second, the range of RF-field frequencies (in Hz) affected around the $\kappa = \frac{1}{2}$ and $\kappa = 1$ conditions becomes considerably narrower at high MAS. The narrowing of the $\kappa = \frac{1}{2}$ and $\kappa = 1$ conditions is consistent with the interpretation that, while CSA and heteronuclear couplings are efficiently averaged out at 40 kHz of MAS, the averaging of proton homonuclear couplings benefits from further increase in the MAS frequency. Nicely, at 60 kHz MAS, we can find a band of frequencies below the $\kappa = \frac{1}{4}$ ratio which very effectively conserves the initial magnetization. After 2.5 ms of spin-lock, more than 95% of the magnetization is preserved for nutation frequencies between 7 kHz and 14 kHz. Other regions of low decay can be found in the following intervals: $\frac{1}{4} < \kappa < \frac{1}{3}$, $\frac{1}{2} < \kappa < 1$, $1 < \kappa < \frac{3}{2}$, $\frac{3}{2} < \kappa < 2$, $\kappa > 2$. At low MAS, however, only frequencies above the $\kappa = 2$ condition efficiently prevent rapid magnetization decay.

4.5.2. Second-order cross-polarization with increased bandwidth

Extending the bandwidth of SOCP is easily achieved by increasing the RF-field strength for both I and S nuclei while preserving n = 0 Hartmann-Hahn matching. The efficiency of the SOCP transfer deteriorates when ν_1^H approaches the $\kappa = \frac{1}{4}$ recoupling condition. However, the fast decay of spin-locked ^{1}H magnetization is avoided when the nutation frequency is carefully selected between the $\kappa = \frac{1}{4}$ and $\kappa = \frac{1}{3}$ ratios. Past the $\kappa = \frac{1}{3}$ ratio however, this approach is not advisable since recoupling conditions are encountered and power deposition in the sample increases with the square of the applied frequency. Increasing the bandwidth of SOCP is best suited when the chemical shift dispersion is small in comparison to the MAS frequency, which is most likely the case for moderate static fields and fast MAS, e.g. $B_0 \leq 14.1\,T$ (600 MHz ^{1}H Larmor frequency) and 60 kHz MAS.

4.5.3. Amplitude-modulated second-order cross-polarization

For higher static fields and very large chemical shift offsets, the SOCP with increased bandwidth approach is not appropriate and an alternative has to be sought. Pulses with a cyclical amplitude modulation are commonly employed for the selective excitation of two resonances[52-54]. A cross-polarization scheme with cosine or sine amplitude modulation has already been presented in solution-state NMR[55]. We thus considered the use of cosine amplitude modulation in combination with low-power CP in order to transfer polarization to multiple regions separated by a large chemical shift offset.

An applied RF pulse is described by a field strength B_1 (T) and a reference transmitter frequency ν_{ref} (Hz). By multiplying this general pulse with a cosine modulation of frequency ν_{mod} (Hz), we obtain (Eq. 2):

$$\text{(Eq. 2)} \quad \begin{aligned} \vec{B}_1^{mod} &= \vec{B}_{[B_1;\,\nu_{ref}]} \cdot \cos\left(2\pi\nu_{mod}t\right) \\ &= B_1 \cdot \left[\cos\left(2\pi\nu_{ref}t\right)\cdot\cos\left(2\pi\nu_{mod}t\right)\cdot\vec{e}_x + \sin\left(2\pi\nu_{ref}t\right)\cdot\cos\left(2\pi\nu_{mod}t\right)\cdot\vec{e}_y\right] \end{aligned}$$

The effect of the modulation results from the product-to-sum trigonometric identity. It can be seen that this is equivalent to irradiation with two fields of half the strength (Eq. 3). Therefore, in order to preserve the properties of the original pulse but transmit it simultaneously at two different offsets, the field strength has to be doubled.

$$\text{(Eq. 3)} \quad \begin{aligned} \vec{B}_1^{mod} &= B_1 \cdot \begin{pmatrix} \frac{1}{2}\left[\cos 2\pi\left(\nu_{ref}-\nu_{mod}\right)t + \cos 2\pi\left(\nu_{ref}+\nu_{mod}\right)t\right]\vec{e}_x \\ +\frac{1}{2}\left[\sin 2\pi\left(\nu_{ref}-\nu_{mod}\right)t + \sin 2\pi\left(\nu_{ref}+\nu_{mod}\right)t\right]\vec{e}_y \end{pmatrix} \\ &= \vec{B}_{\left[\frac{1}{2}B_1;\,\nu_{ref}-\nu_{mod}\right]} + \vec{B}_{\left[\frac{1}{2}B_1;\,\nu_{ref}+\nu_{mod}\right]} \end{aligned}$$

MOD-CP is achieved by application of a spin-lock pulse on ^{1}H and an amplitude-modulated spin-lock pulse on the S spin (Figure 4c). For two sites of interest, with isotropic chemical shifts δ_A and δ_B (ppm), the frequency of the amplitude modulation (in Hz) is $\nu_{mod} = \frac{1}{2} \cdot |\delta_A - \delta_B| \cdot \nu_{Larmor}$. The reference transmitter position for the S spin (in ppm) is set to the middle frequency between the two sites: $\Omega_{ref} = \frac{1}{2} \cdot |\delta_A + \delta_B|$. Compared to the regular SOCP, the applied field strength (B_1) for the rare spin is doubled. The original field strength applied on ^{1}H and carrier position are preserved. Following from (Eq. 3), n = 0 Hartmann-Hahn matching is established at resonance frequencies $\nu_{ref} - \nu_{mod}$ and $\nu_{ref} + \nu_{mod}$. Additionally, the final phase for each excitation band can be controlled independently[53,56].

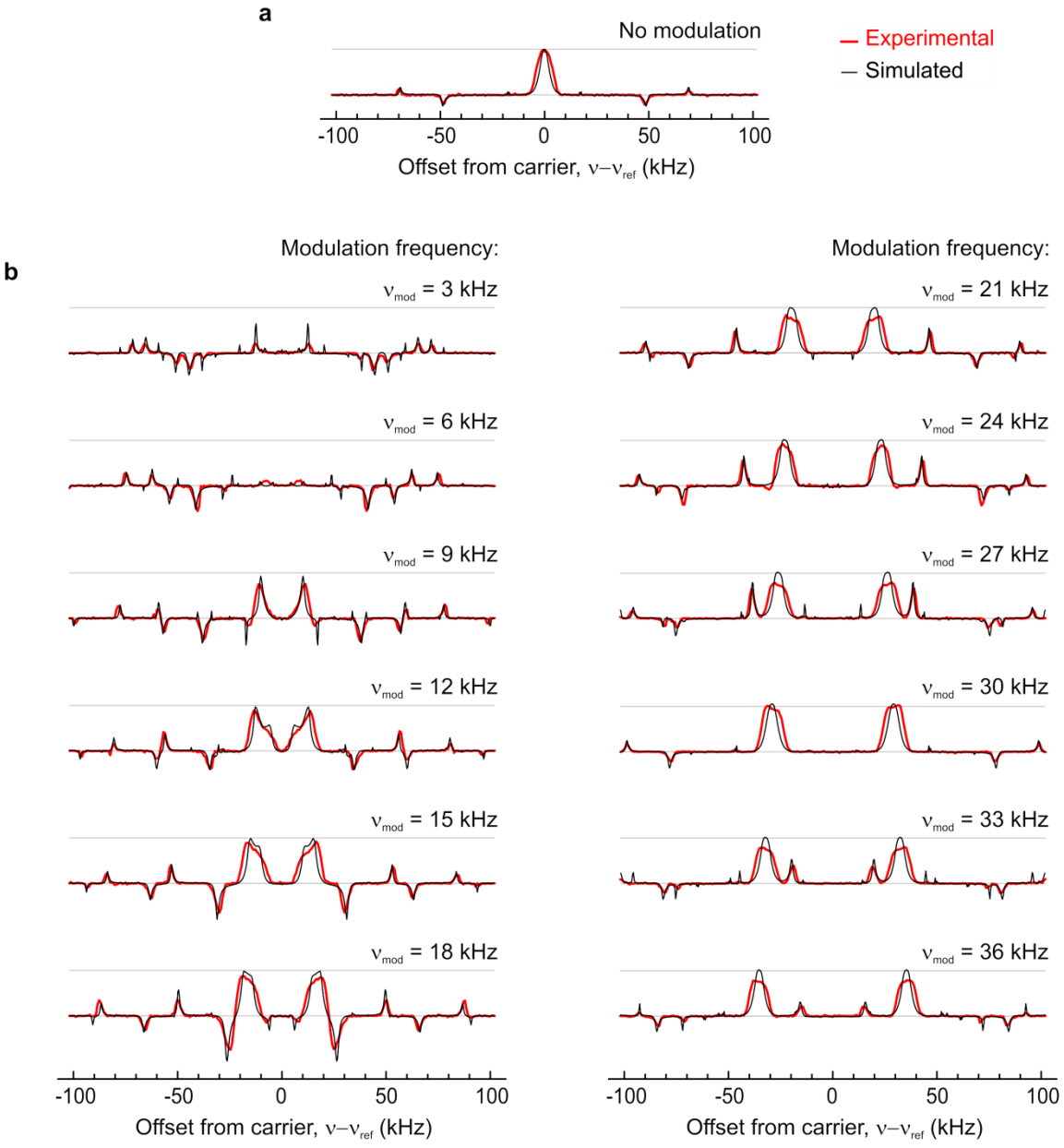
a
No modulation
Experimental
Simulated
-100
-50
0
50
100
Offset from carrier, ν−ν_ref (kHz)
b
Modulation frequency:
ν_mod = 3 kHz
ν_mod = 6 kHz
ν_mod = 9 kHz
ν_mod = 12 kHz
ν_mod = 15 kHz
ν_mod = 18 kHz
Modulation frequency:
ν_mod = 21 kHz
ν_mod = 24 kHz
ν_mod = 27 kHz
ν_mod = 30 kHz
ν_mod = 33 kHz
ν_mod = 36 kHz
-100
-50
0
50
100
Offset from carrier, ν−ν_ref (kHz)

Figure 2: Excitation profiles as a function of the carrier offset. For the experimental profiles (red), the signal intensity is measured on the ^{15}N resonances of glutamine after 5 ms of cross-polarization. Numerical simulations of the excitation profiles are shown in black. **a)** SOCP, with $\nu_1^H = \nu_1^N = 10\,\text{kHz}$. **b)** MOD-CP, with $\nu_1^H = 10\,\text{kHz}$, $\nu_1^N = 20\,\text{kHz}$, and modulation frequencies ranging from 3 kHz to 36 kHz. Above 9 kHz of modulation frequency, two bands of intense positive transfer are observed at offsets of $-\nu_{mod}$ and $+\nu_{mod}$.

Excitation profiles (Figure 2) confirm that the bandwidth and intensity of transfer remain constant for large modulation frequencies, $\nu_{mod} > \frac{1}{2}\nu_1^S$. From the experimental profiles, one can conclude that MOD-CP is a suitable method for the excitation of regions with large chemical shift separation. All features of the experimental profiles could be well reproduced by profiles simulated numerically within the GAMMA spin-simulation environment[50]. We considered an I_2S spin system as in an NH_2 group with two ^1H-^{15}N dipolar couplings and one ^1H-^1H dipolar coupling, as explained in more detail in the experimental section. Two bands of intense positive transfer are found at offsets of $-\nu_{mod}$ and $+\nu_{mod}$ relative to the carrier frequency, corresponding to on-resonance $n = 0$ Hartmann-Hahn matching (Figure 3). Other transfer conditions, with $n > 0$, are also matched off-resonance; this is seen in the excitation profile as positive (ZQ) or negative (DQ) transfer bands far away from the carrier position. The signal intensity for those bands is however reduced since the axis of the effective RF field is tilted away from the transverse plane.

Simulation and experiments demonstrate the consistent performance of MOD-CP over a wide range of modulation frequencies. A notable limitation is that the modulation frequency must be sufficiently large, $\nu_{mod} > \frac{1}{2}\nu_1^S$ (see Figure 3). Below this threshold, the two excitation bands come close together such that the rare nuclei experience two B_1 fields. The two effective fields have a slightly different axis of

nutation, resulting in dephasing of magnetization rather than spin-lock. In this case, SOCP with increased bandwidth can be employed to complement MOD-CP.

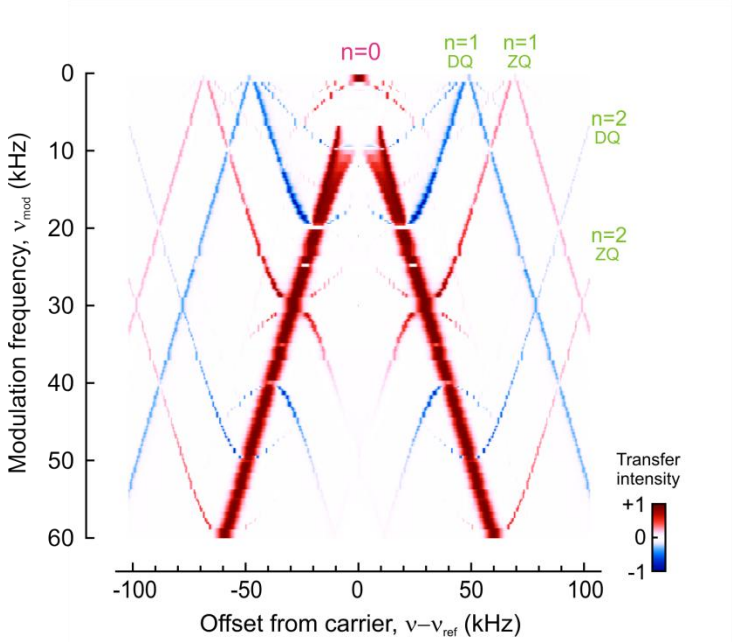

Figure 3: Simulation of magnetization transfer. The intensity of magnetization transfer was simulated for a series of carrier offset and MOD-CP modulation frequency. Positive transfer is indicated in red and negative transfer in blue. The dominant transfer at offsets of $-\nu_{mod}$ and $+\nu_{mod}$ corresponds to an on-resonance n = 0 Hartmann-Hahn condition. Magnetization transfer occurs as well off-resonance at sideband Hartmann-Hahn conditions (n = 1, n = 2), albeit with lesser intensity. Numerical simulations were carried out within the GAMMA spin-simulation environment considering an NH_2 spin system.

4.5.4. Selection of optimal cross-polarization conditions

The efficiency of three cross-polarization schemes was assessed: *i)* high-power CP, *ii)* SOCP, and *iii)* MOD-CP. We acquired ^{13}C CP-MAS spectra in order to compare the three schemes in terms of bandwidth and sensitivity (Figure 4). The optimized experimental parameters for cross-polarization are summarized in Table 1.

The conditions for broadband transfer at high power were optimized for maximal overall signal intensity. A linear amplitude sweep is used on the ^{1}H spin-lock pulse to ensure that the transfer is resilient to Hartmann-Hahn mismatch[57]. In ubiquitin, the best cross-polarization was obtained at the DQ n = 2 condition, with $\overline{\nu_1^H} = 85\,\text{kHz}$ (mean frequency), $\nu_1^C = 35\,\text{kHz}$ during 1.3 ms. In glutamine, best transfer was achieved at the ZQ n = 1 condition, with nutation frequencies of $\overline{\nu_1^H} = 100\,\text{kHz}$, $\nu_1^C = 40\,\text{kHz}$, and a contact time of 0.8 ms.

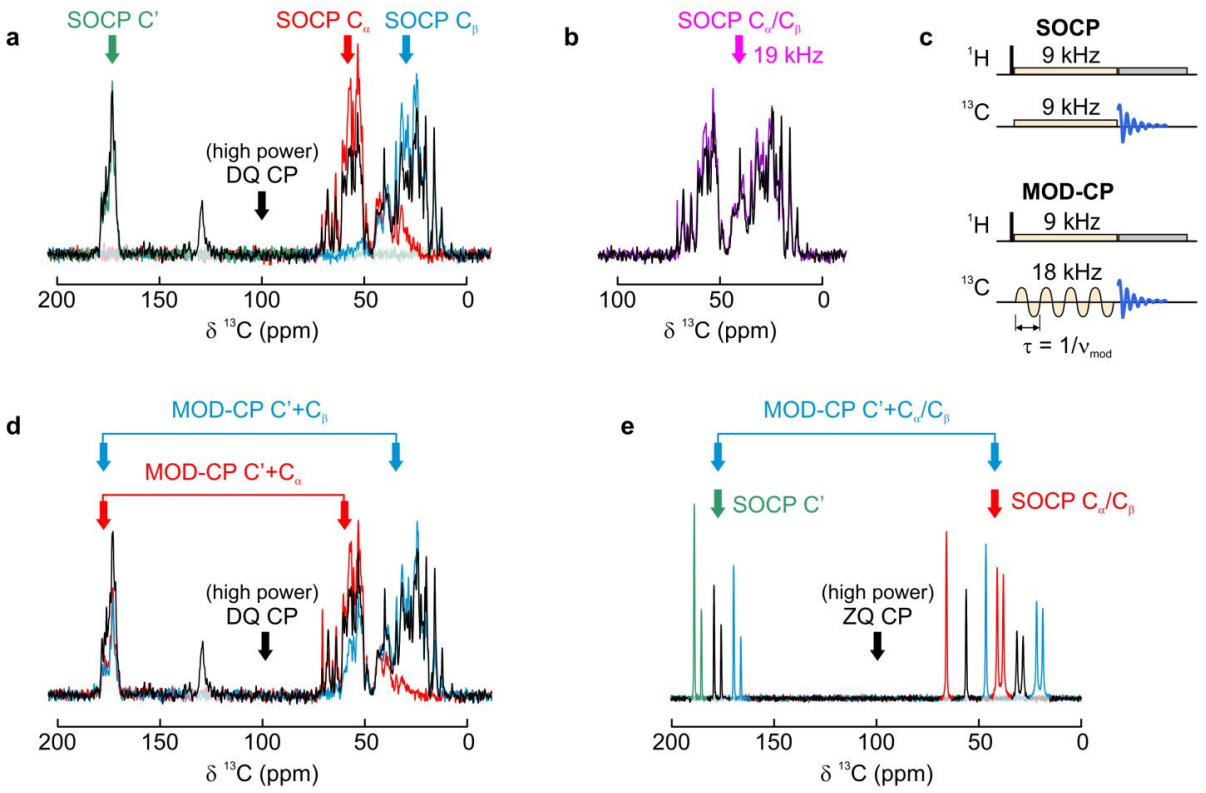

Figure 4: Comparison of cross-polarization efficiencies . **a)** ^{13}C CP-MAS spectra of micro-crystalline ubiquitin utilizing high-power DQ CP (black), or regular SOCP, $\nu_1^H = \nu_1^C = 9\,\text{kHz}$, on the C' (green), C_α (red), or C_β region (blue). The ^{13}C carrier positions are indicated by arrows. **b)** SOCP on the aliphatic region with $\nu_1^H = \nu_1^C = 19\,\text{kHz}$ (pink) is compared to high-power CP (black, as in **a**). **c)** Pulse schemes for SOCP (top) and MOD-CP (bottom). In MOD-CP, a cosine amplitude modulation is applied to the ^{13}C spin-lock pulse, and the frequency ν_1^C is doubled to excite both ^{13}C regions. **d)** MOD-CP can excite both the C' and C_α regions (red), or both the C' and C_β regions (blue). **e)** ^{13}C CP-MAS spectra of glutamine using high-power ZQ CP (black), MOD-CP (blue), and SOCP on the C' (green) or C_α (red) regions. Spectra are shifted from the high-power ZQ CP for better visibility.

Sample		$\overline{\nu_1}$ (kHz)	τ_{cp} (ms)	Region excited	^{13}C Ω_{ref} (ppm)	Notes
Double-quantum (n=2) CP						
Ubiquitin	^{1}H	85	1.3	Broadband	100	100-80% ramp on ^{1}H pulse
	^{13}C	35				
Zero-quantum (n=1) CP						
Glutamine	^{1}H	100	0.8	Broadband	100	100-80% ramp on ^{1}H pulse
	^{13}C	40				
Second-order (n=0) CP						
Ubiquitin	^{1}H	9	2.5	C'	175	
	^{13}C	9		C_α	56	
				C_β	28	
Glutamine	^{1}H	10	5.0	C'	177.5	
	^{13}C	10		C_α/C_β	42.5	
SOCP with increased bandwidth						
Ubiquitin	^{1}H	19	1.4	$C_\alpha+C_\beta$	40	
	^{13}C	19				
Amplitude-modulated SOCP (MOD-CP)						
Ubiquitin	^{1}H	9	2.5	$C'+C_\alpha$	115.5	11.9 kHz modulation on ^{13}C pulse
	^{13}C	18		$C'+C_\beta$	101.5	14.7 kHz modulation on ^{13}C pulse
Glutamine	^{1}H	10	5.0	$C'+C_\alpha/C_\beta$	110	13.5 kHz modulation on ^{13}C pulse
	^{13}C	20				
Amplitude-modulated band-selective CP						
Glutamine	^{1}H	50	3.0	$C'+C_\alpha/C_\beta$	110	13.5 kHz modulation on ^{13}C pulse
	^{13}C	20				

Table 1: Experimental parameters for cross-polarization at ultra-fast MAS. Parameters are specified for a 60 kHz MAS frequency and a 800 MHz ^{1}H Larmor frequency.

$\overline{\nu_1}$: Mean frequency of the RF-field.

τ_{CP}: Contact time.

Ω_{ref}: Transmitter frequency.

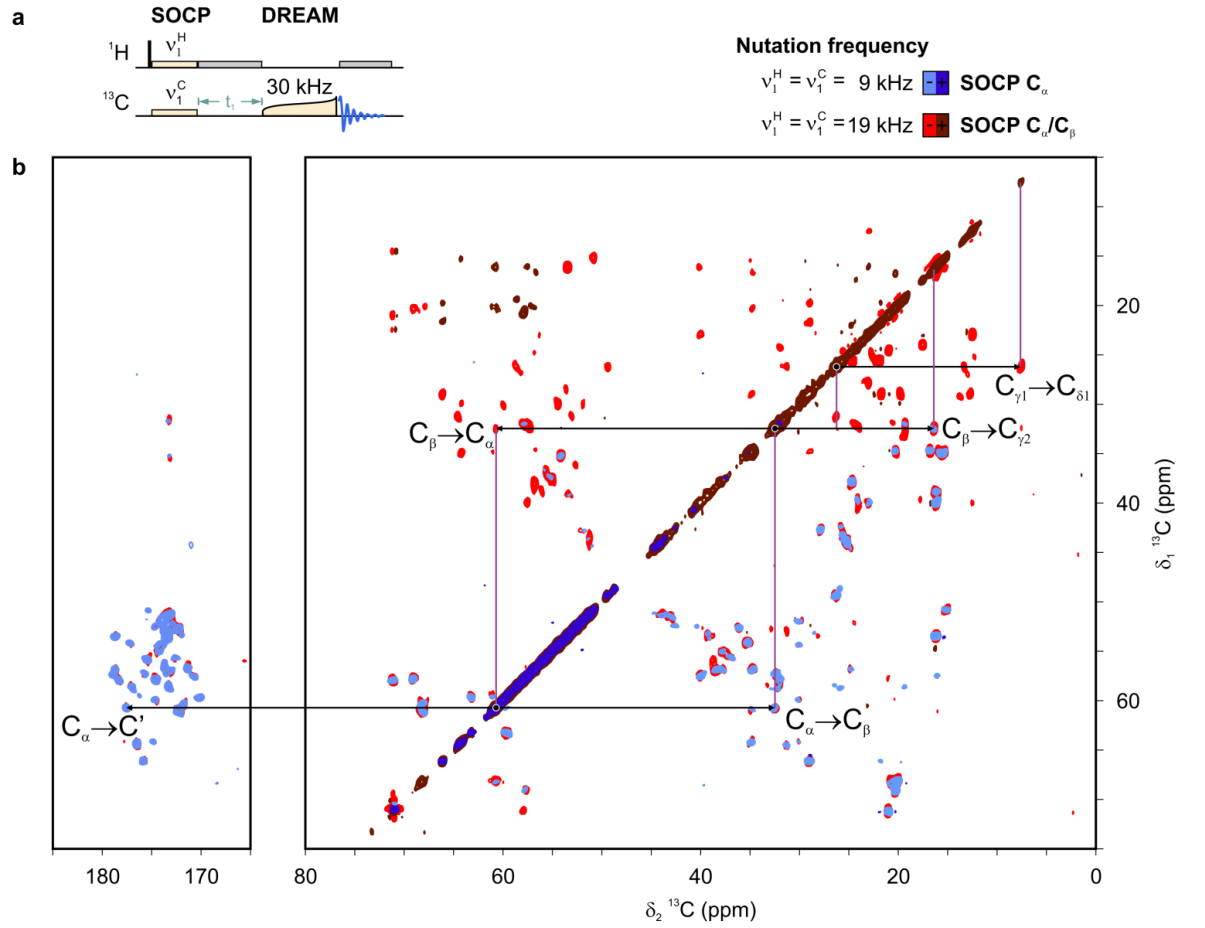

Figure 5: ^{13}C-^{13}C DREAM correlation spectrum of micro-crystalline ubiquitin. **a)** SOCP is used for the initial polarization transfer from ^{1}H to ^{13}C. In one case, a regular SOCP is used with the ^{13}C carrier at 56 ppm to first excite the C_α region. In the other case, SOCP with increased bandwidth is employed with the ^{13}C carrier at 40 ppm to excite the full aliphatic region. A tangential amplitude sweep applied on ^{13}C allows dipolar recoupling of adjacent carbons. **b)** The 2D spectra resulting from those two SOCP conditions are overlayed. Positive and negative peaks are indicated in dark and light blue, respectively, for the regular SOCP (spectrum reproduced from Vijayan et al., ChemPhysChem, 2009); and in dark and light red for SOCP with increased bandwidth. For illustrative purposes, cross-peaks enabling the assignment of the Ile23 spin-system are indicated.

Much lower nutation frequencies are employed for SOCP: 2.5 ms of spin-lock at 9 kHz for ubiquitin, and 5 ms at 10 kHz for glutamine. The higher sensitivity of regular SOCP compared to high-power CP is readily apparent (Figure 4a), and is explained by various reasons. An intrinsic feature of SOCP is that the initial magnetization can originate from protons not directly coupled to the S spin. In the thermodynamic limit, a narrow ^{13}C bandwidth also contributes to enhanced signal, since magnetization is shared among a lesser number of carbons. Matching at the n = 0 condition makes the SOCP scheme less sensitive to RF field inhomogeneities and thermal drift of the amplifiers[38]. Finally, the ^{1}H spin-lock is most efficient at low RF power, as previously discussed.

4.5.5. Application to protein samples

The excitation of the full ^{13}C aliphatic region at 60 kHz MAS, from about 5 to 75 ppm, is illustrated for uniformly labeled ubiquitin by the spectrum of SOCP with increased bandwidth (Figure 4b). Nutation frequencies of 19 kHz are used during 1.4 ms.

We acquired a 2D ^{13}C-^{13}C DREAM spectrum (Figure 5) employing a SOCP with $\nu_1^H = \nu_1^C = 19\,\text{kHz}$ as the initial cross-polarization step and compared it to a similar spectrum employing a SOCP with $\nu_1^H = \nu_1^C = 9\,\text{kHz}$ [18]. All cross-peaks from the regular SOCP spectrum appear at the same position in the increased-bandwidth SOCP spectrum. In addition, the latter spectrum contains many cross-peaks which are absent in the regular SOCP spectrum. This offers the possibility of identifying all ^{13}C-^{13}C correlations within the spin system of an amino acid. The assignment of ^{13}C resonances from an isoleucine residue (Ile23), from the carbonyl to the methyl carbons, is highlighted in Figure 5.

MOD-CP is demonstrated on ubiquitin (Figure 4d) and glutamine (Figure 4e). In ubiquitin, magnetization is transferred simultaneously to the C' and C_α regions by applying the ^{13}C pulse at 115.5 ppm with a modulation of 11.9 kHz. Alternatively, the C' and C_β regions are excited with the ^{13}C spin-lock pulse at 101.5 ppm and an amplitude modulation of 14.7 kHz. In both cases, RF-field frequencies are $\nu_1^H = 9\,\text{kHz}$ and $\nu_1^C = 18\,\text{kHz}$, with a contact time of 2.5 ms. In glutamine, MOD-CP excites all five ^{13}C resonances when the ^{13}C spin-lock pulse is applied at 110 ppm with a modulation of 13.5 kHz. RF-field frequencies are $\nu_1^H = 10\,\text{kHz}$ and $\nu_1^C = 20\,\text{kHz}$, with a contact time of 5 ms. With the exception of C', which is slightly reduced, all ^{13}C resonances exhibit greater transfer intensity with MOD-CP and increased-bandwidth SOCP than with the high-power CP schemes.

4.5.6. Amplitude modulation in combination with other CP schemes

Under particular circumstances, a given cross-polarization scheme might be advantageous compared to another one. Thus, it was verified that the amplitude modulation approach can be used in combination with various CP schemes. We used band-selective ^1H-^{13}C CP (ref. [37]) in combination with a modulated ^{13}C pulse to simultaneously excite C' and C_α/C_β (Figure 6). The band-selective ^1H-^{13}C CP could likely be preferred in cases where the site of interest is scarcely protonated, since SOCP requires at least two protons coupled to each other with at least one of them coupled to the S spin. Indeed, band-selective ^1H-^{13}C CP works very well for transfer to carbonyls. In this study, SOCP was preferred because it is currently the CP scheme with the lowest power requirement.

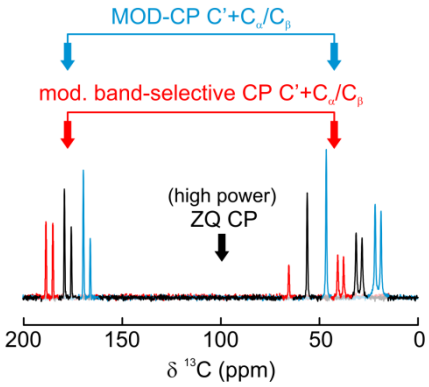

Figure 6: Amplitude modulation in combination with various CP schemes. In this case, CP-MAS spectra were acquired in glutamine using either an amplitude-modulated band-selective ^{1}H-^{13}C CP (red, $\nu_1^H = 50$ kHz, $\nu_1^C = 20$ kHz, 3 ms), or an amplitude-modulated SOCP (blue, $\nu_1^H = 10$ kHz, $\nu_1^C = 20$ kHz, 5 ms). The spectra are compared to a high-power ZQ CP (black, $\overline{\nu_1^H} = 100$ kHz, $\nu_1^C = 40$ kHz, 0.8 ms) and were shifted for better visibility.

4.6. Discussion

The two proposed strategies to extend the ^{13}C bandwidth are complementary and suited to different situations. The first strategy, consisting of SOCP transfer with increased RF power levels, is appropriate for small chemical shift dispersion. For instance, by selecting the ^{1}H and ^{13}C nutation frequency between the $\kappa = \frac{1}{4}$ and $\kappa = \frac{1}{3}$ ratios, one can excite the full ^{13}C aliphatic region in a spectrometer operating at 18.8 T (800 MHz ^{1}H Larmor frequency). This would not be possible with MOD-CP; at 18.8 T, the C_α and C_β regions have a separation of 5.6 kHz, which is lower than the desired nutation frequency, $\frac{1}{2}\nu_1^C \approx 9$ kHz. The second strategy, MOD-CP, is best suited for two regions with a large chemical shift offset.

Three variations of the SOCP scheme are now available for low-power pulse sequences at fast MAS: regular SOCP, SOCP with increased bandwidth, and MOD-CP.

Our results show that all SOCP-based schemes are more efficient than high-power CP for their respective bandwidth, while requiring less RF power. Regular SOCP still offers the highest sensitivity albeit at the cost of low bandwidth. MOD-CP and increased-bandwidth SOCP allow the precise selection of chemical shifts for rare nuclei, extending the spectral editing capability of SOCP.

In this study, we recorded a 2D ^{13}C-^{13}C correlation spectrum that contains ^{13}C-^{13}C correlations for complete amino acid spin systems, including carbonyl, aromatic and methyl carbons, as a demonstration of SOCP with increased bandwidth. MOD-CP supports a wide range of modulation frequencies (>36 kHz), which is advantageous for the study of biomolecules; e.g. in proteins, ^{13}C nuclei have a large chemical shift dispersion of ca. 190 ppm.

4.7. Conclusion

The proposed schemes are able to tailor cross-polarization to desired spectral regions with high efficiency and low RF power. The low power requirements of these schemes prevent RF heating and alteration of the sample. The deleterious effects of heating on spectral quality as well as the strain on the instrument are consequently reduced. In addition, sensitivity enhancement by fast acquisition and decreased recycle time resulting from paramagnetic relaxation is only feasible if entirely low-power sequences are available. Those factors advocate for a general use of SOCP-based schemes as an alternative to high-power CP. We therefore expect that their use will be beneficial for the investigation of biomolecular solids at high resolution and sensitivity.

4.8. Future prospects

The spectral editing capability now available can particularly benefit experiments containing multiple ^{1}H CP steps, for instance ChhC and NhhC experiments[58,59].

As proton homonuclear decoupling techniques improve[60-64], MOD-CP could become useful for low-power hetero-nuclear correlation (HETCOR) experiments.

Many other nuclei, such as ^{31}P, ^{15}N, ^{29}Si, and ^{19}F, cover a large range of isotropic chemical shifts[65]. Along with developments in probe head technology, the study of materials containing those nuclei can also benefit from fast MAS and SOCP-based transfer schemes.

4.9. References

1. Lesage, A. Recent advances in solid-state NMR spectroscopy of spin $I=^1/_2$ nuclei. *Physical Chemistry Chemical Physics* **11**, 6876-91 (2009).
2. McDermott, A. Structure and Dynamics of Membrane Proteins by Magic Angle Spinning Solid-State NMR. *Annual Review of Biophysics* **38**, 385-403 (2009).
3. Ernst, M., Samoson, A., Meier, B. H. Low-power decoupling in fast magic-angle spinning NMR. *Chemical Physics Letters* **348**, 293-302 (2001).
4. Peck, T. L., Magin, R. L., Lauterbur, P. C. Design and Analysis of Microcoils for NMR Microscopy. *Journal of Magnetic Resonance Series B* **108**, 114-24 (1995).
5. Ernst, M., Detken, A., Bockmann, A., Meier, B. H. NMR spectra of a microcrystalline protein at 30 kHz MAS. *Journal of the American Chemical Society* **125**, 15807-10 (2003).
6. de Lacaillerie, J. B. D., Jarry, B., Pascui, O., Reichert, D. "Cooking the sample": Radiofrequency induced heating during solid-state NMR experiments. *Solid State Nuclear Magnetic Resonance* **28**, 225-32 (2005).
7. Stringer, J. A., Bronnimann, C. E., Mullen, C. G., Zhou, D. H. H., Stellfox, S. A., Li, Y., Williams, E. H., Rienstra, C. M. Reduction of RF-induced sample heating with a scroll coil resonator structure for solid-state NMR probes. *Journal of Magnetic Resonance* **173**, 40-8 (2005).
8. Doty, F. D., Kulkarni, J., Turner, C., Entzminger, G., Bielecki, A. Using a cross-coil to reduce RF heating by an order of magnitude in triple-resonance multinuclear MAS at high fields. *Journal of Magnetic Resonance* **182**, 239-53 (2006).
9. Gor'kov, P. L., Chekmenev, E. Y., Li, C. G., Cotten, M., Buffy, J. J., Traaseth, N. J., Veglia, G., Brey, W. W. Using low-E resonators to reduce RF heating in biological samples for static solid-state NMR up to 900 MHz. *Journal of Magnetic Resonance* **185**, 77-93 (2007).
10. Krahn, A., Priller, U., Emsley, L., Engelke, F. Resonator with reduced sample heating and increased homogeneity for solid-state NMR. *Journal of Magnetic Resonance* **191**, 78-92 (2008).
11. Wu, C. H., Grant, C. V., Cook, G. A., Park, S. H., Opella, S. J. A strip-shield improves the efficiency of a solenoid coil in probes for high-field solid-state NMR of lossy biological samples. *Journal of Magnetic Resonance* **200**, 74-80 (2009).
12. Grant, C. V., Yang, Y., Glibowicka, M., Wu, C. H., Park, S. H., Deber, C. M., Opella, S. J. A Modified Alderman-Grant Coil makes possible an efficient cross-coil probe for high field solid-state NMR of lossy biological samples. *Journal of Magnetic Resonance* **201**, 87-92 (2009).
13. McNeill, S. A., Gor'kov, P. L., Shetty, K., Brey, W. W., Long, J. R. A low-E magic angle spinning probe for biological solid state NMR at 750 MHz. *Journal of Magnetic Resonance* **197**, 135-44 (2009).

14. Linser, R., Chevelkov, V., Diehl, A., Reif, B. Sensitivity enhancement using paramagnetic relaxation in MAS solid-state NMR of perdeuterated proteins. *Journal of Magnetic Resonance* **189**, 209-16 (2007).
15. Wickramasinghe, N. P., Shaibat, M. A., Jones, C. R., Casabianca, L. B., de Dios, A. C., Harwood, J. S., Ishii, Y. Progress in ^{13}C and ^{1}H solid-state nuclear magnetic resonance for paramagnetic systems under very fast magic angle spinning. *Journal of Chemical Physics* **128** (2008).
16. Wickramasinghe, N. P., Parthasarathy, S., Jones, C. R., Bhardwaj, C., Long, F., Kotecha, M., Mehboob, S., Fung, L. W. M., Past, J., Samoson, A., Ishii, Y. Nanomole-scale protein solid-state NMR by breaking intrinsic ^{1}H T_1 boundaries. *Nature Methods* **6**, 215-8 (2009).
17. Laage, S., Sachleben, J. R., Steuernagel, S., Pierattelli, R., Pintacuda, G., Emsley, L. Fast acquisition of multi-dimensional spectra in solid-state NMR enabled by ultra-fast MAS. *Journal of Magnetic Resonance* **196**, 133-41 (2009).
18. Vijayan, V., Demers, J. P., Biernat, J., Mandelkow, E., Becker, S., Lange, A. Low-Power Solid-State NMR Experiments for Resonance Assignment under Fast Magic-Angle Spinning. *Chemphyschem : a European journal of chemical physics and physical chemistry* **10**, 2205-8 (2009).
19. Detken, A., Hardy, E. H., Ernst, M., Meier, B. H. Simple and efficient decoupling in magic-angle spinning solid-state NMR: the XiX scheme. *Chemical Physics Letters* **356**, 298-304 (2002).
20. Ernst, M., Samoson, A., Meier, B. H. Low-power XiX decoupling in MAS NMR experiments. *Journal of Magnetic Resonance* **163**, 332-9 (2003).
21. Ernst, M., Meier, M. A., Tuherm, T., Samoson, A., Meier, B. H. Low-power high-resolution solid-state NMR of peptides and proteins. *Journal of the American Chemical Society* **126**, 4764-5 (2004).
22. Bennett, A. E., Rienstra, C. M., Auger, M., Lakshmi, K. V., Griffin, R. G. Heteronuclear Decoupling in Rotating Solids. *Journal of Chemical Physics* **103**, 6951-8 (1995).
23. Kotecha, M., Wickramasinghe, N. P., Ishii, Y. Efficient low-power heteronuclear decoupling in ^{13}C high-resolution solid-state NMR under fast magic angle spinning. *Magn Reson Chem* **45**, S221-S30 (2007).
24. Scholz, I., Hodgkinson, P., Meier, B. H., Ernst, M. Understanding two-pulse phase-modulated decoupling in solid-state NMR. *Journal of Chemical Physics* **130**, 114510 (2009).
25. Weingarth, M., Bodenhausen, G., Tekely, P. Low-power decoupling at high spinning frequencies in high static fields. *Journal of Magnetic Resonance* **199**, 238-41 (2009).
26. Nielsen, N. C., Bildsoe, H., Jakobsen, H. J., Levitt, M. H. Double-quantum homonuclear rotary resonance: Efficient dipolar recovery in magic-angle spinning nuclear magnetic resonance. *Journal of Chemical Physics* **101**, 1805-12 (1994).
27. Kehlet, C., Vosegaard, T., Khaneja, N., Glaser, S. J., Nielsen, N. C. Low-power homonuclear dipolar recoupling in solid-state NMR developed using optimal control theory. *Chemical Physics Letters* **414**, 204-9 (2005).
28. Verel, R., Baldus, M., Ernst, M., Meier, B. H. A homonuclear spin-pair filter for solid-state NMR based on adiabatic-passage techniques. *Chemical Physics Letters* **287**, 421-8 (1998).
29. Verel, R., Ernst, M., Meier, B. H. Adiabatic dipolar recoupling in solid-state NMR: The DREAM scheme. *Journal of Magnetic Resonance* **150**, 81-99 (2001).
30. Bennett, A. E., Griffin, R. G., Ok, J. H., Vega, S. Chemical shift correlation spectroscopy in rotating solids: Radio frequency-driven dipolar recoupling and longitudinal exchange. *Journal of Chemical Physics* **96**, 8624-7 (1992).
31. Bayro, M. J., Ramachandran, R., Caporini, M. A., Eddy, M. T., Griffin, R. G. Radio frequency-driven recoupling at high magic-angle spinning frequencies: Homonuclear recoupling *sans* heteronuclear decoupling. *Journal of Chemical Physics* **128**, 11 (2008).
32. Bayro, M. J., Maly, T., Birkett, N. R., Dobson, C. M., Griffin, R. G. Long-Range Correlations between Aliphatic ^{13}C Nuclei in Protein MAS NMR Spectroscopy. *Angewandte Chemie-International Edition* **48**, 5708-10 (2009).
33. Scholz, I., Huber, M., Manolikas, T., Meier, B. H., Ernst, M. MIRROR recoupling and its application to spin diffusion under fast magic-angle spinning. *Chemical Physics Letters* **460**, 278-83 (2008).
34. Weingarth, M., Demco, D. E., Bodenhausen, G., Tekely, P. Improved magnetization transfer in solid-state NMR with fast magic angle spinning. *Chemical Physics Letters* **469**, 342-8 (2009).

35. De Paepe, G., Lewandowski, J. R., Loquet, A., Bockmann, A., Griffin, R. G. Proton assisted recoupling and protein structure determination. *Journal of Chemical Physics* **129** (2008).
36. Lewandowski, J. R., De Paepe, G., Eddy, M. T., Struppe, J., Maas, W., Griffin, R. G. Proton Assisted Recoupling at High Spinning Frequencies. *Journal of Physical Chemistry B* **113**, 9062-9 (2009).
37. Laage, S., Marchetti, A., Sein, J., Pierattelli, R., Sass, H. J., Grzesiek, S., Lesage, A., Pintacuda, G., Emsley, L. Band-Selective ^{1}H–^{13}C Cross-Polarization in Fast Magic Angle Spinning Solid-State NMR Spectroscopy. *Journal of the American Chemical Society* **130**, 17216-7 (2008).
38. Lange, A., Scholz, I., Manolikas, T., Ernst, M., Meier, B. H. Low-power cross polarization in fast magic-angle spinning NMR experiments. *Chemical Physics Letters* **468**, 100-5 (2009).
39. Lewandowski, J. R., De Paepe, G., Griffin, R. G. Proton assisted insensitive nuclei cross polarization. *Journal of the American Chemical Society* **129**, 728-9 (2007).
40. Lewandowski, J. R., De Paepe, G., Eddy, M. T., Griffin, R. G. ^{15}N–^{15}N Proton Assisted Recoupling in Magic Angle Spinning NMR. *Journal of the American Chemical Society* **131**, 5769-76 (2009).
41. Scholz, I., Meier, B. H., Ernst, M. NMR polarization transfer by second-order resonant recoupling: RESORT. *Chemical Physics Letters* **485**, 335-42 (2010).
42. Stejskal, E. O., Schaefer, J., Waugh, J. S. Magic-angle spinning and polarization transfer in proton-enhanced NMR. *Journal of Magnetic Resonance* **28**, 105-12 (1977).
43. Sardashti, M., Maciel, G. E. Effects of sample spinning on cross polarization. *Journal of Magnetic Resonance* **72**, 467-74 (1987).
44. Meier, B. H. Cross polarization under fast magic angle spinning: thermodynamical considerations. *Chemical Physics Letters* **188**, 201-7 (1992).
45. Hediger, S., Meier, B. H., Ernst, R. R. Cross polarization under fast magic angle sample spinning using amplitude-modulated spin-lock sequences. *Chemical Physics Letters* **213**, 627-35 (1993).
46. Hindman, J. C. Proton Resonance Shift of Water in Gas and Liquid States. *Journal of Chemical Physics* **44**, 4582-92 (1966).
47. Morcombe, C. R., Zilm, K. W. Chemical shift referencing in MAS solid state NMR. *Journal of Magnetic Resonance* **162**, 479-86 (2003).
48. Cochran, W., Penfold, B. R. The Crystal Structure of L-Glutamine. *Acta Crystallogr* **5**, 644-53 (1952).
49. Wagner, A., Luger, P. Charge density and topological analysis of L-glutamine. *Journal of Molecular Structure* **595**, 39-46 (2001).
50. Smith, S. A., Levante, T. O., Meier, B. H., Ernst, R. R. Computer Simulations in Magnetic Resonance. An Object-Oriented Programming Approach. *Journal of Magnetic Resonance Series A* **106**, 75-105 (1994).
51. Scholz, I., Meier, B. H., Ernst, M. Operator-based triple-mode Floquet theory in solid-state NMR. *Journal of Chemical Physics* **127**, 204504 (2007).
52. Gonzalez-Mendez, R., Engeseth, H., Gibson, A. A. B., Deolivares, J., Litt, L., James, T. L. The Modulation Theorem in Tailored Radiofrequency Excitation and its Application to a Notch Filter. *Journal of Magnetic Resonance* **78**, 308-13 (1988).
53. Boyd, J., Soffe, N. Selective Excitation by Pulse Shaping combined with Phase Modulation. *Journal of Magnetic Resonance* **85**, 406-13 (1989).
54. Patt, S. L. Single- and multiple-frequency-shifted laminar pulses. *Journal of Magnetic Resonance* **96**, 94-102 (1992).
55. Artemov, D., Bhujwalla, Z. M., Glickson, J. D. Band-Selective Heteronuclear Cross Polarization In Liquids. *Journal of Magnetic Resonance Series B* **107**, 286-8 (1995).
56. Croasmun, W. R., Carlson, R. M. K. *Two-Dimensional NMR Spectroscopy: Applications for Chemists and Biochemists*. 2nd edn, 180-181 (John Wiley & Sons, 1994).
57. Metz, G., Wu, X. L., Smith, S. O. Ramped-Amplitude Cross Polarization in Magic-Angle-Spinning NMR. *Journal of Magnetic Resonance Series A* **110**, 219-27 (1994).
58. Wilhelm, M., Feng, H., Tracht, U., Spiess, H. W. in *Wallace Brey Symposium.* 255-60 (Academic Press Inc).

59. Lange, A., Seidel, K., Verdier, L., Luca, S., Baldus, M. Analysis of proton-proton transfer dynamics in rotating solids and their use for 3D structure determination. *Journal of the American Chemical Society* **125**, 12640-8 (2003).
60. Amoureux, J. P., Hu, B. W., Trebosc, J., Wang, Q., Lafon, O., Deng, F. Homonuclear dipolar decoupling schemes for fast MAS. *Solid State Nuclear Magnetic Resonance* **35**, 19-24 (2009).
61. Salager, E., Stein, R. S., Steuernagel, S., Lesage, A., Elena, B., Emsley, L. Enhanced sensitivity in high-resolution ^{1}H solid-state NMR spectroscopy with DUMBO dipolar decoupling under ultra-fast MAS. *Chemical Physics Letters* **469**, 336-41 (2009).
62. Paul, S., Thakur, R. S., Goswami, M., Sauerwein, A. C., Mamone, S., Concistre, M., Forster, H., Levitt, M. H., Madhu, P. K. Supercycled homonuclear dipolar decoupling sequences in solid-state NMR. *Journal of Magnetic Resonance* **197**, 14-9 (2009).
63. Leskes, M., Madhu, P. K., Vega, S. Why does PMLG proton decoupling work at 65 kHz MAS? *Journal of Magnetic Resonance* **199**, 208-13 (2009).
64. Mao, K., Pruski, M. Homonuclear dipolar decoupling under fast MAS: Resolution patterns and simple optimization strategy. *Journal of Magnetic Resonance* **203**, 144-9 (2010).
65. Harris, R. K., Mann, Brian E. *NMR and the periodic table*. 88 (Academic Press, 1978).

4.10. Appendix

Source file for GAMMA simulation of HHN spin-system (File HHN_cos_3.cc)

```
#include "gamma.h"
using namespace std;

int main (int argc, char *argv[])
{
 spin_system ABC (3);          //set up a 3-spin system
    //spin 0:  H0
    //spin 1:  H1
    //spin 2:  C2
 int p=1;

 double p_dur;                          //acquisition duration
 int p_ori;                             //Number of orientation steps in powder loop
 int p_NCP;                             //Number of steps during 1 rotor period

 //spatial tensors in PAS
 space_T dip01_pas,dip02_pas,dip12_pas;
 space_T cs0_pas,cs1_pas,cs2_pas;

 double omegaR;                         //MAS frequency
 double omegaW;                         //RF (w1 13C) modulation frequency
 double omegaH,omegaC;                  //irradiated frequencies in Hertz
 double dip01,dip02,dip12;              //dipolar couplings
 double r01,r02,r12;
 double delsig=0.;                      //CS anisotropy
 double eta=0.;                         //asymmetry
 double delnu0,delnu1,delnu2;           //isotropic averages

 coord B(0,0,1);
 spin_T TTS0=T_CS2(ABC,0,B);            //spin tensors
 spin_T TTS1=T_CS2(ABC,1,B);
 spin_T TTS2=T_CS2(ABC,2,B);
 spin_T TTD01=T_D(ABC,0,1);
 spin_T TTD02=T_D(ABC,0,2);
 spin_T TTD12=T_D(ABC,1,2);

 string outFileName0;                   //output file names
 string outFileName1;
 string outFileName2;
 string outFileName;

 query_parameter (argc,argv,p++,"output filename    = ", outFileName);
 query_parameter (argc,argv,p++,"Powder orientations= ", p_ori);
 query_parameter (argc,argv,p++,"MAS orientations   = ", p_NCP);
 query_parameter (argc,argv,p++,"acquisition/ms     = ", p_dur);
 query_parameter (argc,argv,p++,"MAS frequency/Hz   = ", omegaR);
 query_parameter (argc,argv,p++,"Mod. frequency/Hz  = ", omegaW);
 query_parameter (argc,argv,p++,"RF-field(1H)/Hz    = ", omegaH);
```

```
query_parameter (argc,argv,p++,"RF-field(13C)/Hz   = ", omegaC);
query_parameter (argc,argv,p++,"Offset(C2)/Hz      = ", delnu2);
query_parameter (argc,argv,p++,"r01/A              = ", r01);
query_parameter (argc,argv,p++,"r02/A              = ", r02);
query_parameter (argc,argv,p++,"r12/A              = ", r12);

int a = static_cast<int>(omegaR);
int b = static_cast<int>(omegaW);

 int c = a % b;
 while(c != 0)
 {
   a = b;
   b = c;
   c = a % b;
 }

   int N_rep = static_cast<int>(omegaR/b);

//spins are on-resonance
delnu0=0.;
delnu1=0.;
//delnu2=0.; // 13C carrier offset is defined by query parameter

//HC pairs
dip02=4*122e3/(sqrt(6.0)*10*1)/(r02*r02*r02);
dip12=4*122e3/(sqrt(6.0)*10*1)/(r12*r12*r12);

//HH pairs
dip01=2*122e3/(r01*r01*r01);

p_ori=abs(13848/p_ori);

outFileName0=outFileName+".H0.dat";
outFileName1=outFileName+".H1.dat";
outFileName2=outFileName+".C2.dat";

double dwtime = 1./omegaR;

int NP = static_cast<int>(p_dur/dwtime/1000/N_rep);  //number of calculated points in FID
double ma = 54.73561;                                //magic angle

row_vector specsum0(NP);            //some arrays for powder loop
row_vector specsum1(NP);
row_vector specsum2(NP);

row_vector spect0(NP);
row_vector spect1(NP);
row_vector spect2(NP);

row_vector data0(NP);
row_vector data1(NP);
row_vector data2(NP);

dip01_pas=A2(0.,dip01,0.,0.,0.,0.); //set up PAS spatial tensors
dip02_pas=A2(0.,dip02,0.,0.,0.,0.);
dip12_pas=A2(0.,dip12,0.,0.,0.,0.);

dip01_pas=dip01_pas.rotate(0.,35.25,0.);
dip02_pas=dip02_pas.rotate(0.,70.5,0.);

cs0_pas=A2(delnu0,delsig,eta,0.,0.,0.);
cs1_pas=A2(delnu1,delsig,eta,0.,0.,0.);
cs2_pas=A2(delnu2,delsig,eta,0.,0.,0.);

gen_op H;                          //hamiltonian
double phi,theta,gamma;            //rotation angles of the powder loop
space_T CS0,CS1,CS2;               //spatial tensors in rotorsystem
space_T CS0R,CS1R,CS2R;            //                  laboratorysystem
space_T SD01,SD02,SD12;
space_T SDR01,SDR02,SDR12;

for (int c=1;c<13848;c=c+p_ori)  //powder loop
{
 cout<<"orientations: "<<c*100/13848<<"%\r"<<flush;
 theta=180./13848*c;                     //theta in [0,180]
 phi=360./13848 * ((107*c)%13848);       //phi   in [0,360]
 gamma=360./13848 * ((271*c)%13848);     //gamma in [0,360]

 gen_op sigma=(Ix(ABC,0)+Ix(ABC,1));     //start with coherence on spin 0,1, 1H
 gen_op detect0=Ix(ABC,0);
 gen_op detect1=Ix(ABC,1);
 gen_op detect2=Ix(ABC,2);

 SD01 = dip01_pas.rotate(phi,theta,gamma);  //rotate spatial parts
 SD02 = dip02_pas.rotate(phi,theta,gamma);
```

```
  SD12 = dip12_pas.rotate(phi,theta,gamma);
  CS0  = cs0_pas.rotate(phi,theta,gamma);
  CS1  = cs1_pas.rotate(phi,theta,gamma);
  CS2  = cs2_pas.rotate(phi,theta,gamma);

  gen_op S;
  gen_op U=Ie(ABC,0);

  for (double h=0;h<N_rep;h++)
  {
   for (double i=0;i<p_NCP;i++)                    //MAS loop
   {
    phi = 360. * (i+0.5)/p_NCP;
    //rotate spatial part around magic angle
    SDR01=SD01.rotate(phi,ma,0.0);
    SDR02=SD02.rotate(phi,ma,0.0);
    SDR12=SD12.rotate(phi,ma,0.0);

    CS0R=CS0.rotate(phi,ma,0.0);
    CS1R=CS1.rotate(phi,ma,0.0);
    CS2R=CS2.rotate(phi,ma,0.0);

    H =     CS0R.component(0,0)*TTS0.component(0,0);
    H = H + CS1R.component(0,0)*TTS1.component(0,0);
    H = H + CS2R.component(0,0)*TTS2.component(0,0);

    H = H + CS0R.component(2,0)*TTS0.component(2,0);
    H = H + CS1R.component(2,0)*TTS1.component(2,0);
    H = H + CS2R.component(2,0)*TTS2.component(2,0);

    H = H + SDR02.component(2,0)*Iz(ABC,0)*Iz(ABC,2);
    H = H + SDR12.component(2,0)*Iz(ABC,1)*Iz(ABC,2);

    H = H + SDR01.component(2,0)*TTD01.component(2,0);

      H = H + omegaH * (Ix(ABC,0)+Ix(ABC,1));
    H = H + omegaC * (Ix(ABC,2)) * cos( 2 * PI * omegaW * (h + i/p_NCP) * dwtime );

    S = prop (H,-dwtime/p_NCP);
    U = S*U;
   } //end i
  } //end h

  for (int m1=0;m1<NP;m1++) //calculate spectrum
  {
   //fill data block
   spect0(m1)=sin(theta*PI/180)*trace (sigma,detect0);
   spect1(m1)=sin(theta*PI/180)*trace (sigma,detect1);
   spect2(m1)=sin(theta*PI/180)*trace (sigma,detect2);
   evolve_ip(sigma,U);
  }

  specsum0+=spect0;         //sum up of each orientation
  specsum1+=spect1;
  specsum2+=spect2;
 }//end of powder loop

 for (int l = 0; l<NP;l++)  //only real part
 {
  data0(l)= Re(specsum0(l));
  data1(l)= Re(specsum1(l));
  data2(l)= Re(specsum2(l));
 }

 GP_1D(outFileName0,data0);  //save spectra
 GP_1D(outFileName1,data1);
 GP_1D(outFileName2,data2);
 cout<<"\n";
 return 0;
}
```

5. Sensitivity enhancement in ultra-fast MAS solid-state NMR by recovery of proton magnetization

5.1. Introduction

As presented in Chapters 2–4, ultra-fast MAS offers several attractive advantages over MAS experiments at slower spinning rates[1-3]. Such advantages include the use of low-power pulse elements, the reduction of RF heating, and efficient averaging of the anisotropic part of nuclear interactions such as chemical shift anisotropies, dipolar couplings and quadrupolar couplings. As a consequence, several new applications have been enabled by the use of ultra-fast spinning: study of quantity-limited samples, study of proteins containing paramagnetic centers[4-7], measurement of dynamic processes[8,9], measurement of X–H distances[10], improved coherence lifetimes during through-bond correlations experiments[11-13] and new symmetry-based recoupling sequences[14-17].

At fast MAS (20–40 κHz) and ultra-fast MAS (>40 kHz) however, the signal-to-noise ratio is compromised due to the reduction of the rotor dimensions and decrease of the NMR-active sample volume. Different strategies have been implemented in order to restore a high sensitivity at fast and ultra-fast MAS: paramagnetic doping aiming at acceleration longitudinal ^{1}H relaxation combined with the use of short recycling delays [18-21], proton-detected experiments on protonated materials [22-24] and partially deuterated samples[7,25-28]; on the other hand, ultra-fast MAS probe-heads integrated into a dynamic nuclear polarization (DNP)[29,30] set-up are being actively developed.

Another important concept employed to boost NMR sensitivity stems from the realization that a large portion of magnetization remains unused after an experiment, and gives rise to two different strategies for sensitivity enhancement. In the first strategy, the magnetization remaining on low-gamma nuclei (e.g. ^{13}C) is utilized. One method for sensitivity enhancement of solid-state NMR called RELOAD-CP was proposed, where

the bulk ^{13}C polarization is stored along the $+z$ axis and used to accelerate the recovery of selectively-excitated ^{13}C[31]. In another method, the "afterglow" signal remaining on ^{15}N after a first band-selective double CP to C_α is transfer to the C' carbons for an immediate second detection[32,33]. Similarly, parallel acquisition set-ups have been developed[34] as well as experiments with multiple acquisition periods – simultaneous cross-polarization to ^{15}N and ^{13}C in DUMAS[35,36] and MEIOSIS[37] – or time-shared acquisition with simultaneous acquisition of ^{15}N-^{13}C and ^{13}C-^{13}C correlations in TSTSAR[38].

In the second strategy, the magnetization remaining on protons is recovered and used to accelerate the apparent magnetization recovery rate after an experiment, allowing the shortening of the recycling delay. This strategy is exploited in solution-state NMR[39], for example in the LTROSY[40], SOFAST[41] and COST[42] families of experiments. In 1978, Tegenfeldt and coworkers first proposed to employ this strategy in solid-state NMR for experiments directly detected on a low-gamma nucleus, by applying a flip-back pulse on the ^{1}H channel after cross-polarization and decoupling[43]. A special case where this strategy is particularly efficient is when only few protons contribute to the polarization transfer, for instance when carbons are selectively excited[44] or in the case of natural abundance ^{13}C materials[45]. The flip-back pulse was also employed in recent applications to pharmaceuticals[46] and deuterated proteins[47].

The magnetization recovery strategy suffers however from two limitations in the low MAS (<20 kHz) and fast MAS (20–40 kHz) regimes: *i*) the pulse sequence elements employed on the ^{1}H channel need to preserve a sufficient amount of polarization, *ii*) these pulse elements must be compatible with efficient magnetization transfer and heteronuclear decoupling schemes. Following our previous studies on spin-locked ^{1}H magnetization[48,49], we demonstrate in the current study that favorable conditions are obtained at ultra-fast MAS. The conditions employed provide a general method for

sensitivity enhancement which can be combined with a large variety of CP schemes and which does not require selective carbon excitation, making the recovery enhancement strategy suitable for the recording of broad-band excitation spectra on uniformly-labeled and natural abundance samples altogether. This method can be combined with the Second-Order Cross-Polarization (SOCP) scheme[48] and its broadband variation, the amplitude-modulated SOCP scheme (MOD-CP)[49]. Those two schemes require a low RF power and were shown to offer a sizable enhancement (up to ~1.50) compared to hard-power CP schemes.

Contribution statement

The present chapter forms a manuscript in preparation: "Sensitivity enhancement in ultra-fast MAS solid-state NMR by recovery of proton magnetization", Jean-Philippe Demers, Vinesh Vijayan, Adam Lange. J.P.D recorded ssNMR spectra and analyzed the data.

5.2. Hypotheses and Method Summary

Hypotheses:

A) At ultra-fast MAS, we can simultaneously obtain slow ^{1}H spin-lock decay and efficient ^{1}H-^{13}C decoupling.

B) Since we can simultaneously obtain slow ^{1}H spin-lock decay and efficient ^{1}H-^{13}C cross-polarization using SOCP-based schemes (see Chapter 4, section <4.5.4>), we can expect a significant amount of proton magnetization remaining after a CP-decoupling experiment at ultra-fast MAS.

C) Using a flip-back pulse after a CP-decoupling experiment will allow a faster magnetization recovery and increased sensitivity.

D) The primary mechanism of sensitivity enhancement is the recovery of bulk magnetization and not an increase in longitudinal proton relaxation rates.

E) The recovery enhancement is compatible with a large variety of CP transfer schemes.

Method summary:

Spin-lock curve and decoupling curves were recorded at 65 kHz.

Remaining amounts of ^{1}H magnetization were quantified after different steps of the CP-decoupling experiment.

The mechanism of sensitivity enhancement was characterized through recovery and sensitivity curves.

The remaining ^{1}H amounts and enhancement ratio were determined for seven common cross-polarization conditions.

5.3. Materials and Methods

5.3.1. Sample preparation and solid-state NMR spectroscopy

A 1.3-mm rotor was packed with 2.91 mg of uniformly [^{13}C, ^{15}N]-labeled L-glutamine (Cambridge Isotope Laboratories, Cambridge, MA). All spectra were recorded on a standard-bore 18.8 T instrument (800 MHz ^{1}H Larmor frequency) equipped with a 1.3-mm DVT triple-resonance probe head (Bruker BioSpin, Rheinstetten, Germany). A MAS rate of 65.0 kHz was employed. A sample temperature of 40 °C was obtained by regulating the temperature of the cooling nitrogen gas at -25 °C with a gas flow in the range of 935 L/h to 1200 L/h using a BCU-X accessory.

In order to calibrate the RF nutation frequencies ($\nu_1^{^1H}$ for the proton channel, $\nu_1^{^{13}C}$ for the carbon channel), we recorded nutation experiments at a series of amplifier attenuation values (dB). In the nutation curve, the average difference between two zero-crossing points was used to determine the length of the 180° pulse at a particular attenuation value. The RF nutation frequencies produced by the amplifiers were linear over the full range of used attenuation values ($R^2 = 0.999$), and RF nutation frequencies were calculated by linear regression from the calibrated values.

5.3.2. Extraction of signal intensities

A baseline correction is first applied on the individual frequency-domain spectra by fitting areas devoid of signal with a piecewise polynomial spline function[50] (6 pieces, polynomial order 4). The spectral intensity as a function of frequency, $I_{(\nu)}$ (Eq. 1), results from the addition of the resonance spectra $I^{j}_{(\nu)}$ contributed from each individual nucleus.

[Eq. 1] $$I_{(\nu)} = \sum_{j=1}^{N} I^{j}_{(\nu)}$$

We describe individual resonance spectra $I^{j}_{(\nu)}$ with a mixed Lorentzian/Gaussian function (Voigt profile), which is the convolution ($*$) of a Lorentzian lineshape $L_{(\nu)}$ [Eq. 2] with a Gaussian lineshape $G_{(\nu)}$ [Eq. 3]. The Lorentzian lineshape is associated with the apparent transverse dephasing rate of a resonance peak while the Gaussian lineshape is associated with the heterogeneous broadening of a resonance peak due to inhomogeneity of the sample and static field. Parameters for those functions are the isotropic chemical shift ν_0 (ppm), a Gaussian line-width parameter σ, and a Lorentz line-width parameter Γ.

[Eq. 2] $$L_{(\nu)} = \frac{\Gamma}{2\pi\left(\left(\nu-\nu_0\right)^2 + \left(\frac{1}{2}\Gamma\right)^2\right)}$$

[Eq. 3] $$G_{(\nu)} = \frac{1}{\sigma\sqrt{2\pi}} \cdot e^{\frac{-\nu^2}{2\sigma^2}}$$

The Voigt profile [Eq. 4] has four parameters: ν_0, σ, Γ, and the peak volume a_0 (a.u.). The mixed function was computed from the real part of the Faddeeva function [Eq. 5], where erfc is the complex complementary error function[51].

[Eq. 4] $$I^{j}_{(\nu)} = a_0 \cdot L_{(\nu)} * G_{(\nu)}$$

[Eq. 5] $I^{j}_{(\nu)} = a_0 \cdot \mathrm{Re}\left[w_{\left(\frac{\nu-\nu_0+\frac{1}{2}\Gamma}{\sigma\sqrt{2}}\right)} \right], \; w_{(z)} = e^{-z^2} \cdot \mathrm{erfc}(-iz)$

The full width at half-height (FWHH) for the Lorentzian, Gaussian and Voigt functions are given by[52] [Eq. 6]:

[Eq. 6]
$$f_L = \Gamma$$
$$f_G = \sigma\sqrt{2\ln 2}$$
$$f_V \approx 0.5346 \cdot f_L + \sqrt{0.2166 f_L^2 + f_G^2}$$

For a Free Induction Decay (FID) recorded in a given number of scans n_{scan}, the total signal energy S_{tot} is simply the sum of individual peak volumes a_0 as both $L_{(\nu)}$ and $G_{(\nu)}$ have a constant unit volume [Eq. 7].

[Eq. 7] $S_{tot} = \sum_{j=1}^{N} a_0^j$

The peak volumes for the five ^{13}C resonances of L-glutamine are obtained by least-square fitting of the spectrum with five individual mixed functions $I^{j}_{(\nu)}$. An initial parameter estimate is obtained from the piecewise fitting of spectral regions to a single mixed function; the final fitting optimizes all five mixed functions simultaneously. For Figures 1a, 3 and 4, the parameters ν_0, σ, and Γ are optimized on a reference spectrum (sum of all spectra) and then kept fixed while the peak volumes a_0 are further optimized for each spectrum of a series. For Figure 1b, ν_0 is determined from the reference spectrum, values for σ and a_0 are determined globally for all spectra and successively fixed, then values for Γ are optimized for each individual spectra.

5.3.3. Measurement of remaining ^{1}H magnetization level and ^{1}H magnetization recovery curves

During an arbitrary pulse sequence, the initial ^{1}H magnetization M_0^z reduces to a final level M_f^z [Eq. 8]. The fraction of preserved ^{1}H magnetization f_0 was determined for the following pulse elements: *i*) a ^{1}H spinlock, *ii*) cross-polarization, *iii*) cross-polarization followed by continuous-wave (*cw*) decoupling. After excitation by a 90° pulse on ^{1}H, a 'mock' experiment was carried with the aforementioned pulse elements; the remaining ^{1}H magnetization amount was then read through cross-polarization to ^{13}C. The CP conditions were kept identical for the 'mock' and for the 'read' experiment, such that the reported levels originate solely from the pool of protons that contribute to cross-polarization. Any ^{13}C magnetization already present after the 'mock' experiment was filtered out by phase-cycling of the aforementioned pulse elements. To ensure equal amount of initial ^{1}H magnetization, each repetition of the experiment was preceded by two 6-ms purge pulses at $\nu_1^{^1H}$ = 83 kHz with phase *x*,-*x*, followed by a recycling delay of 10 s. For *i*) and *ii*), the ^{1}H spin-lock pulse and cross-polarization ^{1}H pulse have the same duration and power level, as listed in Table 1). For *iii*) the *cw* decoupling was applied for 8 ms with a RF frequency $\nu_1^{^1H}$ = 13.4 kHz. The cross-polarization ^{1}H pulse and the *cw* decoupling pulse are always applied along the same phase.

[Eq. 8] $M_f^z = f_0 \cdot M_0^z$

Magnetization recovery curves (Figure 4) were recorded in a similar fashion, with cross-polarization followed by *cw* decoupling in the 'mock' experiment, with the addition that a variable recovery delay τ was inserted prior to the 'read' experiment. A recycling delay of 21.5 s was employed. Three series of experiments were recorded: *i*) no pulse is applied, leading to rapid decay of transverse ^{1}H magnetization, *ii*) a 90° ^{1}H

pulse is applied directly after the 'mock' experiment to return magnetization to $+\hat{I}_z$ (flip-back), or *iii*) a 90° ^{1}H pulse placed the magnetization along the $-\hat{I}_z$ axis (flip-down). Depending on the series of experiment, the following value for M_f^z is employed: *i*) $M_f^z = 0$, *ii*) $M_f^z = f_0 \cdot M_0^z$, or *iii*) $M_f^z = -f_0 \cdot M_0^z$.

Assuming a mono-exponential recovery behavior, the magnetization available for the 'read' experiment is described by Eq. 9. Alternatively, a more complex recovery behavior can be better described by a weighted sum of N exponentials, each exponential with individual population p_i, apparent relaxation time $T_{1,i}$ and remaining fraction $f_{0,i}$ [Eq. 10].

[Eq. 9] $$M_{(\tau)}^z = M_{eq} - \left(M_{eq} - M_f^z\right) \cdot \exp\left(-\tau / T_{1,app}^{^1H}\right)$$

[Eq. 10] $$M_{(\tau)}^z = M_{eq} - \sum_{i=1}^{N}\left[p_i \cdot \left(M_{eq} - M_{f,i}^z\right) \cdot \exp\left(-\tau / T_{1,i}\right)\right] \Big/ \sum_{i=1}^{N} p_i$$

5.3.4. Measurement of sensitivity in the steady-state

The sensitivity of a multi-scan experiment as a function of the inter-scan delay τ was measured through cross-polarization. Experiments were recorded in three different conditions: *i*) no pulse applied after decoupling, *ii*) with flip-back pulse, or *iii*) with flip-down pulse. The sensitivity[53] is described in the frequency domain by the signal-to-noise ratio per unit square root time $(S/N)_t$ [Eq. 11]. The signal amplitude extracted from experiment is taken as the total signal energy S_{tot} as described in section 2.2.

[Eq. 11] $$(S/N)_t = \frac{S_{tot}}{\sigma_{noise} \cdot \sqrt{t_{tot}}}$$

The noise amplitude σ_{noise}, as estimated from the mean standard deviation of independent regions of the baseline, was found to increase with the square root of n_{scan} as in [Eq. 12], where k_{noise} is a proportionality constant. The number of scans was adjusted to obtain a total experimental time t_{tot} of at least 200 s per replicate. A sufficient number of dummy scans were employed prior to the first recorded iteration, $n_{dummy} \geq \max\left[0.08 \cdot n_{scan}, 2\right]$, such that the measured magnetization did not deviate by more than 2 % from ideal steady-state.

[Eq. 12] $\sigma_{noise} = k_{noise} \cdot \sqrt{n_{scan}}$

The sensitivity can be modeled as a function of the inter-scan delay for the three series of experiments, since the amount of ^{13}C magnetization detected through cross-polarization is directly related to the amount of ^{1}H magnetization at the beginning of the experiment M_0^z ; the calculated signal energy S_{calc} being related to M_0^z by a proportionally constant [Eq. 13].

[Eq. 13] $S_{calc} = \eta \cdot M_0^z$

The amount M_0^z decreases with every scan in the initial regime, but approaches a steady-state value $M_{0,ss}^z$ after a large number of scans. The value of $M_{0,ss}^z$ for given values of f_0 and $T_{1,app}^{^1H}$ can be found through a geometrical series[39,54] assuming a mono-exponential behavior for the recovery [Eq. 14] or for a multi-exponential exponential behavior [Eq. 15].

[Eq. 14] $$M_{0,ss(\tau)}^z = M_{eq} \cdot \frac{1 - \exp\left(-\tau / T_{1,app}^{^1H}\right)}{1 - f_0 \cdot \exp\left(-\tau / T_{1,app}^{^1H}\right)}$$

$$[\text{Eq. 15}]\quad M^{z}_{0,ss(\tau)} = M_{eq} \cdot \sum_{i=1}^{N}\left[p_i \cdot \frac{1-\exp\left(-\tau/T_{1,i}\right)}{1- f_{0,i} \cdot \exp\left(-\tau/T_{1,i}\right)} \right] \Big/ \sum_{i=1}^{N} p_i$$

5.3.5. Calculation of uncertainties, fitting and hypothesis testing

For the magnetization recovery curves (Figure 4) and the sensitivity curves (Figure 5), experiments were recorded in replicates. Each series of experiments was recorded by interleaving short and long variable delays in order to make measurements robust against temporally-correlated systematic errors, for example due to steady-state effects, RF heating or drift in instrument conditions.

The uncertainty on the signal intensity was estimated individually for each delay value using the pooled standard deviation[55]. For a number of replicates n_j ($n_j \geq 3$ for most data points) and a standard deviation s_j among those replicates, the pooled standard deviation σ_p is calculated according to Eq. 16 where the index j corresponds to each of the three experimental curves (j=1: no flip-back, j=2: with flip-back, and j=3: with flip-down). This uncertainty estimate is used in statistical significance tests and to depict error bars in Figures 4 and 5.

$$[\text{Eq. 16}]\quad \sigma_p = \sqrt{\left(\sum_{j=1}^{3} \left(n_j - 1\right) s_j^{\,2} \right) \Big/ \left(\sum_{j=1}^{3} \left(n_j - 1\right) \right)}$$

The individual curves *i*, *ii* and *iii* (recovery curve, Figure 4; or sensitivity curve, Figure 5) are fitted as a group with either of two models: A) recovery following a mono-exponential behavior [Eq. 9 and 14], B) recovery modeled as the sum of two exponential components [Eq. 10 and 15]. The following parameters are extracted for each of the exponential components: the fraction this component relative to the total proton pool

$p_i/\sum p_i$, the longitudinal ^1H relaxation time $T_{1,i}$ and the amount of remaining ^1H magnetization which is recovered by the flip-back pulse $f_{0,i}$. Values for M_{eq}, p_i, $T_{1,i}$ and $f_{0,i}$ are obtained by minimization of the residual sum of squares between calculated and experimental values ($SS_{Lack\ of\ fit}$).

The validity of the fit was assessed by computing the F score, which compares $SS_{Lack\ of\ fit}$ to the sum of squares due to pure experimental error ($SS_{Pure\ error}$) estimated from the deviation of replicate measurements. An F score larger than the critical F value indicates that the lack of fit is unlikely to be due to chance alone. Furthermore, since the mono-exponential model is nested within the multi-exponential exponential model, we use the F-test to determine whether model B explains the experimental significantly better than model A or whether the reduction in $SS_{Lack\ of\ fit}$ merely results from the increase in number of parameters.

The uncertainty of the fitted parameters (Table 2) was estimated with a Monte Carlo procedure. The Monte Carlo data point y_k^{MC} is generated from the experimental data point y_k^{exp} using [Eq. 10] where σ_k is the uncertainty of this data point as described above and ε is drawn randomly from a normal distribution of mean zero and standard deviation of one. The fitting procedure was repeated for >20,000 iterations and the uncertainty of a parameter is taken as the standard deviation of this parameter in the Monte Carlo fitting results.

[Eq. 17] $y_k^{MC} = y_k^{exp} + \sigma_k \cdot \varepsilon$

5.4. Results

5.4.1. Efficient ^{1}H spin-locking and ^{1}H–^{13}C decoupling is obtained at ultra-fast MAS using low-power RF

In order to obtain a maximal amount of ^{1}H magnetization after a proton-decoupled CP experiment, dephasing has to be avoided during cross-polarization and heteronuclear decoupling.

It has been previously demonstrated that spin-locked ^{1}H magnetization is preserved for longer times at ultra-fast MAS under specific ranges of RF nutation frequencies $\nu_1^{^1H}$ [48,49]. Here, we measured the decay of spin-lock ^{1}H magnetization in uniformly [^{13}C,^{15}N]-labeled glutamine at 65 kHz MAS (Figure 1a and 2a). As ultra-fast MAS strongly reduces homonuclear ^{1}H dipolar couplings, the resonance conditions around $\nu_1^{^1H} \approx \frac{1}{2}\nu_r$ (HORROR[56]) and $\nu_1^{^1H} \approx \nu_r$ (rotary resonance[57,58]) are narrowed considerably. However, higher order recoupling conditions[48] occur at $\nu_1^{^1H} \approx \frac{1}{4}\nu_r$, $\frac{1}{3}\nu_r$ and $\frac{3}{2}\nu_r$. Efficient spin-lock is obtained at low power when the RF nutation frequency $\nu_1^{^1H}$ is in the range of 0.07 to 0.21 times the MAS frequency ν_r.

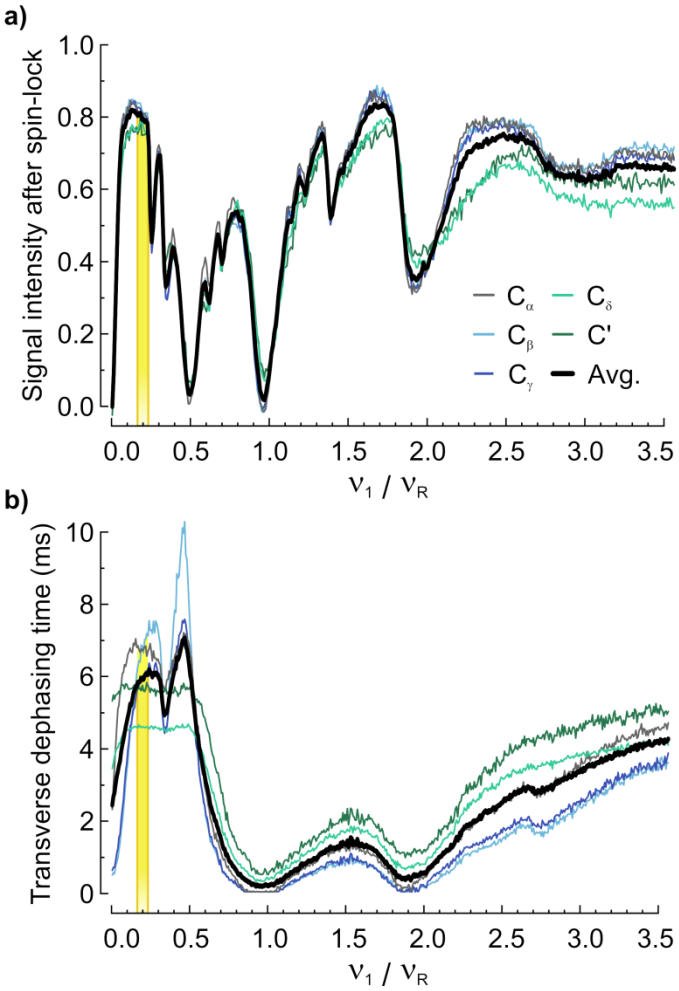

Figure. 1. Low-power *cw* irradiation allows efficient ^{1}H spin-lock and ^{1}H-^{13}C decoupling at 65 kHz MAS in the range of RF frequency from $\nu_1^{^1H} \approx 0.14 \cdot \nu_r$ to $0.21 \cdot \nu_r$, is highlighted by yellow rectangles. The average signal intensities or dephasing times are represented as thick lines. **(a)** ^{1}H Spin-lock efficiency. The total signal intensity was detected on ^{13}C resonances after 2.5 ms of ^{1}H spin-lock in glutamine as a function of the spin-lock frequency $\nu_{1\ SL}^{^1H}$ **(pulse scheme Figure 2a)**. Intensities were normalized against a reference experiment with the spinlock block omitted. **(b)** Decoupling efficiency. The Lorentzian broadening of the glutamine ^{13}C resonance line-shapes is expressed as a transverse dephasing time T_2' (ms) for a series of decoupling RF frequency $\nu_{1\ dec}^{^1H}$ **(pulse scheme Figure 2b)**.

At high power, efficient spin-lock is obtained with $\nu_1^{^1H} \approx 1.3 \cdot \nu_r$ and with the $\nu_1^{^1H} / \nu_r$ ratio in the range 1.6–1.8 and 2.3–2.65. Very few differences in decay behavior are observed between different ^{13}C sites. We measured a rotating-frame longitudinal relaxation time ^1H $T_{1\rho} = 13.9 \pm 0.4$ ms from a spin-lock decay curve recorded at a nutation frequency of 13.4 kHz ($\nu_1^{^1H} \approx 0.21 \cdot \nu_r$).

It has also been demonstrated previously that continuous low-power irradiation produces efficient heteronuclear decoupling at ultra-fast MAS[4,59]. We acquired the CP spectrum of glutamine at 65 kHz varying the RF frequency $\nu_1^{^1H}$ during *cw* decoupling. In addition to the intrinsic relaxation time T_2 of transverse ^{13}C coherences, residual terms of the heteronuclear dipolar coupling due to imperfect decoupling contribute to the total homogeneous line-width Δ'. This line-width is usually measured in the context of a spin-echo[60], with an associated transverse dephasing time $T_2' = (\pi \cdot \Delta')^{-1}$. We quantified the decoupling efficiency (Figure 1b) by determining the Lorentzian broadening of the carbon line-shapes f_L and estimating an associated transverse dephasing time $T_2' \approx (\pi \cdot f_L)^{-1}$. In this case, ^{13}C line-shapes exhibit different behaviors depending on their number of attached protons. For carbonyls ^{13}C (C′ and C_δ), efficient decoupling is obtained for $\nu_1^{^1H} / \nu_r$ ratios in the range of 0.06 to 0.50. A strong recoupling condition occurs at $\nu_1^{^1H} = \frac{1}{3} \cdot \nu_r$ for methylene carbons (C_β and C_γ), requiring at least three dipolar-coupled protons[61], which is almost undetected in non-protonated carbons and attenuated for C_α.

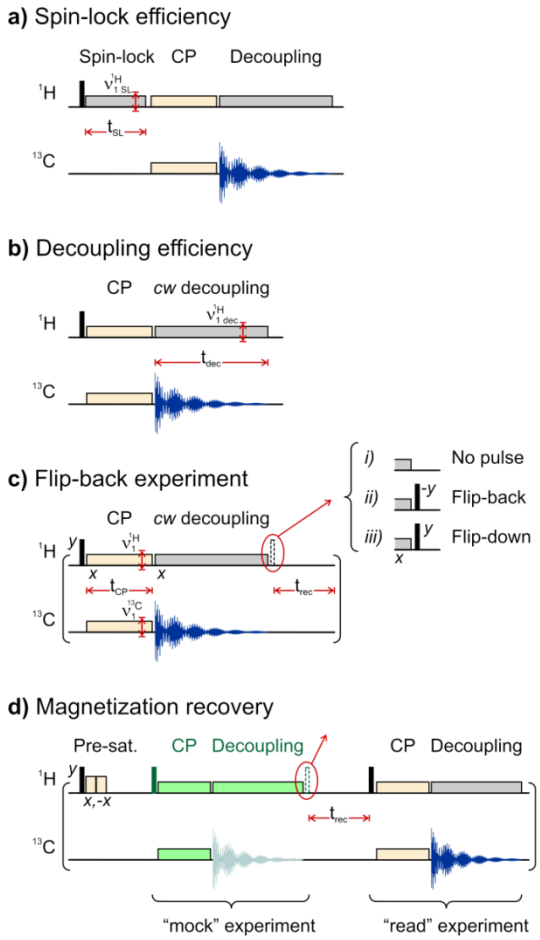

Figure 2. Solid-state NMR pulse schemes for measurement of **(a)** ^{1}H spin-lock efficiency (Figure 1a) **(b)** ^{1}H-^{13}C decoupling efficiency (Figure 1b) **(c)** sensitivity curve (Figure 5) and signal enhancement (Figure 6) **(d)** ^{1}H remaining magnetization (Figure 3) and recovery curve (Figure 4). **(c)** The signal intensity is measured on ^{13}C after a SOCP experiment to aliphatic carbons ($C_\alpha/C_\beta/C_\gamma$) as a function of the recycling delay. A high number of dummy scans were applied prior to recording to ensure measurement in the steady-state regime. **(d)** To ensure a constant initial amount of magnetization, protons are pre-saturated followed by a recycling delay. To know the recovery behavior after a CP-decoupling experiment (Figure 4), a 'mock' SOCP experiment is executed, containing either the flip-back pulse, the flip-down pulse or no pulse. The amount of magnetization regained after a given recovery delay (t_{rec}) is then measured by the 'read' experiment, a SOCP to aliphatic carbons. To know the remaining ^{1}H magnetization after a CP-decoupling experiment (Figure 3), a 'mock' experiment is carried and the remaining ^{1}H magnetization is measured immediately by a second identical 'read' experiment. Magnetization transferred to ^{13}C by the 'mock' experiment is filtered out by phase cycling.

For protonated carbons, the best decoupling condition occurs around $\nu_1^{^1H} \approx 0.46 \cdot \nu_r$; however, nearly as efficient decoupling can be obtained in the low-power regime with $\nu_1^{^1H}$ ranging from 0.14 to $0.3 \cdot \nu_r$. Both regions of efficient ^{1}H-^{13}C decoupling correspond to purely homonuclear ^{1}H-^{1}H recoupling conditions, the HORROR condition[56] at $\nu_1^{^1H} \approx \frac{1}{2}\nu_r$ and a four-spin condition[48] at $\nu_1^{^1H} \approx \frac{1}{4}\nu_r$, suggesting that the decoupling performance is strongly enhanced by self-decoupling[62,63], where fast exchange of magnetization between I spins reduces I-S dipolar couplings[64].

It is thus possible to find a range of ^{1}H RF frequencies which fulfills both requirements of efficient decoupling and magnetization preservation. This range is situated at $\nu_1^{^1H} \approx 0.14 \cdot \nu_r$ to $0.21 \cdot \nu_r$ (Figure 1). We thus selected a proton irradiation frequency of 13.4 kHz ($\nu_1^{^1H} \approx 0.21 \cdot \nu_r$) to be used in low-power CP schemes.

5.4.2. ^{1}H magnetization is well preserved after cross-polarization and decoupling

A series of low-power and high-power CP schemes were tested in order to obtain ^{1}H–^{13}C transfer: band-selective DQ-CP[65], second-order cross-polarization (SOCP)[48], amplitude-modulated second-order cross-polarization (MOD-CP)[49] and high power Hartmann-Hahn CP[66,67]. The very efficient ^{1}H spin-lock conditions previously mentioned ($\nu_1^{^1H} \approx 0.21 \cdot \nu_r$) was employed for SOCP and MOD-CP. The contact time, RF field strengths and carrier offsets were optimized for each CP scheme and are listed in Table 1. Schemes based on the second-order cross-polarization mechanism provide the highest amount of signal (Figure 3). In the case of broad-band schemes, a compromise was chosen to avoid disparate intensities for nuclei that have distinct transfer or

relaxation properties. Such kind of compromise is generally pursued in the case where all types of functional groups must be characterized with equal importance.

We then estimated the amount of remaining ^{1}H magnetization after one of the following pulse elements (Figure 3): *i*) a ^{1}H spinlock, *ii*) cross-polarization, *iii*) cross-polarization followed by *cw* decoupling. For all tested CP schemes, we find that a significant amount of the initial polarization, from 42 % to 24 %, remains available on protons after cross-polarization and *cw* decoupling, (Figure 3, red spectra). The amount of polarization remaining after each step can be easily predicted from spin-lock decay and transfer to carbon as discussed in section 4.1. These results indicate that proton-decoupled CP experiments at very fast MAS are suitable candidates for sensitivity enhancement by ^{1}H magnetization recovery.

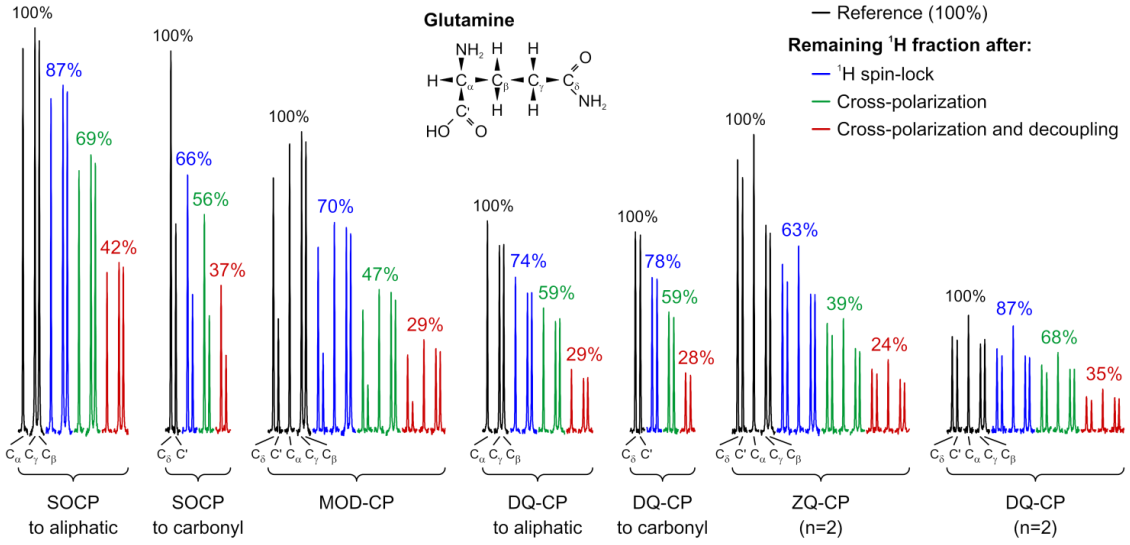

Figure. 3. Significant amounts of ^{1}H magnetization remain after different steps of the CP-decoupling experiment. The remaining levels of ^{1}H magnetization were recorded as described in Figure 2d with a decoupling time of 8 ms. The RF field frequencies and contact times for each CP scheme are detailed in Table 1.

We then focus subsequent investigations on the SOCP to aliphatic ^{13}C transfer scheme, as it offers the largest percentage of remaining magnetization and highest transfer efficiency.

Cross-polarization condition	**$\nu_1^{^1H}$ kHz**	**$\nu_1^{^{13}C}$ kHz**	**Contact time ms**	**Residual ^1H %**
Band-selective conditions				
SOCP to aliphatic (C_α,C_β,C_γ)	13.4	13.1	1.5	41.9
SOCP to carbonyl (C_δ,C')	13.4	13.2	6.0	37.3
DQ CP (n=1) to aliphatic	52.5	11.2 [a]	1.4	28.6
DQ CP (n=1) to carbonyl	52.5	11.6 [a]	1.0	28.4
Broadband conditions				
MOD-CP	13.4	28.0 [b]	4.5	28.6
DQ CP (n=2)	87.5	35.1 [a]	1.3	36.3
ZQ CP (n=1)	116.1	48.4 [a]	2.8	23.4

Table 1: Conditions for cross-polarization at 65 kHz MAS and remaining ^1H magnetization. [a] A 100 % to 80 % ramp of the carbon RF amplitude[68] was applied for non-SOCP based schemes. The average (90 %) ^{13}C RF frequency is reported. [b] For MOD-CP, a cosine modulation of frequency 13.5 kHz was applied to the carbon RF amplitude. To preserve the n=0 matching condition for both excitation bands, the ^{13}C RF frequency must be doubled[49].

5.4.3. Enhanced magnetization recovery leads to higher achievable sensitivity and shorter optimal recycling time

We monitored the recovery of magnetization following a proton-decoupled SOCP to aliphatic ^{13}C experiment (Figure 4). Three sets of experiments were recorded: *i*) reference experiments, where no pulse were applied following decoupling, *ii*) flip-back experiments, with a 90° pulse placing ^1H magnetization back to $+\hat{I}_z$, or *iii*) flip-down experiments, with a 90° pulse placing ^1H down along $-\hat{I}_z$. A significantly larger amount

of magnetization was recovered in the presence of the flip-back pulse compared to the reference, for all delays up to 58 s (Student's *t*-test, 95 % confidence level).

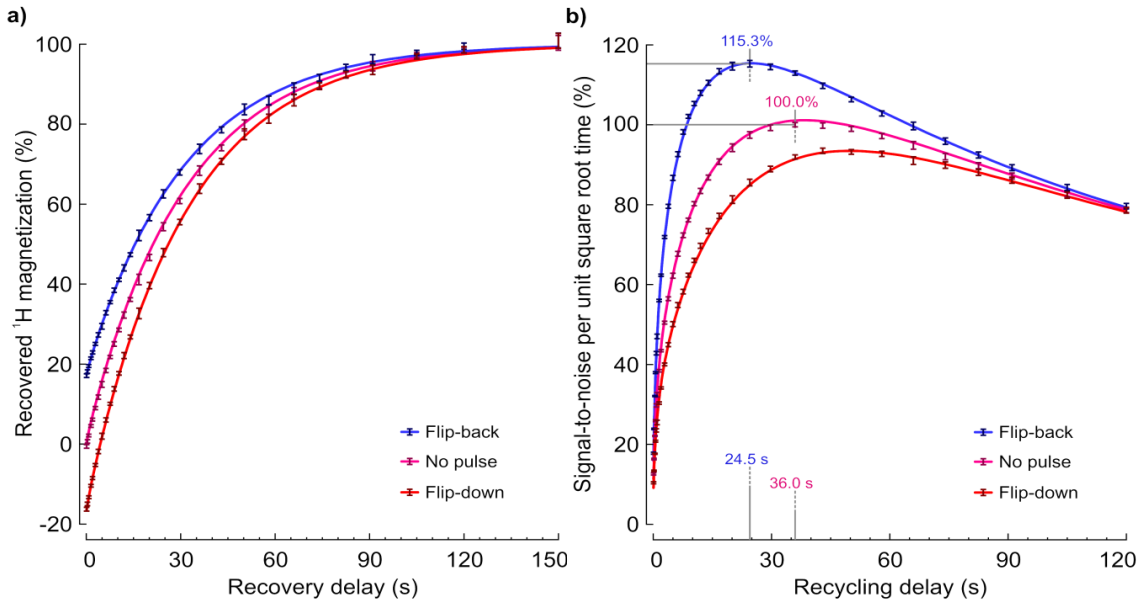

Figure 4. Recovery curve and sensitivity curve in glutamine at 65 kHz MAS following a SOCP to aliphatic carbons with low-power *cw* decoupling. **(a)** Time course of ^{1}H magnetization recovery recorded with the pulse scheme in Figure 2d. The amount of recovered ^{1}H magnetization is larger if the experiment finishes with a flip-back pulse (blue), compared to no final pulse (magenta), or a flip-down pulse (red). Magnetization amounts are normalized to the total equilibrium magnetization as extracted from the fit. **(b)** The sensitivity (signal-to-noise per unit square root time) was measured using the pulse scheme in Figure 2c. The sensitivity is normalized to the maximal experimental sensitivity in the absence of flip-back pulse. Maximal sensitivity is obtained by using the flip-back pulse (blue, 115.3±0.8 %, 24.5 s recycling delay), compared to no recovery of ^{1}H magnetization (magenta, 100.0±0.5 %, 36.0 s recycling delay) or flip-down (red). For (a) and (b), solid lines correspond to the solution of the least-square fit when all experimental data are fitted together with the recovery modeled as the sum of two exponential components, model B (Eq. 10 and 15).

In order to assess the sensitivity gains provided by the flip-back pulse, the signal-to-noise ratio per unit square root time $(S/N)_t$ was measured as a function of the inter-

scan delay for the three sets of experiments (Figure 5). The measurement is performed in the steady-state so as to be independent of the number of scans already performed.

Compared to the reference experiments, flip-back experiments yield a higher $(S/N)_t$ for all measured inter-scan delays up to 120 s; however, when the remaining ^1H magnetization is placed along $-\hat{I}_z$ in the flip-down experiments, the sensitivity is reduced for all inter-scans delays up to 91 s (Student's *t*-test, 95 % confidence level). Accordingly, the highest obtainable $(S/N)_t$ was found to be improved from 100.0 ± 0.5 % in the reference experiment to 115.3 ± 0.8 % with the flip-back pulse.

Another advantage provided by the fastened recovery is the reduction of the recycling delay. If sensitivity is not a limiting factor, a $(S/N)_t$ of 100 % can be reached in only 8.1 s using the flip-back pulse, compared to 36.0 s in the reference experiment. More than four times as many transients are recorded in the same amount of time, which is beneficial for experiments with extended phase-cycling. The shorter duration can also allow smaller increments in the indirect dimension of multi-dimensional experiments. The inter-scan duration is also shortened in the case of sensitivity-limited experiments: the inter-scan duration yielding the highest sensitivity is 36.0 s for the reference experiment compared to 24.5 s when the flip-back pulse is applied, representing a reduction of more than 30 % in inter-scan delay.

5.5. Discussion

5.5.1. Magnetization recovery is a general method for sensitivity enhancement compatible with several cross-polarization schemes

From the results presented in Figure 3, it can be seen that all tested CP schemes are able to preserve significant amounts of ^1H magnetization. This is attributed in part to

the selection of efficient ^{1}H spin-lock conditions, either at low-power ($\nu_1^{^1H} \approx 0.21 \cdot \nu_r$) for SOCP-based schemes or at high-power for other schemes ($\nu_1^{^1H} \approx 0.81 \cdot \nu_r$ for DQ-CP n=1, $\nu_1^{^1H} \approx 1.35 \cdot \nu_r$ for DQ-CP n=2, $\nu_1^{^1H} \approx 1.79 \cdot \nu_r$ for ZQ-CP n=1). The bulk ^{1}H magnetization remaining after ^{1}H spin-lock pulse (blue spectra in Figure 3) follows Eq. 18 where t_{SL} is the spin-lock duration and $T_{1\rho}$ is the ^{1}H longitudinal relaxation time in the rotating frame.

[Eq. 18] $M_{(t_{SL})} = M_0 \cdot \exp\left(-t_{SL}/T_{1\rho}\right)$

Using the experimentally determined value of $T_{1\rho} \approx 13.9\,\text{ms}$ ($\nu_1^{^1H} \approx 0.21 \cdot \nu_r$) and a spin-lock duration of $t_{SL} = 1.5\,\text{ms}$, we calculate a remaining amount of 90 % in agreement with the experimental measure of 87 %. The values of ^{1}H $T_{1\rho}$ for other ^{1}H spin-lock frequencies can be estimated from the spin-lock efficiency curve (Figure 1a). The calculated amounts after spin-lock have a deviation of less than 5% compared to the measured values (Figure 3, blue spectra) except for ZQ-CP which has approximately 20 % less magnetization than calculated.

In addition to spin-lock decay, the ^{1}H magnetization is reduced during CP due to transfer of polarization from ^{1}H to ^{13}C, which is illustrated by the difference between ^{1}H spin-lock (Figure 3, blue spectra) and CP experiments (Figure 3, green spectra). We observe that, for the different CP schemes, the proportion of ^{1}H magnetization contributing to the transfer is roughly proportional to the number of carbons excited by the CP scheme, this proportion increasing by 7 ± 2 % for each additional carbon.

Based on based on the characteristics of the spin-lock, $T_{1\rho} \approx 13.9\,\text{ms}$ during 8 ms, we calculate that 56 % of the magnetization will be preserved through the final *cw* decoupling. Indeed, considering all seven CP schemes, we measured that the intensities

after CP+decoupling (Figure 3, red spectra) have a ratio of 57 ± 7 % compared to CP alone (Figure 3, green spectra).

As initial polarization is preserved for all CP schemes, with amounts ranging from 42 % to 24 % after CP+decoupling experiments, the effect of the flip-back pulse was assessed for three recycling delays τ: 0.5 s, 2.0 s and 20 s (Figure 6). The signal enhancement ranged from 24 % to 50 % with a 0.5 s recycling delay, 24 % to 48 % with a 2.0 s recycling delay and 14 % to 21 % for a 20.0 s recycling delay.

The intensities of individual peaks are conserved between the reference and the flip-back experiment and do not vary significantly when changing the recycling delay. The recovery enhancement method is thus potentially applicable for quantitative experiments and multi-dimensional experiments. A high correlation is also observed between the enhancement factor (Figure 6) and the amount of remaining ^{1}H magnetization as determined in Figure 3.

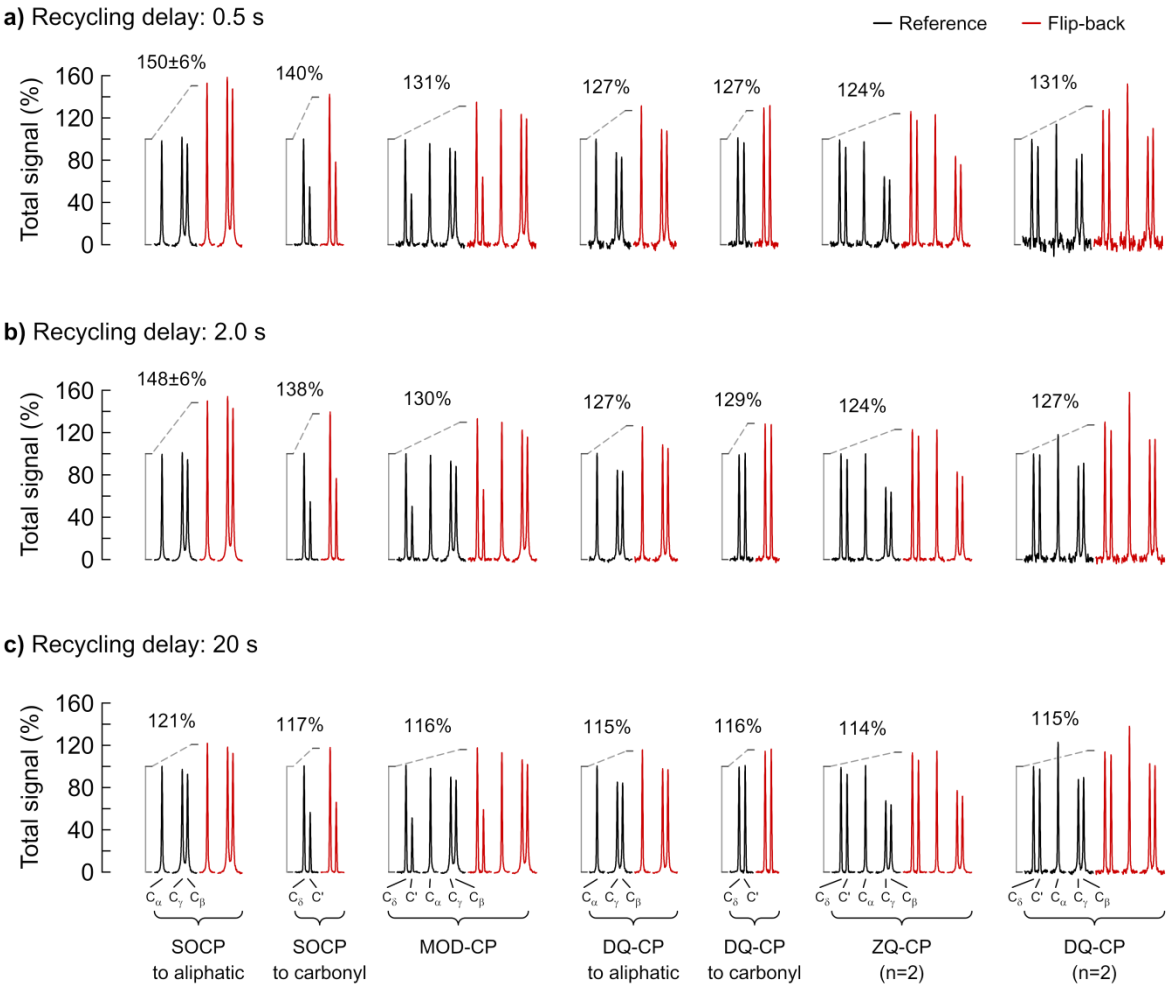

Figure 6. Enhancement in the fast pulsing limit. The total signal intensities are compared to a reference spectrum recorded without flip-back pulse.

5.6. The principal contribution to sensitivity enhancement is the preservation of large magnetization amounts, but magnetization sharing also contributes at fast repetition rates

Several mechanisms can be proposed to explain the increased sensitivity. The simplest mechanism is that using the flip-back pulse brings the system closer to its thermal equilibrium state, without any change in ^{1}H T_1 relaxation rates. An alternative

hypothesis states that the flip-back pulse accelerates the apparent longitudinal relaxation rate of protons directly contributing to heteronuclear transfer[44].

In this second mechanism, contributing and non-contributing protons act as separate magnetization pools, each with their respective population size, longitudinal relaxation time T_1 and residual polarization level prior to recovery. According to the concept of spin temperature[69], non-contributing protons have a higher population of spins in the low-energy state after *cw* decoupling and are thus "colder", while contributing protons are close to saturation, thus "warmer", and have nearly a positive infinite temperature. A heat flow is established between the different protons pools when a perturbation can mediate an exchange of spin order between the magnetization pools. In the case considered, proton-proton dipolar couplings between the two reservoirs mediate this exchange, leading to the establishment of a quasi-equilibrium steady-state after a certain time period[70].

We investigated the presence and the extent of this magnetization sharing mechanism in our system using two diagnostics: the detection of multi-exponential recovery behavior, and the comparison of extracted recovery rates to the bulk longitudinal relaxation rate measured by inversion-recovery. The multi-exponential behavior of the recovery and sensitivity curves arises as contributing protons benefit from both magnetization sharing and longitudinal relaxation at short recovery delays but only benefit from longitudinal relaxation of both pools in the limit of very long recovery delay once as a steady-state has been established[71].

The experimental data were fitted considering two models of magnetization recovery: in model A, a mono-exponential recovery behavior was assumed; in model B, the recovery followed a sum of two exponentials. In addition to recording the sensitivity and recovery curves with no pulse or a flip-back following *cw* decoupling, we also

recorded a series of experiments were the remaining magnetization is flipped 'down' along the $-\hat{I}_z$ axis. By forcing a higher population of spins to occupy the high-energy (unfavorable) state, both proton pools acquire a negative spin temperature. The non-contributing protons have a larger population difference and are considered "warmer" than the contributing protons which are close to saturation. The inclusion of the flip-down series makes it easier to detect a multi-exponential behavior of the magnetization recovery, since the flow of heat is inverted relative to the flip-back series of experiment and magnetization sharing between proton pools slows down the recovery of contributing protons at short recycling delays instead of fastening it.

For the recovery curves (Figure 4), both model A (mono-exponential recovery) and model B (sum of two exponentials) are compatible with the data ($F_{score} < F_{critiral}$, 99 % confidence level); however, the fit is significantly better with model B (F-test, 99 % confidence level). For the sensitivity curves (Figure 5), the experimental data is only compatible when the recovery is modeled as the sum of two exponential components (model B) but is incompatible with a mono-exponential recovery behavior (model A).

We carried a Monte Carlo procedure to estimate the uncertainty of extracted parameters. This procedure reveals that the fitting of recovery data alone is insufficient to allow the precise determination of parameters. The fitting of data to a sum of exponentials is indeed a well-known badly conditioned problem, such that small variations in the data can result in large variations of the extracted parameters[72,73]. On the contrary, the fitting of the sensitivity data alone was sufficient to extract well-defined parameters with low standard deviation obtained in the Monte Carlo routine.

In order to obtain a global model of the data, we carry a simultaneous fit of recovery and sensitivity data using the two-exponential components (model B). The

resulting fit is compatible with both sets of data and yields well-defined parameters (Table 2, Simultaneous fit). A simultaneous fit of recovery and sensitivity data with three exponential components could provide an improved agreement with the data; however, the two main exponential components present the same features as found in model B and the extracted parameters are not well-defined.

The fit with model B reveals the presence of a major (98.7 ± 0.13 %) and a minor (1.3 ± 0.13 %) population components. While the minor component follows a quick apparent relaxation (T_1 = 1.4 ± 0.16 s), the major component relaxes at a slower rate (T_1 = 31.3 ± 0.21 s). This relaxation time is statistically compatible with the longitudinal relaxation time of bulk protons (T_1 = 32 ± 2.2 s) as measured by a standard inversion-recovery experiment. The amount of preserved proton magnetization for the major component is quite large (34.1 ± 0.16 %) and is sufficient alone to explain the sensitivity enhancement and shortening of the optimal recycling time compared to the reference experiment. Indeed, neglecting the minor component only marginally affects the maximal obtainable sensitivity with flip-back, which decreases to 114.3 % from 115.4 %, or the expected optimal recycling time, which increases from 24.8 s to 25.9 s. However, the sensitivity obtained at very short recycling delays is more severely affected, with a reduction of over 14 % for recycling delay of 1.0 s and below.

Model	Component population %	Relaxation time, ^1H T_1 s	Residual ^1H magnetization %	F_{score}	$F_{critical}$ [a]
Fit of recovery curve (Figure 4)					
1 exponential component	(100)	30.9± 0.26	34.0± 0.25	0.64	1.50
2 exponential components	81 ± 28 19 ± 28	37 ± 27 16 ± 8.7	24 ± 13 11 ± 13	0.32	1.51
Fit of sensitivity curve (Figure 5)					
1 exponential component	(100)	28.4± 0.10	34.1± 0.16	10.33	1.48
2 exponential components	98.8± 0.15 1.2± 0.15	30.9± 0.24 1.3± 0.19	33.9± 0.19 25 ± 4.2	0.87	1.49
Simultaneous fit (Figure 4 and 5)					
1 exponential component	(100)	29.06± 0.093	34.4± 0.14	2.41	1.33
2 exponential components	98.7± 0.13 1.3± 0.13	31.3± 0.21 1.4± 0.16	34.1± 0.16 0.9± 0.52	0.58	1.33
Fit of inversion recovery (Figure S1)					
1 exponential component		32 ± 2.2			

Table 2: Extraction of relaxation parameters from recovery and sensitivity curves.
[a]Critical F values were computed at the 99 % confidence level.

5.6.1. Recommended settings and implementation strategy for unlabeled compounds

Sufficiently long acquisition times must be employed to avoid truncation of the signal of the FID, which would lead to broadening of the NMR resonances. This reduction in the spectral resolution is reflected at short acquisition times by a decrease of the ^{13}C peak heights in the reference experiment (Figure 7, red curve). On the other hand, it can be observed that the use of the flip-back pulse provides an improvement in sensitivity for all studied decoupling times up to 30 ms of decoupling (Figure 7, blue curve). However, the magnitude of the enhancement diminishes at longer decoupling times as the amount of preserved ^1H magnetization is reduced. In this study, we selected a decoupling time of 8 ms (highlighted with an arrow in Figure 7) as it provides a high enhancement and does not lead to any significant peak broadening of the reference spectrum. Further gains in sensitivity can be obtained at shorter decoupling times in the special case where resolution can be compromised, for example in the

indirect dimensions of multi-dimensional experiments or if peak positions are known and well separated.

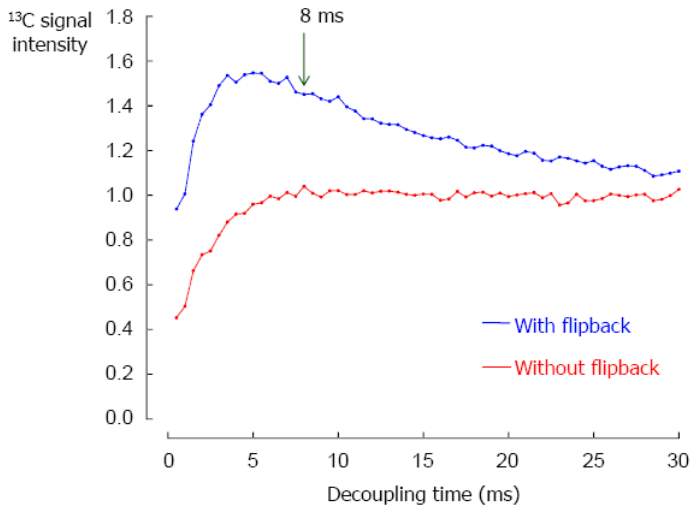

Figure 7. Sensitivity gains and resolution as a function of decoupling time. A series of SOCP to aliphatic carbons CP+decoupling experiments were recorded with flip-back (blue curve) and with no pulse applied after decoupling (red curve), with a 2 s recycle delay. The signal intensities at the central peak frequency were summed for the three aliphatic carbon peaks. At short decoupling times, an incomplete FID is acquired, causing broadening of the Fourier-transformed peaks and reduction in peak height of the reference spectrum (without flip-back, red curve).

For the optimization of parameters for the measurement of natural abundance spectra, we recommend the following procedure:

1) Prior to the experiment, calibrate the X channel power level on a uniformly-labeled sample with similar physical characteristics to the sample of interest. Estimate the required acquisition time and optimize the cross-polarization conditions. For example, adjust the attenuation level (dB) to have a RF strength of $\nu_1^{^{13}C} \approx 0.20 \cdot \nu_r$ for SOCP.

2) Using the natural abundance sample, determine the bulk ^{1}H T_1 relaxation rate. The ^{1}H T_1 can be determined using proton-detected inversion-recovery (180° – τ – 90°) or saturation-recovery experiment (saturation – τ – 90°)[74]. To ensure a constant initial magnetization, a recycling delay of $5 \times T_{1,app}^{^1H}$ must be employed or a pre-saturation element must be applied prior to recycling.
3) Calibrate the ^{1}H channel power level and adjust the attenuation level (dB) to have a ^{1}H RF strength of $\nu_1^{^1H} \approx 0.20 \cdot \nu_r$ (e.g. 13 kHz RF at 65 kHz MAS).
4) Determine the ^{1}H spin-lock decay $T_{1\rho}$ at that power level and determine the remaining amount of ^{1}H magnetization f_0. While the optimal recycling delay without flip-back is $\tau_{opt}^{no} \approx 1.25 \cdot T_{1,app}^{^1H}$, the optimal recycling delay with flip-back pulse is given by $\tau_{opt}^{FB} \approx (1 - f_0) \cdot 1.25 \cdot T_{1,app}^{^1H}$ using the experimental values of $T_{1,app}^{^1H}$ and remaining amount f_0.

5.7. Conclusions

The present study demonstrates that the preservation of ^{1}H magnetization during all employed pulse elements leads to significant sensitivity gains and shortening of the recycling delay. The sensitivity gains do not rely on selective excitation and magnetization sharing, rather on careful conservation of ^{1}H magnetization, preserving more than 55 % of the initial polarization amount after 8 ms of decoupling. This makes our method additionally compatible with broadband experiments and uniformly-

labeled materials, in contrast to application conducted at low MAS (<20 kHz) and fast MAS (20–40 kHz).

Sensitivity enhancement could be obtained with a large variety of CP schemes. The intensity of individual peaks was retained in the enhanced spectra, enabling the use of our method to be employed for quantitative applications. Remaining amounts for each CP scheme could be predicted on the basis of the selected spin-lock conditions and number of excited carbons. The enhancement ratio provided by the flip-back is highly related to the amount of remaining ^{1}H magnetization. With the SOCP to aliphatic CP scheme, the optimal sensitivity was increased to 115.3 % of the initial value and the optimal recycling delay was shortened to 68 % of its original duration. The sensitivity enhancement is combined with the gains already provided by the SOCP scheme, which increases the signal to 150 % compared to high-power CP schemes[48]. Broadband ^{13}C excitation can be realized by the MOD-CP scheme which also provide a higher signal compared to high-power CP schemes[49]. Using these two combinations, completely low-RF power sensitivity-enhanced experiments can be realized.

In contrast to the fast MAS regime (20–40 kHz) where high-power decoupling is required, low-power *cw* irradiation can provide efficient heteronuclear decoupling at ultra-fast MAS due to the reversal of the averaging process[59] and has been used for the recording of the resolved spectrum of uniformly-labeled human superoxide dismutase[4]. The performance of low-power heteronuclear decoupling has been enhanced by rapid phase modulation of the irradiation, for instance with the decoupling sequences low-power XiX[75], low-power TPPM[76], swept low-power TPPM[8], low-amplitude PISSARO[77] and amplitude-modulated low-power XiX[78]. Although these sequences offer longer ^{13}C coherence lifetimes approaching the high-RF power extreme limit reached with micro-coils[79], the timescale of their phase modulation and pulse lengths is on the same order as the rotor period. The rapid pulse phase transitions lead to decoherence of the ^{1}H

magnetization, making these decoupling sequences incompatible with magnetization recovery sensitivity enhancement. It can be envisioned however that ultra-fast MAS decoupling schemes which can afford somewhat longer pulse durations, such as the phase-alternated XiX scheme[75], can be adapted in order to preserve high amounts of ^{1}H magnetization after decoupling.

The sensitivity enhancement strategy can readily be extended to more sophisticated pulse schemes and multi-dimensional experiments. Indeed, many pulse elements employed at ultra-fast MAS[3] comprise a block of *cw* irradiation on ^{1}H, for example PAR[80], PAIN[81], and MIRROR[82,83], which can simultaneously serve as a low-power ^{1}H spin-lock. In this case, the conditions of low decay previously described can be employed. On the other hand, several recoupling elements such as DREAM[84], RFDR[85], and ^{13}C–^{15}N CP[19,20] do not require ^{1}H irradiation at ultra-fast MAS and ^{1}H magnetization can thus be stored along $+\hat{I}_z$ during those periods. As an example, the RELOAD-CP experiment[31] could be easily modified to benefit from the two sensitivity enhancement strategies, ^{1}H recovery and ^{13}C magnetization sharing. Similarly, the complete set of low-power experiments for protein assignment[20] and the pulse sequences used for the PACC approach[19] can be adapted for ^{1}H magnetization recovery.

Although a multi-exponential behavior is clearly detected from the fitting of recovery and sensitivity data, ^{1}H magnetization sharing does not play a large role in sensitivity enhancement. As the proton spin-lock condition employed for SOCP-based experiments is close to a purely homonuclear recoupling condition involving four coupled ^{1}H spins[48], it is likely that rapid proton-proton mixing already occurs in the rotating frame during cross-polarization and decoupling. The magnetization transferred to carbon in SOCP-based experiments is thus already enhanced by the contribution of remote protons.

The processes of longitudinal proton relaxation and proton spin diffusion are severely truncated at ultra-fast spinning and under high external magnetic fields. The fast proton-proton mixing occurring during decoupling explains why the magnetization sharing mechanism does not contribute to recovery enhancement except at very short recycling delays, since a quasi-equilibrium state is already established during the course of decoupling. This observation is supported by the highly similar recovery behaviors observed for different CP schemes. This knowledge could be of high importance in the following years. As even faster-spinning MAS probe-heads are being developed, and as magnet systems with higher external magnetic fields are being manufactured, it is plausible that low-power irradiation is used to accelerate recycling rates through proton mixing in the rotating-frame in order to break further ^{1}H T_1 boundaries.

5.8. References

1. Lesage, A. Recent advances in solid-state NMR spectroscopy of spin I=$^{1}/_{2}$ nuclei. *Physical Chemistry Chemical Physics* **11**, 6876-91 (2009).
2. Samoson, A., Tuherm, T., Past, J., Reinhold, A., Heinmaa, I., Anupõld, T., Smith, M. E., Pike, K. J. *Fast Magic-Angle Spinning: Implications*. 1-20 (John Wiley & Sons, Ltd, 2010).
3. Demers, J.-P., Chevelkov, V., Lange, A. Progress in correlation spectroscopy at ultra-fast magic-angle spinning: Basic building blocks and complex experiments for the study of protein structure and dynamics. *Solid State Nuclear Magnetic Resonance* **40**, 101-13 (2011).
4. Laage, S., Sachleben, J. R., Steuernagel, S., Pierattelli, R., Pintacuda, G., Emsley, L. Fast acquisition of multi-dimensional spectra in solid-state NMR enabled by ultra-fast MAS. *Journal of Magnetic Resonance* **196**, 133-41 (2009).
5. Nadaud, P. S., Helmus, J. J., Sengupta, I., Jaroniec, C. P. Rapid Acquisition of Multidimensional Solid-State NMR Spectra of Proteins Facilitated by Covalently Bound Paramagnetic Tags. *Journal of the American Chemical Society* **132**, 9561-3 (2010).
6. Bertini, I., Emsley, L., Lelli, M., Luchinat, C., Mao, J. F., Pintacuda, G. Ultrafast MAS Solid-State NMR Permits Extensive ^{13}C and ^{1}H Detection in Paramagnetic Metalloproteins. *Journal of the American Chemical Society* **132**, 5558-9 (2010).
7. Knight, M. J., Webber, A. L., Pell, A. J., Guerry, P., Barbet-Massin, E., Bertini, I., Felli, I. C., Gonnelli, L., Pierattelli, R., Emsley, L., Lesage, A., Herrmann, T., Pintacuda, G. Fast Resonance Assignment and Fold Determination of Human Superoxide Dismutase by High-Resolution Proton-Detected Solid-State MAS NMR Spectroscopy. *Angewandte Chemie-International Edition* **50**, 11697-701 (2011).
8. Lewandowski, J. R., Sein, J., Sass, H. J., Grzesiek, S., Blackledge, M., Emsley, L. Measurement of Site-Specific ^{13}C Spin-Lattice Relaxation in a Crystalline Protein. *Journal of the American Chemical Society* **132**, 8252-4 (2010).

9. Tollinger, M., Sivertsen, A. C., Meier, B. H., Ernst, M., Schanda, P. Site-Resolved Measurement of Microsecond-to-Millisecond Conformational-Exchange Processes in Proteins by Solid-State NMR Spectroscopy. *Journal of the American Chemical Society* **134**, 14800-7 (2012).
10. Paluch, P., Pawlak, T., Amoureux, J.-P., Potrzebowski, M. J. Simple and accurate determination of X-H distances under ultra-fast MAS NMR. *Journal of Magnetic Resonance* **233**, 56-63 (2013).
11. Bertini, I., Emsley, L., Felli, I. C., Laage, S., Lesage, A., Lewandowski, J. R., Marchetti, A., Pierattelli, R., Pintacuda, G. High-resolution and sensitivity through-bond correlations in ultra-fast magic angle spinning (MAS) solid-state NMR. *Chemical Science* **2**, 345-8 (2011).
12. Webber, A. L., Pell, A. J., Barbet-Massin, E., Knight, M. J., Bertini, I., Felli, I. C., Pierattelli, R., Emsley, L., Lesage, A., Pintacuda, G. Combination of DQ and ZQ Coherences for Sensitive Through-Bond NMR Correlation Experiments in Biosolids under Ultra-Fast MAS. *Chemphyschem : a European journal of chemical physics and physical chemistry* **13**, 2405-11 (2012).
13. Barbet-Massin, E., Pell, A. J., Knight, M. J., Webber, A. L., Felli, I. C., Pierattelli, R., Emsley, L., Lesage, A., Pintacuda, G. C-13-Detected Through-Bond Correlation Experiments for Protein Resonance Assignment by Ultra-Fast MAS Solid-State NMR. *Chemphyschem : a European journal of chemical physics and physical chemistry* **14**, 3131-7 (2013).
14. Hou, G., Yan, S., Sun, S., Han, Y., Byeon, I. L., Ahn, J., Concel, J., Samoson, A., Gronenborn, A. M., Polenova, T. Spin diffusion driven by R-symmetry sequences: applications to homonuclear correlation spectroscopy in MAS NMR of biological and organic solids. *Journal of the American Chemical Society* **133**, 3943-53 (2011).
15. Lafon, O., Trebosc, J., Hu, B., De Paepe, G., Amoureux, J.-P. Observing C-13-C-13 connectivities at high magnetic fields and very high spinning frequencies. *Chemical Communications* **47**, 6930-2 (2011).
16. Guangjin, H., Byeon, I. J. L., Jinwoo, A., Gronenborn, A. M., Polenova, T. Recoupling of chemical shift anisotropy by R-symmetry sequences in magic angle spinning NMR spectroscopy. *Journal of Chemical Physics* **137**, 134201 (10 pp.)- (10 pp.) (2012).
17. Shen, M., Hu, B. W., Lafon, O., Trebosc, J., Chen, Q., Amoureux, J. P. Broadband finite-pulse radio-frequency-driven recoupling (fp-RFDR) with (XY8)4(1) super-cycling for homo-nuclear correlations in very high magnetic fields at fast and ultra-fast MAS frequencies. *Journal of Magnetic Resonance* **223**, 107-19 (2012).
18. Wickramasinghe, N. P., Shaibat, M. A., Jones, C. R., Casabianca, L. B., de Dios, A. C., Harwood, J. S., Ishii, Y. Progress in ^{13}C and ^{1}H solid-state nuclear magnetic resonance for paramagnetic systems under very fast magic angle spinning. *Journal of Chemical Physics* **128** (2008).
19. Wickramasinghe, N. P., Parthasarathy, S., Jones, C. R., Bhardwaj, C., Long, F., Kotecha, M., Mehboob, S., Fung, L. W. M., Past, J., Samoson, A., Ishii, Y. Nanomole-scale protein solid-state NMR by breaking intrinsic ^{1}H T_1 boundaries. *Nature Methods* **6**, 215-8 (2009).
20. Vijayan, V., Demers, J. P., Biernat, J., Mandelkow, E., Becker, S., Lange, A. Low-Power Solid-State NMR Experiments for Resonance Assignment under Fast Magic-Angle Spinning. *Chemphyschem : a European journal of chemical physics and physical chemistry* **10**, 2205-8 (2009).
21. Parthasarathy, S., Nishiyama, Y., Ishii, Y. Sensitivity and Resolution Enhanced Solid-State NMR for Paramagnetic Systems and Biomolecules under Very Fast Magic Angle Spinning. *Accounts of Chemical Research* **46**, 2127-35 (2013).
22. Zhou, D. H., Shah, G., Cormos, M., Mullen, C., Sandoz, D., Rienstra, C. M. Proton-detected solid-state NMR Spectroscopy of fully protonated proteins at 40 kHz magic-angle spinning. *Journal of the American Chemical Society* **129**, 11791-801 (2007).
23. Marchetti, A., Jehle, S., Felletti, M., Knight, M. J., Wang, Y., Xu, Z.-Q., Park, A. Y., Otting, G., Lesage, A., Emsley, L., Dixon, N. E., Pintacuda, G. Backbone Assignment of Fully Protonated Solid Proteins by 1H Detection and Ultrafast Magic-Angle-Spinning NMR Spectroscopy. *Angewandte Chemie-International Edition* **51**, 10756-9 (2012).
24. Barbet-Massin, E., Pell, A. J., Jaudzems, K., Franks, W. T., Retel, J. S., Kotelovica, S., Akopjana, I., Tars, K., Emsley, L., Oschkinat, H., Lesage, A., Pintacuda, G. Out-and-back C-13-C-13 scalar transfers

in protein resonance assignment by proton-detected solid-state NMR under ultra-fast MAS. *Journal of Biomolecular NMR* **56**, 379-86 (2013).
25. Linser, R., Bardiaux, B., Higman, V., Fink, U., Reif, B. Structure Calculation from Unambiguous Long-Range Amide and Methyl ^{1}H–^{1}H Distance Restraints for a Microcrystalline Protein with MAS Solid-State NMR Spectroscopy. *Journal of the American Chemical Society* **133**, 5905-12 (2011).
26. Lewandowski, J. R., Dumez, J. N., Akbey, U., Lange, S., Emsley, L., Oschkinat, H. Enhanced Resolution and Coherence Lifetimes in the Solid-State NMR Spectroscopy of Perdeuterated Proteins under Ultrafast Magic-Angle Spinning. *Journal of Physical Chemistry Letters* **2**, 2205-11 (2011).
27. Zhou, D. H. H., Nieuwkoop, A. J., Berthold, D. A., Comellas, G., Sperling, L. J., Tang, M., Shah, G. J., Brea, E. J., Lemkau, L. R., Rienstra, C. M. Solid-state NMR analysis of membrane proteins and protein aggregates by proton detected spectroscopy. *Journal of Biomolecular NMR* **54**, 291-305 (2012).
28. Asami, S., Szekely, K., Schanda, P., Meier, B. H., Reif, B. Optimal degree of protonation for H-1 detection of aliphatic sites in randomly deuterated proteins as a function of the MAS frequency. *Journal of Biomolecular NMR* **54**, 155-68 (2012).
29. Barnes, A. B., De Paepe, G., van der Wel, P. C. A., Hu, K. N., Joo, C. G., Bajaj, V. S., Mak-Jurkauskas, M. L., Sirigiri, J. R., Herzfeld, J., Temkin, R. J., Griffin, R. G. High-field dynamic nuclear polarization for solid and solution biological NMR. *Applied Magnetic Resonance* **34**, 237-63 (2008).
30. Maly, T., Debelouchina, G. T., Bajaj, V. S., Hu, K. N., Joo, C. G., Mak-Jurkauskas, M. L., Sirigiri, J. R., van der Wel, P. C. A., Herzfeld, J., Temkin, R. J., Griffin, R. G. Dynamic nuclear polarization at high magnetic fields. *Journal of Chemical Physics* **128** (2008).
31. Lopez, J. J., Kaiser, C., Asami, S., Glaubitz, C. Higher Sensitivity through Selective (13)C Excitation in Solid-State NMR Spectroscopy. *Journal of the American Chemical Society* **131**, 15970-1 (2009).
32. Banigan, J. R., Traaseth, N. J. Utilizing Afterglow Magnetization from Cross-Polarization Magic-Angle-Spinning Solid-State NMR Spectroscopy to Obtain Simultaneous Heteronuclear Multidimensional Spectra. *Journal of Physical Chemistry B* **116**, 7138-44 (2012).
33. Banigan, J. R., Gayen, A., Traaseth, N. J. Combination of N-15 reverse labeling and afterglow spectroscopy for assigning membrane protein spectra by magic-angle-spinning solid-state NMR: application to the multidrug resistance protein EmrE. *Journal of Biomolecular NMR* **55**, 391-9 (2013).
34. Martineau, C., Decker, F., Engelke, F., Taulelle, F. Parallelizing acquisitions of solid-state NMR spectra with multi-channel probe and multi-receivers: Applications to nanoporous solids. *Solid State Nuclear Magnetic Resonance* **55-56**, 48-53 (2013).
35. Gopinath, T., Veglia, G. 3D DUMAS: Simultaneous acquisition of three-dimensional magic angle spinning solid-state NMR experiments of proteins. *Journal of Magnetic Resonance* **220**, 79-84 (2012).
36. Gopinath, T., Veglia, G. Dual Acquisition Magic-Angle Spinning Solid-State NMR-Spectroscopy: Simultaneous Acquisition of Multidimensional Spectra of Biomacromolecules. *Angewandte Chemie-International Edition* **51**, 2731-5 (2012).
37. Gopinath, T., Veglia, G. Orphan spin operators enable the acquisition of multiple 2D and 3D magic angle spinning solid-state NMR spectra. *Journal of Chemical Physics* **138** (2013).
38. Lamley, J. M., Lewandowski, J. R. Simultaneous acquisition of homonuclear and heteronuclear long-distance contacts with time-shared third spin assisted recoupling. *Journal of Magnetic Resonance* **218**, 30-4 (2012).
39. Diercks, T., Daniels, M., Kaptein, R. Extended flip-back schemes for sensitivity enhancement in multidimensional HSQC-type out-and-back experiments. *Journal of Biomolecular NMR* **33**, 243-59 (2005).
40. Pervushin, K., Vogeli, B., Eletsky, A. Longitudinal H-1 relaxation optimization in TROSY NMR spectroscopy. *Journal of the American Chemical Society* **124**, 12898-902 (2002).
41. Schanda, P., Brutscher, B. Very fast two-dimensional NMR spectroscopy for real-time investigation of dynamic events in proteins on the time scale of seconds. *Journal of the American Chemical Society* **127**, 8014-5 (2005).
42. Deschamps, M., Campbell, I. D. Cooling overall spin temperature: Protein NMR experiments optimized for longitudinal relaxation effects. *Journal of Magnetic Resonance* **178**, 206-11 (2006).

43. Tegenfeldt, J., Haeberlen, U. Cross polarization in solids with flip-back of *I*-spin magnetization. *Journal of Magnetic Resonance (1969)* **36**, 453-7 (1979).
44. Giffard, M., Bardet, M., Bersch, B., Covès, J., Hediger, S. Impact of selective excitation on carbon longitudinal relaxation: Towards fast solid-state NMR techniques. *Journal of Magnetic Resonance* **200**, 153-60 (2009).
45. Lupulescu, A., Frydman, L. Sensitizing solid state nuclear magnetic resonance of dilute nuclei by spin-diffusion assisted polarization transfers. *Journal of Chemical Physics* **135**, 7 (2011).
46. Saito, K., Martineau, C., Fink, G., Taulelle, F. Flip-back, an old trick to face highly contrasted relaxation times: application in the characterization of pharmaceutical mixtures by CPMAS NMR. *Solid State Nucl Magn Reson* **40**, 66-71 (2011).
47. Chevelkov, V., Giller, K., Becker, S., Lange, A. Efficient CO-CA transfer in highly deuterated proteins by band-selective homonuclear cross-polarization. *Journal of Magnetic Resonance* **230**, 205-11 (2013).
48. Lange, A., Scholz, I., Manolikas, T., Ernst, M., Meier, B. H. Low-power cross polarization in fast magic-angle spinning NMR experiments. *Chemical Physics Letters* **468**, 100-5 (2009).
49. Demers, J.-P., Vijayan, V., Becker, S., Lange, A. Tailored low-power cross-polarization under fast magic-angle spinning. *Journal of Magnetic Resonance* **205**, 216-23 (2010).
50. Lundgren, J. *SPLINEFIT*, <http://www.mathworks.com/matlabcentral/fileexchange/13812-splinefit> (2010).
51. Weideman, J. A. C. Computation of the complex error function. *SIAM Journal on Numerical Analysis* **31**, 1497-518 (1994).
52. Olivero, J. J., Longbothum, R. L. Empirical fits to the Voigt line width: A brief review. *Journal of Quantitative Spectroscopy and Radiative Transfer* **17**, 233-6 (1977).
53. Ernst, R. R., Bodenhausen, G., Wokaun, A. *Principles of nuclear magnetic resonance in one and two dimensions*. 148-157 (Clarendon Press, 1994).
54. Hiller, S., Wider, G., Etezady-Esfarjani, T., Horst, R., Wuthrich, K. Managing the solvent water polarization to obtain improved NMR spectra of large molecular structures. *Journal of Biomolecular NMR* **32**, 61-70 (2005).
55. Olofsson, G., Angus, S., Armstrong, G. T., Kornilov, A. N. Assignment and Presentation of Uncertainties of the Numerical Results of Thermodynamic Measurements. *Pure and Applied Chemistry* **53**, 1805-26 (1981).
56. Nielsen, N. C., Bildsoe, H., Jakobsen, H. J., Levitt, M. H. Double-quantum homonuclear rotary resonance: Efficient dipolar recovery in magic-angle spinning nuclear magnetic resonance. *Journal of Chemical Physics* **101**, 1805-12 (1994).
57. Levitt, M. H., Oas, T. G., Griffin, R. G. Rotary Resonance Recoupling in Heteronuclear Spin Pair Systems. *Israel Journal of Chemistry* **28**, 271-82 (1988).
58. Oas, T. G., Griffin, R. G., Levitt, M. H. Rotary Resonance Recoupling of Dipolar Interactions in Solid-State Nuclear Magnetic-Resonance Spectroscopy. *Journal of Chemical Physics* **89**, 692-5 (1988).
59. Ernst, M., Samoson, A., Meier, B. H. Low-power decoupling in fast magic-angle spinning NMR. *Chemical Physics Letters* **348**, 293-302 (2001).
60. Lesage, A., Bardet, M., Emsley, L. Through-bond carbon-carbon connectivities in disordered solids by NMR. *Journal of the American Chemical Society* **121**, 10987-93 (1999).
61. Ernst, M., Samoson, A., Meier, B. H. Decoupling and recoupling using continuous-wave irradiation in magic-angle-spinning solid-state NMR: A unified description using bimodal Floquet theory. *Journal of Chemical Physics* **123**, 10 (2005).
62. Sinning, G., Mehring, M., Pines, A. Dynamics of Spin Decoupling in Carbon-13-Proton NMR. *Chemical Physics Letters* **43**, 382-6 (1976).
63. Mehring, M., Sinning, G. Dynamics of Heteronuclear Spin Coupling and Decoupling in Solids. *Physical Review B* **15**, 2519-32 (1977).
64. Tekely, P., Palmas, P., Canet, D. Effect of Proton Spin-Exchange on the Residual C-13 MAS NMR Linewidths - Phase-Modulated Irradiation for Efficient Heteronuclear Decoupling in Rapidly Rotating Solids. *Journal of Magnetic Resonance Series A* **107**, 129-33 (1994).

65. Laage, S., Marchetti, A., Sein, J., Pierattelli, R., Sass, H. J., Grzesiek, S., Lesage, A., Pintacuda, G., Emsley, L. Band-Selective ^{1}H–^{13}C Cross-Polarization in Fast Magic Angle Spinning Solid-State NMR Spectroscopy. *Journal of the American Chemical Society* **130**, 17216-7 (2008).
66. Pines, A., Gibby, M. G., Waugh, J. S. Proton-Enhanced NMR of Dilute Spins in Solids. *Journal of Chemical Physics* **59**, 569-90 (1973).
67. Stejskal, E. O., Schaefer, J., Waugh, J. S. Magic-angle spinning and polarization transfer in proton-enhanced NMR. *Journal of Magnetic Resonance* **28**, 105-12 (1977).
68. Metz, G., Wu, X. L., Smith, S. O. Ramped-Amplitude Cross Polarization in Magic-Angle-Spinning NMR. *Journal of Magnetic Resonance Series A* **110**, 219-27 (1994).
69. Goldman, M. *Spin temperature and nuclear magnetic resonance in solids*. (Clarendon Press, 1970).
70. Levitt, M. H., Suter, D., Ernst, R. R. Spin Dynamics and Thermodynamics in Solid-State NMR Cross-Polarization. *Journal of Chemical Physics* **84**, 4243-55 (1986).
71. Helms, G. Interaction of exchange and differential relaxation in the saturation recovery behavior of the binary spin-bath model for magnetization transfer. *Concepts in Magnetic Resonance Part A* **28A**, 291-8 (2006).
72. De Groen, P., De Moor, B. The fit of a sum of exponentials to noisy data. *Journal of Computational and Applied Mathematics* **20**, 175-87 (1987).
73. Narayanan, A., Hartman, J. S., Bain, A. D. Characterizing Nonexponential Spin-Lattice Relaxation in Solid-State NMR by Fitting to the Stretched Exponential. *Journal of Magnetic Resonance Series A* **112**, 58-65 (1995).
74. Becker, E. D., Ferretti, J. A., Gupta, R. K., Weiss, G. H. Choice of Optimal Parameters for Measurement of Spin-Lattice Relaxation-Times .2. Comparison of Saturation Recovery, Inversion Recovery, and Fast Inversion Recovery Experiments. *Journal of Magnetic Resonance* **37**, 381-94 (1980).
75. Ernst, M., Samoson, A., Meier, B. H. Low-power XiX decoupling in MAS NMR experiments. *Journal of Magnetic Resonance* **163**, 332-9 (2003).
76. Kotecha, M., Wickramasinghe, N. P., Ishii, Y. Efficient low-power heteronuclear decoupling in ^{13}C high-resolution solid-state NMR under fast magic angle spinning. *Magn Reson Chem* **45**, S221-S30 (2007).
77. Weingarth, M., Bodenhausen, G., Tekely, P. Low-power decoupling at high spinning frequencies in high static fields. *Journal of Magnetic Resonance* **199**, 238-41 (2009).
78. Agarwal, V., Tuherm, T., Reinhold, A., Past, J., Samoson, A., Ernst, M., Meier, B. H. Amplitude-modulated low-power decoupling sequences for fast magic-angle spinning NMR. *Chemical Physics Letters* **583**, 1-7 (2013).
79. Vasa, S. K., Janssen, H., Van Eck, E. R. H., Kentgens, A. P. M. High-resolution solid-state C-13 mu MAS NMR with long coherence life times. *Physical Chemistry Chemical Physics* **13**, 104-6 (2011).
80. Lewandowski, J. R., De Paepe, G., Eddy, M. T., Struppe, J., Maas, W., Griffin, R. G. Proton Assisted Recoupling at High Spinning Frequencies. *Journal of Physical Chemistry B* **113**, 9062-9 (2009).
81. Lewandowski, J. R., De Paepe, G., Griffin, R. G. Proton assisted insensitive nuclei cross polarization. *Journal of the American Chemical Society* **129**, 728-9 (2007).
82. Scholz, I., Huber, M., Manolikas, T., Meier, B. H., Ernst, M. MIRROR recoupling and its application to spin diffusion under fast magic-angle spinning. *Chemical Physics Letters* **460**, 278-83 (2008).
83. Scholz, I., Meier, B. H., Ernst, M. MIRROR-CP: A proton-only experiment for the measurement of ^{13}C spin diffusion. *Chemical Physics Letters* **479**, 296-9 (2009).
84. Ernst, M., Meier, M. A., Tuherm, T., Samoson, A., Meier, B. H. Low-power high-resolution solid-state NMR of peptides and proteins. *Journal of the American Chemical Society* **126**, 4764-5 (2004).
85. Bayro, M. J., Ramachandran, R., Caporini, M. A., Eddy, M. T., Griffin, R. G. Radio frequency-driven recoupling at high magic-angle spinning frequencies: Homonuclear recoupling *sans* heteronuclear decoupling. *Journal of Chemical Physics* **128**, 11 (2008).

Part III: Slow to ultra-fast MAS spinning regimes to study inorganic compounds

6. Study of inorganic compounds at slow MAS: ^{29}Si, ^{31}P and ^{119}Sn

6.1. Summary

Low-valent compounds of group 14 elements ($_{6}$C, $_{14}$Si, $_{32}$Ge, $_{50}$Sn, $_{82}$Pb) are of special interest for inorganic chemistry studies[1,2]: they can potentially mimic transition metals and act as activators for small molecules. Compared to carbon-based carbenes, heavier analogues of carbenes (R_2C:) present distinct electronic properties[3] and have not been extensively studied. As well, new ligands have been developed which allow for the stabilization of various low-valent species. In this chapter, the analysis of three types of systems will be presented: N-heterocyclic carbene complexes of silicon (Section 6.2), phosphorus-containing bis-silylenes (Section 6.3) and pincer based ligands-stabilized complexes of tin (Section 6.4). Solid-state NMR (ssNMR) was employed in combination with other physical chemistry techniques to characterize the structure and properties of those novel compounds. The experiments were carried out in the slow (5–20 kHz MAS) and very slow (<5 kHz MAS) Magic-Angle Spinning regimes and in static conditions.

Contribution statement

Some of the results contained in Section 6.2 can be found in the following publication:

"Lewis Base Mediated Dismutation of Trichlorosilane", *Amit Pratap Singh, Rajendra S. Ghadwal, Herbert W. Roesky, Julian J. Holstein, Birger Dittrich, Jean-Philippe Demers, Veniamin Chevelkov, Adam Lange*, **Chemical Communications**, vol. 48(61), pp. 7574–6 (2012)

The compounds were synthesized by Rajendra S. Ghadwal and Amit Pratap Singh. The DFT calculations were carried out by Julian J. Holstein. The ssNMR spectra of compound C were recorded by Veniamin Chevelkov.

Section 6.3 is based on the following publication:

"Zwitterionic Si-C-Si-P and Si-P-Si-P Four-Membered Rings with Two-Coordinate Phosphorus Atoms", Sakya S. *Sen*, *Shabana Khan*, *Herbert W. Roesky*, *Daniel Kratzert*, *Kathrin Meindl*, *Julian Henn*, *Dietmar Stalke*, *Jean-Philippe Demers*, *Adam Lange*, **Angewandte Chemie-International Edition**, vol. 50(10), pp. 2322–5 (2011)

The compounds were synthesized by Sakya S. Sen and Shabana Khan. The DFT calculations were done in the group of Dietmar Stalke.

The results in Section 6.4 are presented in the following publications:

"Preparation of RSn(I)-Sn(I)R with Two Unsymmetrically Coordinate Sn(I) Atoms and Subsequent Opening of the P_4 Tetrahedron", *Shabana Khan, Reent Michel, Johannes M. Dieterich, Ricardo A. Mata, Herbert W. Roesky, Jean-Philippe Demers, Adam Lange, Dietmar Stalke*, **Journal of the American Chemical Society**, vol. 133(44), pp. 17889–94 (2011)

"Lewis Base Mediated Autoionization of $GeCl_2$ and $SnCl_2$", *Amit Pratap Singh, Herbert W. Roesky, Elena Carl, Dietmar Stalke, Jean-Philippe Demers, Adam Lange*, **Journal of the American Chemical Society**, vol. 134(10), pp. 4998–5003 (2012)

"Monomeric Sn(II) and Ge(II) Hydrides Supported by Tridentate Pincer-based Ligand", *Shabana Khan, Prinson P. Samuel, Reent Michel, Johannes M. Dieterich, Ricardo A. Mata, Jean-Philippe Demers, Adam Lange, Herbert W. Roesky, Dietmar Stalke*, **Chemical Communications**, vol. 48, pp. 4890–2 (2012)

The compounds were synthesized by Shabana Khan, Amit Pratap Singh and Prinson P. Samuel. The DFT calculations were carried out in the group of Ricardo A. Mata.

Except when specified, J.P.D. recorded the solid-state NMR spectra and carried out the quantum mechanical simulations and fitting of ssNMR spectra.

6.2. Silicon-29-containing N-heterocyclic carbene complexes

Silicon is, after oxygen, the second most abundant element in the Earth's crust. It mainly naturally occurs in the oxidation form IV. Very few silicon(II) compounds are stable at room temperature[1]. Some compounds have been synthesized, including SiH, SiC, SiO, SiS, SiNC, SiCN, SiC_2 and SiO_2, but their preparation requires high temperatures and strong vacuum, and they either readily condense or disproportionate[2]. Another approach leading to low-valent silicon molecules involves the stabilization of

the silicon atom by coordination with a favorable ligand. A class of such ligand is the N-heterocyclic carbene (NHC) ligand family. The NHC ligands behave similarly to tertiary phosphine but have several with additional favourable properties: tighter binding, higher thermal stability, increased basicity and high yields when produced *in situ*[4].

The NHC ligand family is sub-divided into normal, abnormal and remote categories[5]. In contrast to the normal and abnormal categories, in remote NHC complexes, the bound atom is coordinated by an atom non-adjacent to any heteroatom. In contrast to the normal NHC (nNHC), the abnormal NHC ligands (aNHC) have a mesoionic structure in their free form, i.e. no completely neutral resonance structure can be written and formal charges have to be introduced. While nNHCs are already strong electron donors, aNHCs have been identified as among the strongest carbene donors from DFT calculations[6].

The strategy of using NHC ligands opens the prospect to stabilize highly interesting silicon(II)-containing molecules, including naked Si(II) (i.e. a naked silicon(II) atom would have no covalently-bound atom but would be coordinated by NHCs), dichlorosilane H_2SiCl_2 and chlorosilicon(II) hydride HSiCl. One of the first such application employed an N-heterocyclic carbene (NHC) ligand to stabilize dichlorosilylene $SiCl_2$ [7]. This complex, here referred to as compound **"A"**, could be preserved for long periods at room temperature when protected from moisture and oxygen and was structurally well characterized owing to the formation of high-quality crystals.

“A”

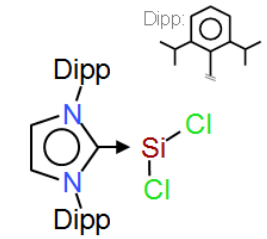

NHC dichlorosilylene

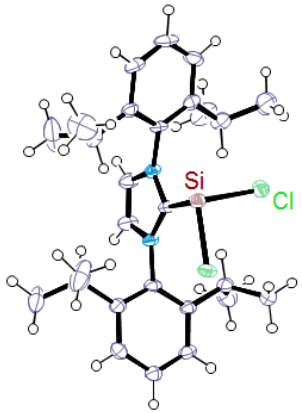

“B”

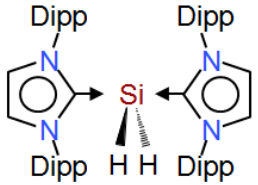

Bis(NHC) silicon(II) hydride

“C”

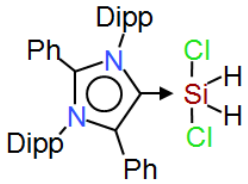

Abnormal NHC dichlorosilane

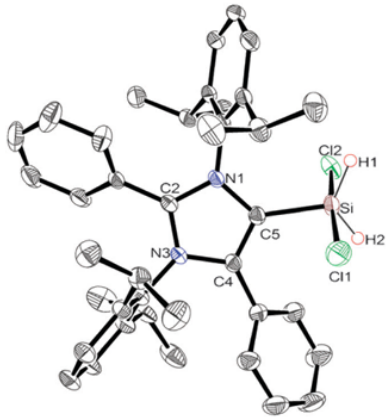

“D”

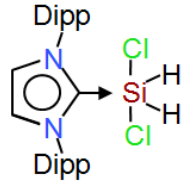

NHC dichlorosilane

“E”

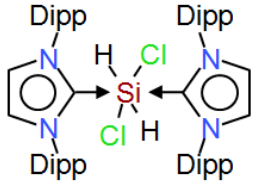

Bis(NHC) dichlorosilane

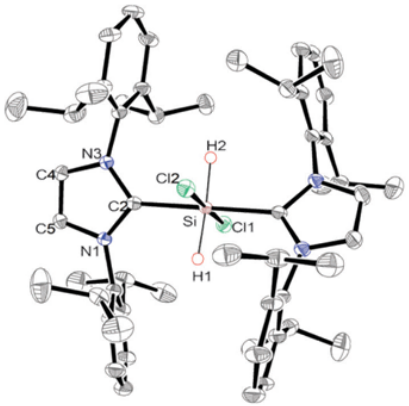

“F”

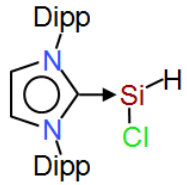

NHC chlorosilicon (II) hydride

Our collaborators of the Institute of Inorganic Chemistry at the Georg-August-Universität Göttingen synthesized a series of NHC complexes of high interest, compounds **"A"** to **"F"**, illustrated on the previous page and described in Ref. [7] and [8], which were analyzed using solid-state NMR. The investigation addressed the two main questions: Are there protons attached to the low-valent silicon? What is the geometry at the silicon sites?

X-ray crystal structures could be obtained for complexes **"A"**, **"C"** and **"E"** and were used as a reference for the analysis of molecular geometry. For instance, compound **"A"** has no proton directly bonded to silicon. The minimal Si-H distance as determined from the X-ray structure is 3.05Å. In addition to various stabilized molecules, the complexes also differ with respect to the stabilizing ligand, for example regular NHC versus an abnormal NHC, and single NHC coordination versus two coordinating NHCs.

Hypotheses:

The silicon atoms in compounds **"A"** (dichlorosilylene) and **"B"** (naked silicon) are not protonated. The silicon atom in complexes **"C"**, **"D"**, **"E"**, and **"F"** is protonated.

Silicon atoms doubly-coordinated by similar ligands **"B"** and **"E"** have a more symmetric chemical environment. Silicon atoms coordinated by regular NHC ligands have a more symmetric environment relative to those coordinated by abnormal NHC ligands (i.e. **"C"**).

Isotropic chemical shifts follow a trend where attached protons increase shielding and attached chlorines decrease shielding.

Method summary:

We measured ^{1}H-^{29}Si cross-polarization build-ups and compared the initial slope and contact time with maximal intensity to known protonated and non-protonated references.

We extracted the ^{29}Si spinning sideband intensities and obtained the principal components of the ^{29}Si Chemical Shift Anisotropy (CSA) tensors by fitting to simulated sideband patterns. When possible, the values were compared to CSA tensor values calculated by density functional theory (DFT) from the crystal strucuture.

6.2.1. Materials and Methods

6.2.1.1. Solid-state NMR

Solid-state NMR spectra were recorded at temperatures of 5–10 °C on a 9.4 T (400 MHz ^{1}H Larmor frequency) wide-bore instrument. Micro-crystals were packed under inert atmosphere into 4.0-mm magic-angle spinning (MAS) rotors. ^{1}H–^{29}Si cross-polarization (CP) spectra were recorded at MAS frequencies of 1250 Hz and 7000 Hz. Proton decoupling was applied during acquisition using the SPINAL-64 sequence[9] with RF field amplitudes in the range of 62.5-83.3 kHz. Chemical shifts were calibrated using external 3-(trimethylsilyl) propanoic acid, sodium salt (TMSP) as a reference for ^{29}Si.

6.2.1.2. Quantum mechanical simulations and DFT calculation

The chemical shift anisotropies of ^{29}Si were extracted by comparison of spinning sideband intensities with the sideband pattern of simulated spectra (Figure 1, Figure 2, Figure 4). Simulated spectra were generated within the numerical simulation routine GAMMA[10] over a large range of possible anisotropy and asymmetry values. The ^{29}Si anisotropic chemical shift was considered as the relevant internal system Hamiltonian, and powder averaging involved 1154 crystallite orientations. Values for the principal components of the CSA tensor which minimize the peak intensity residual sum of

squares were selected in a joint fit of all MAS frequency spectra and were used to produce the back-calculated spectra (red spectra in Fig. 2,3,5). Those values are presented in Table 1 in the result section. The presence of directly bonded protons was assessed by recording ^{1}H–^{29}Si cross-polarization build-up curves (Fig. 6,7) where contact times for CP were increased in the range 0–4 ms.

The following convention is employed for values presented in Table 1, 2 and 3: the principal components of the CSA tensor are δ_{xx}, δ_{yy} and δ_{zz}, with $|\delta_{zz} - \delta_{iso}| \geq |\delta_{xx} - \delta_{iso}| \geq |\delta_{yy} - \delta_{iso}|$; the isotropic chemical shift is $\delta_{iso} = \frac{1}{3}(\delta_{xx} + \delta_{yy} + \delta_{zz})$, the anisotropy is $\delta_{aniso} = \delta_{zz} - \delta_{iso}$, and the asymmetry is $\eta_{asym} = \frac{\delta_{yy} - \delta_{xx}}{\delta_{aniso}}$, where $\eta_{asym} = 0$ is axially symmetric. The CP contact time yielding maximum intensity is denoted τ_{CP}.

NMR chemical shielding tensors were predicted from theoretical geometry optimizations on each whole molecule for **"C"** and **"E"** using the density functional theory (DFT) functional B3LYP and 6-31 g* as the basis set. The whole-molecule approach was developed and successfully applied for silylene complexes before[11]. The ^{29}Si chemical shift of 3-(trimethylsilyl)-propanoic acid (TMSP), calculated by DFT using the same procedure and basis set as for compounds **"C"** and **"E"**, was used as a reference.

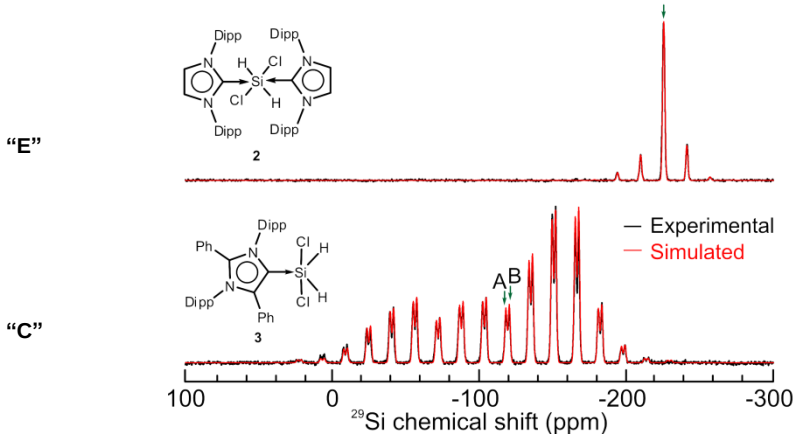

Figure 1: ^{29}Si solid-state NMR cross-polarization spectra of **"E"** (top) and **"C"** (bottom) recorded at 1250 Hz MAS. Isotropic peaks are indicated by green arrows and back-calculated spectra are displayed in red. The high number of spinning sidebands for **"C"** illustrates the large anisotropy of the electronic environment at the silicon nucleus.

6.2.2. Results

To investigate the electronic environment around the silicon center of the various complexes, solid-state ^{29}Si NMR spectra were recorded at multiple MAS rates (850 Hz, 1650 Hz and 7000 Hz). The solution-state ^{29}Si NMR spectra show resonances at –118.2 and –225.2 ppm for **"C"** and **"E"**, respectively, in agreement with ssNMR measurements. Indeed, in solid-state NMR, the isotropic peaks are easily identified as the dominant peaks at 7 kHz MAS (Fig. 3).

Interestingly, two ^{29}Si resonances are found for **"C"**, at –118.0 ppm and –120.4 ppm, which could be due to the presence of two non-equivalent molecules in the crystallographic unit or polymorphism in the sample. The cause of doubling could not be directly resolved by analysis of the X-ray diffraction pattern. Furthermore, the Si–H bond lengths identified by crystallography for this compound differ from the theoretically predicted value[8] which could reflect disorder or large amplitude vibrations. The chemical shift anisotropy (CSA), determined from the intensity of the MAS spinning sideband pattern is +112 ppm for **"C"** and +24 ppm for **"E"**.

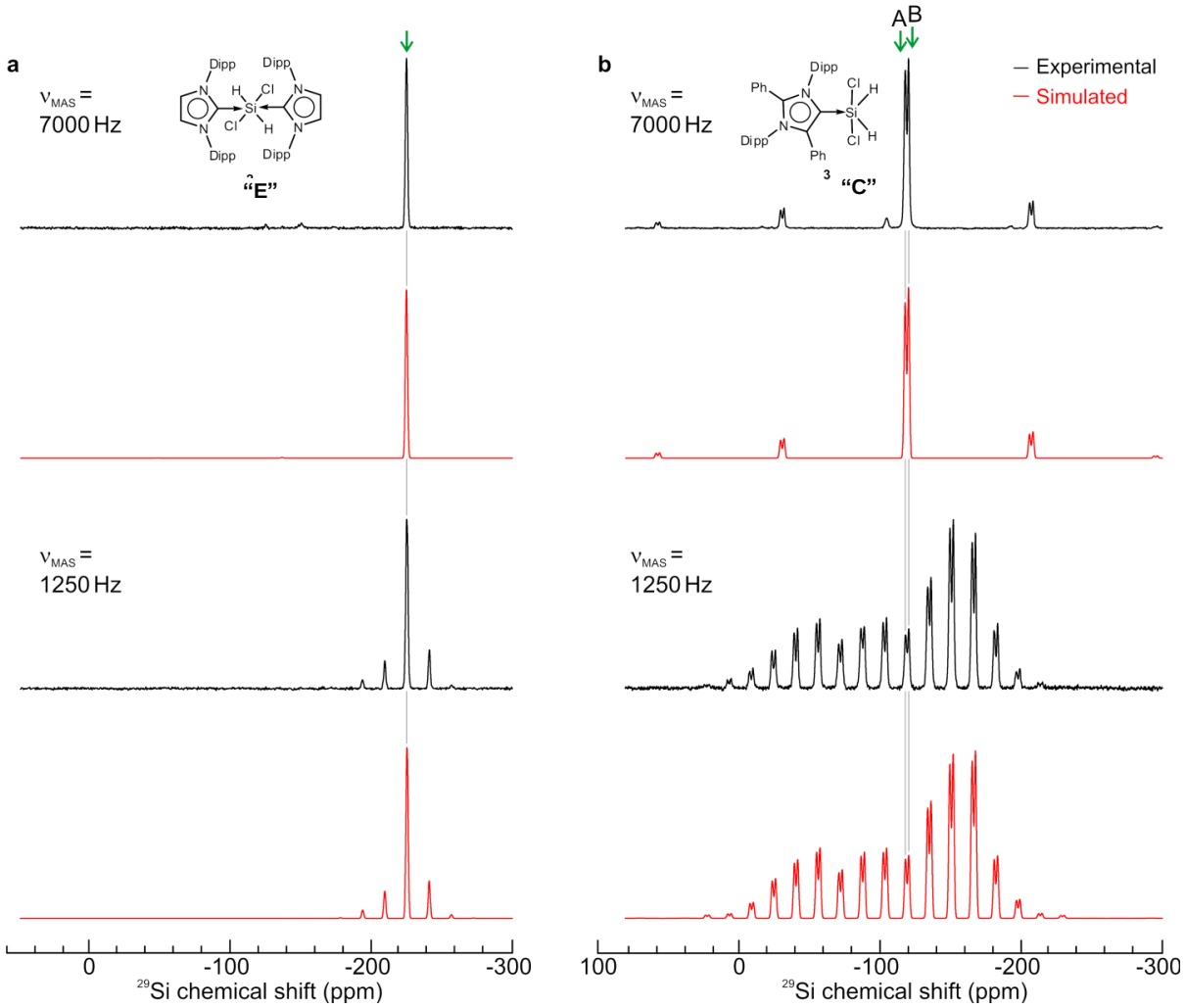

Figure 2: ^{29}Si Cross-polarization spectra of (a) the 2:1 adduct $(NHC)_2SiCl_2H_2$ compound **"E"** and (b) the abnormal 1:1 adduct aNHC $SiCl_2H_2$ compound **"C"**. Experimental spectra are presented in black and back-calculated spectra in red. The spectra were recorded at MAS frequencies of 7000 Hz (top panels) and 1250 Hz (bottom panels). Isotropic peaks are indicated by green arrows, at -225.2 ppm for **"E"** and at -118.0 ppm (site A) and -120.4 (site B) for **"C"**. The two sites have a frequency separation of 190 Hz. The high number of spinning sidebands and large breadth of the spectrum for the five coordinate adduct **"C"** is especially apparent at 1250 Hz MAS, reflecting the large anisotropy of the electronic environment at the Si nucleus. In contrast, spectra of the six-coordinated 2:1 adduct **"E"** present fewer sidebands, as the inherent symmetry of the molecule results in a more isotropic electronic environment at the Si nucleus.

The general trend in ^{29}Si isotropic chemical shifts roughly follows the electronegativity of the attached substituents (Fig. 4). In complex **"A"**, the two chlorine atoms attached to Si deplete the electron density and cause a large shift to a positive ppm value (19.8 ppm). In compound **"F"**, one of the chlorine atom is replaced by a proton. Accordingly, the electronic environment around Si is less depleted and the isotropic peaks moves to the negative direction (-86.2 ppm). However, the trend can also be understood slightly differently: indeed, for **"D"** the ^{29}Si chemical shift is even more negative with two Cl and two H atoms. As H and Si have quite similar electronegativity but Cl is dissimilar (Si: 1.90, H: 2.20, Cl 3.16 on the Pauling scale), the chlorine atoms have a tendency to pull electron density from both Si and H, which results in a delocalization of the ^{1}H electron cloud towards the position of the ^{29}Si nucleus. This suggestion is supported by the comparison of **"B"** and **"E"**: the very negative chemical shift of **"E"** arises as chlorine attracts electron density from the two protons but the electronic environment around Si is not depleted, resulting in an upfield position for **"E"**. The presence of two electron-donating NHC ligands also has a significant influence upon the upfield shift (-100 ppm) for **"E"** compared to "D" which is singly-coordinated.

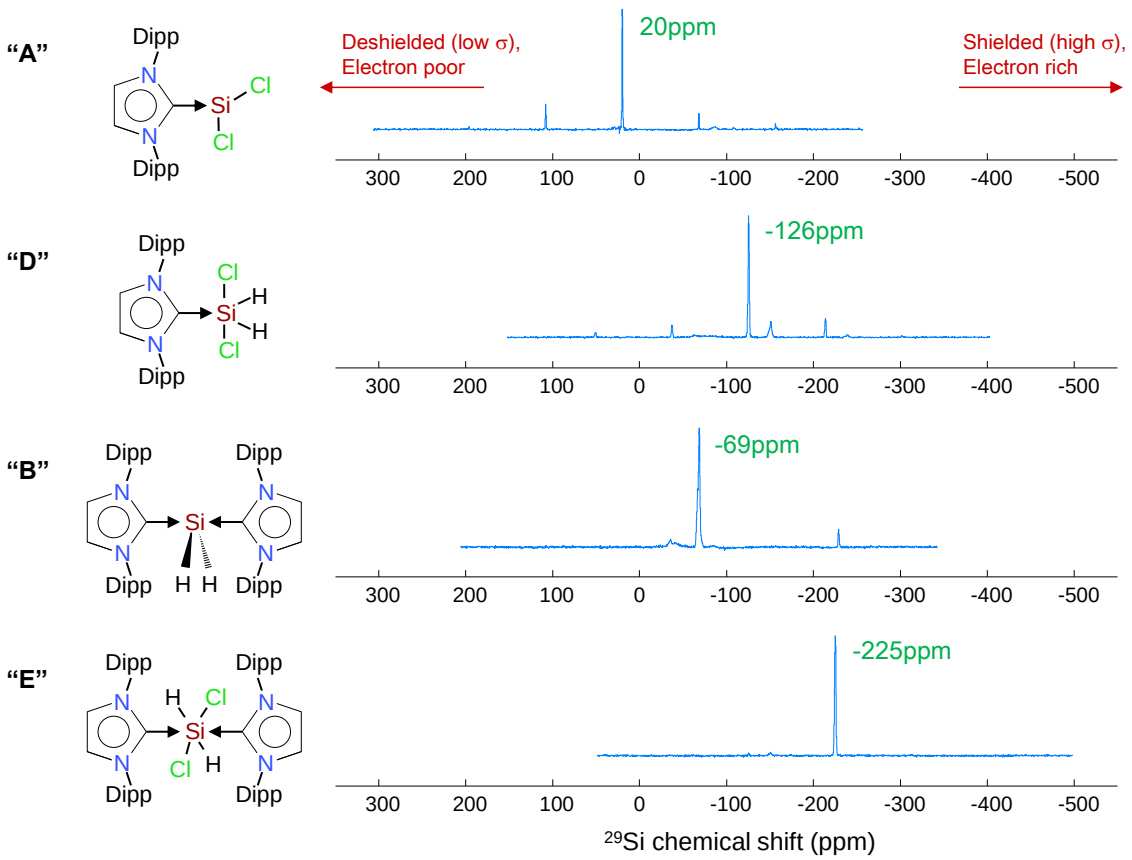

Figure 3: Cross-polarization spectra recorded at 7 kHz MAS for compounds **"A"**, **"D"**, **"B"** and **"E"**. Isotropic chemical shifts are noted in green.

In order to formally assess the trend in isotropic ^{29}Si chemical shift with relation to electronic environment, the chemical shielding tensors were predicted by DFT calculation using the crystal structures of **"C"** and **"E"**. The calculated trend is in agreement with the experimental values, not only for the isotropic shift but as well for the anisotropy and asymmetry parameters.

In addition to isotropic ^{29}Si chemical shifts, the anisotropy and asymmetry of the ^{29}Si CSA tensors were extracted by fitting experimental spinning sideband patterns to simulated spectra. The best fit corresponds to the least residual sum of squares, indicated in dark red in Fig. 5.

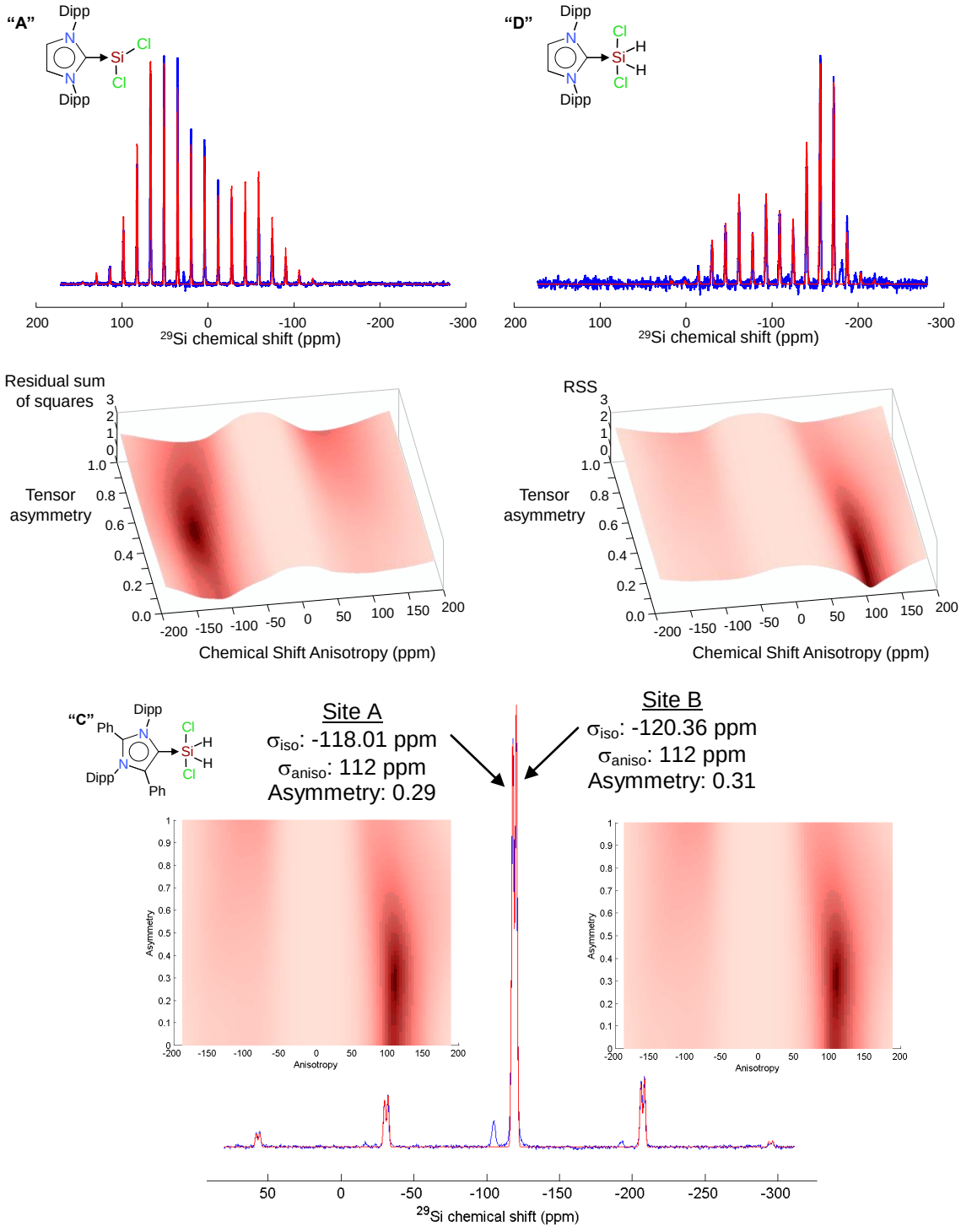

Figure 4: (Top) ^{29}Si CP spectra of compounds **"A"** and **"D"** at 1.25 kHz MAS, with the experimental spectrum in blue and the simulated spectrum in red. (Middle) Extraction of CSA parameters for **"A"**

and **"D"** . The region producing the fit with the lowest residual sum of squares (RSS) is darker. (bottom) Extraction of CSA parameters for **"C"**, and ^{29}Si CP spectrum at 7 kHz MAS. The CSA parameters extracted for the two ^{29}Si sites are highly similar.

Concerning the anisotropy of the electronic environment, single ligands ("A", "C", "D" and "F") generate significantly larger chemical shift anisotropy values (See table 1). However, no significant difference could be observed between regular and abnormal NHC ligands, e.g. "C" and "D" have an anisotropy value of 112 and 108 ppm, respectively.

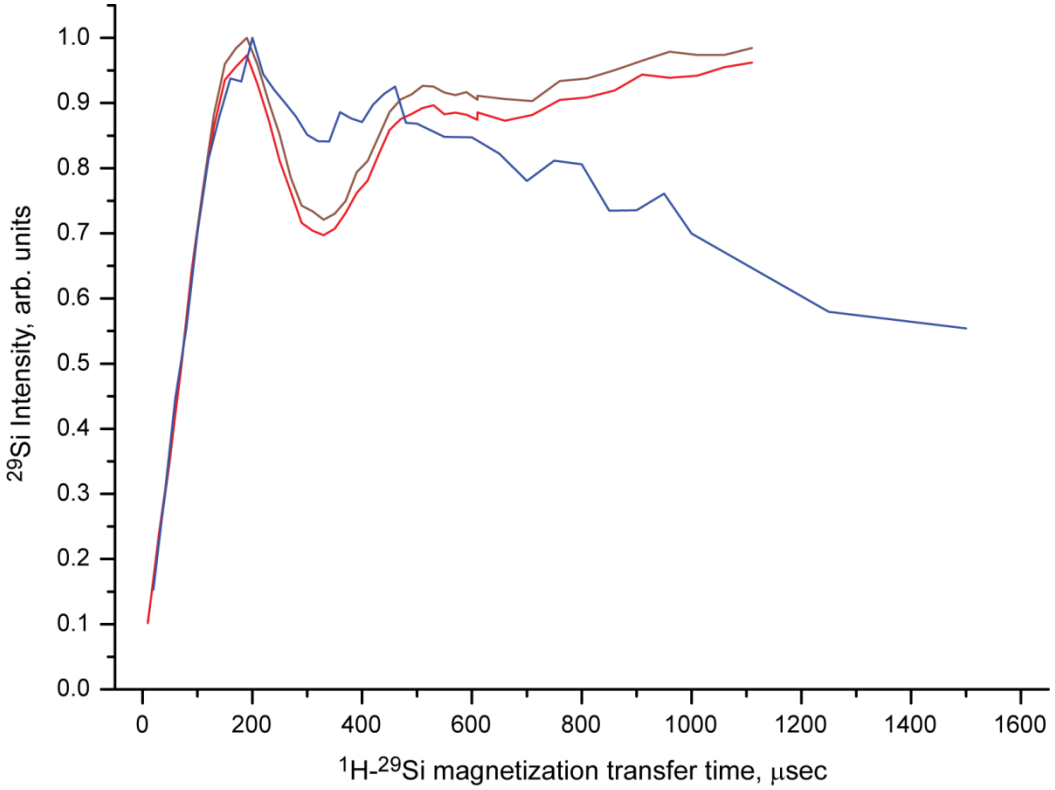

Figure 5: Build-up curves of ^{29}Si signal intensity during ^{29}Si cross-polarization for compound **"E"** (blue) and compound **"C"**. (red, site A; dark red, site B).

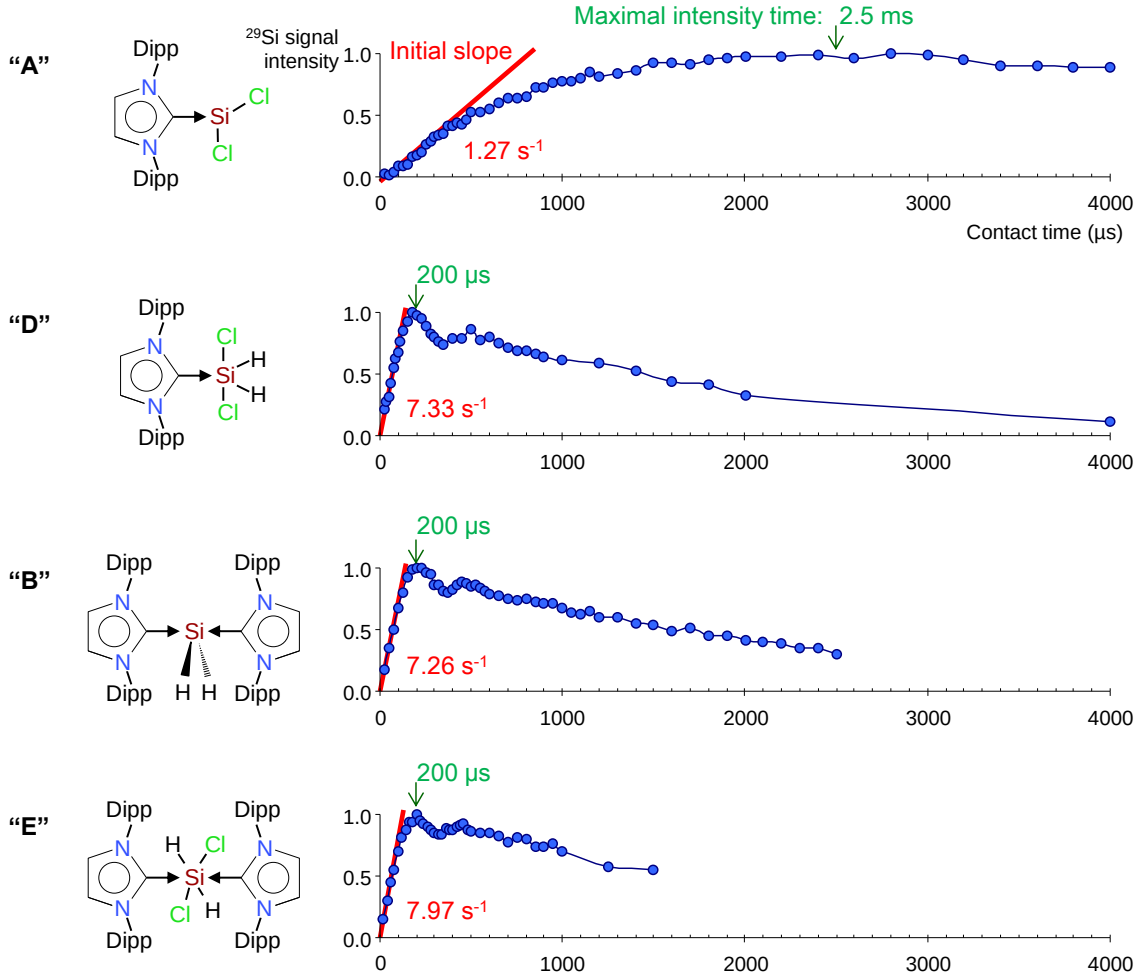

Figure 6: Build-up curves of ^{29}Si signal intensity during ^{29}Si cross-polarization for compound **"A"**, **"D"**, **"B"** and **"E"**.

Cross-polarization build-up curves for **"B"** to **"F"** reach their maximal intensity within 200 µs, confirming the presence of directly bonded protons on Si atoms (Fig. 6,7). The first maxima in signal intensity are obtained at short CP contact times: this fast transfer brought about by strong dipolar couplings can only arise for short ^{1}H–^{29}Si inter-nuclear distances and constitutes a direct confirmation of the presence of protons directly bonded to silicon. In contrast, the magnetization transfer maximum is obtained at 2400 µs for **"A"** and TMSP in the same conditions (not shown), where no proton is directly bonded to the silicon atom.

A summary of all extracted and calculated parameters is presented in the following table:

Table 1: Chemical shift tensor parameters and optimum cross-polarization contact times

Compound	τ_{CP} (μs)	δ_{iso} (ppm)	δ_{aniso} (ppm)	η_{asym}	δ_{xx} (ppm)	δ_{yy} (ppm)	δ_{zz} (ppm)
TMSP	2400	0.0	–	–	–	–	–
"A"	2500	19.8	-112	0.48	102.7	48.9	-92.2
"B"	200	-68.8	-16	0.9	-53.6	-68.0	-84.8
"C" site A	190	-118.0	+112	0.29	-190.2	-157.7	-5.9
"C" site B	190	-120.4	+112	0.31	-193.7	-159.0	-8.3
"C" (theo.)	–	-84.4	+105	0.35	-155.4	-118.3	20.4
"D"	200	-125.7	+108	0.15	-17.7	-171.6	-187.8
"E"	200	-225.2	+24	0.49	-243.1	-231.3	-201.2
"E" (theo.)	–	-185.4	-26	0.88	-161.4	-183.9	-210.9
"F"	200	-86.2	–	–	–	–	–

6.3. Phosphorus-31-containing bis-silylenes

Benzene is the prototype of aromatic compounds, while cyclobutadiene (CBD) (4π electron system) is the template of strained anti-aromatic compounds. CBSi(cyclosilabutadiene) has been postulated as reactive intermediate[12-14] although a stable CBSi is still elusive: in the literature, there are no stable examples known of a four-membered system with four-π electrons involving silicon and phosphorus.

In the current study[15], our collaborators at the Institute of Inorganic Chemistry of the Georg-August-Universität Göttingen have designed and synthesized a four-membered ring with four-π electrons containing Si and P as heteroatoms: 1,3-disilacarbaphosphide **"G"**, an analogue of a stable cyclobutadiene containing three heteroatoms (Fig. 8). The constitution of compound **"G"** was characterized by single crystal X-ray diffraction. The predominant structural feature of **"G"** is the substituent free ("naked") phosphorus atom, which connects the two silicon atoms. The two silicon atoms are four-coordinate each and display a distorted tetrahedral geometry by

coordination with two nitrogen atoms from the amidinato ligand. The remaining two sites of the tetrahedron are occupied by the carbon and phosphorus atom each. Our collaborators also demonstrated a synthesis route to a second CBD analogue: the Si_2P_2 unit stabilized by the amidinato ligand ($L_2Si_2P_2$; L= PhC(N*t*Bu)$_2$), compound **"H"** (Fig. 8), which they could isolated as air- and moisture-sensitive yellow crystals in 60% yield.

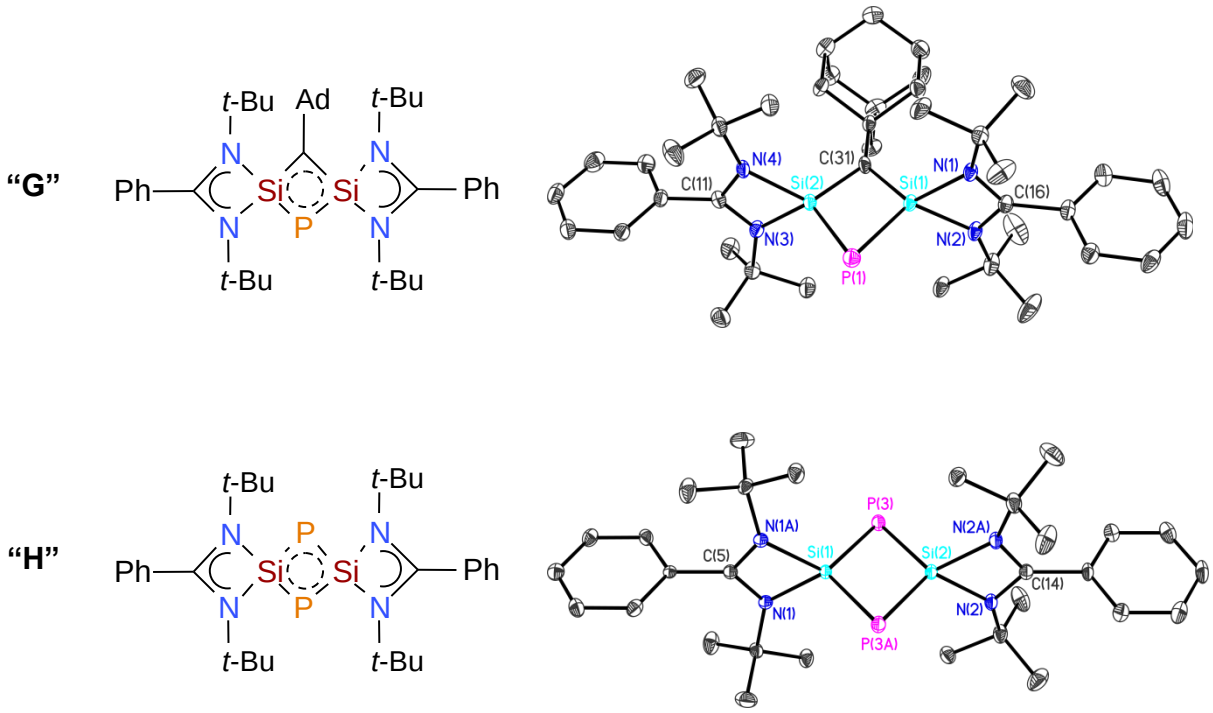

Figure 7

Using solid-state NMR, we confirmed the absence of attached protons on the "naked" Si and P atoms and we characterized the chemical environment of the two compounds for ^{29}Si and ^{31}P nuclei.

Hypotheses:

The silicon atoms in compounds **"G"** and **"H"** are not protonated.

The "naked" phosphorus atoms in compounds **"G"** and **"H"** are not protonated.

The phosphorus atoms in compound **"G"** and **"H"** are traversed by a C_2 symmetry axis. Their chemical environment is expected to be highly symmetric.

Method summary:

We recorded ^{1}H-^{29}Si and ^{1}H-^{31}P CP build-up curves.

We extracted CSA tensors principal values from spinning sideband patterns and compared them to DFT calculations carried out on the crystal structures.

6.3.1. Materials and Methods

6.3.1.1. Solid-state NMR

All reactions and handling of reagents were performed under an atmosphere of dry nitrogen or argon using standard Schlenk techniques or a glove box where the O_2 and H_2O levels were usually kept below 1 ppm.

Solid-state NMR spectra were recorded at temperatures of 5–10 °C on a 9.4 T (400 MHz ^{1}H Larmor frequency) wide-bore instrument. Compounds **"G"** and **"H"** were prepared in micro-crystalline form and packed under inert atmosphere into 2.5-mm and 4.0-mm MAS rotors. The ssNMR probehead was flushed with dry N_2 gas during measurement to mitigate the risk of accidental exposure to moisture. ^{1}H–^{29}Si and ^{1}H–^{13}C cross-polarization (CP) spectra were recorded on 4.0-mm rotors, with MAS frequencies of 1675 Hz, 2860 Hz and 7000 Hz for ^{29}Si, and 11000 Hz for ^{13}C. ^{1}H–^{31}P CP spectra were recorded on 2.5-mm rotors at MAS frequencies of 5700 Hz, 7000 Hz and 20000 Hz. For **"H"**, the 7 kHz ^{1}H–^{31}P spectra were recorded on a 4.0-mm rotor.

The swept-frequency TPPM sequence was used for proton decoupling during acquisition, with an RF field amplitude of 83.3 kHz, sweep window of 0.32 and phase angle of 12.5°[16,17]. Chemical shifts were calibrated using external references: TMS for ^{29}Si, 1M H_3PO_4 for ^{31}P, adamantane for ^{13}C (corresponding to DSS at 0 ppm).

6.3.1.2. Quantum mechanical simulations and DFT calculation

The experimental values of the ^{29}Si and ^{31}P chemical shielding tensors were determined as previously described in Section 6.2.1.2. To elucidate the nature of the chemical bonding, our collaborators performed DFT gas phase optimizations and frequency calculations at the B3LYP/6-311G* level of theory.

6.3.2. Results

In the ^{31}P solid-state NMR spectra of **"G"** the most intense resonance appears at an isotropic chemical shift of -326.1 ppm (Fig. 9a,c). The ^{29}Si NMR resonance with the highest intensity appears at -8.4 ppm. The cross-polarization build-up curves (Fig. 10a,c) show that both Si and P are non-protonated, since maximal intensity is reached after a long contact time of 5.6 ms (^{31}P) or 5.1 ms (^{29}Si).

A similar trend is observed in the ^{29}Si NMR spectrum of **"H"** (δ 25.6 ppm), which is shifted about 30 ppm to the lower field when compared with that of **"G"**, although the magnitude of the coupling constant ($^1J_{Si\text{-}P}$ = 109.02 Hz) remains comparable. Solid-state NMR spectra of **"H"** show a sharp ^{31}P resonance with isotropic chemical shift of -166.4 ppm (Fig. 9b). In the ^{29}Si spectrum, a triplet is observed at 24.0 ppm with a coupling constant of $^1J_{Si\text{-}P}$ = 97.7 Hz (Fig. 9d). The CP build-up curves reach maximal intensity after 11.6 ms (^{31}P) or 7.8 ms (^{29}Si) confirming that Si and P atoms in **"H"** are also non-protonated (Fig. 10b,d).

Isotropic and anisotropic ^{31}P chemical shieldings as determined by theory are in agreement with values extracted from the spinning sideband pattern of solid-state NMR spectra (see Table 2 and Figure 9)

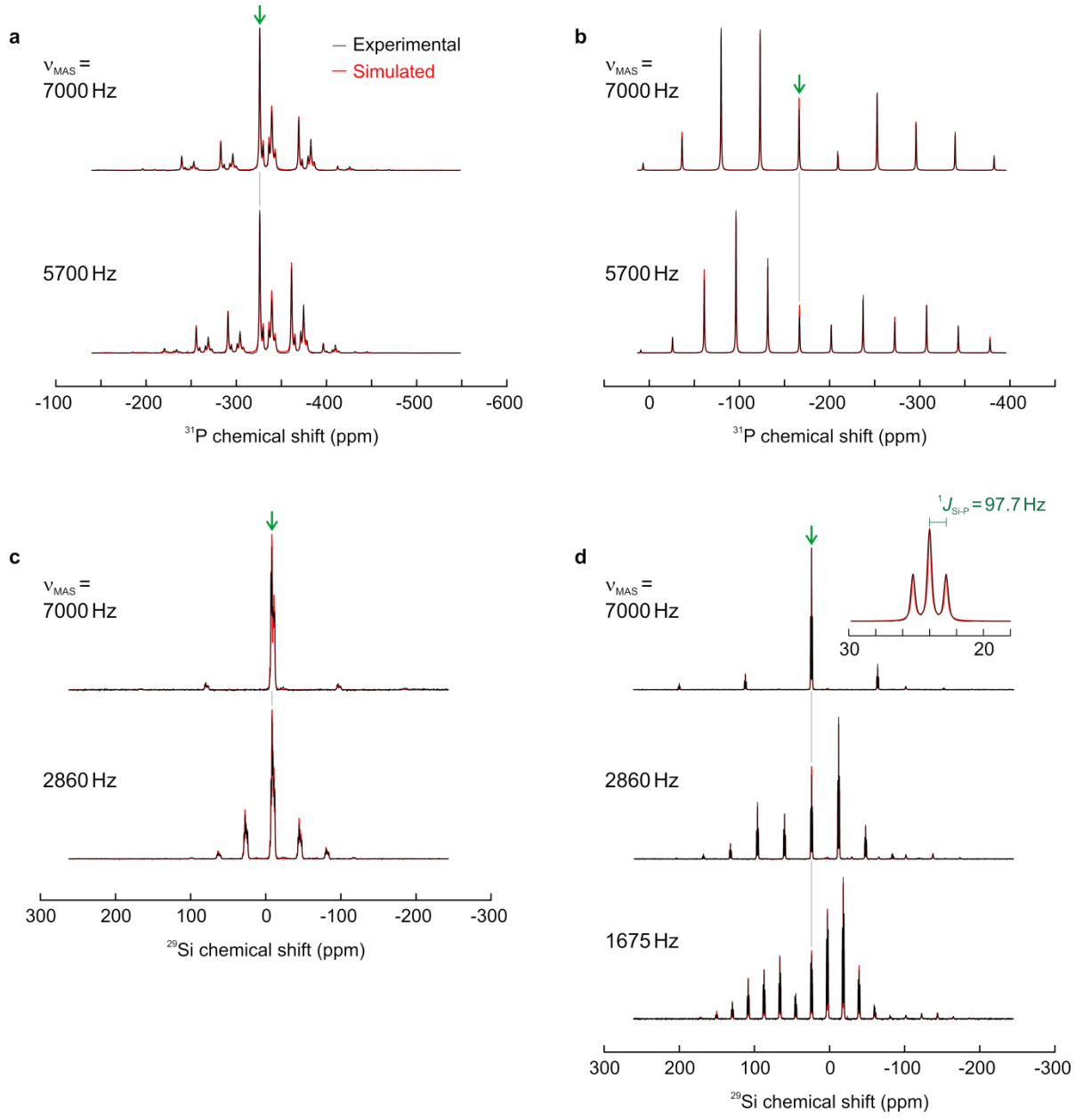

Figure 8: Experimental (black) and simulated (red) spinning sideband patterns for compounds **"G"** (a,c) and **"H"** (b,d). Cross-polarization spectra were recorded on ^{31}P (a,b) and ^{29}Si (c,d) at multiple

magic-angle spinning frequencies (ν_{MAS}). The isotropic peaks are indicated by arrows. The excerpt in (d) presents the multiplet structure of the ^{29}Si resonance of 4 due to silicon-phosphorus *J* coupling.

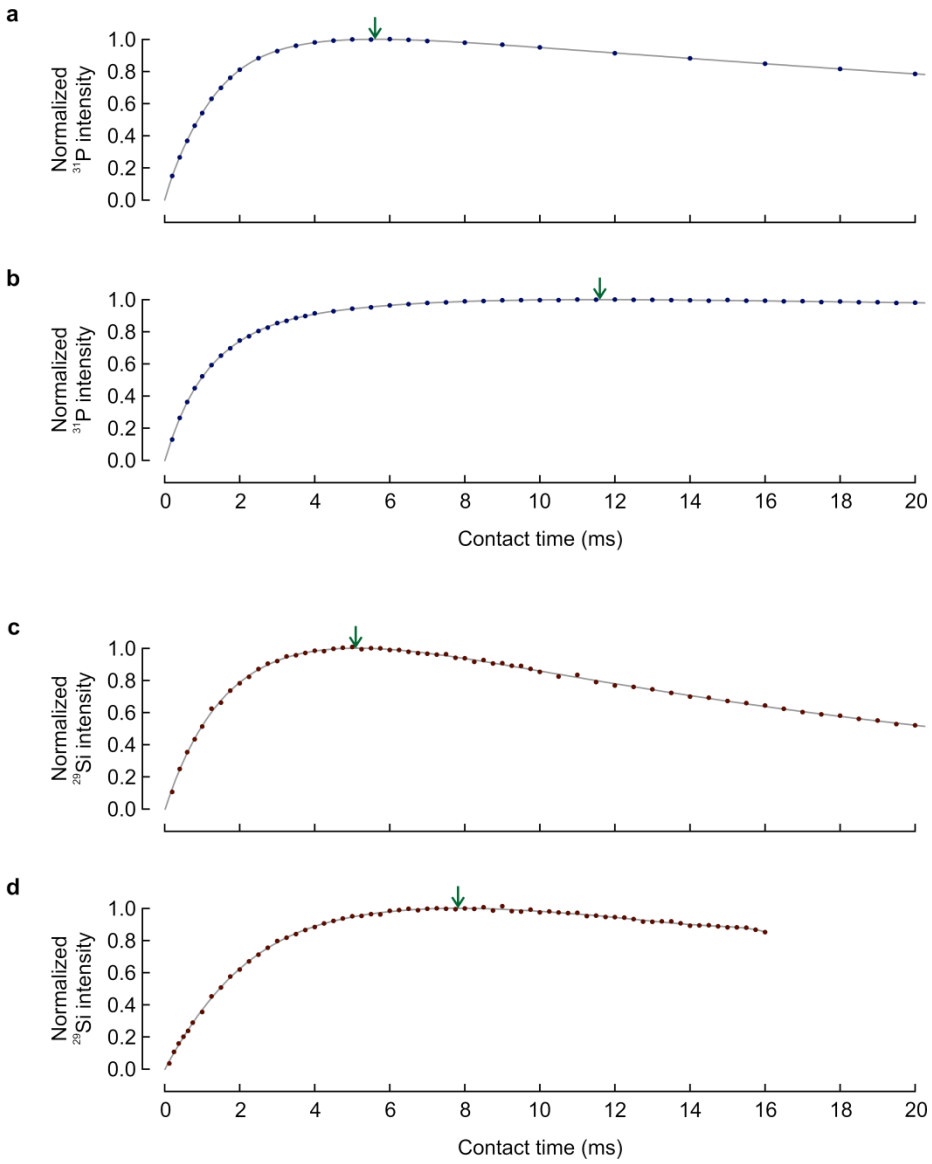

Figure 9: Cross-polarization profiles. The build-up of magnetization for compounds **"G"** (a,c) and **"H"** (b,d) was monitored by incrementing the contact time between ^{1}H and ^{31}P (a,b; 20 kHz MAS), or ^{1}H and ^{29}Si (c,d; 7 kHz MAS). Arrows indicate the point of maximal intensity.

Table 2: Chemical shift tensor parameters and optimum CP contact times

Compound	Nucleus	τ_{CP} (ms)	δ_{iso} (ppm)	δ_{xx} (ppm)	δ_{yy} (ppm)	δ_{zz} (ppm)	η_{asym}	δ_{aniso} (ppm)
"G" (exp.)	^{31}P	5.6	-326.1	-367.7	-367.7	-242.9	0	83.2
"G" (theo.)	^{31}P		-341.1	-405.6	-389.9	-227.9	0.139	113.2
"H" (exp.)	^{31}P	11.6	-166.4	-49.6	-63.4	-386.2	0.063	-219.8
"H" (theo.)	^{31}P		-132.0	39.7	-43.0	-392.8	0.317	-260.8
"G"	^{29}Si	5.1	-8.4	43.8	3.4	-72.4	0.631	-64.0
"H"	^{29}Si	7.8	24.0	-46.2	-21.8	140.0	0.210	116.0

In conclusion, we could confirm the preparation of two inorganic CBD analogues consisting of a Si_2CP and a Si_2P_2 ring, respectively, stabilized by bulky benz-amidinato ligand with *t*Bu substituents on the nitrogen atoms. X-ray structural data, theoretical calculation and solid-state NMR proved concordantly that the phosphorus and silicon atoms in these two rings are "naked", i.e. doubly-coordinated but not covalently bounded to other atoms.

6.1. Pincer based ligands-stabilized complexes of Tin-119

Our collaborators have synthesized tin-containing complexes of three different families: 1) a new type of bis-stannylene **"I"**, 2) a tin hydride **"J"** and 3) a cationic and anionic complex **"K"** (Fig. 12). The bis-stannylene is highly interesting as it is the first example of a compound where two tin atoms in the +1 oxidation state are unsymmetrically coordinated and bound together. On the other hand, main group metal hydrides are extremely important in chemical synthesis. They are notably used as precursors for the preparation of other metal hydrides, as reducing agents for a big variety of inorganic and organic substrates and function as potential feedstocks for hydrogen storage[18-22]. Hydrides are considered as promising candidates for the synthesis of new clusters and nanoparticles by controlled thermolysis[23,24]. Finally, another class of interesting complexes contain cationic and anionic heavier group 14

elements, since the heavier atoms have drastically different geometry depending on their ionic state.

In order to confirm the presence of two chemically different environments for 2,6-bis[N-(2′,6′-diisopropylphenyl)ketimino] phenyl moiety and methyl group attached to the imino group in **"I"**, our collaborators acquired the ^{1}H and ^{13}C solution-state NMR spectra. However, despite their numerous attempts, a ^{119}Sn NMR resonance could not be detected in solution. We thus recorded solid-state NMR spectra to verify the presence of two unequivalent Tin resonances. For compound **"J"**, we were interested in confirming the presence of a proton covalently bound to tin, as no tin hydride had been reported where the Sn-H moiety has no intermolecular stabilization.

Additionally, the studied compound **"K"**, $[(LB)SnCl]^{+}/[SnCl_3]^{-}$ (see Fig. 12), contains two tin centers in close proximity which could be observed by ^{119}Sn solution-state NMR. Both tin atoms are in the low-valent form: Sn(II). The first tin center (A) is covalently bound to one chlorine and has three coordination bonds from the nitrogen atoms of the pincer ligand, here designated Lewis Base (LB). This complex has one formal positive charge. The second Tin center (B) is found in the counter ion $[SnCl_3]^{-}$. To investigate the electronic environment around the tin centers in compound **"K"**, the solution-state ^{119}Sn NMR spectra were recorded at variable temperatures (Figure 11).

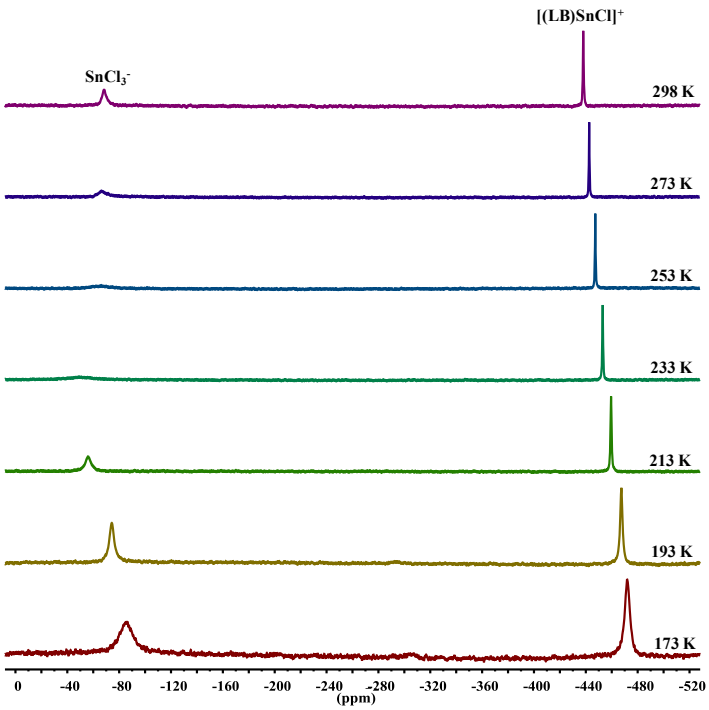

Figure 10: Comparative solution-state ^{119}Sn NMR study of compound **"K"** recorded in THF-d_8 at different temperature[25]

The room temperature solution-state ^{119}Sn NMR spectrum consists of two singlets at -60.2 ppm and -435.0 ppm (Figure 11). These two singlets correspond to two differently coordinated tin(II) atoms present in compound **"K"**. The available literature data[26] suggest that the broad signal at -60.2 ppm corresponds to the $SnCl_3^-$ anion, while the remaining singlet at -435.0 ppm could be assigned to the $[(LB)SnCl]^+$ cation.

The ^{119}Sn NMR spectrum of compound **"K"** at low temperature varying in a range of 298−173 K indicates that the tin center in the $[(LB)SnCl]^+$ cation stays intact. However, a slight broadening observed at 173 K was attributed to the inherent freezing properties of the THF-d_8 solvent, which was used for the experiment.

On the other hand, the downfield resonance at -60.2 ppm for the $SnCl_3^-$ anion showed a non-regular change in the position at low temperature. This irregular change could be due to coordination of THF-d_8 solvent molecules to the $SnCl_3^-$ anion leading to different geometrical species. To test this hypothesis, a series of solid-state ^{119}Sn NMR spectra were recorded at variable temperature for compound **"K"**. In order to further characterize the electronic environment around the tin centers, the CSA parameters were extracted from the spinning sideband intensities at multiple MAS rates.

Hypotheses:

The two tin atoms in bis-stannylene **"I"** are not chemically equivalent, since the two are unsymmetrically coordinated. The two Sn sites of **"K"** are not chemically equivalent

Both Sn sites of **"I"** and the Tin atom of **"K"** are non-protonated; the Tin atom of **"J"** is protonated.

Since a temperature dependence is observed for the chemical shift of **"K"** in solution-state NMR, we hypothesize that the molecular geometry for the $SnCl_3^-$ site of **"K"** undergoes a temperature-dependent rearrangement.

Method summary:

We determined the isotropic chemical shift and the principal value of CSA tensors from spectra recorded at multiple spinning speeds.

We determined the protonation state from ^1H-^{119}Sn CP build-up curves.

We recorded the spectra of **"K"** at 3 different temperatures and compared isotropic chemical shifts and CSA values.

“I”

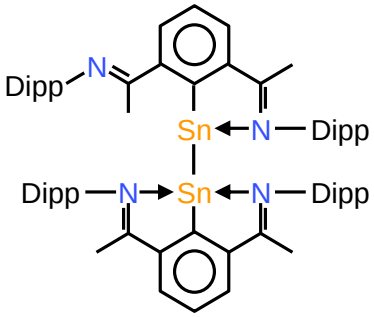
Dipp
N
Sn
N
Dipp
Dipp
N
Sn
N
Dipp

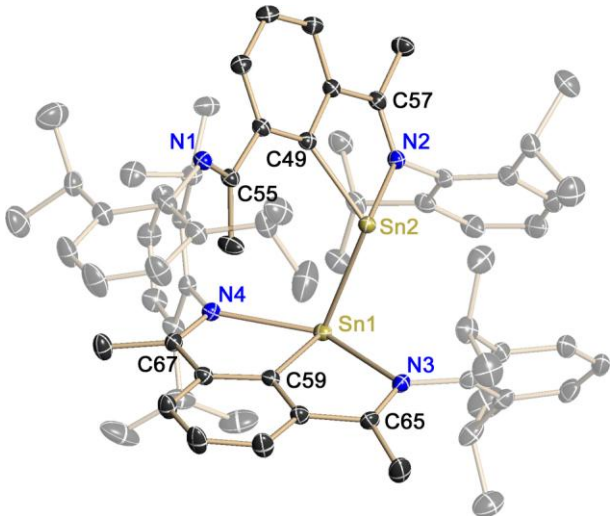
C57
N1
C49
N2
C55
Sn2
N4
Sn1
C67
C59
N3
C65

“J”

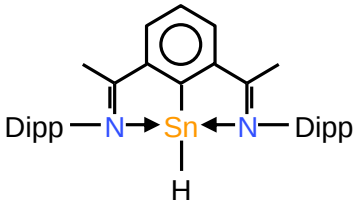
Dipp
N
Sn
N
Dipp
H

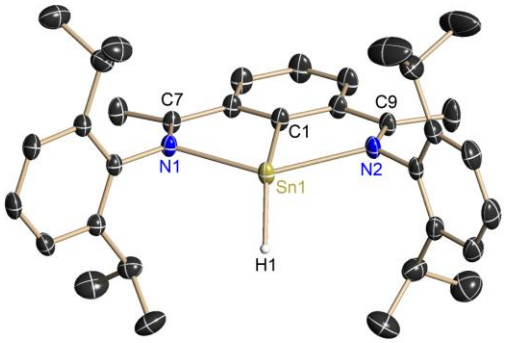
C7
C9
C1
N1
N2
Sn1
H1

“K”

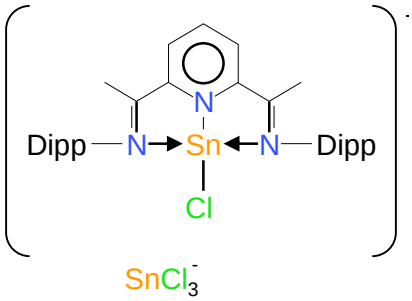
N
Dipp
N
Sn
N
Dipp
Cl
SnCl3

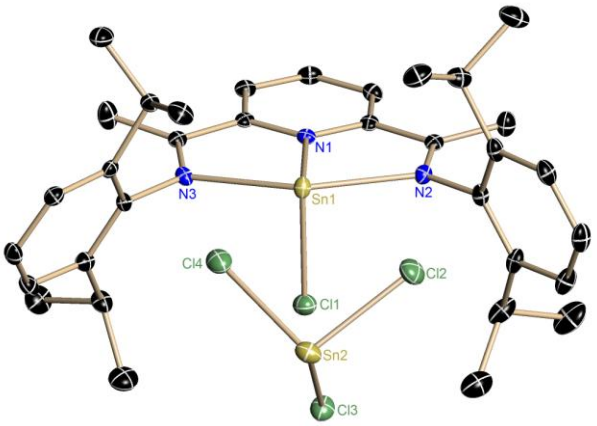
N1
N3
Sn1
N2
Cl4
Cl1
Cl2
Sn2
Cl3

Figure 11: (left) Chemical structure of tin complexes. (right) Crystal structure. Anisotropic displacement parameters are depicted at the 50% probability level. Hydrogen atoms are omitted for clarity.

6.1.1. Materials and Methods

6.1.1.1. Solid-state NMR

All compounds were packed under inert atmosphere into a 4.0 mm MAS rotor. The compound **"K"** forms bright orange crystals in a saturated toluene solution. After evaporation of excess solvent overnight, micro-crystals are packed under inert atmosphere into a 4.0-mm MAS rotor. The inert atmosphere was conserved by employing only dry nitrogen gas for the operation of the MAS, for sample cooling and for de-icing of the cooling junction.

All spectra were recorded on a WB-400 MHz ^{1}H Larmor frequency (9.4 T) instrument using a 4.0-mm HXY probe-head in double-channel mode, with the X channel in the high-frequency tuning range ($\lambda/2$) for ^{119}Sn measurements. Experiments were carried out at magic-angle spinning rates of 11000 Hz or 11800 Hz. The magic angle was adjusted using the $K^{79}Br$ signal.

The CPMAS spectrum of tetracyclohexyltin was used for calibration of ^{119}Sn chemical shifts, using the sharp peak at -97.4 ppm as an external reference, and for optimization of the cross-polarization condition. The CP contact time was 3.5 ms, and rf fields were 55 kHz for ^{119}Sn and 57 kHz for ^{1}H (using a tangential ramp). ^{13}C and ^{1}H chemical shifts were calibrated externally with adamantane, setting the downfield CH_2 resonance to 38.47 ppm.

The longitudinal relaxation rate for bulk ^{1}H was estimated to be 0.21 s as measured by inversion-recovery with pre-saturation, suggesting an optimal recycling

delay of 0.26 s. However, as an acquisition time of 14 ms and 70 kHz of heteronuclear proton decoupling were employed, the recycling delay was set to 1 s.

The full sideband pattern was acquired by recording 9 sub-spectra spanning each a 75200 Hz spectral window, each time moving the ^{119}Sn RF carrier frequency by 37600 Hz. Each sub-spectrum was acquired with the number of scans indicated in Figure 18, and the measurement time for the full spectrum is indicated as well. This technique of variable offset cumulative spectrum (VOCS) was presented by Massiot *et al*[27]. However, the suggested spin-echo was not employed due to a reduction in sensitivity compared to the CPMAS experiment.

The temperature of the cooling nitrogen gas was controlled and monitored with a BCU-5 module. The sample temperature was then calibrated externally using the central peak chemical shift of the nickelocene ^{1}H spectrum [28] with the following calibration:

$$T(K) = -\frac{79477}{\delta(\text{ppm}) - 12.89} \tag{0.1}$$

6.1.1.2. Data processing and data fitting

The ^{119}Sn resonances are quite broad (approx. 8 ppm of full-width at half-height, or 1300 Hz), such that only the first 4 ms of the FID were used. An exponential window function with a line-broadening of 120 Hz is applied. For the spectra used for extraction of CSA parameters (Figure 17), the baseline was corrected independently for each sub-spectrum using a piecewise polynomial spline function. The sideband intensities were then extracted by integration of a small region with a width of 2 ppm. Experimental intensities are compared with sideband intensities simulated within the GAMMA spin-simulation environment (Fig. 17). For the two MAS rates, a grid is generated with an anisotropy step size of 2.5 ppm and an asymmetry step size of 0.015 (Fig. 16). The CSA

parameters are selected which minimize the sum of RMSD for both MAS rates (11kHz and 11.8kHz).

6.1.2. Results

The structure of **"I"** was strongly supported by ^{119}Sn CP-MAS NMR investigations. Two highly anisotropic resonances were detected in the ^{119}Sn solid-state NMR spectrum (Figure 13a). CP-MAS experiments carried out at two MAS frequencies identified the isotropic chemical shifts at 133.9 ppm and 114.8 ppm (referenced to Me_4Sn). The cross-polarization build-up curves confirm that both tin sites are non-protonated. Maximal intensity is reached after more than 5 ms, indicating a large distance separation between tin and the nearest proton. The structure of **"I"** is further supported by the detection of one-bond carbon-tin *J* couplings on the two most downfield ^{13}C resonances, which correspond to the carbons covalently bound to tin (Figure 14a). The magnitude of the *J* couplings (433 Hz and 323 Hz) is in agreement with values in the literature for one-bond carbon-tin couplings[29-31].

In the solid-state NMR spectrum of **"J"**, a single ^{119}Sn resonance is detected at -119.4 ppm (Figure 13b), whereas the solution state ^{119}Sn NMR spectrum shows a singlet at δ -114.3 ppm. The sideband pattern also indicates a large anisotropic environment. The lower ^{119}Sn chemical shift of **"J"** compared to **"I"** is consistent with shielding due to the covalently bound proton. The proposed constitution of **"J"** was further confirmed by single crystal X-ray diffraction studies (Figure 12).

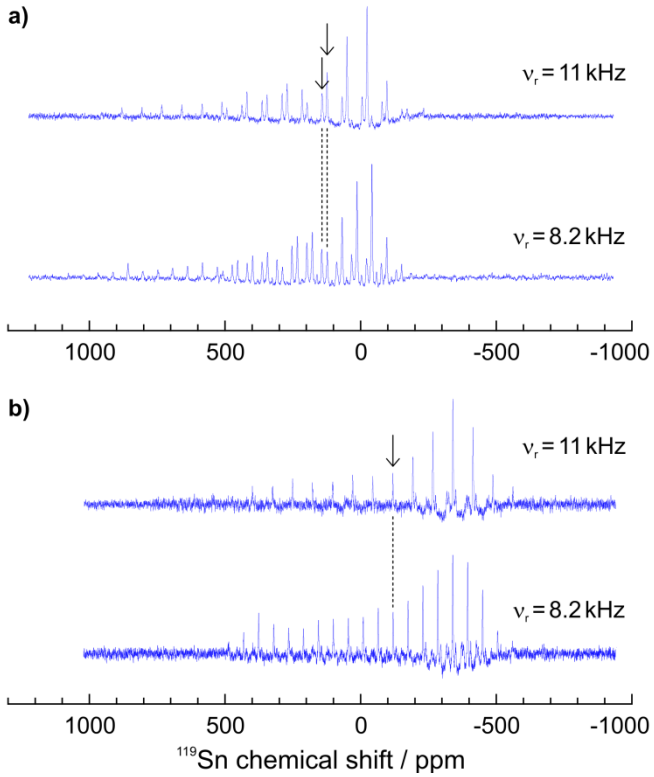

Figure 12: ^{119}Sn solid-state NMR cross-polarization spectra of a) bis(stannylene) **"I"** and b) Sn(II) hydride **"J"**. The spectra were recorded at 8.2 kHz and 11 kHz MAS on a 9.4 T spectrometer. Isotropic chemical shift are indicated by arrows.

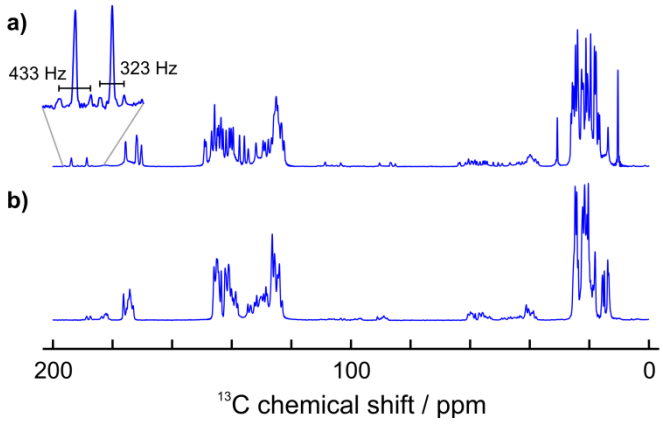

Figure 13: ^{13}C solid-state cross-polarization NMR spectrum of a) bis(stannylene) **"I"** and b) Sn(II) hydride **"J"**. The excerpt highlights the one-bond carbon-tin *J* couplings. The integrals of the satellite peaks (18.9% and 15.9% of total volume) correspond to the combined natural abundance of ^{117}Sn (7.61%) and ^{119}Sn (8.58%). The spectra were recorded at 8.2 KHz MAS on a 9.4 T spectrometer.

The obtained solid-state NMR data confirms the successful synthesis of a new class of pincer based bis(stannylene) with two unsymmetrically coordinated Sn(I) atoms and a monomeric Sn(II) hydride by using the same system with two different reducing agents. The Sn(II) hydride is the first example having no Sn-H intermolecular interactions.

For compound **"K"**, in contrast to what has been observed in solution-state NMR, not two but three Tin sites can be detected in solid-state NMR, highlighted in red, blue and green in Fig. 15. The combination of two MAS rates enables us to identify the isotropic chemical shifts as -77.4 ppm, -415.4 ppm and -431.5 ppm. By similarity to the solution-state ^{119}Sn isotropic chemical shift, site A is assigned to Sn2 in the $SnCl_3^-$ anion. The two latter sites (B and B') exhibit a similar isotropic chemical shift and sideband pattern and can be both assigned to the pincer ligand-coordinated Tin $[(LB)SnCl]^+$. This occurrence of two ^{119}Sn resonances for Sn1 could arise because of polymorphism in the sample with site B' being a minor component. Indeed, the ratio of summed sideband intensities, A:B:B', is 4:3:1, suggesting a stoichiometry of 1:1 between Sn2:Sn1 sites which is in agreement with the crystal structure of **"K"**.

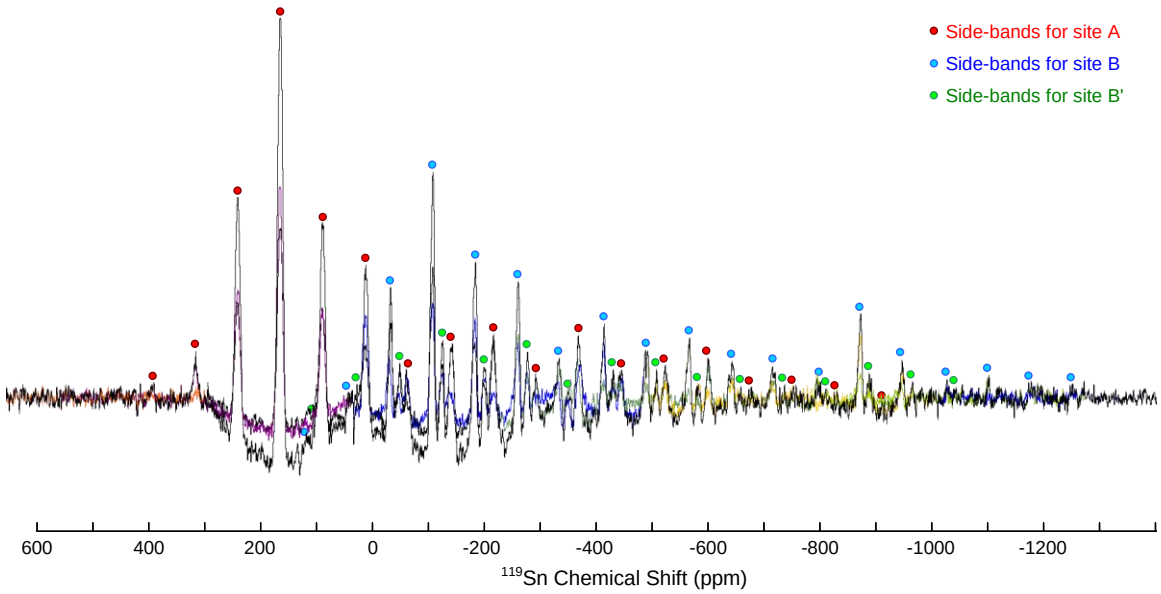

Figure 14: ^{119}Sn cross-polarization spectrum of $[(LB)SnCl]^+/[SnCl_3]^-$ displayed without baseline correction

The sideband pattern intensities could be fitted to the simulated intensities (Fig. 17c and d) enabling to identify unambiguously the anisotropy and asymmetry parameter for the three tin resonances. Fig. 16 shows the RMSD as a function of those two parameters. It can be seen that only a single minimum is present. In addition, the position of the minimum is relatively unchanged if only a single MAS rate is fitted. In the current case, a single low-MAS recording was thus sufficient to define the CSA tensor parameters, but employing multiple spinning rates increases the accuracy of the measurement (values listed in Table 2).

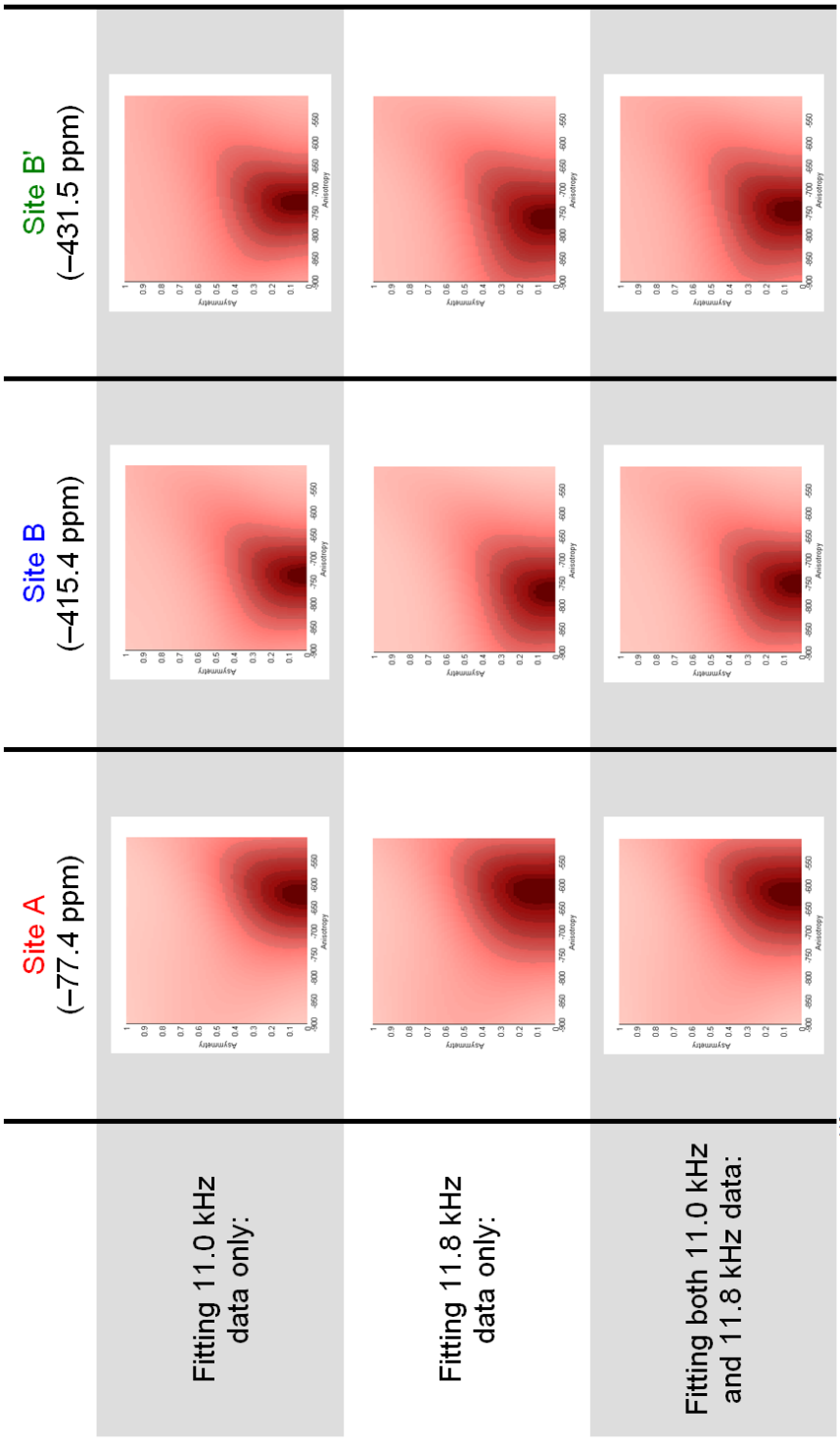

Figure 16: RMSD plots for fitting of ^{119}Sn spinning sideband patterns

Table 3: Chemical Shift Anisotropy tensor parameters of compound **"K"**

	δ_{iso} (ppm)	δ_{aniso} (ppm)	η_{asym}	δ_{xx} (ppm)	δ_{yy} (ppm)	δ_{zz} (ppm)
Site A	–77.4	–617.5	0.03	240.7	222.0	–694.9
Site B	–415.4	–750.0	0.00	–40.4	-40.4	–1165.4
Site B'	-431.5	–744.7	0.03	–48.4	–69.9	–1176.2

The chemical shift anisotropy δ_{aniso} is quite large for all three sites (Table 3). The observed large anisotropies are a distinctive feature of low-valent Sn(II) species[32]. The individual sideband patterns span up to 1200 ppm. The range covered by all three sites is 1400 ppm, which corresponds to 209 kHz at 9.4 T or to 313 kHz at 14.1 T. The asymmetry of the chemical shift anisotropy (CSA) tensor η_{asym} is close to 0 for all sites. Values of the asymmetry such as 0.03 for sites A, B' and 0.0 for site B indicate an axially symmetric CSA tensor.

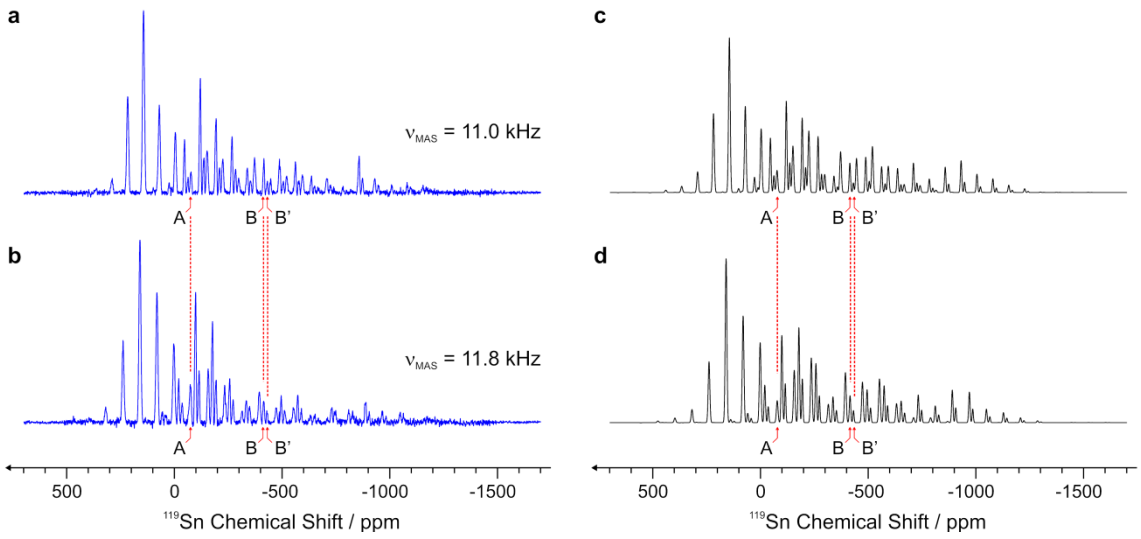

Figure 15: Solid-state ^{119}Sn NMR cross-polarization spectra of compound **"K"** at 11.0 kHz (a and c) and 11.8 kHz (b and d). Experimental (a and b) and simulated (c and d) spectra, as obtained from the fitting of spinning sideband intensities.

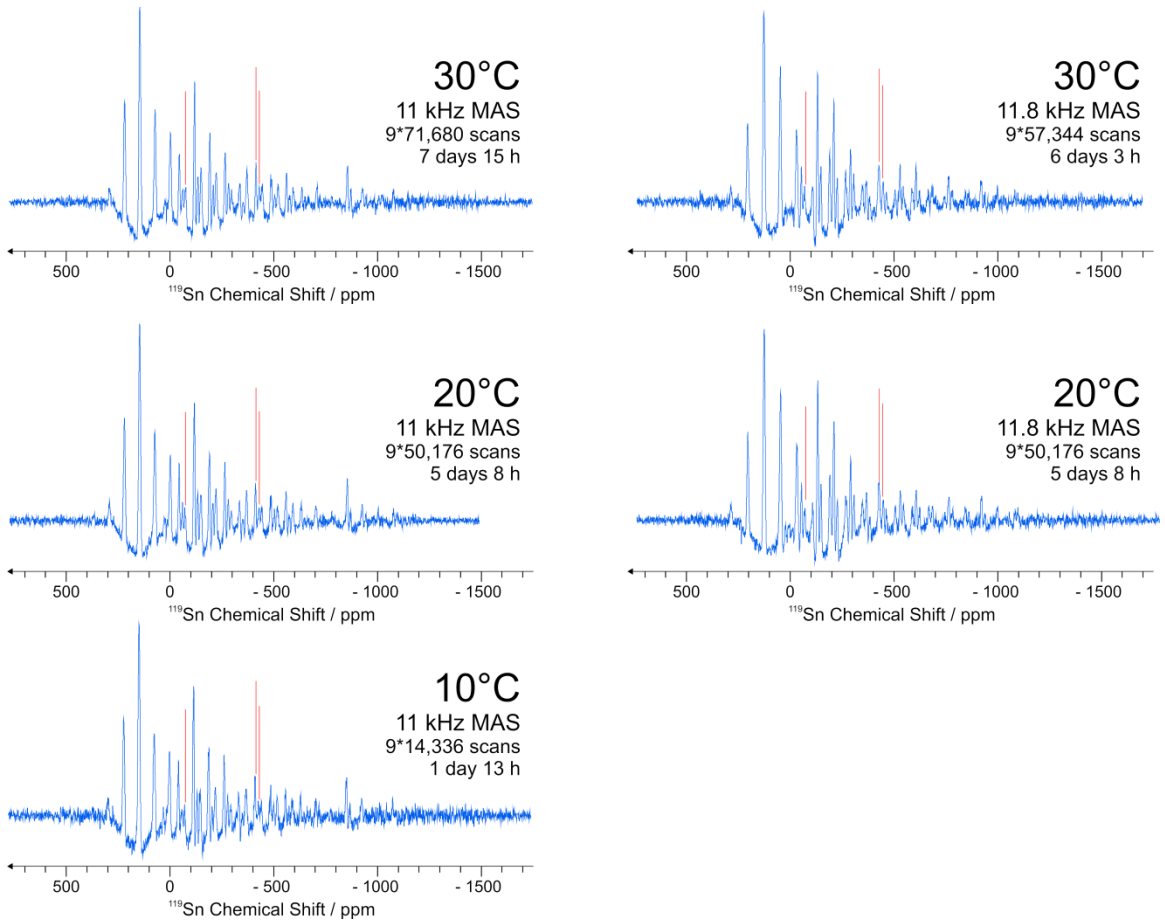

Figure 16: Temperature dependence of ^{119}Sn spectra

The experiments were then repeated at three temperatures in the range of 282 K to 305 K. The spectra obtained were virtually unchanged at all three temperatures. The possibility that a rearrangement of the geometry around the tin centers occurs at lower temperature in the absence of solvent is thus invalidated; the shifts observed in solution-state NMR are rather related to a solvent effect.

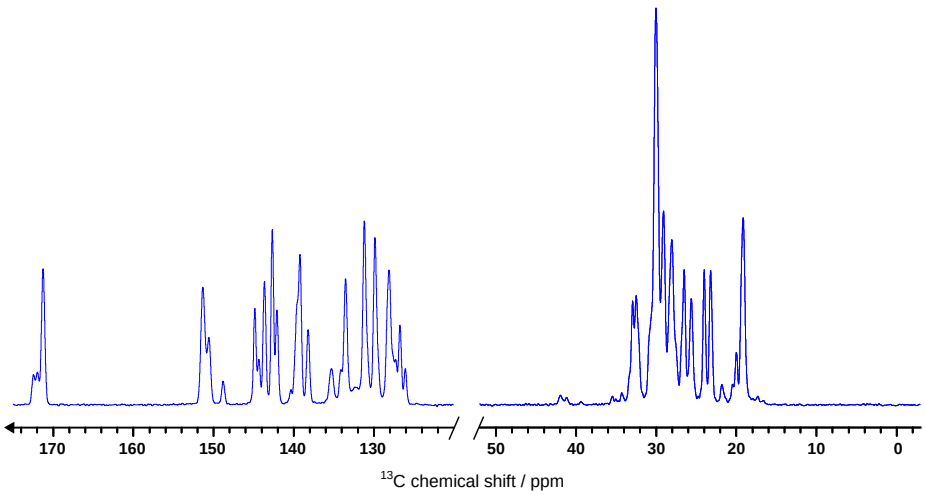

Figure 17: ^{13}C cross-polarization spectrum of $[(LB)SnCl]^+/[SnCl_3]^-$

Interestingly, the broad nature of the tin peaks is not directly reflected in the ^{13}C solid-state NMR spectrum (Fig. 19) where full-widths of 40–60 Hz are observed.

6.2. References.

1. Levason, W., Reid, G., Zhang, W. Coordination complexes of silicon and germanium halides with neutral ligands. *Coordin Chem Rev* **255**, 1319-41 (2011).
2. Roesky, H. W. Chemistry of low valent silicon. *Journal of Organometallic Chemistry* **730**, 57-62 (2013).
3. Ghadwal, R. S., Azhakar, R., Roesky, H. W. Dichlorosilylene: A High Temperature Transient Species to an Indispensable Building Block. *Accounts of Chemical Research* **46**, 444-56 (2013).
4. Arnold, P. L., Pearson, S. Abnormal N-heterocyclic carbenes. *Coordin Chem Rev* **251**, 596-609 (2007).
5. Crabtree, R. H. Abnormal, mesoionic and remote N-heterocyclic carbene complexes. *Coordin Chem Rev* **257**, 755-66 (2013).
6. Gusev, D. G. Electronic and Steric Parameters of 76 N-Heterocyclic Carbenes in Ni(CO)(3)(NHC). *Organometallics* **28**, 6458-61 (2009).
7. Ghadwal, R. S., Roesky, H. W., Merkel, S., Henn, J., Stalke, D. Lewis Base Stabilized Dichlorosilylene. *Angewandte Chemie-International Edition* **48**, 5683-6 (2009).
8. Singh, A. P., Ghadwal, R. S., Roesky, H. W., Holstein, J. J., Dittrich, B., Demers, J.-P., Chevelkov, V., Lange, A. Lewis base mediated dismutation of trichlorosilane. *Chemical Communications* **48**, 7574-6 (2012).
9. Fung, B. M., Khitrin, A. K., Ermolaev, K. An improved broadband decoupling sequence for liquid crystals and solids. *Journal of Magnetic Resonance* **142**, 97-101 (2000).
10. Smith, S. A., Levante, T. O., Meier, B. H., Ernst, R. R. Computer Simulations in Magnetic Resonance. An Object-Oriented Programming Approach. *Journal of Magnetic Resonance Series A* **106**, 75-105 (1994).
11. Ghadwal, R. S., Azhakar, R., Proepper, K., Holstein, J. J., Dittrich, B., Roesky, H. W. N-Heterocyclic Carbene Stabilized Dichlorosilylene Transition-Metal Complexes of V(I), Co(I), and Fe(0). *Inorganic Chemistry* **50**, 8502-8 (2011).

12. Maier, G., Born, D. Small Rings .67. Tri-Tert-Butyl(Trimethylsilyl)Tricyclo 1.1.0.02,4 -Butane - A 2nd Tetrahedrane Derivative. *Angewandte Chemie-International Edition* **28**, 1050-2 (1989).
13. Gee, J. R., Howard, W. A., McPherson, G. L., Fink, M. J. Persistent Triplet Diradicals from the Dimerization of Silacyclobutadienes. *Journal of the American Chemical Society* **113**, 5461-2 (1991).
14. Kon, Y., Ogasawara, J., Sakamoto, K., Kabuto, C., Kira, M. A stable silicon congener of highly strained bicyclo 3.2.0 hepta-1,3,6-triene. *Journal of the American Chemical Society* **125**, 9310-1 (2003).
15. Sen, S. S., Khan, S., Roesky, H. W., Kratzert, D., Meindl, K., Henn, J., Stalke, D., Demers, J.-P., Lange, A. Zwitterionic Si-C-Si-P and Si-P-Si-P Four-Membered Rings with Two-Coordinate Phosphorus Atoms. *Angewandte Chemie-International Edition* **50**, 2322-5 (2011).
16. Thakur, R. S., Kurur, N. D., Madhu, P. K. Swept-frequency two-pulse phase modulation for heteronuclear dipolar decoupling in solid-state NMR. *Chemical Physics Letters* **426**, 459-63 (2006).
17. Chandran, C. V., Madhu, P. K., Kurur, N. D., Brauniger, T. Swept-frequency two-pulse phase modulation (SWf-TPPM) sequences with linear sweep profile for heteronuclear decoupling in solid-state NMR. *Magn Reson Chem* **46**, 943-7 (2008).
18. Bradley, G. F., Stobart, S. R. Reaction of Octacarbonyldicobalt with Organosilanes, Organo-Germanes, and Organostannanes - Formation, Properties, and Vibrational-Spectra of Trimethylgermyltetracarbonylcobalt and Related Complexes. *Journal of the Chemical Society-Dalton Transactions*, 264-9 (1974).
19. Aldridge, S., Downs, A. J. Hydrides of the main-group metals: New variations on an old theme. *Chemical Reviews* **101**, 3305-65 (2001).
20. Rivard, E., Power, P. P. Recent developments in the chemistry of low valent group 14 hydrides. *Dalton Transactions*, 4336-43 (2008).
21. Staubitz, A., Robertson, A. P. M., Manners, I. Ammonia-Borane and Related Compounds as Dihydrogen Sources. *Chemical Reviews* **110**, 4079-124 (2010).
22. Mandal, S. K., Roesky, H. W. Group 14 Hydrides with Low Valent Elements for Activation of Small Molecules. *Accounts of Chemical Research* **45**, 298-307 (2012).
23. Wang, C. F., Xie, S. Y., Lin, S. C., Cheng, X., Zhang, X. H., Huang, R. B., Zheng, L. S. Glow discharge growth of SnO2 nano-needles from SnH4. *Chemical Communications*, 1766-7 (2004).
24. Hessel, C. M., Henderson, E. J., Kelly, J. A., Cavell, R. G., Sham, T.-K., Veinot, J. G. C. Origin of luminescence from silicon nanocrystals: a near edge X-ray absorption fine structure (NEXAFS) and X-ray excited optical luminescence (XEOL) study of oxide-embedded and free-standing systems. *Journal of Physical Chemistry C* **112**, 14247-54 (2008).
25. Singh, A. P., Roesky, H. W., Carl, E., Stalke, D., Demers, J.-P., Lange, A. Lewis Base Mediated Autoionization of GeCl2 and SnCl2. *Journal of the American Chemical Society* **134**, 4998-5003 (2012).
26. Coddington, J. M., Taylor, M. J. Investigations of Tin(II) Halide Aqueous-Solutions and Solvent Extracts by Sn-119 Nuclear Magnetic-Resonance Spectroscopy - Characterization of the Trihalogenostannate(II) Anions SnX3-, SnX2Y-, and SnX(Y)Z - (X, Y, or Z = Cl, Br, or I). *Journal of the Chemical Society-Dalton Transactions*, 2223-7 (1989).
27. Massiot, D., Farnan, I., Gautier, N., Trumeau, D., Trokiner, A., Coutures, J. P. Ga-71 and Ga-69 Nuclear-Magnetic-Resonance Study of beta-Ga2O3 - Resolution of 4-Fold and 6-Fold Coordinated Ga Sites in Static Conditions. *Solid State Nuclear Magnetic Resonance* **4**, 241-8 (1995).
28. Heise, H., Kohler, F. H., Xie, X. L. Solid-state NMR spectroscopy of paramagnetic metallocenes. *Journal of Magnetic Resonance* **150**, 198-206 (2001).
29. Harris, R. K., Mann, Brian E. *NMR and the periodic table*. 88 (Academic Press, 1978).
30. Jastrzebski, J., Grove, D. M., Boersma, J., Vankoten, G., Ernsting, J. M. Sn-119 NMR-Study of Organotin Compounds Having Intramolecular Sn - N Coordination. *Magn Reson Chem* **29**, S25-S30 (1991).
31. Wingerter, S., Gornitzka, H., Bertermann, R., Pandey, S. K., Rocha, J., Stalke, D. Deprotonated iminophosphorane o-C6H4Ph2P=NSiMe3 as a novel ligand to stabilize a diarylstannylene and -plumbylene via side arm donation. *Organometallics* **19**, 3890-4 (2000).

32. Eichler, B. E., Phillips, B. L., Power, P. P., Augustine, M. P. Solid-state and high-resolution liquid Sn-119 NMR spectroscopy of some monomeric, two-coordinate low-valent tin compounds: Very large chemical shift anisotropies. *Inorganic Chemistry* **39**, 5450-3 (2000).

6.3. Appendix

Source file for GAMMA simulation of spinning sideband pattern (File ssb_cl1.cc)

```
#include "gamma.h"
using namespace std;

int main (int argc, char *argv[])
{
  spin_system  A(1);                  //set up a 1-spin system
  coord        B(0,0,1);              //magnetic field along z
  spin_T       TTS = T_CS2(A,0,B);    //CSA spin tensor

  double       sixx,siyy,sizz;        //sixx<siyy<sizz CSA PAS values
  double       omegar,ppm;            //MAS frequency and 1ppm in Hz
  double       lb;                    //Line broadening
  double       sw;                    //spectral window
  int          steps = 12;            //steps in powder loop
  double       thetaPR;
  double       phiPR,phiRL;
  double       gammaPR;
  double       ma = 54.73561;         //magic angle
  int          NR = 128;              //number of rotor periods
  int          ND = 128;
  int          NC = 1024;             //NC>ND
  int          p = 1;
  string       outFileName;
  int          z = 0;

    int arg_min = 8;
    if (argc == 1)
    {
        query_parameter (argc,argv,p++,"output filename        = ", outFileName);
        query_parameter (argc,argv,p++,"MAS frequency   [Hz]   = ", omegar);
        query_parameter (argc,argv,p++,"1 ppm           [Hz]   = ", ppm);
        query_parameter (argc,argv,p++,"sigmaxx         [ppm]  = ", sixx);
        query_parameter (argc,argv,p++,"sigmayy         [ppm]  = ", siyy);
        query_parameter (argc,argv,p++,"sigmazz         [ppm]  = ", sizz);
    query_parameter (argc,argv,p++,"Line broadening [ppm]  = ", lb);
    query_parameter (argc,argv,p++,"Powder steps           = ", steps);
    } else {
        if (argc < arg_min)
        {
            cout<<argv[0]<<": Usage: The following "<<arg_min<<" command-line arguments must be provided:\n\n"<<flush;
            cout<<"1>   output filename\n2>   MAS frequency\n3>   1 ppm\n4>   sigmaxx\n5>   sigmayy\n6>   sigmazz\n7>
lb\n8>   steps\n\n"<<flush;
            return 1;
        }
        outFileName = argv[1];
        omegar = atof(argv[2]);
        ppm = atof(argv[3]);
        sixx = atof(argv[4]);
        siyy = atof(argv[5]);
        sizz = atof(argv[6]);
    lb = atof(argv[7]);
    steps = atoi(argv[8]);
    }

  outFileName = outFileName;

  //sixx<siyy<sizz
  sixx = sixx*ppm;
  siyy = siyy*ppm;
  sizz = sizz*ppm;

  int         NP = int(NR*ND);
  row_vector  spect(NP),specsum(NP),data(NP),dataI(NP);

  space_T     CS_pas; //CSA space tensor in PAS, rotor-fixed, laboratory frame
  space_T     CS_R,CS_L;

  matrix s1(3,3);
         s1.put_h(sixx, 0, 0);  s1.put_h(0.,   0, 1);  s1.put_h( 0.,  0, 2);
                                s1.put_h(siyy, 1, 1);  s1.put_h( 0.,  1, 2);
```

```
                                                    s1.put_h(sizz, 2, 2);
  CS_pas = A2(s1);

  double   dwtime        = 1./omegar;
  int      intervall = int (NC/ND);
  gen_op   detect = Im(A,0);
  gen_op   sigma;
  gen_op   H,P,S;
  gen_op   U[ND]; //propagators for one rotor period


  for (int b=1;b<13848;b+=steps) //powder loop
  {
    cout << "orientations: " << 100*b/13848 << "%\r" << flush;

    thetaPR = double(180.*b/13848.);                  //theta in [0,180]
    phiPR   = double(360./13848. * ((107*b)%13848));  //phi   in [0,360]
    gammaPR = double(360./13848. * ((271*b)%13848));  //gamma in [0,360]

    CS_R = CS_pas.rotate(phiPR,thetaPR,gammaPR);

    for (int m=0;m<ND;m++) //MAS loop
    {
      int  beg = int (m*NC/ND);
      S    = Ie(A,0);
      for (int i=beg;i<beg+intervall;i++)
      {
        phiRL = omegar/norm(omegar)*double(360.) * i/NC;
        CS_L  = CS_R.rotate(phiRL,ma,0.0);

        H = CS_L.component(2,0)*TTS.component(2,0);
        H = H + CS_L.component(0,0)*TTS.component(0,0);

        P = prop (H,-dwtime/NC);
        S = P*S;
      }
      U[m] = S;
    } //MAS loop

    sigma = Ix(A,0);

    for (int n=0; n<NR*ND; n++)
    {
      spect(n) = trace(sigma,detect);
      int i = int(n/ND);
      int m = n - ND*i; //m runs only from 0 to ND-1 while n runs from 0 to NR*ND-1
      evolve_ip(sigma,U[m]);
    }

    spect = sin(thetaPR*PI/180.)* spect;
    specsum += spect; //sum up each orientation
    z++;
  } //powder loop


  row_vector gauss_window(NP);
  gauss_window=Gaussian(NP,0,NP*0.0465/lb);
  //specsum=specsum*gauss_window;

  //exponential_multiply (specsum,-lb); //line broadening

  for (int l = 0; l<NP;l++)  //only real part
  {
    specsum(l)=specsum(l)*gauss_window(l);
  }

  specsum = FFT (specsum);

  sw = ND*omegar;
  cout << "\n" << "powder orientations = "<< z << "\n";

  //arrange chemical shift axis in ppm
  for (int i=0; i<NP; i++)
  {
    data(i) = complex((int(sw*(1.*i/NP - 0.5)))/ppm, Re(specsum(i)));
    dataI(i) = complex((int(sw*(1.*i/NP - 0.5)))/ppm, Im(specsum(i)));
  }

  GP_xy(outFileName + ".dat",data);
  GP_xy(outFileName + ".datI",dataI);
  return 0;
} //main
```

7. Easy characterization of compounds with extremely large CSA using ultra-fast MAS

7.1. Summary

The chemical shift is a highly sensitive probe of the local electronic environment surrounding the nucleus and can provide critical insights on the structure and dynamics of chemical compounds. For heavy spin-$^1/_2$ nuclei, the anisotropy of the electronic distribution in the vicinity of the nucleus can be quite large, resulting in chemical shift anisotropy (CSA) tensors having a breadth exceeding 1000 ppm in some cases. The absorption frequency is broadened in solid-state NMR, which reduces the sensitivity and requires a high-amplitude RF field for excitation. To alleviate these difficulties, we propose an easy approach employing ultra-fast magic angle spinning (MAS), facilitating the acquisition of ultra-wideline spectra for compounds containing multiple non-equivalent heavy spin-$^1/_2$ sites. Due to the small rotor diameters employed, a large RF field can be generated and only minute sample amounts are required. The approach is demonstrated by the recording of spectra for tin(II) oxide (SnO) and for the $[(LB)Sn^{II}Cl]^+/[Sn^{II}Cl_3]^-$ complex at 75 kHz MAS.

Contribution statement

The present chapter forms a manuscript in preparation: "Easy characterization of compounds with extremely large CSA using ultra-fast MAS", Jean-Philippe Demers, Ann-Christin Poeppler, Michal Malon, Amit Pratap Singh, Herbert W. Roesky, Yusuke Nishiyama, Adam Lange. A.P.S. synthesized the $[(LB)Sn^{II}Cl]^+/[Sn^{II}Cl_3]^-$ complex. The ultra-fast MAS solid-state NMR spectra measurements were carried out by M.M. and Y.N. at JEOL RESONANCE Inc. in Japan. J.P.D. prepared the quantum mechanical simulations.

7.2. Introduction

One of the difficulties encountered at low MAS for the measurement of $[(LB)Sn^{II}Cl]^{+}/[Sn^{II}Cl_3]^{-}$ is the constraint of recording with small spectral window and poor excitation. As seen in section 6.4, the use of small spectra windows and low RF fields introduces a phase difference between the different tin sites, which is difficult to remove by zero- and first-order phase correction. A long pre-scan delay also causes a distortion in the baseline of each individual sub-spectrum which needs to be further removed by processing. In total, the time of the recording session as described in section 6.4.1 lasted for over a month due to the low sensitivity since the energy of the ^{119}Sn spectrum is spread over multiple sidebands.

Although the CSA parameters seem to be extracted correctly, there is a discrepancy for some of the spinning sideband intensities. This could be due to the difficulty in producing a uniform excitation of the full sideband pattern. It could be also due to a broad distribution of the anisotropy and asymmetry parameters across the sample. In light of those disadvantages for measurements at low-MAS, we decided to try the recording of ^{119}Sn spectra with extremely large CSA at ultra-fast MAS.

7.3. Hypotheses and Method Summary

Hypotheses:

We wish to demonstrate the following advantages for ultra-fast MAS of heavy spin-$^1/_2$ nuclei:
High RF can be generated without significant heating,
Low-power decoupling can be employed,
The absorption intensity is concentrated in few sidebands,
Spectra are simplified.

Method summary:

The chemical shift calibrations were conducted on tetracyclohexyltin.

Sideband patterns were recorded at multiple MAS frequencies for SnO and $[(LB)Sn^{II}Cl]^{+}/[Sn^{II}Cl_3]^{-}$.

7.4. Materials and Methods

All the NMR spectra were recorded on an ECA600 spectrometer (JEOL RESONANCE Inc.) equipped with a 1.0 mm HXMAS probe at 14.1 T with a sample volume of 0.8 µL. No temperature control was applied. Magic angle was adjusted by monitoring the ^{1}H NMR spectra of glycine at 70 kHz MAS. The ^{1}H and ^{119}Sn RF field strength were calibrated using nutation frequency on a sample of tetracyclohexyltin. The sharp resonance of tetracyclohexyltin at -97.4 ppm was used as chemical shift reference ^{119}Sn[1,2].

For the preparation of the tin complex sample, the $[(LB)SnCl]^{+}/[SnCl3]^{-}$ compound was separated into several vials under an inert atmosphere (evaporated N_2 gas) prior being packed into the rotor at ambient atmosphere directly before the measurements. We carefully inspected the color and appearance of the sample before and after measurements in order to confirm that the sample did not degrade during the NMR measurements.

The simulated spectra where calculated using the numerical simulation routine GAMMA[3] considering the chemical shift anisotropy of the tin nucleus as the relevant internal system Hamiltonian.

7.5. Results and discussion

7.5.1. Tetracyclohexyltin

In order to identify optimal experiment conditions, we employed tetracyclohexyltin as a reference compound. A large amount of active tin nuclei can be packed in the small MAS rotor due to the small molecular weight of this compound. The chemical environment around the tin nucleus is highly isotropic, making the isotropic peak highly intense. The Hartmann-Hahn matching conditions for cross-polarization were optimized at 43 kHz, 55 kHz and 70 kHz MAS. A linear amplitude ramp was applied on the ^{1}H channel during cross polarization.

The signal intensities obtained at 70 kHz MAS as a function of ^{1}H RF field strength and ^{119}Sn RF field strength were mapped into a 2D spectrum (Figure 1). The optimization range covered zero-quantum (ZQ), double-quantum (DQ), and second-order cross-polarization (SOCP)[4] conditions. The 2D map shows that the ZQ conditions at very strong RF field give the strongest signal intensity. The DQ conditions give slightly weaker signal than the ZQ condition. This might be due to partial cancellation of signal intensity by contamination of signal coming from ZQ CP transfer. Since there are ZQ conditions close to DQ conditions which give rise to negative signal intensity, ramping of the ^{1}H irradiation during CP may induce overlap of these two conditions and lead to reduced signal intensity. No significant SOCP effect was observed contrary to our expectation based on the present of an abundant ^{1}H-^{1}H network.

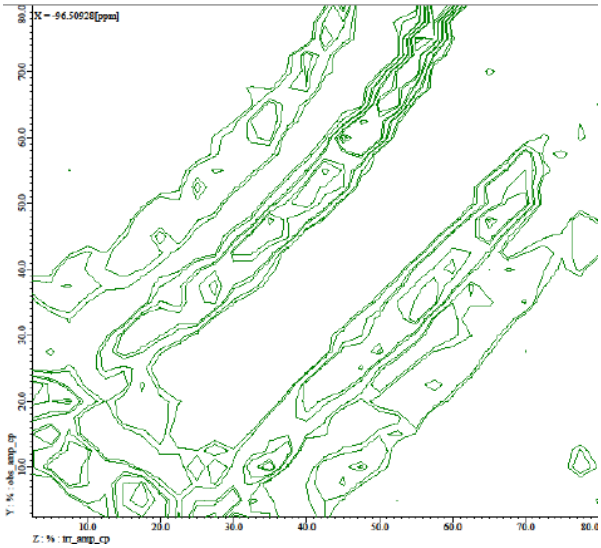

Figure 1: Optimization of Hartmann-Hahn matching conditions at 70 kHz. The horizontal axis shows the ^{1}H RF field strength during Hartmann-Hahn contact and the vertical ^{119}Sn RF field strength.

CW decoupling was employed for heteronuclear decoupling using either high-RF power ^{1}H decoupling or RF irradiation in the low power regime (Table 1). In that case, the ^{1}H RF field strength was adjusted to HORROR condition ($\nu_1 = \nu_r/2$) and with no further optimization was applied.

Spinning frequency (kHz)	Decoupling field strength (kHz)	^{119}Sn chemical shift (ppm)	Calculated Bloch-Siegert shift (ppm)	Relative shift at the same temperature (ppm)	Relative shift at the similar RF field (ppm)
70	280.4	-97.586	-0.035	-0.040	-0.265
70	35.2	-97.546	0.000	0.000	-0.266
55	280.4	-97.437	-0.035	-0.055	-0.116
55	27.3	-97.382	0.000	0.000	-0.102
43	400.6	-97.362	-0.072	-0.082	0.000
43	280.4	-97.321	0.035	0.041	0.000
43	21.3	-97.280	0.000	0.000	0.000

Table 1: Dependence of ^{119}Sn chemical shift on spinning frequency (in kHz) and ^{1}H decoupling field strength (in kHz)

No significant differences in linewidth were observed between the low power and high power ^{1}H decoupling at different MAS rates. The experimental results show that the peak positions depend on both spinning frequency and ^{1}H decoupling RF field strength. The former effect is caused by the increase in temperature due to friction loss during sample spinning. The latter is ascribed to the heteronuclear Bloch-Siegert shift (Table 1). The relative shifts at the same MAS rate were compared, corresponding to the effect of RF-field strength. The experiment values agree with the calculated Bloch-Siegert shift. The relative shifts at similar RF strength are also shown in Table 1, showing that a raise in temperature induces a small resonance frequency shift.

7.5.2. SnO

The ^{119}Sn NMR spectra of SnO were observed by single pulse excitation at 43 kHz, 55 kHz and 75 kHz MAS (Fig. 2). No baseline correction was applied in the processing. The signal intensities for each sideband correspond well with the intensities predicted from simulated spectra (Fig. 3).

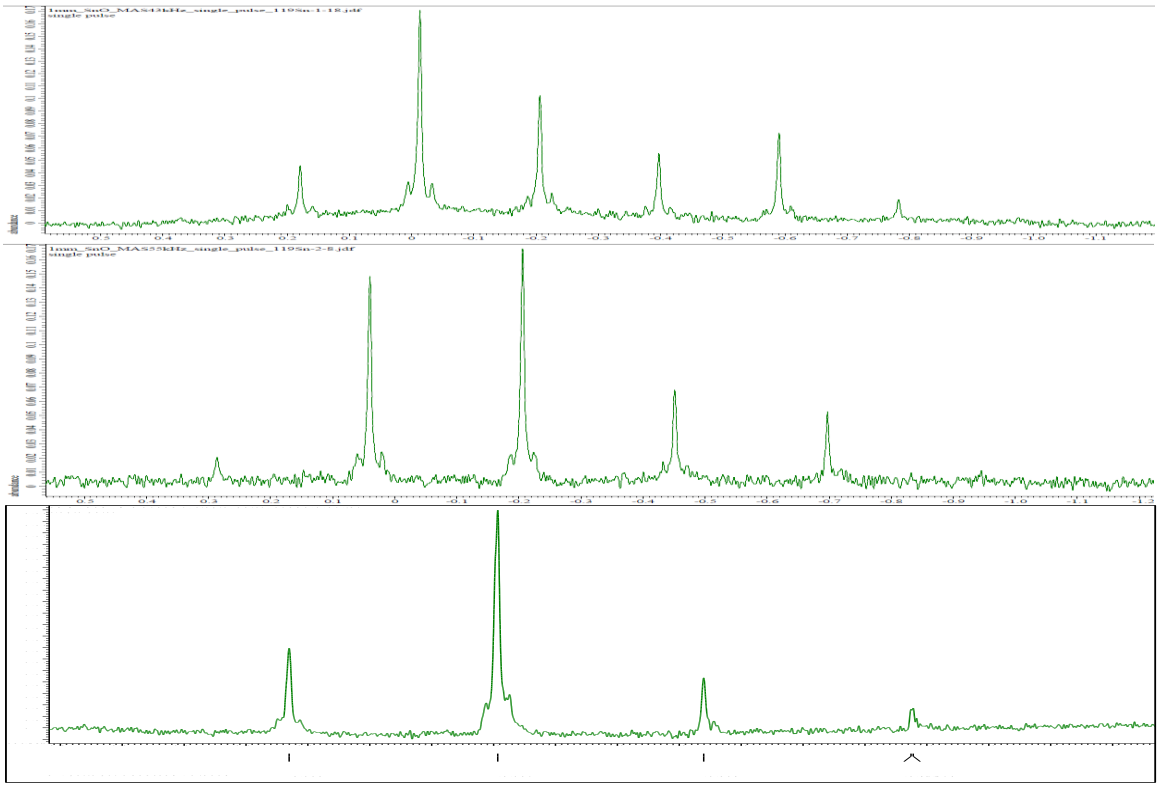

Figure 2: ^{119}Sn spectrum of tin(II) oxide observed at **a)** 43 kHz (40960 scans, total time: 11 hr 37 min) , **b)** 55 kHz (16384 scans, total time: 4 hr 39 min), **c)** 75 kHz (40960 scans, total time: 11 hr 37 min). No baseline correction was applied, however backward linear correction was used (order: 16, sample: 64, reconstruct: 4). LB factor was 200 Hz, offset: -304.1 ppm, sweep: 400 kHz, frequency (^{119}Sn): 223.81 MHz, points: 8192, acquisition time: 20.48 ms, resolution: 48.83 Hz, relaxation delay: 1 s.

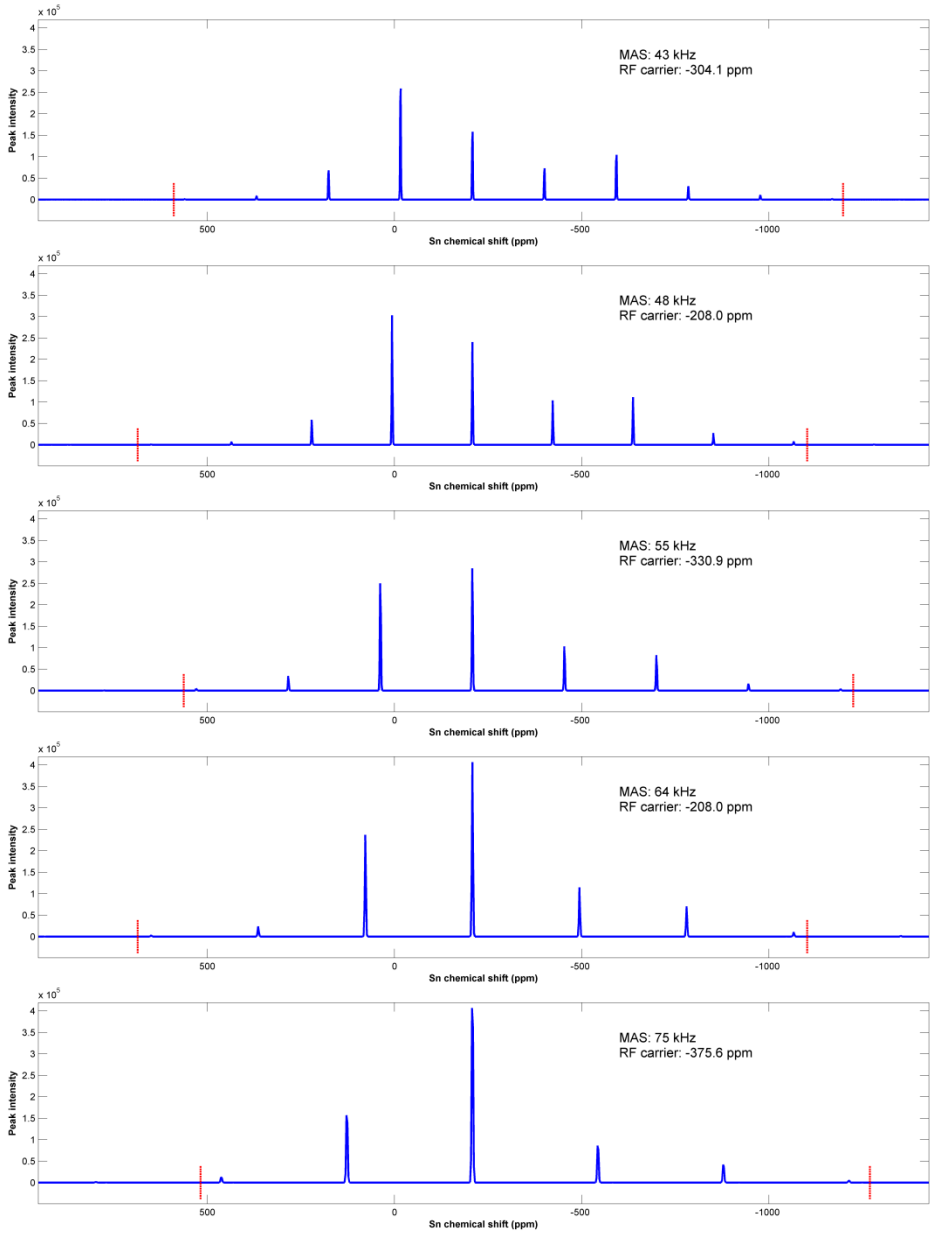

Figure 3: Simulation of the SnO spinning sideband pattern as a function of the MAS rate. The parameters were: $\omega_0^{^{119}Sn} / 2\pi = 223.792$ Hz, $\delta_{11} = \delta_{22} = 117$ ppm, $\delta_{33} = -858$ ppm.

7.5.3. The [(LB)SnCl]$^+$/[SnCl$_3$]$^-$ tin complex

The ZQ CP conditions and low power CW ^{1}H decoupling were used to record all spectra. The ^{1}H T_1 relaxation times of the sample were determined at 43 kHz, 55 kHz,

and 70 kHz. The T_1 relaxation time increases at fast MAS as shown in Table 2. This could be due to slowdown of ^1H-^1H spin diffusion at very fast MAS.

δ (in ppm)	**T_1 (s), 43 kHz MAS**	**T_1 (s), 55 kHz MAS**	**T_1 (s), 70 kHz MAS**
-0.82	1.35	1.45	1.79
0.16	1.41	1.54	1.68
0.73	1.41	1.54	1.70
1.91	1.37	1.55	1.79
4.59	1.34	1.48	1.62
5.90	1.51	1.70	1.91
6.71	1.54	1.79	2.08
8.33	1.48	1.79	2.23

Table 2: Longitudinal ^1H T_1 relaxation values observed by the saturation recovery at 43, 55 and 70 kHz MAS, respectively.

Two center-bands and no B' resonance were observed (Fig. 4) in contrast to the spectra recorded at low temperature and slow MAS (section 6.2.2). A shift of peak positions compared to that observed at 9.4T and moderate MAS rate was also observed. This might be due to B_0 field dependent shifts or temperature dependent shifts. Due to the extremely large anisotropy of the resonance, very fast transverse dephasing of the wideline signals occurs already a few miliseconds after excitation. The dead-time, or delay between excitation and start of digital acquisition thus requires the use of very large values for p_1, the first-order phase correction of the spectrum, in order to obtain all resonances as in-phase peak; otherwise, peaks of the A-site and B-site have different phases or different signs. A slight baseline distortion is introduced by the large p_1 values employed for phasing but this can be corrected by standard baseline correction procedures.

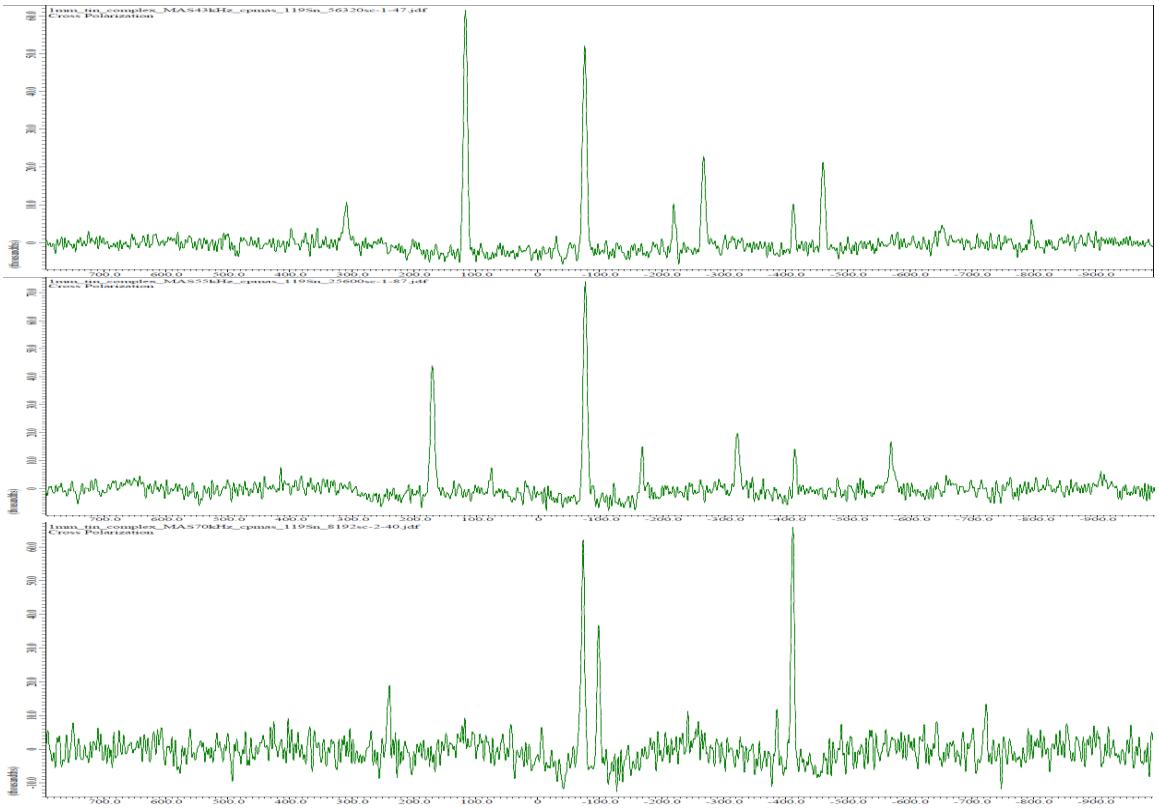

Figure 4: ^{119}Sn spectra of the tin complex observed at **a)** 43 kHz (56320 scans, 1 day 13 hr 56 min), **b)** 55 kHz (25600 scans, 17 hr 57 min), **c)** 70 kHz (8192, 6 hr 12 min). No baseline correction was applied. LB factor was 200 Hz and backward linear prediction was used (16-64-4). Offset: -100.0 ppm, sweep: 400 kHz, frequency (^{119}Sn): 223.81 MHz, points: 8192, acquisition time: 20.48 ms, resolution: 48.83 Hz, contact time: 3.5 ms, relaxation delay: 2.4–2.7 s, low power decoupling (21.3 kHz).

The sample was visually checked before and after measurements: no significant change in color or appearance was observed. The stability of the complex is also supported by ^{1}H MAS spectra recorded at 70 kHz before and after the ^{119}Sn CPMAS experiments (Fig. 5).

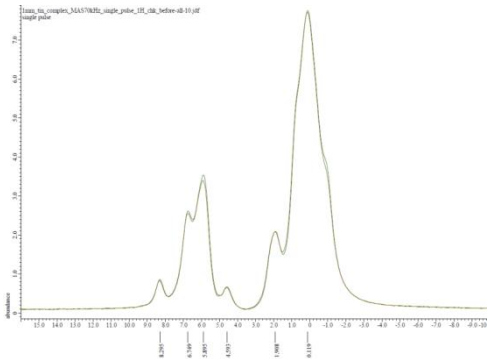

Figure 5: ^{1}H MAS spectra of the tin complex at 70 kHz before (green) and after experiments (brown), respectively.

7.6. Conclusion

Using ultra-fast MAS, it was possible to record simplified spectra of tin-containing compounds where the ^{119}Sn resonances have extremely large chemical shift anisotropies. At MAS frequency of 70 kHz, only few sidebands are present, simplifying the interpretation of spectra. The spectra can be acquired in lower-RF power conditions. When using high-RF power, no major change was observed in the spectra, indicating the small contribution of irradiation heating, consistent with high quality factor of the RF coil due to the small diameter of the coil. This new method could have several advantages for the study of complex mixtures containing heavy spin-½ nuclei.

7.7. References

1. Reuter, H., Sebald, A. On the Hydrolysis of Monoorganotin Trihalides .5. Solid-State Sn-119-NMR and IR-Spectra of the [(I-PrSn)12O14(OH)6]2+ Ion. *Zeitschrift Fur Naturforschung Section B-a Journal of Chemical Sciences* **48**, 195-8 (1993).
2. Eychenne-Baron, C., Ribot, F., Steunou, N., Sanchez, C., Fayon, F., Biesemans, M., Martins, J. C., Willem, R. Reaction of butyltin hydroxide oxide with p-toluenesulfonic acid: Synthesis, X-ray crystal analysis, and multinuclear NMR characterization of {(BuSn)(12)O-14(OH)(6)}(4-CH3C6H4SO3)(2). *Organometallics* **19**, 1940-9 (2000).
3. Smith, S. A., Levante, T. O., Meier, B. H., Ernst, R. R. Computer Simulations in Magnetic Resonance. An Object-Oriented Programming Approach. *Journal of Magnetic Resonance Series A* **106**, 75-105 (1994).
4. Lange, A., Scholz, I., Manolikas, T., Ernst, M., Meier, B. H. Low-power cross polarization in fast magic-angle spinning NMR experiments. *Chemical Physics Letters* **468**, 100-5 (2009).

Part IV: Structural determination of Type-Three Secretion System needles

8. Introduction to bacterial Type-Three Secretion

In this Chapter, the main bacterial protein secretion systems are briefly presented, as well as general characteristics of bacterial invasion and the steps of invasion in *Shigella* bacterial species. The structure and components of the Type-Three Secretion System (T3SS) are subsequently introduced.

8.1. Protein Secretion Systems in Gram-negative bacteria

Secretion of protein to the cell surface and out of the cell is essential to the proliferation of bacteria[1]. The proteins secreted can form surface organelles related to important cellular functions such as flagella (cell mobility), pili or fimbriae (cell adhesion), conjugation pili (transmission of genetic material), or be translocated directly to a target cell (bacterial invasion).

Six major protein secretion systems have been found in gram-negative bacteria[2,3]:

Name	Components	Secreted proteins
T1SS	- HlyB: is an ATP binding cassette transporter (ABC transporter) or a proton antiporter; - HlyD: Adaptor protein bridging the inner membrane and outer membrane; - TolC: Outer membrane pore component.	- Cytotoxins in the RTX (repeats-in-toxin) family; - Proteases, lipases, microcins, adhesins and colicins.
T2SS	-Approximately 16 proteins are required for full export; -The first translocation through the inner membrane takes place using the Sec translocon or the Tat pathway within the periplasm; -The effector protein is then pushed by	- Effector protein such as lipase, elastase, cellulase, alkaline phosphatase, and exotoxin (e.g. cholera toxin).

	a pseudopilus through the outer membrane using the secretin complex by the effect of the GspE ATPase.	
T3SS	- Composed of more than 20 different proteins; - Large supra-molecular structure crossing the bacterial cell envelope; - Translocation energy furnished by the Spa47 cytoplasmic ATPase.	- Virulence factors that are exported directly into eukaryotic host cells; - Proteins of the flagellar apparatus.
T4SS	- 12 required proteins (VirB1–VirB11, VirD4); - Translocation pores are present at the inner and outer membrane; - Two ATPases, VirB11 and VirB4, energize the transport; - Substrates are transported along a pilus formed of the VirB2 pilin.	- Transport of virulent proteins and DNA plasmids into eukaryotic cells; - Transport of DNA plasmids from one bacterium to another during conjugation.
T5SS	- Substrates are translocated to the periplasmic space through the Sec pathway; - For auto-transporter, a C-terminal β-barrel domain favors the export of the passenger domain; - In the two-partner system, the TspB protein forms an outer membrane channel and the TspA protein is secreted; - The energy could be provided by extra-cellular folding or the BAM complex could be involved.	- Substrates include auto-transporter proteins which act as toxins, proteases or other enzymes; - Other substrates are large virulence proteins which are transported through the two-partner system.
T6SS	-The recently discovered apparatus comprises ~12–20 gene products forming two complexes: - VipA/B form a dynamic bacteriophage T4 tube-like structure; - Hcp forms a smaller tubular structure which is membrane-associated and spans the periplasm and cell envelope; - The ClpV ATPase has been identified as a potential source of energy for transport.	- VgrG-like proteins, including RTX toxins; - Other effectors have been identified but not studied in detail.

The translocation is carried out in one step for T1SS, T3SS, T4SS and T6SS but an intermediate periplasmic transport step occurs for T2SS and T5SS. In T3SS, T4SS and T6SS, the substrates can be directly injected into the target cells in a contact-dependent manner[2].

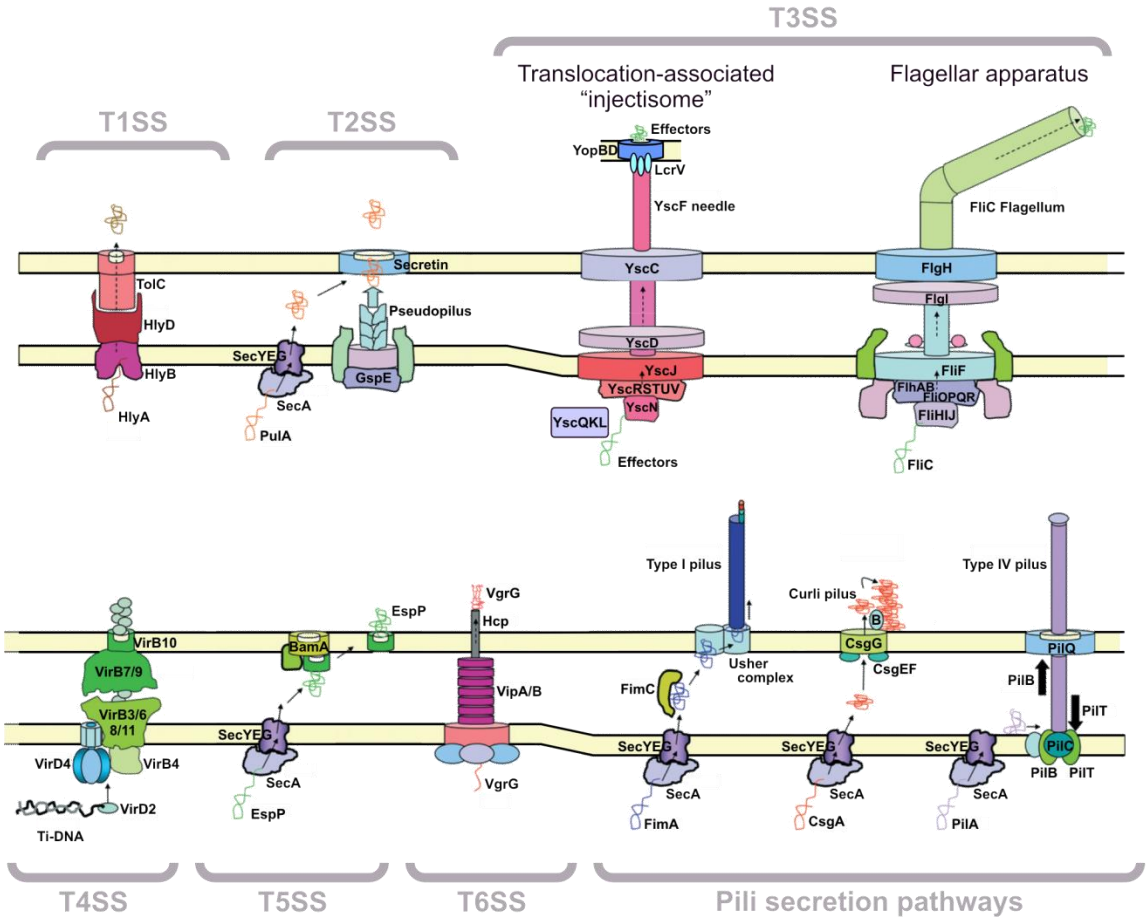

Figure 1: Major bacterial secretion systems. Adapted from Dalbey *et al*[2].

8.2. Bacterial invasion

8.2.1. Bacteria possessing the T3SS and associated diseases

T3SS are found in animal and plant pathogens [4]. Human pathologies involving type-three secretion include bacillary dysentery (*Shigella*), intestinal inflammations and

diarrhea (Salmonella, *Escherichia, Aeromonas*), melioidosis (*Burkholderia*), the plague (*Yersinia*), cholera (*Vibrio*) and pneumonia (*Pseudomonas*) [5]. Shigellosis, the pathology associated with *Shigella* infections, is responsible for 165 million infections and 1.5 million deaths annually [6-8].

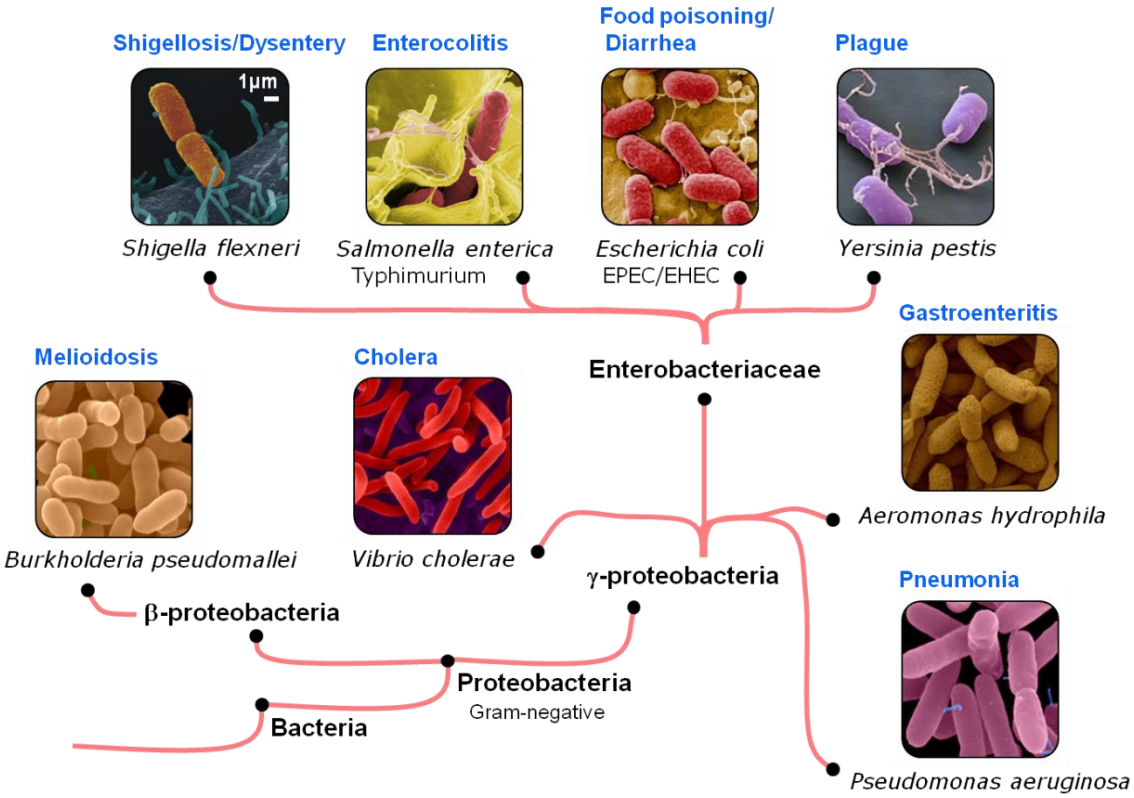

Figure 2. Some bacteria possessing T3SS needles. All bacteria possessing T3SS needles are all part of the Proteobacteria phylum. An abridged taxonomic tree is shown in red, with representative bacteria species presented in scanning electron micrographs. Most common human diseases are indicated in blue.

8.2.2. Progression of bacterial infection in *Shigella* spp.

The Type Three Secretion System (T3SS) is a secretion machinery used by Gram-negative bacteria to deliver virulence factors into eukaryotic host cells [9,10]. Upon contact, translocator proteins form a pore through which effector proteins enter and subsequently alter host cell processes during infection [8,11].

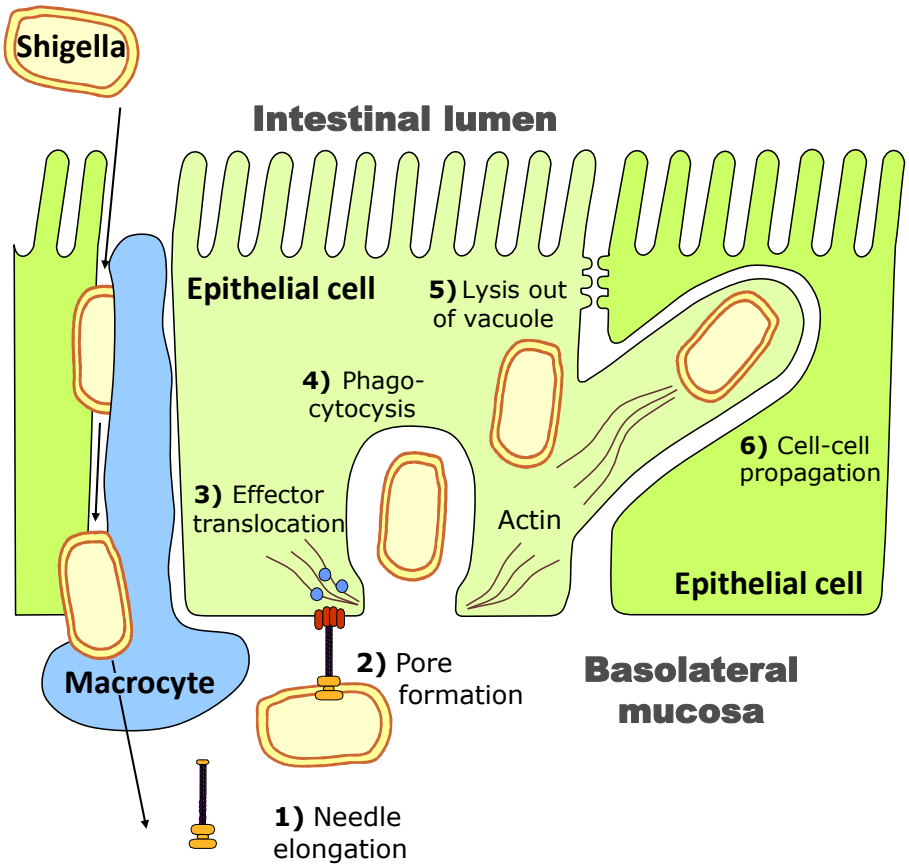

Figure 3. Time-course of *Shigella* bacterial invasion, adapted from Parsot *et al*.[12]

8.3. Structure and components of the Type Three Secretion System

8.3.1. Definition of Type Three Secretion Systems (T3SSs)

The appellation Type Three Secretion System was introduced[13] following the discovery of a new secretory pathway in the animal pathogen *Yersinia enterocolitica*[14] and in the plant pathogen *Pseudomonas solanacearum*[15].

The Type Three Secretion System, abbreviated T3SS[16], has been defined as a protein supra-molecular assembly found in Gram-negative bacteria which spans the inner membrane, periplasmic space and outer membrane forming a continuous protected channel serving to export proteins out of the cell, with an hollow filamentous

appendage extending from the outer membrane. A defining feature of T3SSs is that they secrete independently of the Sec machinery but require a conserved ATPase protein for secretion. T3SSs are divided into two sub-classes: i) flagellar apparatus and ii) translocation-associated T3SS, also called injectisome (or secreton in older literature). Among the proteins forming the T3SS, eight are part of highly-conserved families with homologs in both the flagellar apparatus and injectisome[17]. Additionally, the translocation-associated T3SSs contain a protein part of the highly-conserved secretin family, also present in T2SSs[13].

The Gram-positive flagellar export apparatus show sequence conservation to the flagellar apparatus found in Gram-negative bacteria[16] but is not considered a T3SS.

The molecular components of the T3SS assemble to form two main structures: i) the basal body, anchored in both the inner and outer membrane and spanning the periplasmic space of the bacterium, and ii) a hollow extracellular organelle: either the flagellum or the needle filament. Translocation-associated T3SSs also have a tip complex at the end of the needle filament and assemble a translocon pore upon contact with a target eukaryotic cell. Multiple proteins are present at the entry of the secretion channel in the bacterial cytoplasm, notably proteins forming a sorting platform for T3S substrates and an ATPase providing the energy necessary for secretion.

When considering the full assembly including accessory proteins, the T3SS contains 20-25 different proteins[18] with most proteins present in multiple copies (Table 1). Approximately 15 of those proteins have a structural role while the others are regulatory and can be present at various locations during the various stages of bacterial invasion.

Loc.	Function	Amino acids	*Shigella*	*Salmonella*	*Escherichia*	*Yersinia*	Flagellum
HM	Translocon	580	IpaB	SipB	EspD	YopB	-
	Translocon	363	IpaC	SipC	EspB	YopD	-
EC	Needle tip	332	IpaD	SipD	(EspA)	LcrV	-
	Needle filament	83	MxiH	PrgI	EscF	YscF	(FliC)
OM/peri.	Secretin; OM ring	566	MxiD	InvG	EscC	YscC	-
	Pilotin; secretin insertion	142	MxiM	InvH	-	YscW	-
IM	Inner rod protein	97	MxiI	PrgJ	EscI	YscI	-
	Smaller IM protein	241	MxiJ	PrgK	EscJ	YscJ	FliF
	Larger IM protein	371	MxiG	PrgH	EscD	YscD	FliG
	Export apparatus	216	Spa24	SpaP	EscR	YscR	FliP
	Export apparatus	256	Spa29	SpaR	EscT	YscT	FliR
	Export apparatus; substrate switching	342	Spa40	SpaS	EscU	YscU	FlhB
	Export apparatus	686	MxiA	InvA	EscV	YscV	FlhA
	Export apparatus	86	Spa9	SpaQ	EscS	YscS	FliQ
cyto.	ATPase	430	Spa47	InvC	EscN	YscN	FliI
	Sorting platform	293	Spa33	SpaO	EscQ	YscQ	FliMN
	Sorting platform	172	MxiK	OrgA	Orf4	YscK	-
	Sorting platform	226	MxiN	OrgB	EscL	YscL	FliH
Various	Chaperone	112	Spa13	InvI	-	YscO	FliJ
	Gatekeeper	355	MxiC	InvE	SepL	YopN	-
	Ruler protein	292	Spa32	InvJ	Orf16	YscP	(FliK)
	?	135	MxiL	OrgC	-	-	-
	Chaperone	580	IpgC	SicA	-	-	CesD

Table 1: Protein naming convention in common bacterial pathogens.
Highly conserved protein families are highlighted in yellow[9]. Proteins with no sequence homology but similar biological function are noted in parenthesis.
The number of amino acids is indicated for *Shigella flexneri* serotype X[18].
Location (Loc.): HM, Host cell Membrane; EC, Extracellular; OM/peri., Outer bacterial Membrane/periplasm; IM, Inner bacterial Membrane; cyto., cytoplasm

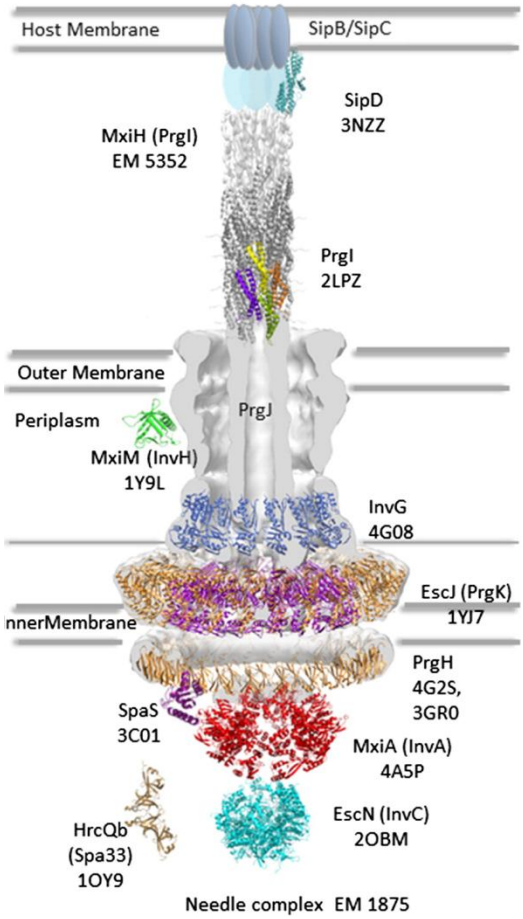

Figure 4. Structural components of the T3SS, from Strynadka *et al*[19].

8.3.2. Basal structure

The basal structure, sometimes called needle complex (NC) for injectisomes or basal body for the flagellar apparatus, is the main cellular structure of the T3SS with its components forming a channel through the inner bacterial membrane, perisplasmic space and outer membrane. The basal structure was first visualized in electron microscopy images of *Salmonella typhimurium* [20] and its major protein components were identified as the invG (mxiD), prgH (mxiG) and prgK (mxiJ) gene products. The basal structure of *Shigella flexneri*[21] and Enteropathogenic *Escherichia coli*[22] spp. were analyzed,

confirming that the homologous proteins MxiD/EscC, MxiG/EscD and MxiJ/EscJ form the basal structure.

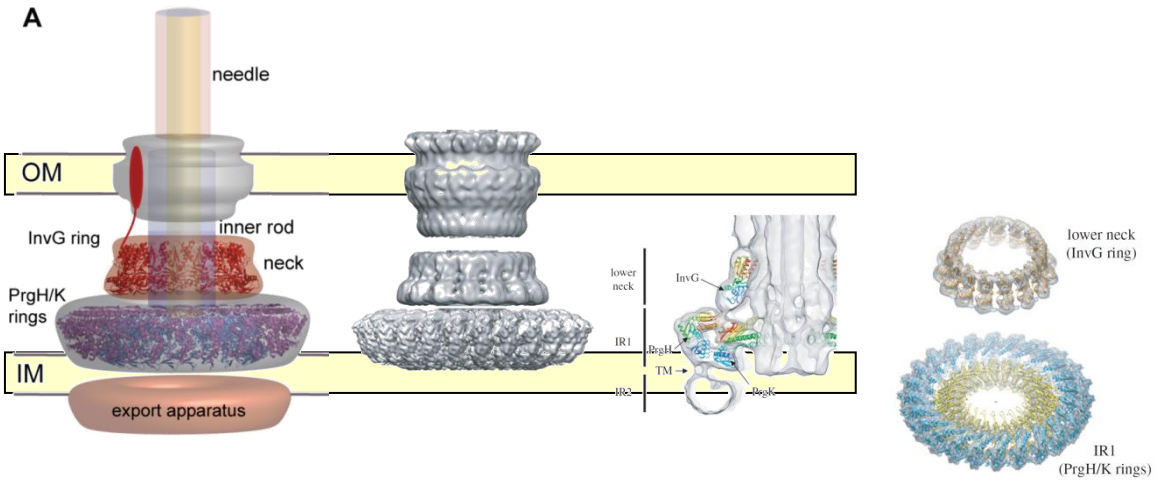

Figure 5: Basal structure of the injectisome, from Marlovits *et al*[18].

The supramolecular structure of NCs was studied on three different types of samples: i) isolated NCs extracted from bacteria[21,23-25], ii) recombinant proteins reconstituted into stable rings of the NC[26], iii) NCs visualized *in situ* in whole bacteria[27].

Electron density maps for isolated NCs were obtained first at low resolution for *Salmonella* (EMD-1100, 17 Å)[24] and *Shigella* (EMD-1617, 17 Å)[21], (21–25 Å)[25], then at high resolution for *Salmonella*(4.7–11.7 Å)[26].

More recently, an electron density map of the NC was obtained *in situ* in Yersinia enterocolitica at 40-Å resolution by cryo-electron tomography (cryo-ET)[27].

Outer membrane ring and periplasmic proteins

The outer membrane ring is formed by the MxiD protein; the OM ring is sub-divided into OM1, OM2, OM3. This protein also forms a ring in the periplasmic space,

the "neck" ring. This family of proteins, called secretins, aids in the structural assembly of the invasion complex [28]. Secretins are also present in T2SS.

The inner rod is formed by the MxiI protein which possesses some homology with the needle protein. On the basis of multiple sequence alignment, it was proposed that the MxiH protein is conserved in a wider variety of species, whereas the MxiI protein is less conserved[21]. However, the C-terminal domain is moderately conserved.

MxiM, a *Shigella* pilot protein also called "pilotin", is essential for the assembly and membrane association of the *Shigella* secretin MxiD. MxiM contains an orthologous secretin component and has a specific binding domain for the acyl chains of bacterial lipids. The C-terminal domain of MxiD hinders lipid binding to MxiM[29].

Inner membrane MS-ring

MxiJ forms the smaller inner membrane ring. MxiJ is also described as a lipoprotein. The flagellar M-ring protein FliF also shares a low level of similarity with the MxiJ family[30].

MxiG forms the outermost part of the inner membrane ring. Its *Salmonella* analog, PrgH, was localized to the base of isolated needles by immuno-electron microscopy[20]. PrgH was shown to be required for secretion[31]. It is also a structural component of the needle complex [24,32].

Inner membrane C-ring

The C ring is constituted of the proteins Spa24, Spa29, Spa40, MxiA, and Spa9.

Spa24 is an homolog of the flagellar FliP protein which is a 30-kDa protein containing three or four transmembrane regions; Spa29 is a membrane-associated

protein which shares homology with the flagellar protein FliR. Spa40 is membrane-associated and involved in the substrate specificity switching of the T3SS. MxiA is integral to membrane and related to the flagellar protein FlhA. Spa9 is a surface antigen-presentation protein; by homology with the fliQ gene product, it is hypothesized to be a small integral membrane protein containing two transmembrane regions[33].

8.3.3. Needle filament

Needle proteins such as MxiH, YscF, EscF, PscF, EprI form the needle of the injectisome and a required for translocation of toxic effector proteins into eukaryotic host cells[34]. The typical needle lengths vary: in *Shigella*, MxiH polymerizes to form up to 50-nm needle[35]; *Salmonella* needles are 80-nm long and 13-nm wide[20]; for EPEC, needles have an average length 93nm and maximal length of 688nm[22].

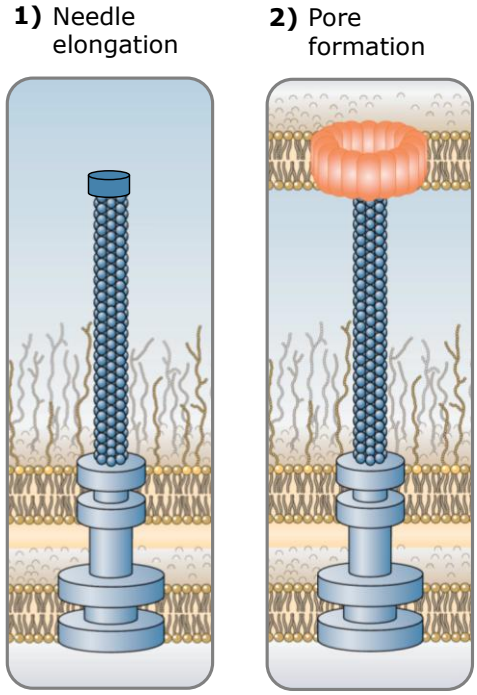

Figure 6: Type-Three Secretion System 1) at early invasion stage and 2) after contact with the host cell. Adapted from Troisfontaines and Cornelis[36].

8.3.4. Needle tip and needle extensions

The IpaB, IpaC, and IpaD proteins form a multi-protein complex which induces the phagocytosis after which the bacterium is internalized by the epithelial cells[37].

IpaD controls the level of secretion of IpaB and IpaC and blocks secretion in the absence of a secretion-inducing signal. Its N-terminus contains an intra-molecular chaperone which sequesters the coil-coil region which normally interacts with needle subunits or other IpaD subunits. The C-terminus is thought to oligomerize at the tip of the needle and regulate the secretion of effectors[38,39].

Another extra-cellular structure only present in *E. coli* is constituted by the EspA protein, which forms a sheath-like structure[22]. This large structure is transiently expressed and forms a bridge between the bacterium and the host cell [40,41].

8.3.5. Translocon

The translocon is a complex which is made of multiple copies of the IpaB and IpaC proteins. Those proteins are delivered to the tip of the needle and form a translocation pore across the eukaryotic membrane through which toxic effector proteins pass to the host cell cytoplasm. In *Salmonella* and *Shigella*, IpaB is required for the internalisation of the bacterium inside the epithelial cell[42]. In addition, IpaB and IpaC not only form the pore but is toxic by itself and is also secreted to the host cytoplasm.

In the cytoplasm, IpaB activates macrophage apoptosis by binding to the ICE enzyme (interleukin-1 beta converting enzyme). Another target of IpaB is the human MAD2L2 protein. When binding to this protein, IpaB activates an anaphase-promoting complex. This induces a cell cycle arrest which prevents the gut epithelium from

regenerating itself by cell division. This arrest allows *Shigella* bacteria to colonize the intestine[43,44].

On the other hand, IpaC can activate some human kinases and promote the uptake of the bacterium[45]. One proposed mechanism, which would involve the C-terminal domain of IpaC, is the activation of the GTPases Cdc42 and Rac of the rho-family; these activations result in the reorganization of actin polymerization.

8.3.6. Cytoplasmic export apparatus

On the bacterial cytosolic side, successful export through the T3SS requires 1) an ATPase, 2) a substrate sorting platform and 3) accessory regulatory proteins.

Sorting platform

The sorting platform comprises the proteins Spa33, MxiK and MxiN. Spa33 is partially homologous to the flagellar FliN protein. MxiK and MxiN interact with the ATPase.

ATPase

The ATPase protein, Spa47 in *Shigella*, contributes the energy necessary to export through the T3SS machinery[46]. Its catalytic activity is:

$$ATP + H_2O + H^+(In) = ADP + phosphate + H^+(Out).$$

However, it is not clear if the energy is directly coupled to a mechanical activity involved in transport or rather part of a proton pump activity[47,48]. Spa47 has extensive homology to the ATP synthase F1 beta subunit.

Other proteins

Spa13 is a T3S chaperone. The *Salmonella* homolog InvI is required for uptake of the bacterium into the host cell[33,49].

MxiC is a regulator of translocation, also called "gatekeeper". The *Salmonella* homolog InvE interacts with the SipB, SipC, SipD and SicA proteins[50]. In Yersinia, the homolog could block the substrates from accessing the T3SS before the extracellular organelle has touched the target cell[51].

Spa32 is a regulator of the needle length[52]. It has been proposed to be a molecular ruler and it is involved in substrate specificity switching[35].

IpgC is a cytoplasmic chaperone protein which ensures the proper folding of IpaB. It also prevents the binding of IpaB to IpaC, as premature formation of that complex in the absence of IpgC leads to its degradation[53]. Once it is bound to IpaB, it binds to IpaC and impedes their premature association that would lead to their degradation in the absence of IpcG.

8.4. References

1. Thanassi, D. G., Bliska, J. B., Christie, P. J. Surface organelles assembled by secretion systems of Gram-negative bacteria: diversity in structure and function. *Fems Microbiology Reviews* **36**, 1046-82 (2012).
2. Dalbey, R. E., Kuhn, A. Protein Traffic in Gram-negative bacteria - how exported and secreted proteins find their way. *Fems Microbiology Reviews* **36**, 1023-45 (2012).
3. Moal, V. L. L., Servin, A. L. Pathogenesis of Human Enterovirulent Bacteria: Lessons from Cultured, Fully Differentiated Human Colon Cancer Cell Lines. *Microbiol Mol Biol Rev* **77**, 380-439 (2013).
4. Nguyen, L., Paulsen, I. T., Tchieu, J., Hueck, C. J., Saier, M. H., Jr. Phylogenetic analyses of the constituents of Type III protein secretion systems. *J Mol Microbiol Biotechnol* **2**, 125-44 (2000).
5. Coburn, B., Sekirov, I., Finlay, B. B. Type III secretion systems and disease. *Clinical Microbiology Reviews* **20**, 535-49 (2007).
6. Kotloff, K. L., Winickoff, J. P., Ivanoff, B., Clemens, J. D., Swerdlow, D. L., Sansonetti, P. J., Adak, G. K., Levine, M. M. Global burden of Shigella infections: implications for vaccine development and implementation of control strategies. *Bulletin of the World Health Organization* **77**, 651-66 (1999).
7. Niyogi, S. K. Shigellosis. *Journal of Microbiology* **43**, 133-43 (2005).

8. Schroeder, G. N., Hilbi, H. Molecular pathogenesis of Shigella spp.: Controlling host cell signaling, invasion, and death by type III secretion. *Clinical Microbiology Reviews* **21**, 134-56 (2008).
9. Cornelis, G. R. The type III secretion injectisome. *Nat Rev Microbiol* **4**, 811-25 (2006).
10. Galán, J. E., Wolf-Watz, H. Protein delivery into eukaryotic cells by type III secretion machines. *Nature* **444**, 567-73 (2006).
11. Ghosh, P. Process of protein transport by the type III secretion system. *Microbiol Mol Biol Rev* **68**, 771-95 (2004).
12. Parsot, C., Sansonetti, P. J. Invasion and the pathogenesis of Shigella infections. *Bacterial Invasiveness* **209**, 25-42 (1996).
13. Salmond, G. P. C., Reeves, P. J. Membrane Traffic Wardens and Protein Secretion in Gram-Negative Bacteria. *Trends in Biochemical Sciences* **18**, 7-12 (1993).
14. Michiels, T., Cornelis, G. R. Secretion of Hybrid Proteins by the Yersinia Yop Export System. *Journal of Bacteriology* **173**, 1677-85 (1991).
15. Gough, C. L., Genin, S., Zischek, C., Boucher, C. A. Hrp Genes of Pseudomonas-Solanacearum are Homologous to Pathogenicity Determinants of Animal Pathogenic Bacteria and are Conserved Among Plant Pathogenic Bacteria. *Molecular Plant-Microbe Interactions* **5**, 384-9 (1992).
16. Desvaux, M., Hebraud, M., Henderson, I. R., Pallen, M. J. Type III secretion: what's in a name? *Trends in microbiology* **14**, 157-60 (2006).
17. Gophna, U., Ron, E. Z., Graur, D. Bacterial type III secretion systems are ancient and evolved by multiple horizontal-transfer events. *Gene* **312**, 151-63 (2003).
18. Kosarewicz, A., Konigsmaier, L., Marlovits, T. C. The blueprint of the type-3 injectisome. *Philosophical Transactions of the Royal Society B-Biological Sciences* **367**, 1140-54 (2012).
19. Burkinshaw, B. J., Strynadka, N. C. J. Assembly and structure of the T3SS. *Biochim. Biophys. Acta* (2014).
20. Kubori, T., Matsushima, Y., Nakamura, D., Uralil, J., Lara-Tejero, M., Sukhan, A., Galan, J. E., Aizawa, S. Supramolecular structure of the Salmonella typhimurium type III protein secretion system. *Science* **280**, 602-5 (1998).
21. Blocker, A., Jouihri, N., Larquet, E., Gounon, P., Ebel, F., Parsot, C., Sansonetti, P., Allaoui, A. Structure and composition of the Shigella flexneri 'needle complex', a part of its type III secreton. *Molecular Microbiology* **39**, 652-63 (2001).
22. Sekiya, K., Ohishi, M., Ogino, T., Tamano, K., Sasakawa, C., Abe, A. Supermolecular structure of the enteropathogenic Escherichia coli type III secretion system and its direct interaction with the EspA-sheath-like structure. *Proceedings of the National Academy of Sciences of the United States of America* **98**, 11638-43 (2001).
23. Marlovits, T. C., Kubori, T., Lara-Tejero, M., Thomas, D., Unger, V. M., Galan, J. E. Assembly of the inner rod determines needle length in the type III secretion injectisome. *Nature* **441**, 637-40 (2006).
24. Marlovits, T. C., Kubori, T., Sukhan, A., Thomas, D. R., Galan, J. E., Unger, V. M. Structural insights into the assembly of the type III secretion needle complex. *Science* **306**, 1040-2 (2004).
25. Hodgkinson, J. L., Horsley, A., Stabat, D., Simon, M., Johnson, S., da Fonseca, P. C. A., Morris, E. P., Wall, J. S., Lea, S. M., Blocker, A. J. Three-dimensional reconstruction of the Shigella T3SS transmembrane regions reveals 12-fold symmetry and novel features throughout. *Nature Structural & Molecular Biology* **16**, 477-85 (2009).
26. Schraidt, O., Marlovits, T. C. Three-dimensional model of Salmonella's needle complex at subnanometer resolution. *Science* **331**, 1192-5 (2011).
27. Kudryashev, M., Stenta, M., Schmelz, S., Amstutz, M., Wiesand, U., Castano-Diez, D., Degiacomi, M. T., Munnich, S., Bleck, C. K., Kowal, J., Diepold, A., Heinz, D. W., Dal Peraro, M., Cornelis, G. R., Stahlberg, H. In situ structural analysis of the Yersinia enterocolitica injectisome. *eLife* **2**, e00792-e (2013).
28. Galan, J. E. Molecular genetic bases of Salmonella entry into host cells. *Molecular Microbiology* **20**, 263-71 (1996).

29. Lario, P. I., Pfuetzner, R. A., Frey, E. A., Creagh, L., Haynes, C., Maurelli, A. T., Strynadka, N. C. Structure and biochemical analysis of a secretin pilot protein. *EMBO journal* **24**, 1111-21 (2005).
30. Yip, C. K., Kimbrough, T. G., Felise, H. B., Vuckovic, M., Thomas, N. A., Pfuetzner, R. A., Frey, E. A., Finlay, B. B., Miller, S. I., Strynadka, N. C. Structural characterization of the molecular platform for type III secretion system assembly. *Nature* **435**, 702-7 (2005).
31. Pegues, D. A., Hantman, M. J., Behlau, I., Miller, S. I. PhoP/PhoQ transcriptional repression of Salmonella typhimurium invasion genes: evidence for a role in protein secretion. *Molecular Microbiology* **17**, 169-81 (1995).
32. Allaoui, A., Sansonetti, P. J., Menard, R., Barzu, S., Mounier, J., Phalipon, A., Parsot, C. MxiG, a membrane protein required for secretion of Shigella spp. Ipa invasins: involvement in entry into epithelial cells and in intercellular dissemination. *Molecular Microbiology* **17**, 461-70 (1995).
33. Groisman, E. A., Ochman, H. Cognate gene clusters govern invasion of host epithelial cells by Salmonella typhimurium and Shigella flexneri. *EMBO journal* **12**, 3779-87 (1993).
34. Deane, J. E., Roversi, P., Cordes, F. S., Johnson, S., Kenjale, R., Daniell, S., Booy, F., Picking, W. D., Picking, W. L., Blocker, A. J., Lea, S. M. Molecular model of a type III secretion system needle: Implications for host-cell sensing. *Proceedings of the National Academy of Sciences of the United States of America* **103**, 12529-33 (2006).
35. Magdalena, J., Hachani, A., Chamekh, M., Jouihri, N., Gounon, P., Blocker, A., Allaoui, A. Spa32 regulates a switch in substrate specificity of the type III secreton of Shigella flexneri from needle components to Ipa proteins. *Journal of Bacteriology* **184**, 3433-41 (2002).
36. Troisfontaines, P., Cornelis, G. R. Type III secretion: More systems than you think. *Physiology* **20**, 326-39 (2005).
37. Turbyfill, K. R., Hartman, A. B., Oaks, E. V. Isolation and characterization of a Shigella flexneri invasin complex subunit vaccine. *Infection and immunity* **68**, 6624-32 (2000).
38. Menard, R., Sansonetti, P., Parsot, C. The Secretion of the Shigella-flexneri Ipa Invasins is Activated by Epithelial-Cells and Controlled by IpaB and IpaD. *EMBO journal* **13**, 5293-302 (1994).
39. Picking, W. L., Nishioka, H., Hearn, P. D., Baxter, M. A., Harrington, A. T., Blocker, A., Picking, W. D. IpaD of Shigella flexneri is independently required for regulation of Ipa protein secretion and efficient insertion of IpaB and IpaC into host membranes. *Infection and immunity* **73**, 1432-40 (2005).
40. Knutton, S., Rosenshine, I., Pallen, M. J., Nisan, I., Neves, B. C., Bain, C., Wolff, C., Dougan, G., Frankel, G. A novel EspA-associated surface organelle of enteropathogenic Escherichia coli involved in protein translocation into epithelial cells. *EMBO journal* **17**, 2166-76 (1998).
41. Hartland, E. L., Daniell, S. J., Delahay, R. M., Neves, B. C., Wallis, T., Shaw, R. K., Hale, C., Knutton, S., Frankel, G. The type III protein translocation system of enteropathogenic Escherichia coli involves EspA-EspB protein interactions. *Molecular Microbiology* **35**, 1483-92 (2000).
42. Kaniga, K., Tucker, S., Trollinger, D., Galan, J. E. Homologs of the Shigella IpaB and IpaC invasins are required for Salmonella typhimurium entry into cultured epithelial cells. *Journal of Bacteriology* **177**, 3965-71 (1995).
43. Thirumalai, K., Kim, K. S., Zychlinsky, A. IpaB, a Shigella flexneri invasin, colocalizes with interleukin-1 beta-converting enzyme in the cytoplasm of macrophages. *Infection and immunity* **65**, 787-93 (1997).
44. Iwai, H., Kim, M., Yoshikawa, Y., Ashida, H., Ogawa, M., Fujita, Y., Muller, D., Kirikae, T., Jackson, P. K., Kotani, S., Sasakawa, C. A bacterial effector targets Mad2L2, an APC inhibitor, to modulate host cell cycling. *Cell* **130**, 611-23 (2007).
45. Carlson, S. A., Jones, B. D. Inhibition of Salmonella typhimurium invasion by host cell expression of secreted bacterial invasion proteins. *Infection and immunity* **66**, 5295-300 (1998).
46. Woestyn, S., Allaoui, A., Wattiau, P., Cornelis, G. R. YscN, the putative energizer of the Yersinia Yop secretion machinery. *Journal of Bacteriology* **176**, 1561-9 (1994).
47. Dreyfus, G., Williams, A. W., Kawagishi, I., Macnab, R. M. Genetic and biochemical analysis of Salmonella typhimurium FliI, a flagellar protein related to the catalytic subunit of the F0F1 ATPase and to virulence proteins of mammalian and plant pathogens. *Journal of Bacteriology* **175**, 3131-8 (1993).

48. Fenselau, S., Bonas, U. Sequence and expression analysis of the hrpB pathogenicity operon of Xanthomonas campestris pv. vesicatoria which encodes eight proteins with similarity to components of the Hrp, Ysc, Spa, and Fli secretion systems. *Mol Plant Microbe Interact* **8**, 845-54 (1995).
49. Boyd, E. F., Li, J., Ochman, H., Selander, R. K. Comparative genetics of the inv-spa invasion gene complex of Salmonella enterica. *Journal of Bacteriology* **179**, 1985-91 (1997).
50. Kubori, T., Galan, J. E. Salmonella type III secretion-associated protein InvE controls translocation of effector proteins into host cells. *Journal of Bacteriology* **184**, 4699-708 (2002).
51. Schubot, F. D., Jackson, M. W., Penrose, K. J., Cherry, S., Tropea, J. E., Plano, G. V., Waugh, D. S. Three-dimensional structure of a macromolecular assembly that regulates type III secretion in Yersinia pestis. *Journal of molecular biology* **346**, 1147-61 (2005).
52. Tamano, K., Katayama, E., Toyotome, T., Sasakawa, C. Shigella Spa32 is an essential secretory protein for functional type III secretion machinery and uniformity of its needle length. *Journal of Bacteriology* **184**, 1244-52 (2002).
53. Menard, R., Sansonetti, P., Parsot, C., Vasselon, T. Extracellular association and cytoplasmic partitioning of the IpaB and IpaC invasins of S. flexneri. *Cell* **79**, 515-25 (1994).

9. The Common Structural Architecture of *Shigella flexneri* and *Salmonella typhimurium* Type Three Secretion Needles

9.1. Summary

The Type Three Secretion System (T3SS), or injectisome, is a macromolecular infection machinery present in many pathogenic Gram-negative bacteria. It consists of a basal body, anchored in both bacterial membranes, and a hollow needle through which effector proteins are delivered into the target host cell. Two different architectures of the T3SS needle have been previously proposed. First, an atomic model of the *Salmonella typhimurium* needle was generated from solid-state NMR data. The needle subunit protein, PrgI, comprises a rigid-extended N-terminal segment and a helix-loop-helix motif with the N-terminus located on the outside face of the needle. Second, a model of the *Shigella flexneri* needle was generated from a high-resolution 7.7-Å cryo-electron microscopy density map. The subunit protein, MxiH, contains an N-terminal α-helix, a loop, another α-helix, a 14-residue-long β-hairpin (Q51-Q64) and a C-terminal α-helix, with the N-terminus facing inward to the lumen of the needle. In the current study, we carried out solid-state NMR measurements of wild-type *Shigella flexneri* needles polymerized *in vitro* and identified the following secondary structure elements for MxiH: a rigid-extended N-terminal segment (S2-T11), an α-helix (L12-A38), a loop (E39-P44) and a C-terminal α-helix (Q45-R83). Using immunogold labeling *in vitro* and *in vivo* on functional needles, we located the N-terminus of MxiH subunits on the exterior of the assembly, consistent with evolutionary sequence conservation patterns and mutagenesis data. We generated a homology model of *Shigella flexneri* needles compatible with both experimental data: the MxiH solid-state NMR chemical shifts and the state-of-the-art cryoEM density map. These results corroborate the solid-state NMR structure previously solved for *Salmonella typhimurium* PrgI needles and establish that *Shigella flexneri* and *Salmonella typhimurium* subunit proteins adopt a conserved structure and

orientation in their assembled state. Our study reveals a common structural architecture of T3SS needles, essential to understand T3SS-mediated infection and develop treatments.

Contribution statement

The results of the current chapter are contained in the following publication:

"The Common Structural Architecture of Shigella flexneri and Salmonella typhimurium Type Three Secretion Needles", *Demers, Jean-Philippe, Nikolaos G. Sgourakis, Rashmi Gupta, Antoine Loquet, Karin Giller, Dietmar Riedel, Britta Laube, Michael Kolbe, David Baker, Stefan Becker, Adam Lange*, **PLOS Pathogens**, vol. 9(3), e1003245

K.G. and S.B. expressed, purified and polymerized in vitro T3SS needles. J.P.D. performed solid-state NMR experiments. J.P.D., A. Loquet and A. Lange analyzed solid-state NMR data. N.G.S and D.B. performed modeling studies. D.R., R.G. and M.K. performed electron microscopy studies. R.G. and M.K. performed and analyzed secretion assays. J. P.D. carried out the multiple sequence alignment.

9.2. Background and Motivation

Earlier studies of *Shigella flexneri* T3SS needles by X-ray fiber diffraction and cryo-electron microscopy (cryoEM) showed that the MxiH subunits are disposed in a helical arrangement, with 5.6 subunits per turn and a 24-Å helical pitch [1]. The atomic structures of C-terminal truncation mutants, resulting in non-functional soluble needle subunits, were determined for BsaL$^{C\Delta5}$ by solution-state NMR [2], MxiH$^{C\Delta5}$ by X-ray crystallography [3], and PrgI$^{C\Delta5}$ by solution-state NMR [4]. All three structures exhibit two α-helical segments separated by a loop at the P-(S/D)-(D/N)-P motif.

In order to gain further insight into the function of Type Three Secretion Systems, it is necessary to obtain an atomic structure of wild-type (WT) needles in their assembled state. The pseudoatomic T3SS needle architecture of *Shigella* was modeled by Deane and

coworkers [3] by docking semi-rigid MxiH$^{C\Delta 5}$ crystal monomers into a 16-Å cryoEM density map [1], with a topology where the N-terminus of the MxiH subunit is facing the inside of the tubular structure. More recently, a refined model of the *Shigella* MxiH needle was presented by Fujii and coworkers [5] based on a 7.7-Å cryo-electron microscopy (cryoEM) map. In this model (Fig. 1*A*), the segment ranging from Q51 to Q64, observed as α-helical in the X-ray structure [3], was remodeled as a β-hairpin structure during the molecular docking, while preserving the inwards-facing N-terminus. We have recently presented an atomic model of the *Salmonella typhimurium* T3SS needle [6] based on solid-state NMR distance restraints collected directly on assembled needles and symmetry from scanning transmission electron microscopy (STEM) data [7]. In this atomic model (Fig. 1*B*), the N-terminus of the subunit is located at the surface of the needle, as confirmed by immunogold labeling experiments performed both *in vitro* and *in vivo* [6].

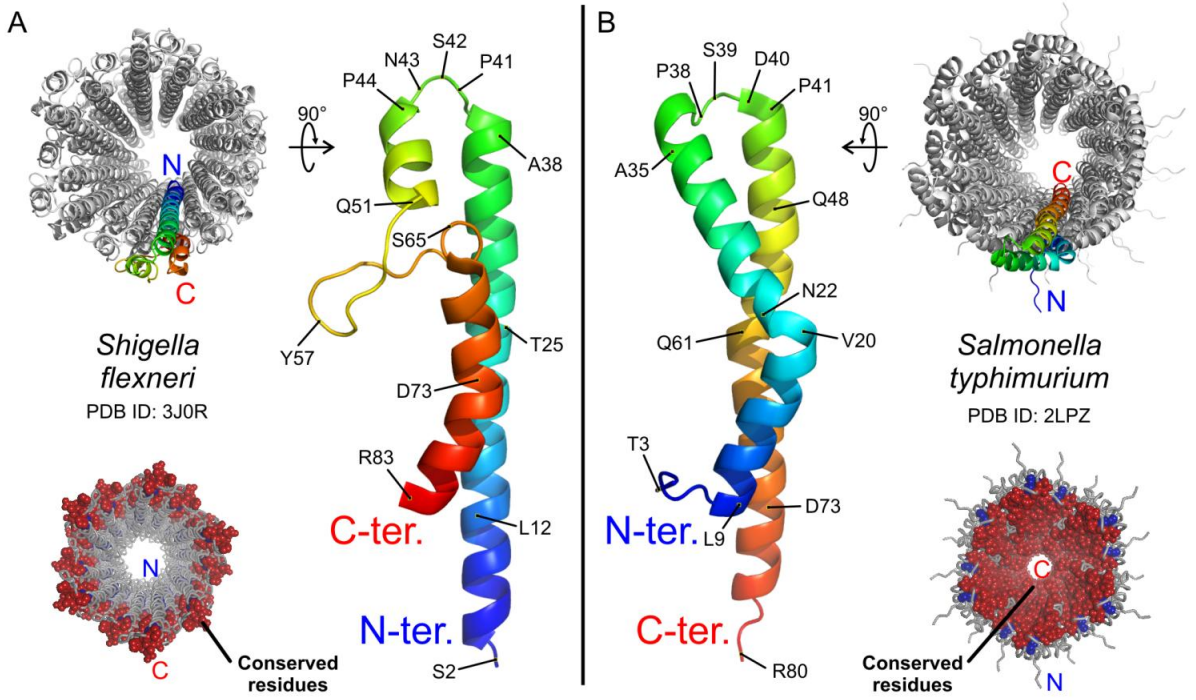

Figure 1: Proposed topologies for T3SS needle proteins in the needle assembly. *A,* Model of *Shigella flexneri* T3SS needle based on a 7.7-Å cryoEM map, according to Ref. [5], PDB ID: 3J0R. The structure of the MxiH subunit protein contains an α-helix (S2-A38), a loop (K39-P44), an α-helix (Q45-Y50), a 14-residue-long β-hairpin (Q51-Q64) and an α-helix (S65-R83) with a kink at D73. The N-terminus faces inward to the lumen of the needle. *B,* Solid-state NMR atomic model of the *Salmonella typhimurium* T3SS needle according to Ref. [6], PDB ID: 2LPZ. The structure of the PrgI subunit protein comprises a rigid-extended conformation (T3-Y8), an α-helix (L9-A35) with a kink at N22, a loop (A36-P41), and an α-helix (A42-R80). The N-terminus is located at the surface of the needle. Top views of the needle assemblies are shown in the top corners. The structures in the bottom corners present the location of highly conserved residues that were identified from multiple sequence alignment (Fig. 3). The atoms of conserved amino acids are represented as spheres and are colored respectively blue or red depending if their amino acid belongs to the N- or the C-terminal region. Conserved residues are lining the lumen of the needle in the *Salmonella* model but are exposed to the extracellular milieu in the *Shigella* model.

Although the two proposed models show fundamental differences in their topology, MxiH and PrgI present a high sequence identity (>60%, Fig. 3). From these two models, strong experimental predictions regarding the orientation of termini and

the secondary structure present in *S. flexneri* T3SS needles can be made and experimentally verified. In the current study, we thus present solid-state NMR data and immunogold labeling results obtained on WT needles of *S. flexneri* which allow us to address the discrepancy between the two models and establish the common architecture of T3SS needles.

9.3. Hypotheses and Method Summary

Hypotheses:

The topology proposed for *Salmonella* needles (Loquet et al.) is conserved in *Shigella flexneri* T3SS needles.

The secondary structure elements identified in *Salmonella* – a rigid-extended N-terminal segment, an α-helix, a loop and a C-terminal α-helix – can be found in *Shigella*.

The N-terminus of *Shigella* needle subunits is located on the outside surface of the assembly and the C-terminus is found facing the inside luminal surface.

The high-resolution cryoEM density map is compatible with the topology proposed for *Salmonella typhimurium* needles.

There is a common architecture for all T3SS needles, which is reflected in the organization of the amino acid sequences for needle subunit proteins.

Method summary:

In order to determine the secondary structure, we determined the solid-state NMR assignment of *in vitro* polymerized needles.

To determine the subunit orientation, we carried out immuno-gold labeling on *in vitro* polymerized needles and on *in vivo* bacterial strains.

To assess whether with all experimental data, cryoEM and ssNMR, could be explained by a single structural model, we constructed a homology model of the *Shigella* needle following the topology of the *Salmonella* needle.

To determine if there is a common T3SS needle architecture, we constructed a multiple sequence alignment of primary sequences among bacterial types.

9.4. Materials and Methods

9.4.1. *In vitro* needle polymerization

MxiH was expressed and purified following the protocol established for *S. typhimurium* PrgI needles [6]. Similarly, the N-terminal hepta-Histidine (His) tag was cleaved using tobacco etch virus protease, releasing MxiH proteins containing the non-native N-terminal residues glycine and histidine. The protein concentration was raised to 0.2 mM during polymerization, which took place at 37 °C for sixteen days. Approximately 20 mg of needle proteins were produced for each sample. MxiH needles were ultra-centrifuged and transferred into 4.0-mm magic-angle spinning rotors.

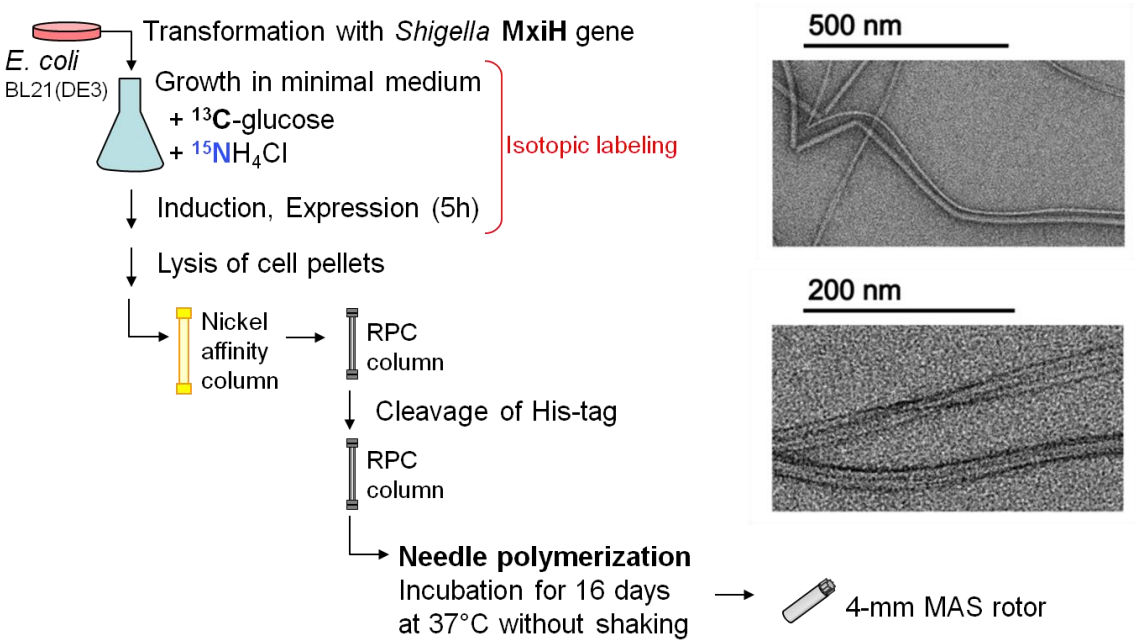

Figure 2: *In vitro* polymerization of MxiH needles. (Left) Sketch of the protein expression and purification protocol. (Right) Electron micrograph of *in vitro* polymerized MxiH needles.

9.4.2. Isotopic labelling

Three isotopic labeling schemes were employed. All three samples were labeled with $^{15}NH_4Cl$ as nitrogen source and either D-[uniform-$^{13}C_6$]glucose ([U-$^{13}C_6$]Glc), D-[1-^{13}C]glucose or D-[2-^{13}C]glucose as carbon source.

9.4.3. Solid-state NMR

Solid-state NMR experiments were conducted at 600 MHz, 800 MHz and 850 MHz ^{1}H frequencies on Avance I and Avance III spectrometers (Bruker Biospin, Germany) at a spinning rate of 11 kHz and a temperature of 5.5 °C.

A ramped cross-polarization with contact time of 0.7-1.2 ms was used for the initial ^{1}H-^{13}C and ^{1}H-^{15}N transfers. For ^{13}C-^{13}C correlation experiments, carbon-carbon mixing was accomplished via proton-driven spin diffusion (PDSD) [8] with the indicated mixing times. Additionally, double quantum-single quantum correlation spectra were measured using the SPC5 sequence[9]. For ^{15}N-^{13}C correlation experiments, nitrogen-carbon transfer was carried out through n=1 double-quantum SPECIFIC-CP[10] with r.f. fields of 6.5 kHz on ^{13}C and 4.5 kHz on ^{15}N using a tangential ramp during 8.5 ms and 83.3 kHz of *cw* decoupling on ^{1}H. Transfers were carried out in a band-selective fashion except for the N-CX experiment where broadband Hartman-Hahn matching was employed. In N-CA-CX and N-CO-CX experiments, a second transfer step to further carbon nuclei was carried out using DARR[11] for 70 ms. Proton decoupling with an r.f. frequency of 83.3 kHz was employed during evolution periods and acquisition, using either SPINAL-64[12] or SWf-TPPM[13] with a $\mathrm{R\bar{R}\bar{R}R}$ supercycle[14] and a tangential sweep[15] (N = 11, sweep window d = 0.25, cut-off angle tco = 55°, phase angle θ = 15°). Carbon-nitrogen scalar couplings were removed by applying c.a. 2 kHz of waltz-16[16] decoupling on ^{15}N during acquisition and ^{13}C evolution periods, or with a 180° pulse on ^{13}C during

^{15}N evolution. The sample temperature was maintained at 5.5°C as determined from the ^{1}H chemical shift of water in reference to DSS[17].

Additional experimental details can be found in supplementary Table <9.2>. For the calculation of secondary chemical shifts (Δδ), average random coil chemical shifts were taken from Ref. [18].

9.4.4. Immunolabelling

Recombinantly-produced MxiH needles were labeled using an Anti-penta-Histidine tag monoclonal antibody (Invitrogen). The labeling was performed using a 1:200 diluted antibody and 10-nm protein A Gold (Posthuma, Utrecht). Non-polar *Shigella mxiH*-knockout cells (*ΔmxiH*) were complemented with either wild-type *mxiH*, *mxiH* with N-terminal Strep-tag or *mxiH* with a C-terminal Strep-tag in pASK-IBA vectors (IBA lifesciences) and induced with 0.2 µg/ml anhydrotetracycline for 1 hr. The cells were fixed in 2 % paraformaldehyde and immunogold labeled using 1:40 diluted StrepMAB-Classic (IBA lifesciences) for 1 hr followed by 1:40 diluted 12-nm gold-conjugated secondary antibody for 1 hr. Protein secretion assays were performed by addition of 20 µg/ml CR followed by western blot analysis against IpaB, IpaC and DnaK.

9.4.5. Multiple sequence alignment

Sequences of commonly studied T3SS needle proteins were aligned using Clustal W version 2 [19] with default settings and the GONNET substitution matrix [20]. A first round of alignment revealed two clusters of highly conserved patterns in the loop and C-terminal region with the N-terminal regions presenting a higher variability. In a second round, the two sequence clusters were aligned as two separate groups. The

conservation level and consensus sequence for each cluster were calculated using JalView [21]. Uniprot accession identifiers for the primary sequences are specified in supplementary Table S3. Pairwise sequence alignments used in the Rosetta modeling were generated using BLAST [22].

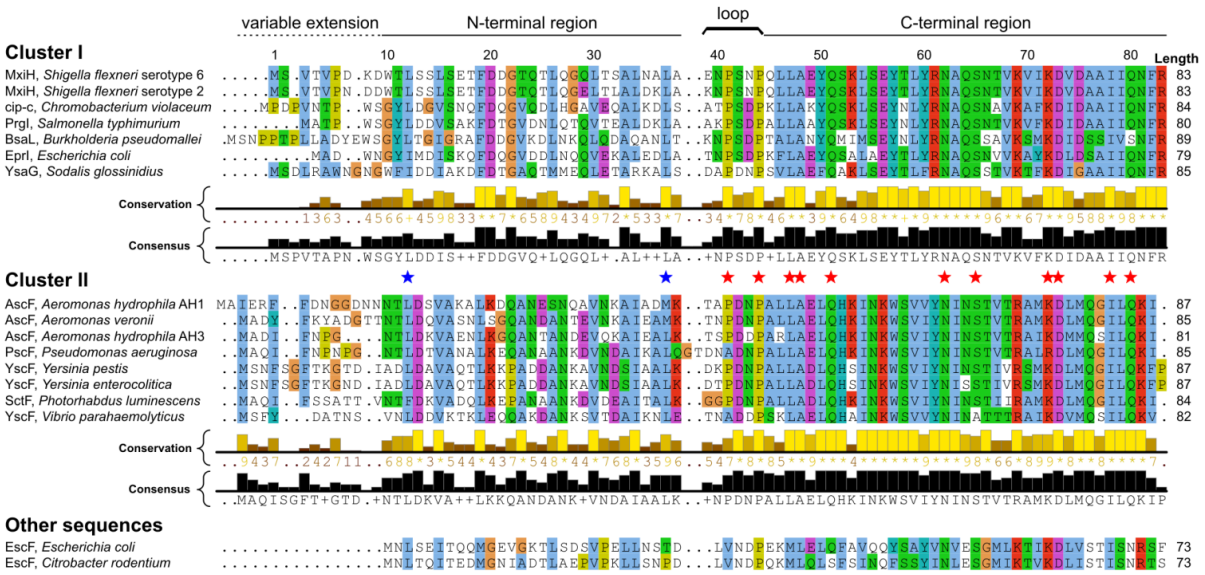

Figure 3: Multiple sequence alignment of T3SS needle proteins. Conserved residues are colored according to amino acid type following the Clustal X color scheme [23]. Highly conserved residues (≥ 12 identical amino acids in both clusters) are highlighted with a star (N-terminal region: blue; C-terminal region: red). The numbering of residues corresponds to the sequence of MxiH. Database accession identifiers for the primary sequences are given in supplementary Table S3.

9.4.6. Homology modeling

We used the Rosetta symmetric modeling framework [24] to generate a full 29-subunit model of MxiH based on the solid-state NMR structure of the PrgI needle (PDB ID: 2LPZ). This framework makes conformational sampling in symmetric systems more efficient by 1) only considering conformations that are consistent with the symmetry of the system and 2) performing a minimal number of energy and derivative evaluations by explicitly simulating only a subset of the interacting monomers and propagating conformational changes to symmetry-related subunits. The PrgI template was used to

define the initial rigid-body placement and backbone conformation of the MxiH subunits as well as their relative orientation with respect to each other, therefore dictating the helical symmetry parameters. Unaligned residues at the N-termini of the subunits were remodeled using symmetric, Monte Carlo based 3- and 9-residue backbone fragment insertions in a coarse-grained representation of a helically-arrayed 29-subunit system. The entire structure, including all backbone, side chain and rigid body degrees of freedom was subsequently refined using a physically realistic all-atom energy function [25]. 1,000 homology-based models were generated of which the 10 lowest in energy showed strong convergence with 0.6 Å backbone RMSD for the entire complex, excluding the 11 residues comprised in the N-terminal variable extension. The final models did not diverge significantly from the starting PrgI template structure (0.8 Å backbone RMSD) and present almost identical helical parameters to the initial template (5.6 subunits/turn, 23.5 Å radius, 4.2 Å axial rise/monomer). Evaluation of the full-atom energy of the previous cryoEM model by Fujii *et al.* was done in the following manner: the full 29-subunit assembly was generated from the coordinates of the monomeric subunit using the symmetry-related operations described in the header of the PDB file (PDB ID: 3J0W), followed by the aforementioned symmetric refinement in Rosetta. The refinement led only to minor changes relative to the starting coordinates (<1 Å backbone RMSD for the rigid helical parts of the structure, <0.5 Å change in axial rise/monomer and radius, <10° in rotation/monomer). 100 models were generated in this manner and the median energy of the 10 lowest-energy models was reported (Table 1). Fitting of the homology model to the EM density map and calculation of the EM correlations were done using the program UCSF Chimera [26,27].

9.5. Results

9.5.1. MxiH subunits are rigid and highly ordered in the assembly

The protocol developed for the *in vitro* preparation of functional *Salmonella* T3SS needles [6] was employed to produce WT *Shigella* T3SS needles (Fig. 4*A*). The needles were analyzed by magic-angle spinning solid-state NMR. Solid-state NMR is a method of choice [28-30] to obtain atomic-level structural information on insoluble proteins [31-34], including supramolecular assemblies [35-39], and can be employed directly on MxiH needles. The measurement of ^{13}C cross-polarization spectra (Fig. 4*B*) reveals that the recombinant needle samples are structurally highly homogeneous. The ^{13}C line-widths measured for [1-^{13}C]glucose (Glc)- and [2-^{13}C]Glc-labeled needles range from 0.09 to 0.25 ppm (between 20 and 55 Hz on an 850 MHz spectrometer), on par with other protein samples showing the highest resolution in solid-state NMR: microcrystalline GB1 [40,41], the HET-s(218-289) prion domain [42], and *S. typhimurium* PrgI T3SS needles [6,43].

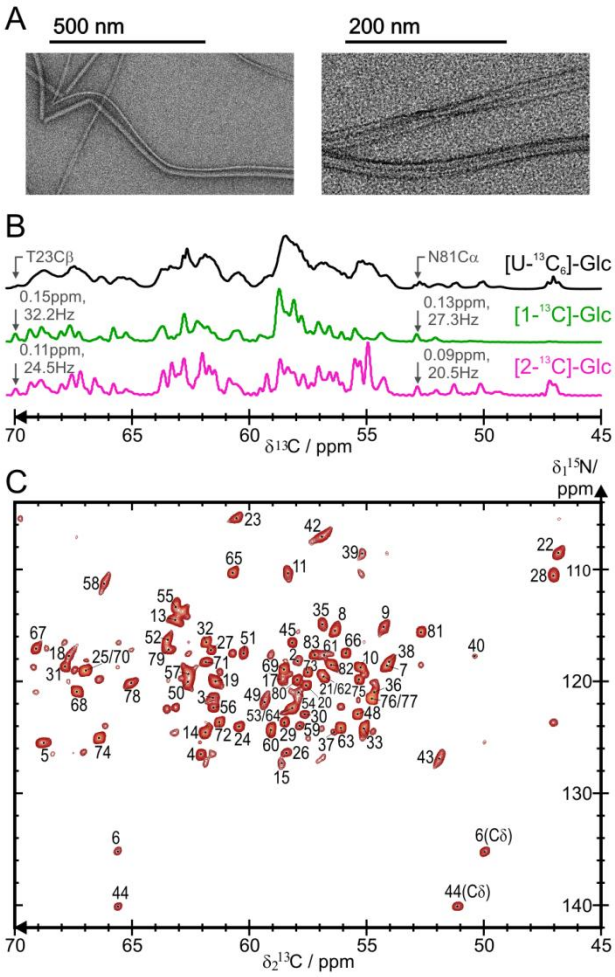

Figure 4: Solid-state NMR spectroscopy of Shigella flexneri MxiH needles. *A*, Transmission electron microscopy images of WT *Shigella flexneri* needles used for solid-state NMR measurements. *B*, 1D ^{13}C cross-polarization spectra of [uniform-$^{13}C_6$]glucose (Glc)-labeled (black), [1-^{13}C]Glc-labeled (green) and [2-^{13}C]Glc-labeled (magenta) needles. Representative line-widths are indicated for two resonances (T23Cβ and N81Cα) for the sparsely-labeled samples. The free-induction decay of the signal was recorded for a total of 8192 scans, with signal remaining after an acquisition time of 60 ms. No apodization function was employed in the processing. *C*, N-Cα spectrum of [2-^{13}C]Glc-labeled needles. The 2D spectrum correlates backbone amide nitrogen frequencies ($\delta_1{}^{15}N$) to backbone Cα frequencies ($\delta_2{}^{13}C$). N-Cα cross-peaks are numbered according to the MxiH amino acid sequence and N-Cδ cross-peaks of prolines are indicated. Unmarked cross-peaks correspond to sequential correlations. Spectra were recorded at a magnetic field of 21.1 T (850 MHz ^1H resonance frequency) at 5.5 °C.

The solid-state NMR assignment of ^{13}C and ^{15}N chemical shifts (supplementary Table S2) was carried out using standard experiments, 2D ^{13}C-^{13}C, ^{15}N-^{13}C and ^{15}N-(^{13}C)-^{13}C experiments. Due to the high spectral resolution of the sample, most of the assignment could be carried out on uniformly-labeled ([U-$^{13}C_6$]Glc) needles using 2D spectroscopy. An example of the spectral resolution obtained in [U-$^{13}C_6$]Glc needles is presented in a ^{13}C-^{13}C proton-driven spin diffusion (PDSD) spectrum (supplementary Fig. 9). A near-complete resonance assignment (96 %) was obtained using an extensive dataset of 2D spectra (supplementary Table S1) recorded on [U-$^{13}C_6$]Glc and ^{13}C spin diluted (produced with [1-^{13}C]Glc- and [2-^{13}C]Glc) T3SS needles. In sparsely-labeled samples, the dilution of ^{13}C spins results in an improved ^{13}C resolution due to the removal of one-bond ^{13}C-^{13}C dipolar and J_{CC} couplings, and in the simplification of spectra [43] (Fig. 4*C*). For instance, the complementarity of the [1-^{13}C]Glc- and [2-^{13}C]Glc labeling patterns [43-46] enabled the facile assignment of the repetitive LSSLS motif (L12-S16) of MxiH.

Residues extending from S2 to R83 in the MxiH sequence are all observed in cross-polarization based solid-state NMR spectra, indicating a high structural rigidity. Consequently, with the exception of Met1 detected in an INEPT ^{1}H-^{13}C spectrum, all residues in the MxiH subunit protein exhibit a rigid conformation.

No peak doubling could be observed in solid-state NMR spectra (Figs. 4*C* and 9), denoting the absence of polymorphism in the needle samples. This is in contrast to the X-ray structure of monomeric MxiH$^{C\Delta 5}$ (PDB ID: 2CA5) where two distinct conformations of MxiH are present in the unit cell [3], molecules A and B. Conformation B, which was not consistent with the low-resolution EM density, had been attributed either to crystal packing or to a different activation state of the needle [3].

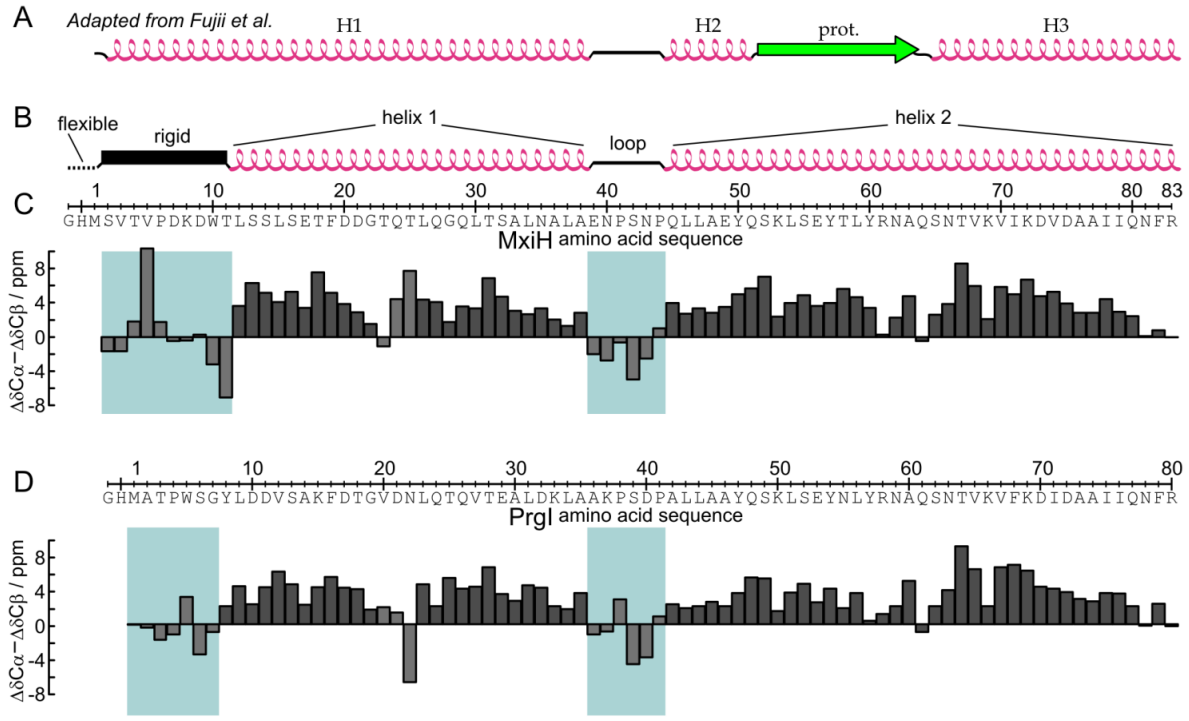

Figure 5: Identification of secondary structure elements. *A,* Secondary structure elements identified in the cryoEM model of Fujii *et al.*; adapted from Fig. 1e in Ref. [5] where H1, H2, and H3 indicate the position of α-helices and "prot" that of the β-hairpin between H2 and H3. *B,* Secondary structure elements of MxiH needles determined by solid-state NMR (this study). *C,* Secondary chemical shifts (ΔδCα – ΔδCβ) of the *Shigella flexneri* MxiH protein in the assembled needle. Regions which do not present α-helical propensity are highlighted. *D,* Secondary chemical shifts of the *Salmonella tympimurium* PrgI protein in the assembled needle taken from Ref. [43].

9.5.2. MxiH and PrgI proteins adopt a similar conformation in the assembled state

As backbone chemical shifts are strongly correlated to secondary structure [18,47,48], the secondary structure elements present in the MxiH subunit can be identified from our assignment (Figs. 5*B* and 5*C*). Positive values of secondary chemical shifts (Δδ) are indicative of α-helical propensity while negative values indicate β-sheet propensity [18]. The analysis of Δδ thus reveals two stretches of predominantly positive values corresponding to two long α-helices. The first α-helix is 27-residues long (L12 to A38),

the second α-helix comprises 39 residues and extends up to the C-terminus (Q45 to R83). The intervening region of negative values (E39 to P44) corresponds to a rigid loop and contains the conserved P-(S/D)-(D/N)-P turn structure previously identified in structures of monomeric [2-4,49] and assembled [5,6] T3SS needle subunits. Kinks or bends in the α-helices can be inferred from the isolated negative values of Δδ at T23 and Q64. The N-terminal segment from S2 to T11 is not α-helical but adopts instead a more extended conformation, as identified from the presence of negative Δδ values.

Local protein conformations can be directly compared on the basis of the secondary chemical shifts, as they are not influenced by amino acid type. The similarity in secondary chemical shifts between the MxiH and PrgI needles is remarkable (Figs. 5*C* and 5*D*), suggesting that the local structure of these needle subunits is highly similar. The agreement is especially apparent in the two α-helical regions, and the slight bend in the C-terminal helix occurs at the same position in both subunits, Q64 for MxiH corresponding to Q61 for PrgI. Two minor differences are observed: the kink appears at T23 for MxiH rather than at T25 (which would correspond to N22 in PrgI); more importantly, the rigid-extended region spans a larger region in MxiH, which has three additional residues, and the deviations of Δδ from random coil values are more pronounced. On the other hand, the secondary structure elements proposed in the model of Fujii *et al*. are not compatible with the experimental chemical shifts of MxiH (Fig. 5*A*). In order to quantitatively compare the cryoEM model to our chemical shift values, we back-predicted secondary chemical shifts from the cryoEM model (Fig. 10*B*) using SPARTA+ [50]. It was reported that the back-prediction of solid-state NMR ^{13}C chemical shifts in SPARTA produces outliers, i.e. predictions deviating from experimental shifts by more than 3 ppm, in approximately 4% of cases [51]. The number of ^{13}C chemical shift outliers for the cryoEM-based model of Fujii *et al.*, 13.1%, is

significantly higher, showing that its secondary structure cannot be reconciled with our NMR data.

Despite the aforementioned discrepancies in secondary structure between the MxiH [5] and PrgI [6] models, there is a striking similarity in the shape of the 3D envelope of their constituting subunits (Fig. 1). We thus wanted to test whether the architecture identified in PrgI needles could explain all experimental data for MxiH needles, both solid-state NMR chemical shifts and the 7.7-Å cryoEM density map. We generated homology models of the MxiH needle by Rosetta modeling calculations [52] using the structure of the PrgI needle as a template. A representative model from this ensemble (Fig. 6) shows good overlap with the cryoEM density map (EM correlation of 0.66), demonstrating that the architecture found in the PrgI needle (Fig. 1*B*) is compatible with all experimental data.

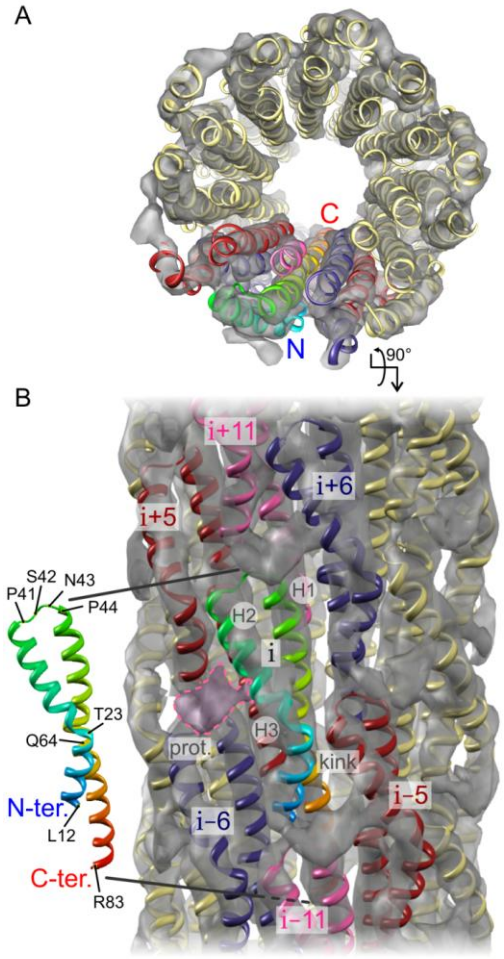

Figure 6: Structural model of the T3SS Shigella needle. *A,* Top and *B,* side views of the T3SS needle assembly of *Shigella flexneri*. The homology model of the 29-subunit MxiH needle assembly generated by Rosetta modeling (cartoon representation) shows a correlation of 0.66 with the 7.7-Å cryoEM density map (grey surface). Using the nomenclature of Fujii *et al.*, the EM density regions H1, H2 and H3 are indicated for the central subunit (i), as well as the kink in region H3. The first 11 N-terminal residues are not depicted due to the poor sequence homology of the rigid-extended segment (Fig. 3); however the protrusion in the EM map at subunit (i), labeled prot. and highlighted by a purple dashed contour trace, may be well explained by the N-terminus of subunit (i+5). The central subunit (i), colored as in Fig. 1*B*, forms a lateral interface with subunits (i±5), in red, and subunits (i±6), in dark blue. The axial interface is formed with subunits (i±11) shown in pink.

Using the nomenclature of Fujii *et al.*, the long C-terminal α-helix identified in PrgI occupies the density region H1 facing towards the needle pore in the cryoEM map of MxiH (Fig. 6*B*). The density regions H2 and H3 are filled by the N-terminal α-helix. The kink present in density region H3 corresponds to the kink identified at T23 from the analysis of secondary chemical shifts.

9.5.3. The N-terminus of MxiH is exposed on the exterior of the assembly

In order to determine the placement of the N- and the C-terminus in the MxiH needle, immunogold labeling experiments were performed both *in vitro* and *in vivo*. For *in vitro* experiments, the MxiH protein was expressed as a N-terminal His tag fusion construct, *mxiH*-N(His), and needles were polymerized. The tag is recognized by an Anti-His tag antibody which is imaged using protein A Gold (Fig. 7*B*). Immunogold labeling was not observed for WT needles lacking the His tag (Fig. 7*A*) and for *mxiH*-N(His) needles incubated without the Anti-His tag antibody (Fig. 7*C*), excluding the possibility that the labeling resulted from non-specific binding of the primary antibody or protein A Gold. *mxiH* expressed as a C-terminal His tag fusion construct prevented needle polymerization as previously reported [49]. Similar results were obtained for *in vivo* immunogold labeling experiments, where *ΔmxiH Shigella* cells were complemented with WT *mxiH* (Fig. 7*E*), an N-terminal Strep-tag fusion construct, *mxiH*-N(Strep), (Fig. 7*F*) or a C-terminal Strep-tag fusion construct, *mxiH*-C(Strep), (Fig. 7*G*). The strains expressing WT *mxiH* and *mxiH*-N(Strep) could assemble secretion-competent needles, as shown in a protein secretion assay (Fig. 7*D*), but the strain expressing *mxiH*-C(Strep) did not assemble any needle (Fig. 7*G*) and was not competent for secretion, consistent with previous mutagenesis data showing that C-terminal insertions compromise needle assembly and secretion function [53].

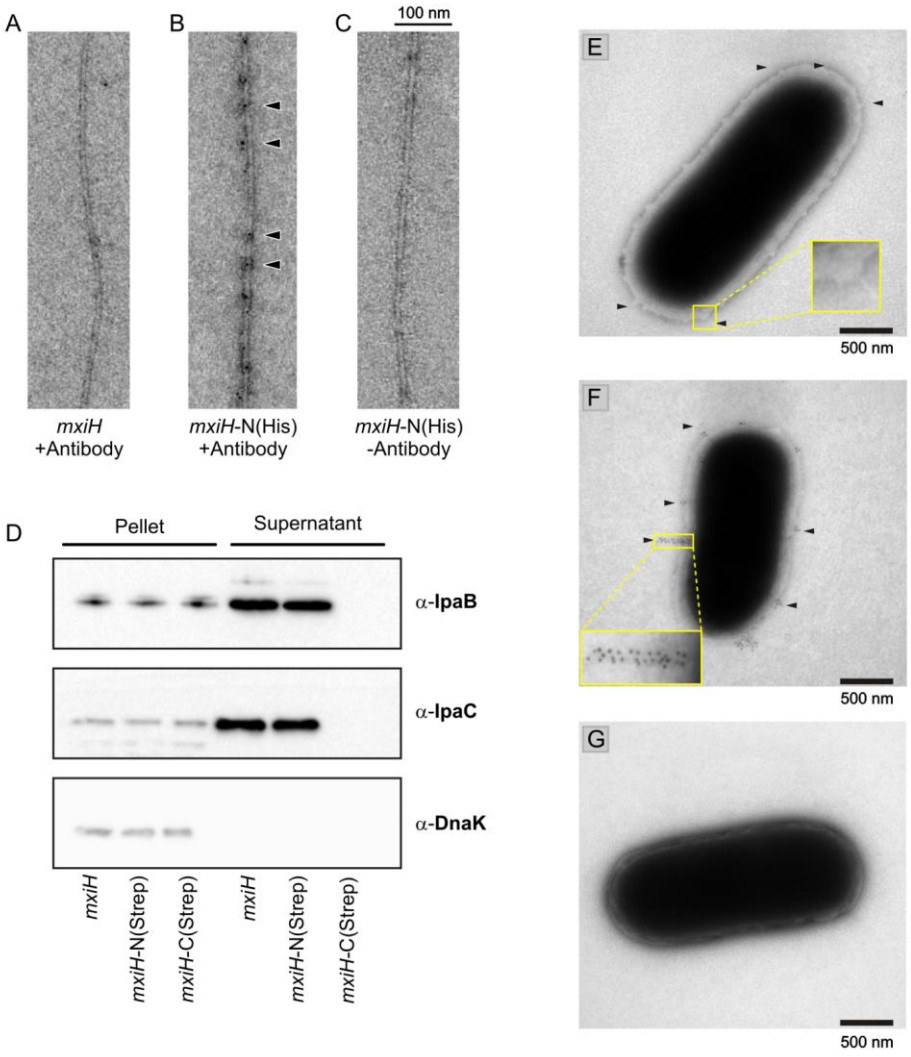

Figure 7: Localization of the MxiH subunit N-terminus in vitro and in vivo . *A–C,* Immunogold labeling of recombinant *Shigella flexneri* MxiH needles using a monoclonal Anti-His tag antibody. *A,* WT MxiH needles *B,* needles polymerized from N-terminal His tag fusion construct, *mxiH*-N(His), *C, mxiH*-N(His) needles labeled without primary Anti-His tag antibody. In *B*, some gold particles are indicated by arrows. Proteins expressed from a C-terminal His tag fusion construct did not polymerize. *D,* Effector protein secretion assay of *Shigella* strains used in Fig. *E–G* by addition of Congo Red (CR) followed by western blot analysis against IpaB, IpaC and DnaK. *E–G,* Non-polar *Shigella* mxiH-knockout cells (*ΔmxiH*) expressing *E,* wild-type *mxiH*, *F,* mxiH with N-terminal Strep-tag, *mxiH*-N(Strep) or *G,* MxiH with C-terminal Strep-tag, *mxiH*-C(Strep). In *E* and *F*, needles are indicated by arrows and two needles complexes are highlighted.

The strain expressing *mxiH*-N(Strep) formed needles decorated with gold particles. These results show that the MxiH subunit N-terminus is exposed at the surface of the needle and corroborate that MxiH needles adopt the topology found in the PrgI needle solid-state NMR structure [6] but not the topology of previous MxiH needle models [3,5].

9.5.4. The common T3SS structural architecture is reflected in sequence conservation patterns

As T3SS are employed by a variety of bacterial pathogens [54], we generated a multiple sequence alignment of T3SS needle proteins to evaluate the generality of the needle architecture. The sequences group in two clusters based on a pattern of highly conserved residues in the loop and C-terminal region (Fig. 3). Three distinct regions of the protein are identified according to the conservation level: the first ~10 residues forming the N-terminal extension are poorly conserved (average conservation level of 2.1), the subsequent N-terminal region is moderately conserved (6.5), and the loop (7.2) and C-terminal region (8.7) are highly conserved. Both MxiH and PrgI belong to the same cluster, in contrast to the needle protein of *Yersinia pestis*, YscF, which shows lower sequence identity to MxiH (25%). Sequences for EscF proteins are more evolutionary distant and were not included in any of the clusters. They also lack the canonical P-(S/D)-(D/N)-P loop motif and the variable extension.

The loop and C-terminal region contain a large number of residues, 11, that are highly conserved in both clusters, compared to only two residues in the N-terminal region. Those highly conserved residues, indicated with stars in Fig. 3, are all located lining the lumen of the needle in the PrgI needle structure (Fig. 1*B*, bottom right corner); however, no conserved residues are present in the interior of the needle in the cryoEM MxiH model (Fig. 1*A*, bottom left corner).

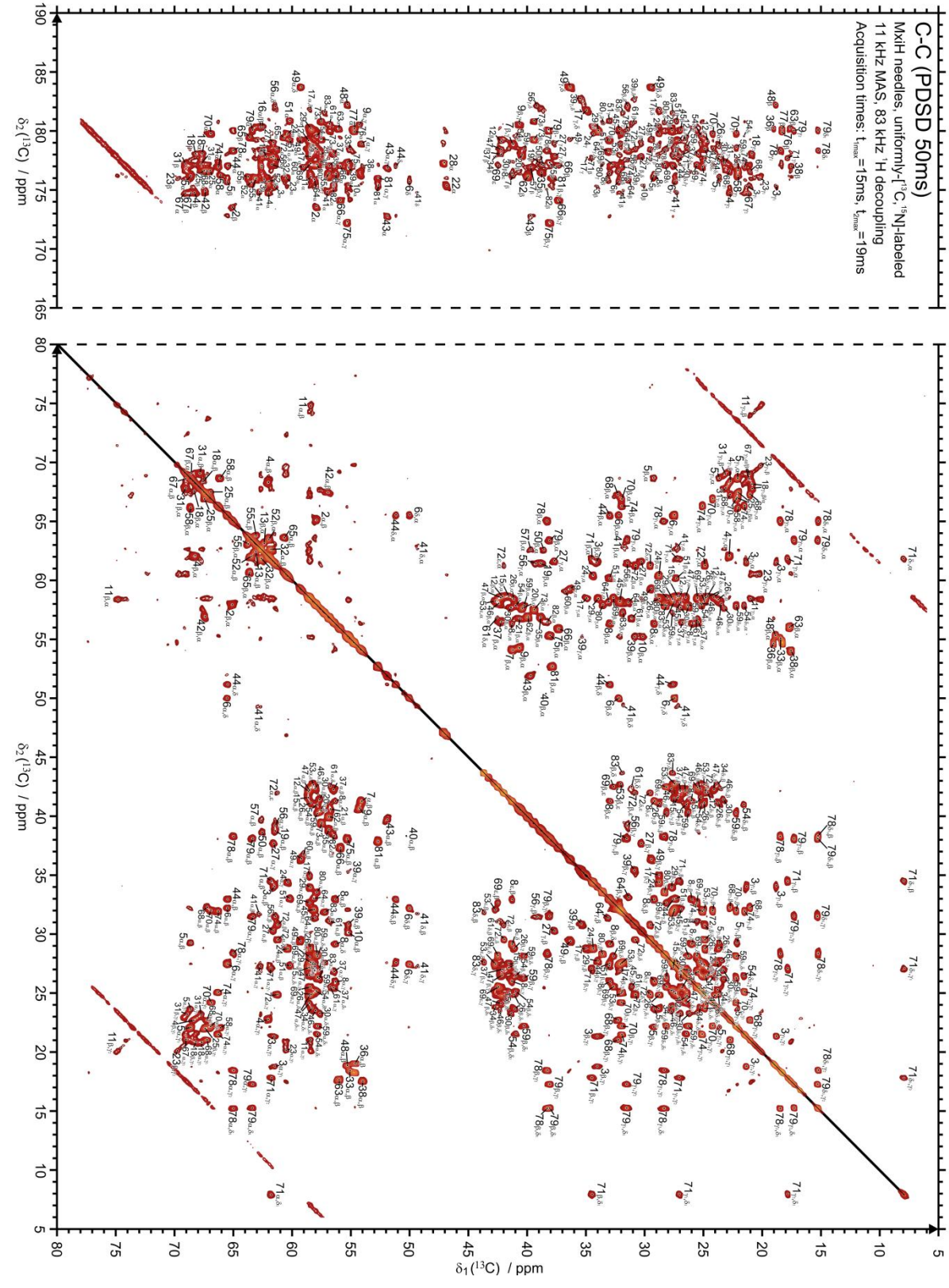
C-C (PDSD 50ms)
MxiH needles, uniformly-[13C, 15N]-labeled
11 kHz MAS, 83 kHz 1H decoupling
Acquisition times: t1max=15ms, t2max=19ms
δ1(13C) / ppm
δ2(13C) / ppm

Figure 8: Solid-state NMR ^{13}C-^{13}C spectrum of MxiH needles. The aliphatic-carbonyl (left) and aliphatic-aliphatic (right) regions from the solid-state NMR ^{13}C-^{13}C correlation spectrum of [uniform-$^{13}C_6$]glucose-labeled MxiH needles are presented. The spectrum was recorded with a proton-driven spin diffusion (PDSD) mixing time of 50 ms on an 850 MHz spectrometer at 11 kHz MAS and at 5.5°C. Intra-residue cross-peaks are numbered according to the MxiH amino acid sequence, with the specific ^{13}C atoms involved in the ^{13}C-^{13}C correlation indicated in subscript (F_1, then F_2). The C' symbol was omitted for correlations involving the backbone carbonyl. A few sequential correlations, especially in the C_α-C_α region, were assigned but are not marked in the figure.

9.6. Discussion and Conclusion

In the current study, WT *S. flexneri* needle assemblies were prepared by *in vitro* polymerization and studied by solid-state NMR. The MxiH needle subunit is predominantly rigid (S2-R83). Our chemical shift assignment (supplementary Table S2) provides for the first time empirical information on the conformation of the MxiH termini in the context of the needle assembly, as the first 19 (molecule A) or 14 (molecule B) residues are disordered in the crystal structure of MxiH$^{C\Delta5}$, as well as the last 2 (molecule A) or 8 (molecule B) C-terminal residues [3].

The following secondary structure elements were identified for MxiH: a rigid-extended N-terminal conformation (S2-T11), followed by the N-terminal α-helix (L12-A38) with a kink at T23, a loop (E39-P44) and the C-terminal α-helix (Q45-R83). The conformation of *Shigella* MxiH and *Salmonella* PrgI subunits in their needle assembled state is highly similar, as revealed by the comparison of secondary chemical shifts (Figs. 5*C* and 5*D*). Equally, the structure of the PrgI subunit solved by solid-state NMR comprises a rigid-extended N-terminal conformation (T3-Y8), an α-helix (L9-A35) with a kink at N22, a loop (A36-P41), and a C-terminal α-helix (A42-R80).

In contrast, the chemical shifts observed in this work are incompatible with the secondary structure identified in the previous MxiH needle model [5] (Figs. 5*A* and 9). Two major discrepancies exist between this model (Fig. 1*A*) and the experimental chemical shifts: the first 11 N-terminal residues were previously modeled as an α-helix and the segment extending from residues Q51 to Q64 was previously modeled as a β-hairpin. One explanation for the discrepancy in secondary structure elements in MxiH subunits between the current study and the model of Fujii *et al*. is that the measurements were carried out on *S. flexneri* serotype 6 (this study) and serotype 2. Compared to serotype 6, the sequence of serotype 2 has the following mutations: D7N, K8D, Q29E, S32L, N35D, A36K and E39K. Since no amino acid substitutions between the two serotypes are located in the conjectured β-hairpin region of MxiH (Q51-Q64), rearrangement of the secondary structure of the C-terminal helix by these mutations would likely involve even greater alterations locally at the site of the mutation, which are not observed. The finding that PrgI sustains a significantly greater number of N-terminal substitutions while preserving a C-terminal conformation highly similar to MxiH further discredits this hypothesis. We conclude that the incompatibility between this model and the experimental data results from remodeling of the monomeric subunit structure to fit the cryoEM density map without the guidance of site-specific local structural information such as experimentally-determined dihedral angles and distance restraints.

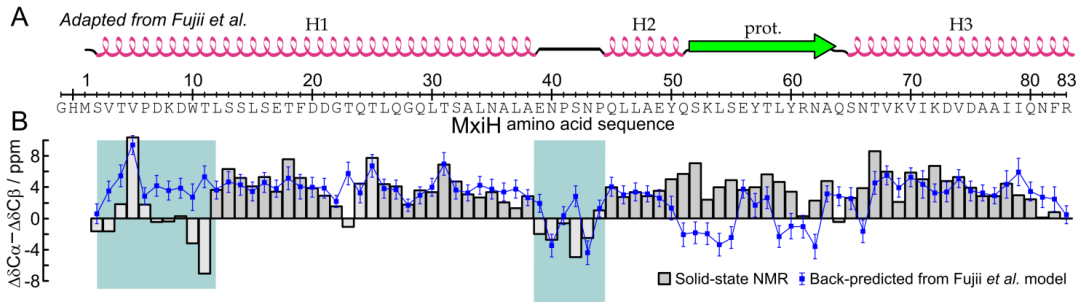

Figure 9: Back-prediction of secondary chemical shifts. *A*, Secondary structure elements identified in the cryoEM model (adapted from of Fujii *et al.*, *Proc. Natl. Sci. Acad. U.S.A.*, **2012**, Fig. 1e) where H1, H2, and H3 indicate the position of α-helices and "prot" that of the β-hairpin between H2 and H3. *B*, Secondary chemical shifts of the *Shigella flexneri* MxiH protein in the assembled needle measured by solid-state NMR (grey bars). Secondary chemical shifts back-predicted from the cryoEM model of Fujii *et al.* (blue squares) using SPARTA+. Error bars correspond to the estimated prediction error (s.d.).

As shown here and recently for the T3SS needle of *S. typhimurium* [6], solid-state NMR data can be used in complementation to cryoEM data for the generation or the validation of structural models of large assemblies. Owing to the high similarity of secondary chemical shifts between PrgI and MxiH, we generated a homology model of *S. flexneri* needles which accounts for all available experimental data, including the 7.7-Å cryoEM density map. Although the correlation to the cryoEM density is higher for the previous model by Fujii *et al.* (0.72) compared to our PrgI-based homology model (0.66), this is expected as no EM bias was used in the building of the current homology model. The previous model also has significantly higher full-atom energy after Rosetta refinement (Table 1). It is notable that the symmetry and helical parameters of the PrgI-based homology model are highly similar to the parameters derived from the cryoEM density map (Table 1), consistent with the view that *Shigella* and *Salmonella* needles are built upon a common architecture. From a methodological point of view, it is also interesting that both independent procedures, solid-state NMR in combination with results from STEM and Rosetta modeling — and high-resolution cryoEM, result in the same obtained symmetry. Furthermore, the fact that the homology model of PrgI fits

well into the completely independently and simultaneously determined high-resolution cryoEM map (Fig. 6) supports the validity of the PrgI structure (Fig. 1*B*).

Using immunogold labeling, we confirmed that the N-terminus is oriented on the outside face of the needle assembly (Fig. 7). This subunit orientation is consistent with sequence conservation patterns observed by multiple sequence alignment (Fig. 3), where residues in the C-terminal helix are more frequently conserved, and with mutagenesis data, where sequence alterations are more easily tolerated at the N-terminus. Indeed, deletion of 2-5 residues or addition of 3-6 residues at the C-terminus results in dysfunctional needles as detected in effector secretion assays and Congo Red (CR) induction assays [5,53] for MxiH, or in epithelial cell invasion assays [49] for PrgI. In contrast, deletion of 2-3 residues or addition of 3-7 residues at the N-terminus of MxiH subunits still produces functional needles (Ref. [5] and Fig. 7*D*). Moreover, PrgI subunits still assemble into functional T3SS needles when expressed with a deletion or addition of six residues at their N-terminus [49] as well as with a 8-residue N-terminal Strep-tag [6], as demonstrated by epithelial cell invasion assays. A deletion of eight N-terminal residues resulted in a *S. typhimurium* strain incapable of invasion [49], indicating that the two residues G7 and Y8 must be preserved to form the axial interface connecting subunits (i) and (i±11) and necessary for the polymerization of PrgI subunits [6].

As the biological role of the T3SS needle is to ensure the secretion of effector proteins, it is consequent that the residues lining the lumen, directly involved in the transport of effectors, are highly conserved (Fig. 1*B*). On the other hand, the diversity of residues exposed at the surface of the needle can confer a selective advantage to pathogenic bacteria, which must evade recognition by host cells [55-57]. Accordingly, the *mxiH* gene was shown to be the most variable gene in the virulence plasmid of *S. flexneri* [58].

In their assembled state, the only characteristic structural distinction observed between the homologous MxiH and PrgI proteins on the basis of the secondary structure analysis is the length of the N-terminal rigid-extended segment, which is composed of 10 residues for MxiH and six for PrgI. An important observation for the understanding of needle elongation is that T3SS needle proteins from different species are not interchangeable. For instance, Yop effector secretion could not be restored in a *yscF* null mutant strain of *Yersinia enterocolitica* by the expression of MxiH [59], which can be attributed to the low sequence identity of the two sequences (25%). However, despite the high sequence identity between MxiH and PrgI (>60%), a *Shigella flexneri mxiH* null mutant strain could not be complemented by PrgI and was not invasive due to the lack of needle formation [4]. Similarly, purified T3SS needles could be elongated *in vitro* from soluble monomer subunits of their own species, but not from subunits of other species, *Salmonella typhimurium* with MxiH* and *Shigella flexneri* with PrgI* [49]. Differences in the electrostatic surfaces from soluble monomeric subunit structures were suggested to explain the incompatibilities between needle subunits [4]. Our findings hint that the N-terminal rigid-extended segment could also play a crucial role in determining the species specificity. The excellent NMR spectral quality of needle samples produced by the *in vitro* preparation protocol [6] paves the way for the determination of high-resolution structures of MxiH filaments. Ongoing investigations in our group will thus address the question of the atomic structure of the rigid-extended N-terminal segment in MxiH needles.

In this study, it was found that *Shigella flexneri* and *Salmonella typhimurium* needles present a common architecture, providing a structural basis essential for the interpretation of previous functional data on type-three secretion in *Shigella*. Knowledge of the correct needle topology is essential to develop a key understanding of the operating mechanism of T3SS. The topology has an impact on the study of needle-tip interactions [60-64], needle-basal body interactions [65-69] and regulation of secretion [53,70-73],

which can contribute to the development of treatments against T3SS-mediated pathologies.

9.7. References

1. Cordes, F. S., Komoriya, K., Larquet, E., Yang, S. X., Egelman, E. H., Blocker, A., Lea, S. M. Helical structure of the needle of the type III secretion system of Shigella flexneri. *J Biol Chem* **278**, 17103-7 (2003).
2. Zhang, L. L., Wang, Y., Picking, W. L., Picking, W. D., De Guzman, R. N. Solution structure of monomeric BsaL, the type III secretion needle protein of Burkholderia pseudomallei. *Journal of molecular biology* **359**, 322-30 (2006).
3. Deane, J. E., Roversi, P., Cordes, F. S., Johnson, S., Kenjale, R., Daniell, S., Booy, F., Picking, W. D., Picking, W. L., Blocker, A. J., Lea, S. M. Molecular model of a type III secretion system needle: Implications for host-cell sensing. *Proceedings of the National Academy of Sciences of the United States of America* **103**, 12529-33 (2006).
4. Wang, Y., Ouellette, A. N., Egan, C. W., Rathinavelan, T., Im, W., De Guzman, R. N. Differences in the electrostatic surfaces of the type III secretion needle proteins PrgI, BsaL, and MxiH. *Journal of molecular biology* **371**, 1304-14 (2007).
5. Fujii, T., Cheung, M., Blanco, A., Kato, T., Blocker, A. J., Namba, K. Structure of a type III secretion needle at 7-A resolution provides insights into its assembly and signaling mechanisms. *Proceedings of the National Academy of Sciences of the United States of America* **109**, 4461-6 (2012).
6. Loquet, A., Sgourakis, N. G., Gupta, R., Giller, K., Riedel, D., Goosmann, C., Griesinger, C., Kolbe, M., Baker, D., Becker, S., Lange, A. Atomic model of the type III secretion system needle. *Nature* **486**, 276-9 (2012).
7. Galkin, V. E., Schmied, W. H., Schraidt, O., Marlovits, T. C., Egelman, E. H. The structure of the Salmonella typhimurium type III secretion system needle shows divergence from the flagellar system. *Journal of molecular biology* **396**, 1392-7 (2010).
8. Szeverenyi, N. M., Sullivan, M. J., Maciel, G. E. Observation of spin exchange by two-dimensional fourier-transform ^{13}C cross-polarization magic-angle spinning. *Journal of Magnetic Resonance* **47**, 462-75 (1982).
9. Hohwy, M., Rienstra, C. M., Jaroniec, C. P., Griffin, R. G. Fivefold symmetric homonuclear dipolar recoupling in rotating solids: Application to double quantum spectroscopy. *Journal of Chemical Physics* **110**, 7983-92 (1999).
10. Baldus, M., Petkova, A. T., Herzfeld, J., Griffin, R. G. Cross polarization in the tilted frame: assignment and spectral simplification in heteronuclear spin systems. *Molecular Physics* **95**, 1197-207 (1998).
11. Takegoshi, K., Nakamura, S., Terao, T. ^{13}C–^{1}H dipolar-assisted rotational resonance in magic-angle spinning NMR. *Chemical Physics Letters* **344**, 631-7 (2001).
12. Fung, B. M., Khitrin, A. K., Ermolaev, K. An improved broadband decoupling sequence for liquid crystals and solids. *Journal of Magnetic Resonance* **142**, 97-101 (2000).
13. Thakur, R. S., Kurur, N. D., Madhu, P. K. Swept-frequency two-pulse phase modulation for heteronuclear dipolar decoupling in solid-state NMR. *Chemical Physics Letters* **426**, 459-63 (2006).
14. Augustine, C., Kurur, N. D. Supercycled SWf-TPPM sequence for heteronuclear dipolar decoupling in solid-state nuclear magnetic resonance. *Journal of Magnetic Resonance* **209**, 156-60 (2011).
15. Chandran, C. V., Madhu, P. K., Kurur, N. D., Brauniger, T. Swept-frequency two-pulse phase modulation (SWf-TPPM) sequences with linear sweep profile for heteronuclear decoupling in solid-state NMR. *Magn Reson Chem* **46**, 943-7 (2008).
16. Shaka, A. J., Keeler, J., Frenkiel, T., Freeman, R. An Improved Sequence for Broad-Band Decoupling - WALTZ-16. *Journal of Magnetic Resonance* **52**, 335-8 (1983).

17. Bockmann, A., Gardiennet, C., Verel, R., Hunkeler, A., Loquet, A., Pintacuda, G., Emsley, L., Meier, B. H., Lesage, A. Characterization of different water pools in solid-state NMR protein samples. *Journal of Biomolecular NMR* **45**, 319-27 (2009).
18. Wang, Y. J., Jardetzky, O. Probability-based protein secondary structure identification using combined NMR chemical-shift data. *Protein Sci* **11**, 852-61 (2002).
19. Larkin, M. A., Blackshields, G., Brown, N. P., Chenna, R., McGettigan, P. A., McWilliam, H., Valentin, F., Wallace, I. M., Wilm, A., Lopez, R., Thompson, J. D., Gibson, T. J., Higgins, D. G. Clustal W and clustal X version 2.0. *Bioinformatics* **23**, 2947-8 (2007).
20. Gonnet, G. H., Cohen, M. A., Benner, S. A. Exhaustive matching of the entire protein-sequence database. *Science* **256**, 1443-5 (1992).
21. Waterhouse, A. M., Procter, J. B., Martin, D. M. A., Clamp, M., Barton, G. J. Jalview Version 2-a multiple sequence alignment editor and analysis workbench. *Bioinformatics* **25**, 1189-91 (2009).
22. Altschul, S. F., Madden, T. L., Schaffer, A. A., Zhang, J., Zhang, Z., Miller, W., Lipman, D. J. Gapped BLAST and PSI-BLAST: a new generation of protein database search programs. *Nucleic Acids Research* **25**, 3389-402 (1997).
23. Thompson, J. D., Gibson, T. J., Plewniak, F., Jeanmougin, F., Higgins, D. G. The CLUSTAL_X windows interface: flexible strategies for multiple sequence alignment aided by quality analysis tools. *Nucleic Acids Research* **25**, 4876-82 (1997).
24. DiMaio, F., Leaver-Fay, A., Bradley, P., Baker, D., Andre, I. Modeling symmetric macromolecular structures in Rosetta3. *PLOS One* **6**, e20450 (2011).
25. Bradley, P., Misura, K. M. S., Baker, D. Toward high-resolution de novo structure prediction for small proteins. *Science* **309**, 1868-71 (2005).
26. Pettersen, E. F., Goddard, T. D., Huang, C. C., Couch, G. S., Greenblatt, D. M., Meng, E. C., Ferrin, T. E. UCSF Chimera—A visualization system for exploratory research and analysis. *Journal of Computational Chemistry* **25**, 1605-12 (2004).
27. Goddard, T. D., Huang, C. C., Ferrin, T. E. Visualizing density maps with UCSF Chimera. *Journal of structural biology* **157**, 281-7 (2007).
28. Bockmann, A. 3D protein structures by solid-state NMR spectroscopy: Ready for high resolution. *Angewandte Chemie-International Edition* **47**, 6110-3 (2008).
29. Renault, M., Cukkemane, A., Baldus, M. Solid-State NMR Spectroscopy on Complex Biomolecules. *Angewandte Chemie-International Edition* **49**, 8346-57 (2010).
30. Hong, M., Zhang, Y., Hu, F. H. in *Annual Review of Physical Chemistry* Vol. 63 *Annual Review of Physical Chemistry* 1-24 (Annual Reviews, 2012).
31. Goldbourt, A., Gross, B. J., Day, L. A., McDermott, A. E. Filamentous phage studied by magic-angle spinning NMR: Resonance assignment and secondary structure of the coat protein in Pf1. *Journal of the American Chemical Society* **129**, 2338-44 (2007).
32. Han, Y., Ahn, J., Concel, J., Byeon, I.-J. L., Gronenborn, A. M., Yang, J., Polenova, T. Solid-State NMR Studies of HIV-1 Capsid Protein Assemblies. *Journal of the American Chemical Society* **132**, 1976-87 (2010).
33. Chen, B., Tycko, R. Structural and dynamical characterization of tubular HIV-1 capsid protein assemblies by solid state nuclear magnetic resonance and electron microscopy. *Protein Sci* **19**, 716-30 (2010).
34. Byeon, I.-J. L., Hou, G., Han, Y., Suiter, C. L., Ahn, J., Jung, J., Byeon, C.-H., Gronenborn, A. M., Polenova, T. Motions on the Millisecond Time Scale and Multiple Conformations of HIV-1 Capsid Protein: Implications for Structural Polymorphism of CA Assemblies. *Journal of the American Chemical Society* **134**, 6455-66 (2012).
35. Nieuwkoop, A. J., Rienstra, C. M. Supramolecular Protein Structure Determination by Site-Specific Long-Range Intermolecular Solid State NMR Spectroscopy. *Journal of the American Chemical Society* **132**, 7570-1 (2010).
36. Jehle, S., Rajagopal, P., Bardiaux, B., Markovic, S., Kuehne, R., Stout, J. R., Higman, V. A., Klevit, R. E., van Rossum, B.-J., Oschkinat, H. Solid-state NMR and SAXS studies provide a structural basis for

the activation of alpha B-crystallin oligomers. *Nature Structural & Molecular Biology* **17**, 1037-U1 (2010).
37. Goldbourt, A., Day, L. A., McDermott, A. E. Intersubunit Hydrophobic Interactions in Pf1 Filamentous Phage. *J Biol Chem* **285**, 37051-9 (2010).
38. Bayro, M. J., Debelouchina, G. T., Eddy, M. T., Birkett, N. R., MacPhee, C. E., Rosay, M., Maas, W. E., Dobson, C. M., Griffin, R. G. Intermolecular Structure Determination of Amyloid Fibrils with Magic-Angle Spinning and Dynamic Nuclear Polarization NMR. *Journal of the American Chemical Society* **133**, 13967-74 (2011).
39. Qiang, W., Yau, W.-M., Luo, Y., Mattson, M. P., Tycko, R. Antiparallel beta-sheet architecture in Iowa-mutant beta-amyloid fibrils. *Proceedings of the National Academy of Sciences of the United States of America* **109**, 4443-8 (2012).
40. Franks, W. T., Zhou, D. H., Wylie, B. J., Money, B. G., Graesser, D. T., Frericks, H. L., Sahota, G., Rienstra, C. M. Magic-angle spinning solid-state NMR spectroscopy of the beta 1 immunoglobulin binding domain of protein G (GB1): N-15 and C-13 chemical shift assignments and conformational analysis. *Journal of the American Chemical Society* **127**, 12291-305 (2005).
41. Franks, W. T., Wylie, B. J., Schmidt, H. L. F., Nieuwkoop, A. J., Mayrhofer, R. M., Shah, G. J., Graesser, D. T., Rienstra, C. M. Dipole tensor-based atomic-resolution structure determination of a nanocrystalline protein by solid-state NMR. *Proceedings of the National Academy of Sciences of the United States of America* **105**, 4621-6 (2008).
42. Wasmer, C., Lange, A., Van Melckebeke, H., Siemer, A. B., Riek, R., Meier, B. H. Amyloid fibrils of the HET-s(218-289) prion form a beta solenoid with a triangular hydrophobic core. *Science* **319**, 1523-6 (2008).
43. Loquet, A., Lv, G., Giller, K., Becker, S., Lange, A. ^{13}C spin dilution for simplified and complete solid-state NMR resonance assignment of insoluble biological assemblies. *Journal of the American Chemical Society* **133**, 4722-5 (2011).
44. Hong, M. Determination of multiple phi-torsion angles in proteins by selective and extensive ^{13}C labeling and two-dimensional solid-state NMR. *Journal of Magnetic Resonance* **139**, 389-401 (1999).
45. Lundström, P., Teilum, K., Carstensen, T., Bezsonova, I., Wiesner, S., Hansen, D. F., Religa, T. L., Akke, M., Kay, L. E. Fractional C-13 enrichment of isolated carbons using [1-C-13]- or [2-C-13]-glucose facilitates the accurate measurement of dynamics at backbone C-alpha and side-chain methyl positions in proteins. *Journal of Biomolecular NMR* **38**, 199-212 (2007).
46. Loquet, A., Giller, K., Becker, S., Lange, A. Supramolecular Interactions Probed by ^{13}C–^{13}C Solid-State NMR Spectroscopy. *Journal of the American Chemical Society* **132**, 15164-6 (2010).
47. Wishart, D. S., Sykes, B. D., Richards, F. M. Relationship between nuclear magnetic resonance chemical shift and protein secondary structure. *Journal of molecular biology* **222**, 311-33 (1991).
48. Luca, S., Filippov, D. V., van Boom, J. H., Oschkinat, H., de Groot, H. J. M., Baldus, M. Secondary chemical shifts in immobilized peptides and proteins: A qualitative basis for structure refinement under Magic Angle Spinning. *Journal of Biomolecular NMR* **20**, 325-31 (2001).
49. Poyraz, O., Schmidt, H., Seidel, K., Delissen, F., Ader, C., Tenenboim, H., Goosmann, C., Laube, B., Thuenemann, A. F., Zychlinsky, A., Baldus, M., Lange, A., Griesinger, C., Kolbe, M. Protein refolding is required for assembly of the type three secretion needle. *Nature Structural & Molecular Biology* **17**, 788-U26 (2010).
50. Shen, Y., Bax, A. SPARTA plus : a modest improvement in empirical NMR chemical shift prediction by means of an artificial neural network. *Journal of Biomolecular NMR* **48**, 13-22 (2010).
51. Seidel, K., Etzkorn, M., Schneider, R., Ader, C., Baldus, M. Comparative analysis of NMR chemical shift predictions for proteins in the solid phase. *Solid State Nuclear Magnetic Resonance* **35**, 235-42 (2009).
52. Das, R., Andre, I., Shen, Y., Wu, Y., Lemak, A., Bansal, S., Arrowsmith, C. H., Szyperski, T., Baker, D. Simultaneous prediction of protein folding and docking at high resolution. *Proceedings of the National Academy of Sciences of the United States of America* **106**, 18978-83 (2009).

53. Kenjale, R., Wilson, J., Zenk, S. F., Saurya, S., Picking, W. L., Picking, W. D., Blocker, A. The needle component of the type III secreton of Shigella regulates the activity of the secretion apparatus. *J Biol Chem* **280**, 42929-37 (2005).
54. Nguyen, L., Paulsen, I. T., Tchieu, J., Hueck, C. J., Saier, M. H., Jr. Phylogenetic analyses of the constituents of Type III protein secretion systems. *J Mol Microbiol Biotechnol* **2**, 125-44 (2000).
55. West, N. P., Sansonetti, P., Mounier, J., Exley, R. M., Parsot, C., Guadagnini, S., Prevost, M. C., Prochnicka-Chalufour, A., Delepierre, M., Tanguy, M., Tang, C. M. Optimization of virulence functions through glucosylation of Shigella LPS. *Science* **307**, 1313-7 (2005).
56. Phalipon, A., Sansonetti, P. J. Shigella's ways of manipulating the host intestinal innate and adaptive immune system: a tool box for survival? *Immunology and Cell Biology* **85**, 119-29 (2007).
57. Schroeder, G. N., Hilbi, H. Molecular pathogenesis of Shigella spp.: Controlling host cell signaling, invasion, and death by type III secretion. *Clinical Microbiology Reviews* **21**, 134-56 (2008).
58. Lan, R. T., Stevenson, G., Reeves, P. R. Comparison of two major forms of the Shigella virulence plasmid pINV: Positive selection is a major force driving the divergence. *Infection and immunity* **71**, 6298-306 (2003).
59. Allaoui, A., Schulte, R., Cornelis, G. R. Mutational analysis of the Yersinia enterocofitica virC operon: characterization of yscE, F, G, I, J, K required for Yop secretion and yscH encoding YopR. *Molecular Microbiology* **18**, 343-55 (1995).
60. Johnson, S., Roversi, P., Espina, M., Olive, A., Deane, J. E., Birket, S., Field, T., Picking, W. D., Blocker, A. J., Galyov, E. E., Picking, W. L., Lea, S. M. Self-chaperoning of the type III secretion system needle tip proteins IpaD and BipD. *J Biol Chem* **282**, 4035-44 (2007).
61. Zhang, L., Wang, Y., Olive, A. J., Smith, N. D., Picking, W. D., De Guzman, R. N., Picking, W. L. Identification of the MxiH needle protein residues responsible for anchoring invasion plasmid antigen D to the type III secretion needle tip. *J Biol Chem* **282**, 32144-51 (2007).
62. Rathinavelan, T., Tang, C., De Guzman, R. N. Characterization of the Interaction between the Salmonella Type III Secretion System Tip Protein SipD and the Needle Protein PrgI by Paramagnetic Relaxation Enhancement. *J Biol Chem* **286**, 4922-30 (2010).
63. Chatterjee, S., Zhong, D., Nordhues, B. A., Battaile, K. P., Lovell, S., De Guzman, R. N. The crystal structures of the Salmonella type III secretion system tip protein SipD in complex with deoxycholate and chenodeoxycholate. *Protein Sci* **20**, 75-86 (2011).
64. Lunelli, M., Hurwitz, R., Lambers, J., Kolbe, M. Crystal Structure of PrgI-SipD: Insight into a Secretion Competent State of the Type Three Secretion System Needle Tip and its Interaction with Host Ligands. *PLoS pathogens* **7** (2011).
65. Marlovits, T. C., Kubori, T., Sukhan, A., Thomas, D. R., Galan, J. E., Unger, V. M. Structural insights into the assembly of the type III secretion needle complex. *Science* **306**, 1040-2 (2004).
66. Marlovits, T. C., Kubori, T., Lara-Tejero, M., Thomas, D., Unger, V. M., Galan, J. E. Assembly of the inner rod determines needle length in the type III secretion injectisome. *Nature* **441**, 637-40 (2006).
67. Marlovits, T. C., Stebbins, C. E. Type III secretion systems shape up as they ship out. *Current Opinion in Microbiology* **13**, 47-52 (2010).
68. Schraidt, O., Lefebre, M. D., Brunner, M. J., Schmied, W. H., Schmidt, A., Radics, J., Mechtler, K., Galán, J. E., Marlovits, T. C. Topology and Organization of the *Salmonella typhimurium* Type III Secretion Needle Complex Components. *PLoS pathogens* **6**, e1000824 (2010).
69. Schraidt, O., Marlovits, T. C. Three-dimensional model of Salmonella's needle complex at subnanometer resolution. *Science* **331**, 1192-5 (2011).
70. Davis, A. J., Mecsas, J. Mutations in the Yersinia pseudotuberculosis type III secretion system needle protein, YscF, that specifically abrogate effector translocation into host cells. *Journal of Bacteriology* **189**, 83-97 (2007).
71. Quinaud, M., Ple, S., Job, V., Contreras-Martel, C., Simorre, J.-P., Attree, I., Dessen, A. Structure of the heterotrimeric complex that regulates type III secretion needle formation. *Proceedings of the National Academy of Sciences of the United States of America* **104**, 7803-8 (2007).

72. Botteaux, A., Sory, M. P., Biskri, L., Parsot, C., Allaoui, A. MxiC is secreted by and controls the substrate specificity of the Shigella flexneri type III secretion apparatus. *Molecular Microbiology* **71**, 449-60 (2009).
73. Martinez-Argudo, I., Blocker, A. J. The Shigella T3SS needle transmits a signal for MxiC release, which controls secretion of effectors. *Molecular Microbiology* **78**, 1365-78 (2010).

9.8. Appendix

	Subunits per turn	**Axial rise per monomer / Å**	**Needle Radius / Å**	**EM correlation**	**Full-atom energy***
This study	5.65	4.21	23.51	0.66	-184
Fujii *et al.* [5]	5.62	4.30	23.06	0.72	-133**

Table 1: Structural statistics of different needle models
* Full-atom interface energy in Rosetta energy units, median value of the 10 lowest-energy models.
**After refinement of the PDB coordinates.

Correlation	Mixing element	Labeling	Spectrometer frequency $\nu_1{}^1H$	Acquisition time t_1	Acquisition time t_2	Total time
			MHz	*m*s	*m*s	
C-C	PDSD 50 ms	uniform	850	15	19	1d 17h
N-CA	Selective CP	uniform	850	15	15	24h
N-CA-CX	Selective CP, DARR 70 ms	uniform	850	19	15	4d
N-CO	Selective CP	uniform	850	19	15	12h
N-CO-CX	Selective CP, DARR 70 ms	uniform	850	19	15	3d 14h
N-CX	Broadband H.-H. CP	uniform	800	14	13.5	2d 9h
C-C	PDSD 75 ms	uniform	800	12	20	2d
C-C	PDSD 200 ms	uniform	800	14	14	3d
C-C DQ-SQ	SPC5 0.5 ms	uniform	800	8	20	20h
H-C	INEPT	uniform	800	12	25	1d 12h
C-C	PDSD 100 ms	uniform	600	8	17	4d
C-C	PDSD 200 ms	uniform	600	8	17	4d
N-CA	Selective CP	1-glc	800	14	17	1d 5h
C-C	PDSD 100 ms	1-glc	850	15	19	2d 10h
C-C	PDSD 400 ms	1-glc	850	17	21	4d 17h
C-C	PDSD 850 ms	1-glc	850	18	22	6d 16h
C-C	PDSD 700 ms	1-glc	800	8.5	14.5	7d 22h
N-CA	Selective CP	2-glc	850	17	30	15h
C-C	PDSD 50 ms	2-glc	850	15	21	1d 7h
C-C	PDSD 400 ms	2-glc	850	15	21	2d 23h
C-C	PDSD 850 ms	2-glc	850	16	21	6d 12h
C-C	PDSD 850 ms	2-glc	800	8.5	14	9d 1h
C-C	PDSD 300 ms	2-glc	600	17	21	4d 20h

Table 2: List of 2D solid-state NMR experiments
Maximal acquisition times in the indirect (t1) and direct (t2) dimensions are indicated as well as the total measurement time for each experiment.

Table 3: Chemical shifts of Shigella flexneri MxiH needles

	N	C	C_α	C_β	$C_\gamma/C_{\gamma 1}$	$C_{\gamma 2}$	$C_\delta/C_{\delta 1}$	$C_{\delta 2}$	$C_\varepsilon/C_{\varepsilon 1}$	$C_{\varepsilon 2}$	$C_{\varepsilon 3}$	C_ζ	$C_{\zeta 2}$	$C_{\zeta 3}$	$N_{\delta 2}/N_{\varepsilon 2}$	N_ε	N_ζ
G-1																	
H0								120.0	136.6								
M1									16.8								
S2	118.0	173.5	57.9	65.1													
V3	121.2	175.3	61.5	34.1	18.8	21.3											
T4	126.3	174.7	62.1	68.4		22.7											
V5	125.3	176.1	68.7	29.3	22.1	23.6											
P6	135.1	175.7	65.6	32.2	27.4		50.0										
D7	118.4	176.2	54.1	41.3	178.9												
K8	115.3	176.4	56.4	33.0	26.0		29.2		41.3								33.0
D9	114.9	176.5	54.3	40.7	180.5												
W10	118.5	175.4	55.3	30.1	109.7		128.9	130.8		139.0	121.2		113.2	120.7			
T11	110.0	176.1	58.4	73.7		21.1											
L12	120.0	179.2	58.6	42.1	27.0		26.5	24.6									
S13	114.3	176.0	63.2	62.4													
S14	124.4	177.8	61.8	62.2													
L15	127.2	178.3	58.7	41.6	27.5		27.2	25.1									
S16	113.4	180.3	62.5	62.7													
E17	119.5	177.8	58.5	28.7	35.0		181.8										
T18	117.6	178.0	67.7	68.3		20.8											
F19	119.8	177.2	61.5	38.8	139.0					130.4							
D20	120.1	178.0	57.6	40.4	178.3												
D21	119.5	179.9	56.8	40.6	178.2												
G22	108.2	175.4	46.8														
T23	105.2	175.9	60.6	69.8		20.1											
Q24	123.9	179.7	60.4	28.7	34.4		174.8								126.2		
T25	118.8	176.6	67.0	67.5		22.0											
L26	126.2	178.7	58.4	41.1	28.8		24.9	23.7									
Q27	117.0	178.9	61.6	30.2	37.7		177.8								118.1		
G28	110.4	177.3	47.1														
Q29	123.5	180.2	58.5	27.7	33.9		180.0								112.0		
L30	122.7	177.3	57.7	41.4	27.0		26.2	23.3									
T31	118.5	177.1	67.8	69.1		23.1											
S32	116.3	177.2	61.8	62.7													
A33	124.0	178.4	55.1	18.4													
L34	119.2	177.7	58.3	42.7	27.6		25.3	23.8									
N35	114.6	177.1	56.9	38.8	176.5										115.8		
A36	120.9	180.2	54.7	19.0													
L37	124.3	178.0	56.5	42.2	26.9		25.4	25.5									
A38	118.0	177.0	54.0	17.5													
E39	108.3	176.8	55.2	30.9	35.4		182.8										
N40	117.5	171.4	50.4	38.4	190.1										132.8		

	N	C	C_α	C_β	$C_\gamma/C_{\gamma1}$	$C_{\gamma2}$	$C_\delta/C_{\delta1}$	$C_{\delta2}$	$C_\varepsilon/C_{\varepsilon1}$	$C_{\varepsilon2}$	$C_{\varepsilon3}$	C_ζ	$C_{\zeta2}$	$C_{\zeta3}$	$N_{\delta2}/N_{\varepsilon2}$	N_ε	N_ζ
P41	130.0	174.8	62.8	31.8	27.2		49.3										
S42	106.7	174.9	56.9	67.4													
N43	126.8	172.7	51.9	39.7	176.9										111.3		
P44	140.1	177.0	65.6	32.9	27.5		51.2										
Q45	116.3	180.1	58.2	26.9	32.1										118.3		
L46	121.3	178.8	58.0	42.3	27.7		25.2	23.5									
L47	118.1	178.5	58.6	42.2	26.5		24.8	24.1									
A48	122.7	182.2	55.3	18.8													
E49	121.6	179.3	59.3	29.4	36.3		183.7										
Y50	119.9	177.1	62.6	38.6				132.7				157.8					
Q51	117.4	180.8	60.2	27.3	33.0		179.2								112.9		
S52	116.0	175.7	63.5	62.0													
K53	122.2	178.9	58.2	32.0	24.9		27.4		42.7								32.1
L54	120.8	179.5	57.9	41.0	26.4		25.1	21.5									
S55	113.2	176.1	63.1	63.7													
E56	122.1	177.6	61.5	31.5	39.2		182.1										
Y57	119.1	176.9	62.7	39.7			132.0	132.5	118.3								
T58	111.1	176.3	66.2	68.7		22.0											
L59	123.7	178.5	57.9	40.3	26.3		28.1	22.2									
Y60	124.1	177.0	59.1	36.7	129.3		132.0	134.1	116.3	118.3							
R61	117.5	180.5	56.8	31.1	25.5		42.5					159.7				80.6	
N62	119.2	176.2	56.9	39.9	176.0										111.6		
A63	123.9	180.2	56.0	17.6													
Q64	122.1	175.8	58.2	31.4	33.1		178.3								122.6		
S65	110.1	179.4	60.7	63.6													
N66	117.3	177.1	55.9	37.3	174.1										110.2		
T67	116.9	174.7	69.1	68.6		21.1											
V68	120.7	176.6	67.3	32.2	21.0	22.7											
K69	118.8	177.1	58.5	32.7	25.5		28.1		42.5								33.6
V70	118.8	179.8	66.9	32.0	22.2	24.2											
I71	118.0	177.7	61.9	34.5	27.1	17.8	7.9										
K72	123.5	178.4	61.3	30.8	24.9		29.5		42.0								32.3
D73	119.1	180.8	57.5	39.4	179.3												
V74	124.9	176.9	66.3	31.9	21.5	25.1											
D75	119.6	177.3	55.3	38.1	172.2												
A76	121.4	179.9	54.8	18.3													
A77	121.4	180.1	54.7	18.2													
I78	119.8	178.3	65.1	38.3	28.3	18.4	15.2										
I79	117.0	180.0	63.5	38.1	31.5	17.2	15.2										
Q80	119.7	177.2	57.9	28.3	33.6		180.7										
N81	115.4	175.4	52.7	37.9	176.0										111.4		
F82	118.3	175.2	56.5	38.2	140.3		129.6										
R83	117.6	181.5	57.3	31.9	27.6		43.7									84.3	

Table 3: Chemical shifts of Shigella flexneri MxiH needles
Chemical shifts are indicated in ppm relative to DSS.

Protein name	Bacterial organism	UniProt identifier	Length
Cluster I			
MxiH	*Shigella flexneri* serotype 6	Q6XVY0_SHIFL	83
MxiH	*Shigella flexneri* serotype 2	MXIH_SHIFL	83
cip-c	*Chromobacterium violaceum*	Q7NVC1_CHRVO	84
PrgI	*Salmonella typhimurium*	PRGI_SALTY	80
BsaL	*Burkholderia pseudomallei*	Q63K18_BURPS	89
EprI	*Escherichia coli*	Q8X2T4_ECO57	79
YsaG	*Sodalis glossinidius*	Q6R8E1_SODGL	85
Cluster II			
AscF	*Aeromonas hydrophila* AH1	Q1EHA3_AERHY	87
AscF	*Aeromonas veronii*	Q6WG33_9GAMM	85
AscF	*Aeromonas hydrophila* AH3	Q699P8_AERHY	81
PscF	*Pseudomonas aeruginosa*	PSCF_PSEAE	85
YscF	*Yersinia pestis*	O68691_YERPE	87
YscF	*Yersinia enterocolitica*	YSCF_YEREN	87
SctF	*Photorhabdus luminescens*	Q7N0U8_PHOLL	84
YscF	*Vibrio parahaemolyticus*	Q87P24_VIBPA	82
Other sequences			
EscF	*Escherichia coli*	Q7DB83_ECO57	73
EscF	*Citrobacter rodentium*	Q93FJ3_CITRO	73

Table 4: Source of primary sequences for multiple sequence alignment

10. Hybrid approach for structural determination of large insoluble biomolecular assemblies at atomic resolution using solid-state NMR and electron microscopy

10.1. Summary

Large biological assemblies play key roles in many important cellular functions, however their structure determination by conventional crystallography and solution NMR methods is challenging. Here, we present a general hybrid approach which combines data originating from two experimental techniques: extensive datasets of constraints obtained by solid-state NMR spectroscopy (ssNMR) and a high-resolution electron density map obtained by cryo-electron microscopy (cryo-EM). The approach employs Rosetta modeling to integrate the two experimental datasets with an energy function based on physical principles. Cryo-EM and ssNMR data complement each other as the cryo-EM density helps restrain the rigid-body placement of protein subunits, while the ssNMR constraints and Rosetta energy define the local protein domain structure and inter-subunit interfaces.

The new hybrid approach was implemented to determine the atomic structure of a large protein assembly present in Gram-negative bacteria, the Type-Three Secretion System (T3SS) needle of *Shigella flexneri* bacteria, which is used during pathogenic infection for the injection of toxic effector proteins inside their target eukaryotic host cell. First, we collected a large number of intra-subunit and inter-subunit distance constraints using ssNMR methods on *in vitro* polymerized needles: carbon-carbon constraints were obtained from sparse ^{13}C-labeled samples and proton-proton constraints from uniformly ^{13}C-labeled samples. Then, Rosetta structure calculations were performed to integrate the ssNMR datasets with a previously published cryo-EM density map (7.7-Å resolution) of isolated needles (Fujii et al, *PNAS* 2012). The hybrid atomic models notably specify

the placement of the non-conserved N-terminus of the needle subunit, and constitute a valuable basis for an atomic understanding of the mechanism of bacterial protein secretion through the T3SS needle.

The structures obtained for the lowest-energy models were cross-validated using an independent set of ssNMR constraints not used in the structure calculations. The calculation results confirm that polymerized needles and isolated needles adopt compatible structures at the atomic level; this compatibility being corroborated at the macroscopic level by scanning transmission electron microscopy (STEM) measurements on polymerized needles. By integrating different sources of experimental data, the new hybrid approach provides the structural basis for understanding a conserved Type-Three secretion mechanism and can be readily applied for high-resolution structural studies of other important, yet poorly characterized, large protein complexes.

Contribution statement

The present chapter forms a manuscript in preparation: "Hybrid approach for structural determination of large biomolecular assemblies at atomic resolution using solid-state NMR and cryo-electron microscopy", Jean-Philippe Demers, Birgit Habenstein, Antoine Loquet, Suresh Kumar Vasa, Stefan Becker, David Baker, Adam Lange, Nikolaos G. Sgourakis.

Karin Giller and S.B. expressed, purified and polymerized in vitro T3SS needles. J.P.D recorded solid-state NMR experiments and prepared processed spectra. J.P.D. and B.H. analyzed the spectra to collect ssNMR constraints. Joe Wall and Beth Lin (Brookhaven National Laboratory) recorded the STEM data. J.P.D. and S.K.V. analyzed the STEM data. N.G.S performed the structural calculation. J.P.D. and N.G.S. carried out the cross-validation of the structure ensemble.

10.2. Background and Motivation

Large molecular assemblies are omnipresent in living cells and responsible for a broad spectrum of biological functions such as cellular motion (molecular motors), cellular structure (cytoskeletal filaments) and molecular transport (bacterial secretion systems). Traditionally, structures of large biomolecular systems have been solved by X-ray crystallography, solution-state Nuclear Magnetic Resonance (NMR) and cryo-electron microscopy (EM). Large systems however pose technical challenges for atomic structural studies using conventional methods[1]: finding an appropriate crystallization condition is a strenuous effort for large multi-component systems; crystallization can be prevented by the presence of flexible or disordered regions or domains; and systems with noncrystallographic symmetry lack the long-range order required to produce a discrete diffraction pattern. On the other hand, very large systems do not exhibit sufficiently fast molecular tumbling to be directly studied by solution-state NMR spectroscopy. As well, the study of small isolated molecular components is not sufficient for a molecular understanding of a large biological system as proteins can adopt different conformations in isolation compared to their assembled form.

Two methods are emerging to tackle the structure determination of intact large assemblies towards gaining a mechanistic insight into their biological function. Technically, both solid-state NMR[2-5] (ssNMR) and cryo-EM [6,7] are not limited by the molecular size of the assembly that they can detect. Density data from cryo-EM defines an overall envelope of the supramolecular assembly under study in a resolution range of 20–8 Å for standard applications and up to 6 Å for favorable systems[1]. Solid-state NMR data provide crucial information on the local structure such as the secondary structure propensity, backbone dihedral angles and inter-atomic distances of up to ~10 Å, which can be detected both within the individual protein domains and across the inter-molecular subunit interfaces.

Cryo-EM and ssNMR data are in principle highly complementary and their use in combination holds great promise for future structural studies. However, a general framework to integrate the different sources of structural information into high-resolution models of multimeric assemblies has been limited by 1) the different levels of resolution provided by each technique that complicates their use in computational methods, the fine-tuning of constraint weights and the assessment of self-consistency between these fundamentally different datasets and 2) the availability of computational methods that would determine the range of conformations consistent with the experimental data, as a function of the degrees of freedom considered.

We introduce a generalized hybrid approach for high-resolution structure determination of supramolecular assemblies which combines high-resolution cryo-EM density maps with extensive datasets of distance constraints obtained from solid-state NMR. We demonstrate the new approach by determining the structure of the T3SS needle of *Shigella flexneri* at atomic resolution (0.4 Å backbone RMSD). The Type Three Secretion System (T3SS), or injectisome, is a supramolecular assembly found in Gram-negative bacteria, such as *Shigella*, *Salmonella*, *Escherichia*, *Pseudomonas* or *Yersinia*[8], which serves to deliver toxic effector proteins into their target eukaryotic host cell during infection[9,10]. The extracellular transport needle forms a super-helical assembly of multiple copies of the needle subunit protein called MxiH in *Shigella flexneri* and PrgI in *Salmonella typhimurium*. The current study thus extends our structural studies of T3SS needles, which include the atomic model of *Salmonella typhimurium*[11,12] using ssNMR data and helical parameters from scanning transmission electron microscopy (STEM), the ssNMR resonance assignment of *Shigella flexneri* MxiH needles[13] which allowed to identify a common architecture for T3SS needles, the study of dynamics and conformational heterogeneity of MxiH needles using DNP-enhanced ssNMR[14], and assignment strategy using sparse ^{13}C samples[15-17] or highly deuterated proteins[18].

The hybrid approach (Fig. 1) combines the 7.7-Å cryo-EM density map reconstructed using 100 000 needle segment images[19] with extensive structural information obtained from ssNMR: 162 backbone dihedral angles and 996 carbon-carbon distance constraints from proton-driven spin diffusion (PDSD)[20] experiments. The data is integrated together with a high-resolution energy function using the program Rosetta to produce a hybrid atomic structure of the T3SS needle of *Shigella flexneri*. The calculated structures are validated using 691 independent carbon-carbon and proton-proton distance constraints from ChhC and NhhC experiments[21,22]. With 12 distance constraints per residue in the calculation set and 8 distance constraints in the validation set, the calculated models are among the most well-defined structures in solid-state NMR. Moreover, the atomic resolution structures establish the beforehand unknown arrangement of the N-terminal segment (residues 1-11), which are not conserved and adopt a species-specific conformation.

10.3. Hypotheses and Method Summary

Hypotheses:

The atomic structure of *Shigella flexneri* T3SS needles is similar to the structure of *Salmonella typhimurium* needles for the region L12-R83. The inter-molecular interfaces observed in *Salmonella* needles will be present in *Shigella* needles.

T3SS needles obtained by shearing off from the bacterial surface and needles produced by *in vitro* polymerization adopt the same subunit structure and helical arrangement. The distance constraints detected in solid-state NMR experiments are compatible with the cryo-EM density map of sheared needles.

The N-terminal rigid extension S2-T11 is longer in *Shigella* needles and can occupy the protrusion observed in the cryo-EM density map between subunits *i* and *i* – 5.

Method summary:

The generalized hybrid approach presented here comprises six tasks, including 4 steps for atomic structure determination and 2 steps for validation (Fig. 1):

1) Collection of ssNMR and cryo-EM structural information

Backbone dihedral angles are obtained from the secondary chemical shifts of the needle subunit protein. Carbon-carbon distance constraints were obtained from PDSD experiments recorded on 1-glucose- and 2-glucose-labeled *Shigella* needles. Proton-proton distance constraints were obtained from ChhC and NhhC experiments recorded on uniformly-^{13}C-labeled needles.

2) Disambiguation of ssNMR chemical shift ambiguities

The fold and inter-molecular interfaces are first identified using unambiguous cross-peaks and large numbers of distance constraints between amino acids pairs and a preliminary map of the needle architecture is produced. Using this map, distance cross-peaks are further classified as unambiguous or ambiguous.

3) Disambiguation of ssNMR subunit ambiguity

The interface assignment of distance constraints is determined through successive rounds of structure calculations.

4) Flexible structure calculation integrating ssNMR and cryo-EM data

Structure calculations start from an array of helical polypeptides and employ the "fold-and-dock" Rosetta protocol. In addition to ssNMR constraints, an EM density correlation term is applied during the structure calculation. Chemical shift and interface ambiguities are verified at each iteration, followed by a final refinement stage.

5) Cross-validation of atomic structure using independent local data

The individual models are cross-validated using an extensive dataset of solid-state NMR constraints not used in the calculation.

6) Confirmation of macroscopic compatibility for different sample preparations

The structural compatibility of the sample preparations is confirmed by the correlation to the cryo-EM density map and by the independent determination of *in vitro*-polymerized needle mass-per-length by STEM measurements.

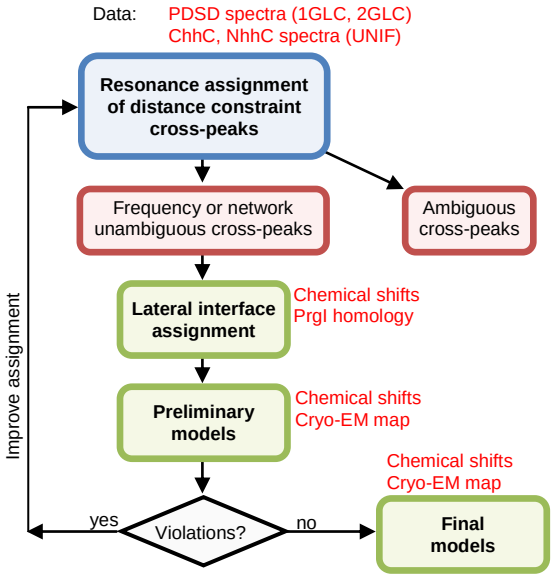

Figure 1: Flow-diagram of iterative assignment and modeling procedure. Flow chart presenting the assignment of NMR distance constraints and molecular modeling through the hybrid structural determination approach. Steps of NMR data analysis are colored blue, with the resulting datasets illustrated as red rounded rectangles. Rosetta modeling steps are colored green and the additional data used at each modeling step, including the high-resolution cryo-EM density map, is indicated on the side in red font. The preliminary models are derived from a reduced set of distance constraints coming only from 2-glucose spectra. The final models employ distance constraints from all datasets. Cross-peaks determined to be structurally ambiguous from the last preliminary models are used as ambiguous constraints.

10.4. Materials and Methods

10.4.1. Sample preparation

WT *Shigella flexneri* T3SS needles were prepared following the established protocol[11,13] for expression, purification and *in vitro* polymerization of T3SS needle proteins. Three samples were produced by labeling the subunit protein MxiH during

bacterial expression employing $^{15}NH_4Cl$ as nitrogen source and either [U-$^{13}C_6$]glucose (uniform labeling), [1-^{13}C]glucose (1-Glc labeling) or [2-^{13}C]glucose (2-Glc labeling) as carbon source. The polymerization was carried out at 37 °C during sixteen days and produced approximately 20 mg of labeled material each time. Pellets of MxiH needles were obtained by ultra-centrifugation (40,000 rpm at 15°C during 30 min in a Beckman TL-100.1 rotor), washed 5× by re-suspending the pellets in fresh buffer and ultra-centrifugation, and then transferred into 4.0-mm MAS rotors.

10.4.2. Solid-state NMR

Solid-state NMR experiments were conducted on spectrometers operating at 600 MHz, 800 MHz and 850 MHz ^{1}H Larmor frequency (Avance I and Avance III, Bruker Biospin, Germany) at MAS rates in the range 10.5–12.5 kHz. The sample temperature was maintained at 5.5°C by monitoring the temperature using the ^{1}H chemical shift of water in reference to the methyl ^{1}H signal of DSS[23]. A ramped cross-polarization with contact time of 0.7-1.2 ms was used for the initial ^{1}H-^{13}C and ^{1}H-^{15}N transfers. For ^{13}C-^{13}C correlation experiments, carbon-carbon mixing was accomplished via PDSD with the mixing times ranging from 300 ms to 850 ms. Experiments with short mixing times (50 ms or 100 ms) were also recorded to identify intra-residual and sequential correlations. Proton decoupling with an r.f. frequency of 83.3 kHz was employed during evolution periods and acquisition, using either SPINAL-64[24] or SWf-TPPM[25] with a RFDR supercycle[26] and a tangential sweep[27] (N = 11, sweep window d = 0.25, cut-off angle tco = 55°, phase angle θ = 15°). For spectra recorded on 800 MHz and 850 MHz spectrometers, carbon-nitrogen scalar couplings were removed by applying c.a. 2 kHz of waltz-16[28] decoupling on ^{15}N during acquisition and ^{13}C evolution periods. On the 600 MHz ^{1}H frequency spectrometer, spectra were recorded in double-resonance mode to increase sensitivity.

Nuclei	Mixing	Labeling	^{1}H freq. (MHz)	AQ_1; AQ_2 (ms)	TD_1; TD_2	SW_1; SW_2 (ppm)	Recycling delay (s)	No. of scans	Total time
^{13}C-^{13}C	PDSD 300 ms	1-Glc	600 MHz	14 ; 16	1120; 1274	265; 265	3.0	64	2d 19h
^{13}C-^{13}C	PDSD 850 ms	1-Glc	600 MHz	15 ; 17	900; 1354	199; 265	3.0	128	5d 16h
^{13}C-^{13}C	PDSD 700 ms	1-Glc	800 MHz	8.5; 13.7	520; 1600	153; 292	2.2	448	7d 22h
^{13}C-^{13}C	PDSD 400 ms	1-Glc	850 MHz	17 ; 21	1722; 2992	237; 334	2.5	80	4d 17h
^{13}C-^{13}C	PDSD 850 ms	1-Glc	850 MHz	18 ; 22	1824; 3134	237; 334	2.4	96	6d 16h
^{13}C-^{13}C	PDSD 850 ms	1-Glc	850 MHz	8.5; 17	530; 2420	146; 334	2.0	720	12d 17h
^{13}C-^{13}C	PDSD 300 ms	2-Glc	600 MHz	17 ; 21	1360; 1674	265; 265	3.1	80	4d 20h
^{13}C-^{13}C	PDSD 850 ms	2-Glc	600 MHz	15.5; 17	930; 1354	199; 265	2.6	176	6d 12h
^{13}C-^{13}C	PDSD 850 ms	2-Glc	800 MHz	8.7; 13.7	512; 1600	146; 292	2.2	496	9d 1h
^{13}C-^{13}C	PDSD 400 ms	2-Glc	850 MHz	15 ; 21	1520; 2992	237; 334	2.2	64	2d 23h
^{13}C-^{13}C	PDSD 850 ms	2-Glc	850 MHz	16 ; 20	1620; 2846	237; 334	2.6	96	6d 12h
^{15}N-^{13}C	NhhC 250 µs	Uniform	800 MHz	11.5; 15	80; 2076	43; 346	2.0	7168	13d 15h
^{13}C-^{13}C	ChhC 250 µs[a)]	Uniform	800 MHz	9 ; 15	432; 2076	120; 346	2.0	1344	13d 15h
^{13}C-^{13}C	ChhC 250 µs[b)]	Uniform	800 MHz	9 ; 15	432; 2076	120; 346	2.0	928	9d 15h

Table 1: List of NMR experiments used in obtaining long-range constraints

a) 87.5 µs for all CP contact times, b) 300 µs for initial CP contact time, 255 µs for bracketing CP contact times

For both 1-Glc and 2-Glc labeling schemes, PDSD spectra were recorded in multiple conditions (Table 1). From the cross-peak tally for 2-Glc spectra (Table 2), we observe that the proportion of long-range cross-peaks increases compared to intra-residue and sequential cross-peaks. This demonstrates that long mixing time allows sufficient time for spin diffusion to remote distances. However, even longer mixing times (>1s) would not be advisable as sensitivity would reduce due to ^{13}C longitudinal relaxation and increase in measurement times.

Experiment	Intra	Seq.	IR(2-4)	LR(>4)	Total	Ambig.
PDSD 400ms, 850MHz	441	309	103	**58**	911	42
PDSD 850ms, 850MHz	360	399	168	**109**	1036	51
PDSD 300ms, 600MHz	609	552	176	**150**	1487	89
PDSD 850ms, 600MHz	635	841	476	**436**	2388	318
PDSD 850ms, 800MHz	673	795	440	**384**	2292	293
Total	2718	2896	1363	1137	8114	793

Table 2: Number of assigned cross-peaks in [2-^{13}C]-Glc spectra

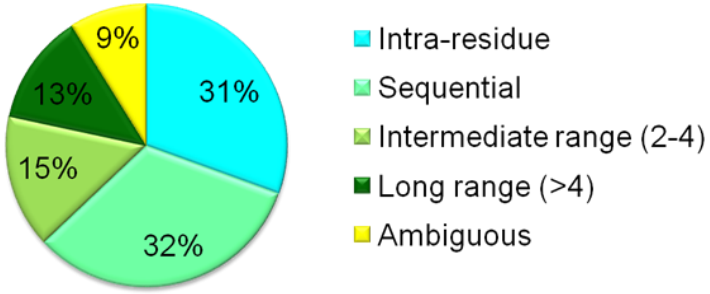

Figure 2: Distribution of cross-peaks in [2-^{13}C]-Glc labeled spectra

Since a prolonged spin diffusion time distributes the initial magnetization to a large number of labeled carbons, measurement with a high SNR is critical in order to obtain a spectrum with high information content. Indeed, most long-range cross-peaks are obtained from two spectra, long mixing time PDSD spectra (850ms) recorded on the 600 MHz and 800 MHz spectrometers, both acquired with high SNR.

When possible, SW_1 was reduced by setting the upper limit of the spectrum at ≈143 ppm in the indirect dimension and using time proportional phase incrementation (TPPI) acquisition mode (Figure 3). This results in the folding of the carbonyl band (~172 to 183 ppm) to a region where few resonances are present (~126 to 115 ppm). The carbonyl band is subsequently recovered during processing.

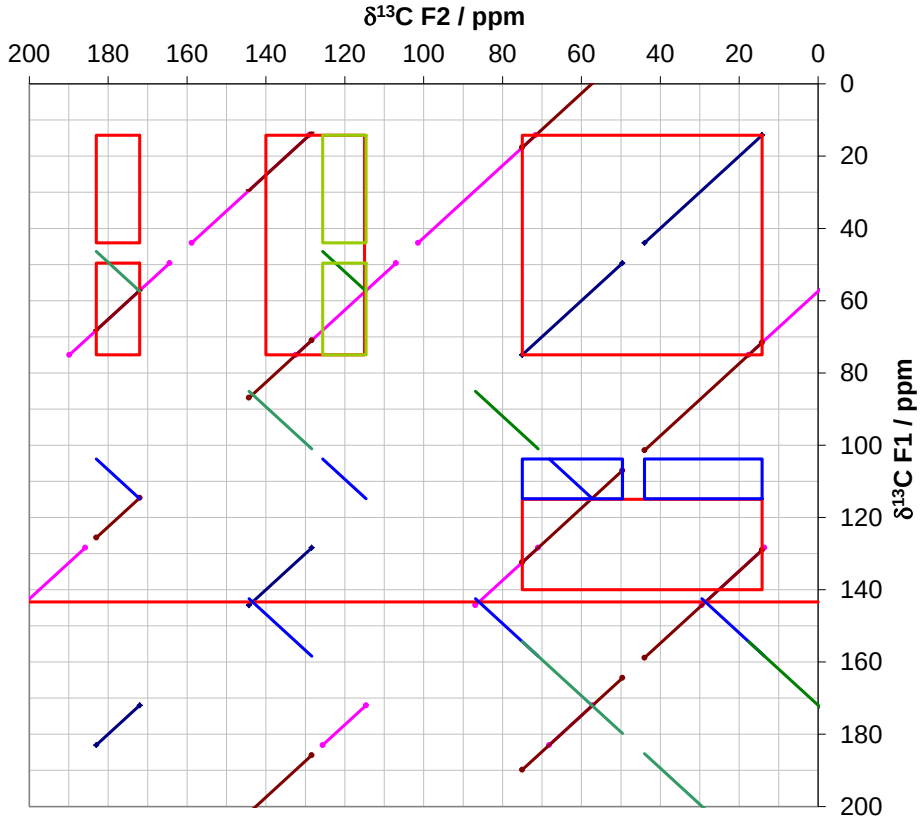

Figure 3: Prediction of diagonal side-bands and spectral folding for a ^{13}C–^{13}C PDSD spectrum. The ^{1}H Larmor frequency is 800 MHz and the MAS frequency is 11.5 kHz. An equivalent spectrum can be recorded at 850 MHz with a MAS frequency of 12.2 kHz. Red boxes indicate the regions where spin diffusion cross-peaks are expected. In the indirect dimension, the spectrum is recorded in a spectral window spanning 0–142 ppm. This results in the folding of the carbonyl-aliphatic cross-peaks (blue boxes, ~110 ppm in F_1). The green boxes (~120 ppm in F_2) indicate the position of the first side-bands for aliphatic-carbonyl cross-peaks, which partially overlaps with the aromatic-aliphatic cross-peaks (red box at ~130 ppm in F_2).

10.4.3. Processing and peak picking of ssNMR spectra

Spectra were processed using Bruker Topspin 2.1 and the NMRpipe software[29]. A quadratic sine window function is employed in both dimensions, with sine bell shift (SSB) parameters in the range 3.4–3.8, and FIDs are zero-filled up to the second-next power of two. Polynomial baseline correction was applied in both frequency domains. Spectra were analyzed with Sparky [30] and CcpNmr Analysis[31,32].

We carried out peak picking manually on the basis of our previously reported sequential chemical shift assignment of MxiH needles[13] (available in BMRB entry 18651). We first discarded peaks corresponding to artifacts such as spinning sidebands and reflections of the auto-peak diagonal and we assigned peaks corresponding to intra-residual and sequential correlations, for which cross-peaks are generally also present in short mixing time PDSD spectra (50 ms – 100 ms). Other cross-peaks correspond to intermediate range correlations (between residue *j* and k, $2 \leqslant |j-k| \leqslant 4$) or long range correlations ($|j-k| \geqslant 5$, either intra-molecular or inter-molecular).

The average resonance frequency for a given nucleus is obtained from intra-residue and sequential cross-peaks for all spectra (BMRB entry 18651) or for a single spectral dimension if a sufficient number of cross-peaks are available in one spectrum (>5).

To be retained for analysis, a cross-peak must have a signal-to-noise ratio higher than 4.2. The noise in each spectrum is estimated by taking the average of the central 16 out of 20 trials, each trial computing the noise as median of 128 randomly sampled absolute data heights from the spectrum.

10.4.4. Determination of experimental isotopic labeling pattern

The use of sparse ^{13}C labeling schemes and the high spectral homogeneity of the MxiH protein affords very high ^{13}C resolution, with ^{13}C line-widths ranging from 0.09 to 0.25 ppm (Figure 9.3).

The resonance assignment uncertainty, i.e. the standard deviation of peak positions over all spectra, is very small (Fig. 4) as well: on average 0.04 ppm for ^{13}C and 0.03 for ^{15}N, and at most 0.09 ppm in both cases (see BMRB entry 18651).

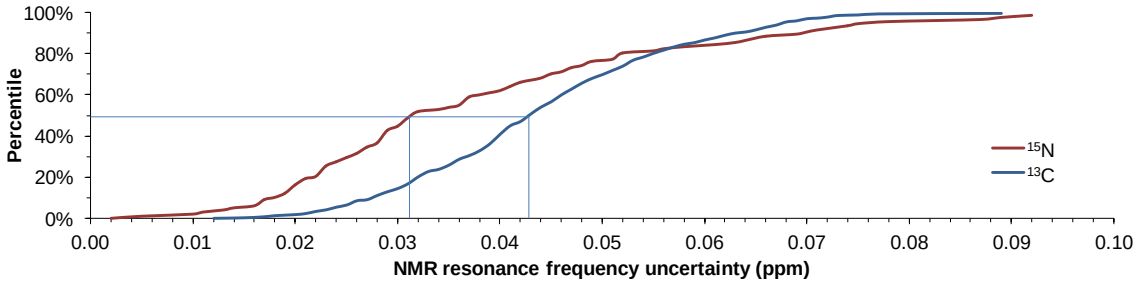

Figure 4: Distribution of uncertainty for the chemical shift assignment of MxiH needles

In order to further improve the accuracy of the chemical shift assignment for long mixing-time experiments, we re-calculated the full table of average resonance frequencies on an individual basis for each dimension of each spectrum, when enough intra-residue and sequential cross-peaks were available for that spectrum. This corrects for small but systematic spectrum-to-spectrum deviations, which can be due to differences in acquisition parameters or processing, slightly different sample temperatures or differences in recoupling conditions (which can vary according to the ^{13}C labeling scheme).

Combined with the high sample homogeneity, our method allows the use of small tolerance windows, which results in a drastic reduction of the number of assignment possibilities for distance cross-peaks. For ^{13}C resonances, we used tolerance

windows of ±0.15 ppm for sparsely-labeled spectra and ±0.2 ppm for uniformly-labeled spectra. For ^{15}N resonances, ±0.2 ppm windows were used.

Figure 5 illustrates the relation between the width of the tolerance window and the number of assignment ambiguities per cross-peak, as computed from the assignment of MxiH needle subunits. The number of isolated resonances and resonances with one ambiguity falls off rapidly as the window becomes larger. For the same window, the proportion of resonances with low ambiguity is lower for the sparse labeling schemes as the reduced number of carbons results in significant spectral simplification. The average number of ambiguities scales nearly linearly with the size of the tolerance window. For a long mixing PDSD step where magnetization can potentially be transferred from one carbon to any other carbon resonance, the number of ambiguities scale as $n_{amb} \propto w_1 \cdot w_2$, where w_n is the size of the window in the n^{th} dimension, or $n_{amb} \propto w^2$ for windows of identical sizes. Uniform and 2-Glc labeling, with respective tolerance windows of 0.20 ppm and 0.15 ppm, therefore have an average number of ambiguities of 3.1 and 1.8 for a resonance line in a 1D spectrum, but these numbers are increased to 9.5 and 3.4 ambiguities for a cross-peak in a 2D PDSD spectrum. The number of ambiguities for distance cross-peaks can also be reduced by increasing the number of recorded dimensions, combining multiple steps of short-range and long-range magnetization transfer. For example, an approach combining 2-glucose ^{13}C labeling and the recording of 3D NCACX (SPECIFIC-CP, PDSD) spectra was presented for the sequential assignment and the collection of distance constraints on *Salmonella typhimurium* T3SS needles[16].

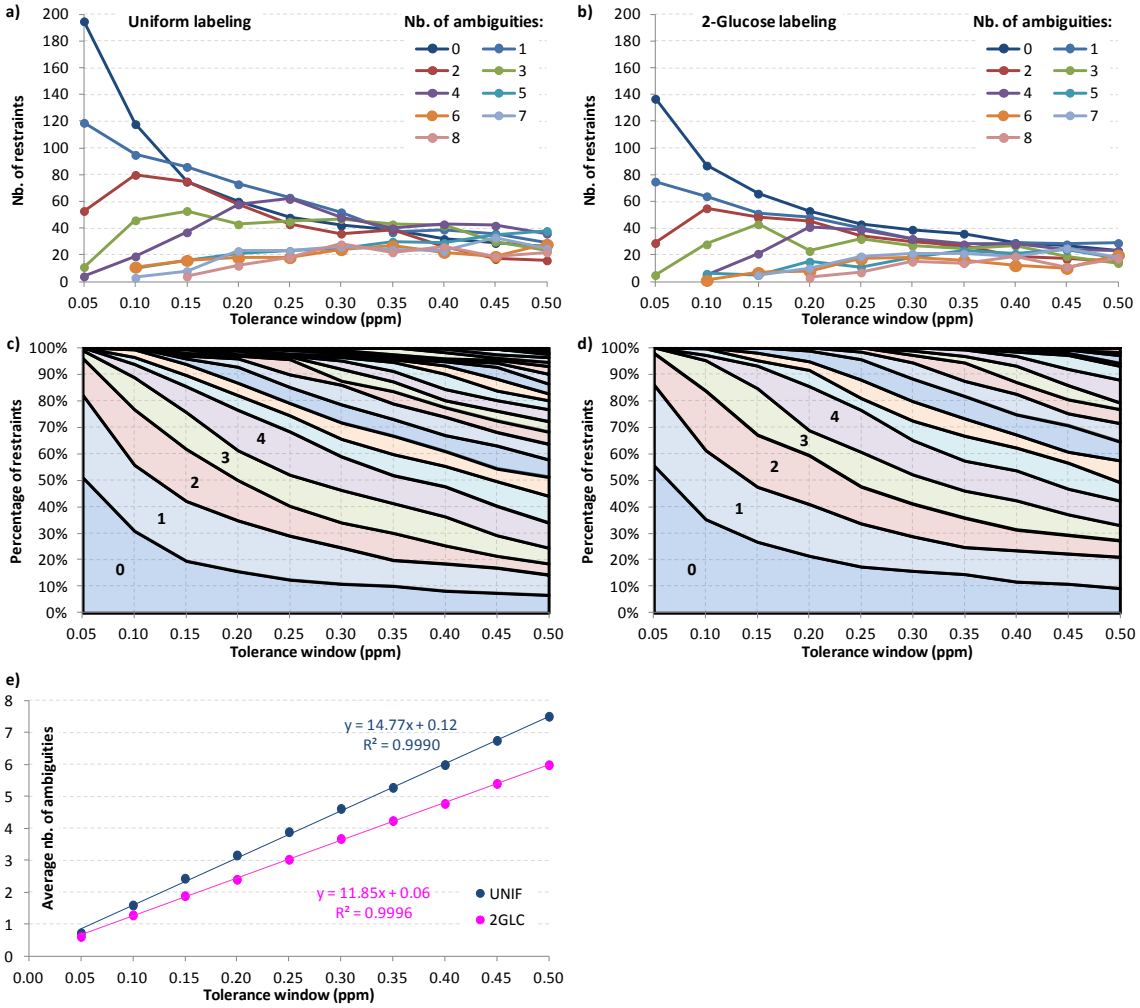

Figure 5: Influence of chemical shift tolerance window. For all ^{13}C frequencies, the number of additional frequencies present in the tolerance window was counted including all resonances (uniform labeling, **a** and **c**) or only those theoretically present[33], excluding scrambling, in the 2-glucose labeling (**b** and **d**).

According to Figure 5, the uniformly-labeled sample would yield spectra which are nearly three times as ambiguous as sparsely-labeled samples. However, we also observed that the experimental ^{13}C labeling patterns for the two sparse labeling schemes differ from the ideal patterns previously reported for 1-glucose[34] and 2glucose[33]. We therefore aimed to avoid cross-peak assignments which were incompatible with the isotopic labeling pattern produced by 1-Glc and 2-Glc labeling schemes. For this

purpose, the ideal labeling patterns of glucose-labeled samples was initially considered[33,34]. However, other unexpected intra-residue cross-peaks are observed in short and intermediate mixing time PDSD spectra in addition to the strong cross-peaks predicted on the basis of the ideal labeling patterns. As evaluated from the signal intensity of unexpected intra-residue cross-peaks, the scrambling is less present in [2-^{13}C]-glucose-labeled proteins compared to [1-^{13}C]-glucose. The scrambling can be due to subsequent rounds in the citric acid cycle or involvement of other metabolic pathways[17]. The precise labeling patterns for glucose-labeled samples were confirmed by inference from intra-residual and sequential cross-peaks. A detailed analysis was carried for [2-^{13}C]-glucose labeling (Figure 6).

Many instances of scrambling are detected; however, some atom combinations are never labeled simultaneously. A stark example is the neighboring C′ and C_α atoms, for which cross-peaks were not detected in 12 types of amino acid, and extremely weak cross-peaks were detected for glycine, alanine and serine residues. Although scrambling is present, sharp spectral lines are preserved for the 2-glucose labeling. It can thus be inferred that the probability of simultaneous labeling is low, and that the scrambling is much less intense compared to [2-^{13}C]-glycerol and [1,3-^{13}C]-glycerol samples, which have a lower resolution but a higher sensitivity compared to [2-^{13}C]-glucose samples[12].

Glycine (G, Gly)

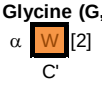

Alanine (A, Ala)

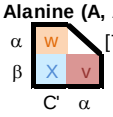

Serine (S, Ser)

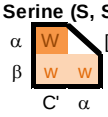

Aspartic acid (D, Asp)

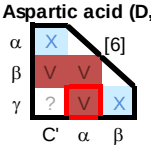

Asparagine (N, Asn)

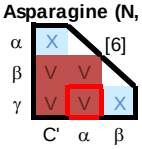

Threonine (T, Thr)

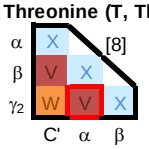

Glutamic acid (E, Glu)

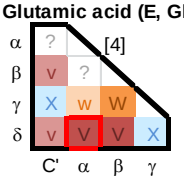

Glutamine (Q, Gln)

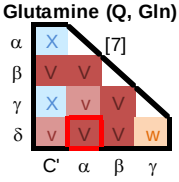

Proline (P, Pro)

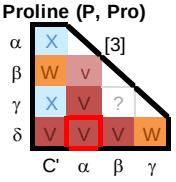

Arginine (R, Arg)

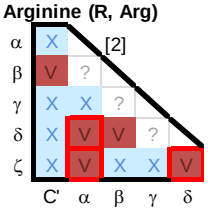

Isoleucine (I, Ile)

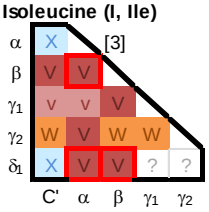

Lysine (K, Lys)

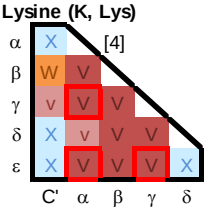

Phenylalanine (F, Phe)
Tyrosine (Y, Tyr)

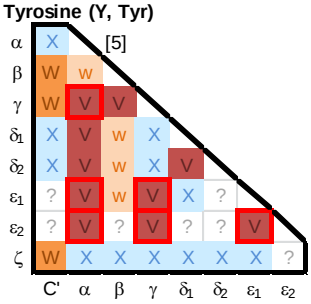

Leucine (L, Leu)

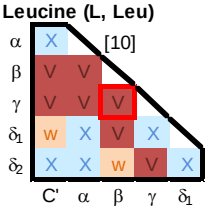

Valine (V, Val)

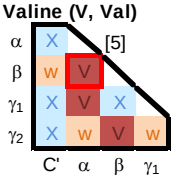

Legend

X	No peaks observed
w	Very weak peaks observed, for only few residues
W	Weak peaks observed for a majority of residues
v	Weak and strong peaks observed
V	Strong peaks observed for a majority of residues
?	Too few data, inconclusive
	Expected strong peaks, according to ideal labeling pattern

Tryptophan (W, Trp)

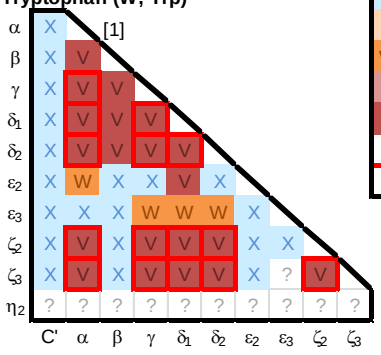

Figure 6: Experimental [2-^{13}C]-Glc isotopic labeling pattern. Observed intra-residue cross-peak patterns for the 17 amino acid types present in solid-state NMR spectra of MxiH needles. The number of residues for each type is indicated in square brackets. Due to the similarity of their anabolism pathway, the tallies for phenylalanine and tyrosine have been combined.

10.4.5. Assignment of chemical shift ambiguities

For each cross-peak, all resonance assignment possibilities within the tolerance window are considered. If only a single possibility exists, the cross-peak is classified as frequency unambiguous. The classification of remaining cross-peaks is done as follows:

For a given cross-peak, assignment possibilities highly incompatible with the preliminary map (Fig. 8) are eliminated. If a single assignment possibility remains, the cross-peak is classified as network unambiguous. In the case of multiple remaining possibilities, the cross-peak is classified as network unambiguous only if the average chemical shift deviation of one assignment is significantly smaller than for other possibilities (at least 0.05 ppm less); otherwise the cross-peak is classified as ambiguous.

10.4.6. Rosetta structure calculations

The structure calculations were performed by our collaborators at the University of Washington and at the Laboratory of Chemical Physics, NIDDK/NIH. The structure calculations were done using the Rosetta symmetric modeling framework[35] extended to helical symmetry[11]. Starting from a helical array of 29 polypeptide chains (83-residue), the fold-and-dock protocol uses symmetric, backbone fragment and sidechain Monte-Carlo trials in torsion angle space to explore internal subunit conformations, and rigid-body moves to explore the subunit arrangement that are propagated to symmetry-related subunits according to a user-defined set of transformations provided as a symmetry definition file (supplementary material). While the MxiH needle solid-state

NMR chemical shifts[13] were used to select 3- and 9- residue backbone fragments, the NMR distance constraints were used to restrain the internal degrees of freedom (backbone dihedral angles and sidechain torsions) together with the 6-rigid body degrees of freedom that define the subunit arrangement and helical parameters of the needle filament.

In each round of structure calculations, we used two criteria to assign the raw NMR data (atom pairs) into the different interfaces and exclude outliers that are consistently violated in the low-energy models:

a) A constraint was included in the next round if it was satisfied in more than 30% of the previous round 10 lowest-energy models, according to an upper limit of 12 Å and

b) A constraint was included in the next round if it can be consistently assigned to the same interface in more than 70% of the previous round 10 lowest-energy models.

Using this iterative Ansatz, we concluded to a refined peaklist to be used for the subsequent round of structure calculation. An energy term that measures correlation of the entire 29-subunit system to the 7.7-Å cryoEM density map was also applied as described previously[36] to restrain the helical parameters of the needle filament. The EM and NMR constraint weights were optimized in a series of calculations performed with increasing weights while monitoring the total number of violations and Rosetta energy in the resulting models (Fig. 7).

The procedures for ranking, selection and validation of final 3D structure models are described in the results section. A detailed description of the protocol as well as example script files are available in supplementary information.

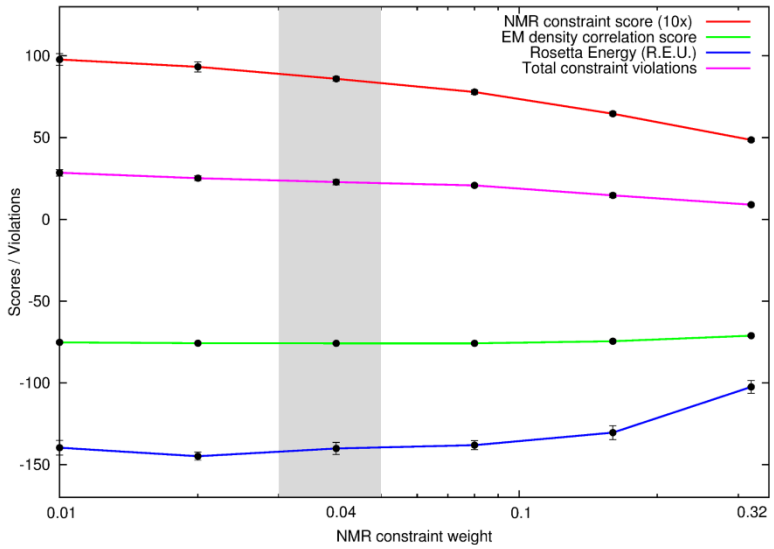

Figure 7: Calibration of ssNMR constraint weights. Individual score terms and total ssNMR constraint violations as a function of increasing weight of the NMR constraint term (relative to the Rosetta force field4) used in independent structure refinement calculations (x-axis, in logarithmic scale). The EM score (green) measures agreement with the 7.7 Å cryo-EM density map1 in negative units, as described previously5. Error bars represent 1 standard deviation observed in 10 calculated structures for each weight value. The EM correlation term is reported in the same scale as the Rosetta Energy (blue), while the plotted NMR constraint penalty score (red) is scaled up by a factor of 10. A favorable range of weights (0.03–0.05) used in the final calculations is indicated with the shaded area. A constant EM score weight of 0.05 was used in all refinement calculations, optimized using a similar grid-search procedure. The NMR constraint score uses a flat-bottom potential with an upper limit of 9 Å and an exponential penalty function, as outlined in online methods. R.E.U: Rosetta Energy Units.

10.4.7. Scanning Transmission Electron Microscopy (STEM)

Measurements were carried out at the STEM facility of the Brookhaven National Laboratory (Upton, NY, USA). The BNL microscope (Fig. 14b) operates at a voltage of 40 keV and produces a finely focused electron beam of approximately 0.25 nm in diameter.

Three sample preparations were investigated: straight MxiH needles, 3x diluted needles and 10x diluted needles (Table 3), with most images obtained from the 10x dilution. Tobacco mosaic virus (TMV) particles were added for internal calibration and

as a quality control for the sample preparation. Samples are deposited on a thin carbon substrate and quickly freeze-dried. The sample is maintained at -160°C during measurement, which eliminates contamination and reduces mass loss. The mass loss for protein samples is typically 2.5% at a dose of 10 el/Å^2 used on a 0.512 micron scan and is corrected by the internal calibration of STEM images.

Dilution	Scan width (μm)	Number of images used for analysis	Number of TMV image segments	Number of needle image segments
1x	1.024	3	32	381
3x	1.024	5	72	456
3x	0.512	2	21	92
10x	1.024	60	1035	3138
10x	0.512	1	13	12
	Total:	71	1173	4079

Table 3: Preparation of MxiH needles for STEM

The analysis of the images was done using the PCmass 3.2 software. The default quality-of-fit parameters specified in the software (e.g. r.m.s.d. of background pixels, and r.m.s.d. image minus best-fit model) were used to determine the validity of each individual image segment. Image segments are selected for well-separated individual needles in areas of uniform background (Fig. 13). The TMV particle segments are fitted with the "TMV Rod" model and the MxiH needle segments are fitted with the "9nm Rod-GC" model (solid rod). For each scan size (0.512 or 1.024 μm), the size of the integration radius was calibrated for the two models (Table 4). Continuous mass-per-length values for a single TMV particle or MxiH needle were obtained by following the filament trace. The tracing was repeated for different radii. The normalized mass-per-length values are present in Figure 8, with the error bars corresponding to the standard deviation.

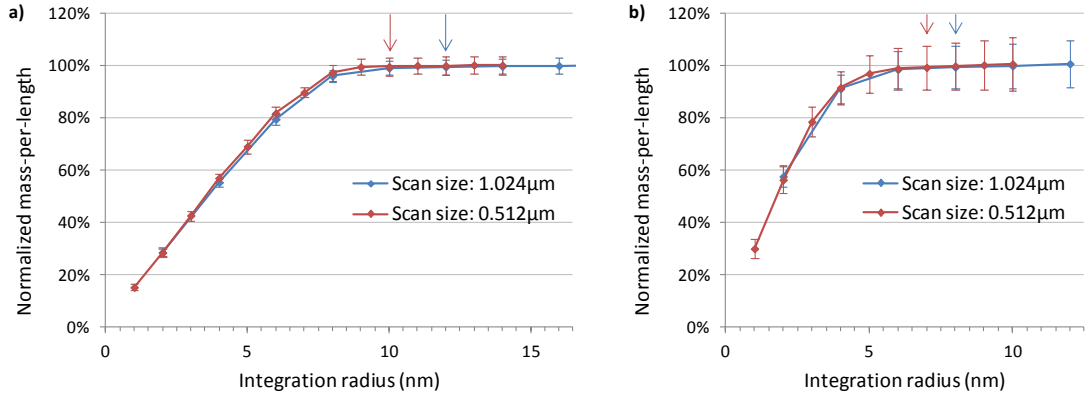

Figure 8: Calibration of integration radius for STEM image analysis. Values were normalized to the average of the three largest integration radii. a) TMV Rod model used for integration of TMV particles, b) 9nm Rod-GC used for the integration of MxiH needles. The radii in image analysis are indicated by arrows.

Scan width (µm)	Model	Integration radius (nm)	Integration length (nm)
1.024	TMV Rod	12	36
0.512	TMV Rod	10	36
1.024	9nm Rod-GC	8	30
0.512	9nm Rod-GC	7	30

Table 4: Calibrated integration parameters for STEM image analysis

10.5. Results and Discussion

10.5.1. Collection of ssNMR constraints and rapid identification of the fold and inter-molecular interfaces

We have previously realized the NMR chemical shift assignment of MxiH needles[13], allowing us to identify the secondary structure of MxiH subunit proteins in their assembled state. Solid-state NMR experiments employing short PDSD mixing times (<100ms) were employed to obtain intra-residue and sequential amino acid connection information. We now recorded a set of diverse and complementary experiments employing long PDSD mixing times (Table 1) which provided a large number of cross-peaks corresponding to intermediate and long-range distance

constraints. Long mixing time PDSD experiments[20,37] were recorded on [1-^{13}C]glucose (1-Glc) and [2-^{13}C]glucose (2-Glc) labeled protein samples (Fig. 10). ChhC and NhhC experiments[21,22] were recorded on a uniform-^{13}C labeled sample. In order to ease the detection of long-range cross-peaks, we recorded individual spectra with high signal-to-noise ratio.

From the 1-Glc and 2-Glc sets of spectra, we can rapidly identify pairs of amino acids which are certain to be in close distance proximity due to unambiguous cross-peaks and large numbers of distance constraints between those amino acids. Those anchor points, in addition to the previously established secondary structure[13], serve to determine the fold of the MxiH subunits in the context of the needle assembly. Amino acid pairs related by at least two frequency-unambiguous cross-peaks or by four or more cross-peaks in a given labeling scheme are used as anchors to produce a preliminary map of the *Shigella* needle architecture (Fig. 9a).

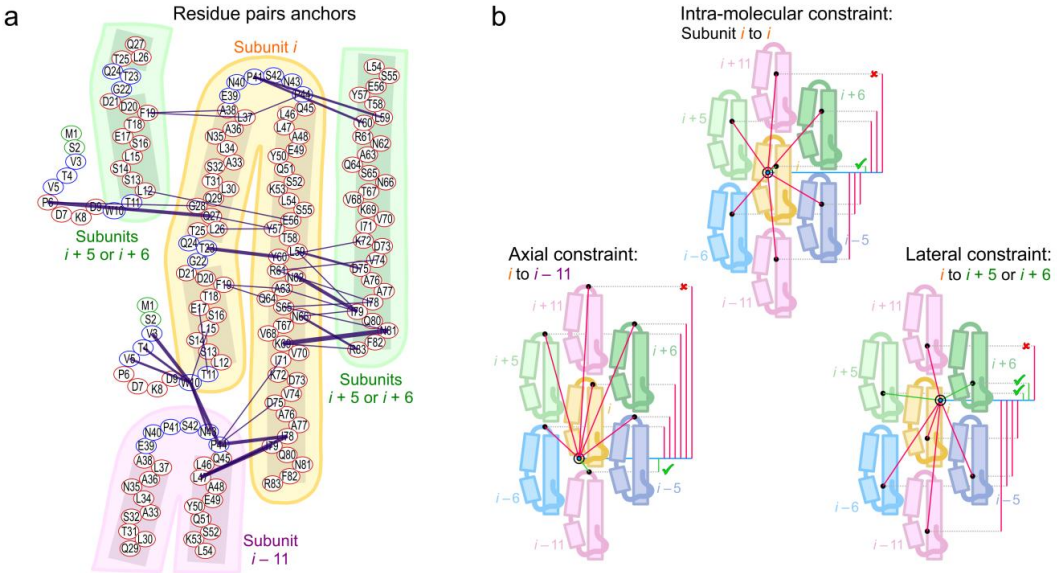

Figure 9: Preliminary map of the Shigella flexneri needle architecture. **(a)** Anchor point identification. Proximity anchors are identified by at least two unambiguous (corresponding to well-resolved and readily assigned cross-peaks) or abundant (≥ 4) contacts in spectra of [1-^{13}C]-glucose and [2-^{13}C]-glucose labeled MxiH needles (blue lines, line thickness proportional to the number of contacts). **(b)** Three examples for ssNMR constraint ambiguities arising from distinct intra-molecular and inter-molecular interfaces in MxiH needles. Pink lines indicate interface assignments of a given contact that are inconsistent with the MxiH needle structure and green lines the correct interface assignments.

A cluster of contacts between the two anti-parallel alpha-helices (e.g. F19-A63/Q64, T23-Y60, L26/Q27-Y57) indicates that MxiH subunits adopt a typical helix-loop-helix fold. Residues N43, P44 and L47 in the loop region make contacts with the end of the C-terminal alpha-helix (e.g. P44-I78, L47-I78/79) as well as with the rigid N-terminal segment (W10-N43/P44), indicating that subunit (*i*) and subunit (*i* – 11) of the helical assembly are arranged head to tail on top of each other forming an inter-molecular axial interface. An extensive lateral interface comprises a dense network of contacts formed between the C-terminal regions L59-K69 of subunit (*i*) and K72-R83 of subunits (*i* + 5) and (*i* + 6). Lateral contacts are also found between the loop region and both the N-terminal helix (F19-L37/A38) and the C-terminal helix (P41-L59/Y60). The rigid N-terminal extension (S2 to T11) is curved in its middle as indicated by multiple contacts between tryptophan W10 and N-terminal residues V3-V5. Further contacts (P6-Q27/G28) indicate a lateral inter-molecular association between the N-terminal extension and the central region of the N-terminal helix which follows a slight kink at residues G22-Q24. This map confirms that the protein fold and inter-molecular interfaces identified in *Salmonella typhimurium* T3SS needles[11] are also present in *Shigella flexneri* needles.

10.5.2. Assignment of a large number of distance constraints and disambiguation of chemical shift ambiguities

Using the preliminary map, we proceed to the disambiguation of all ssNMR distance constraint cross-peaks collected in the 1-Glc and 2-Glc spectra (Fig. 10a). Assignment ambiguity exists at two levels: chemical shift ambiguity and subunit ambiguity. Chemical shift ambiguity relates to the identification of carbon nuclei which give rise to the cross-peak. Subunit ambiguity exists as each cross-peak can arise due to either of 1 intra-subunit and 6 different inter-subunit atom pair combinations (Fig. 9b): intra-subunit, (*i*) to (*i*); inter-subunit, lateral: (*i*) to (*i* ± 5), or (*i*) to (i ± 6); and inter-subunit, axial: (*i*) to (*i* ± 11). The presence of multiple, distinct interfaces could potentially complicate the subunit-subunit assignment of ssNMR constraints. However, it is possible to take advantage of the particular architecture of helical assemblies, as the symmetry of the architecture dictates that subunits (*i* ± 5) and (*i* ± 6) are located within 1 axial translation (l) relative to subunit (*i*), and subunits (*i* ± 11) within 2 axial translations.

As demonstrated in Fig. 9b, we can utilize the short axial translation between two amino acid pairs in the preliminary map in order to classify a distance constraint as intra-molecular, axial or lateral. One subunit ambiguity remains however for lateral constraints, as subunit (*i* + 5) and (i + 6) have similar axial translation within the assembly. Using this strategy, the need to produce an additional mixed-labeled sample in order to identify inter-molecular interactions is eliminated. Chemical shift ambiguities which clearly do not fit any of the three categories are also excluded, allowing further disambiguation of cross-peaks. The distance restraints collected from the 1-Glc and 2-Glc spectra were classified as unambiguous if the chemical shift ambiguities could be resolved (Total: 1190 correlations in the initial list, 1-Glc: 424, 2-Glc: 766), or as ambiguous cross-peaks otherwise. Ambiguous correlations and correlations from the uniformly $^{13}C/^{15}N$-labeled dataset (ChhC and NhhC) were set aside to be used for cross-validation of the final models.

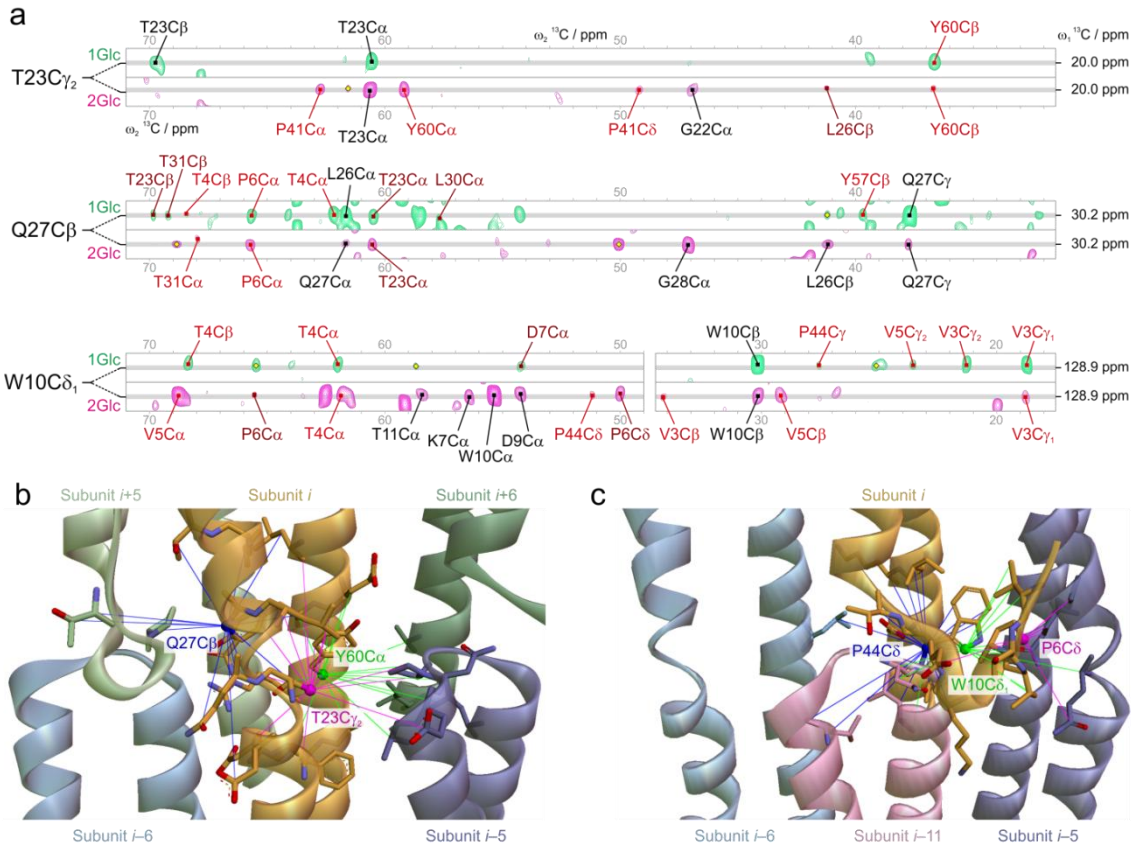

Figure 10: Identification of ssNMR contacts leading to high-resolution structural features. **(a)** PDSD spectra recorded using [1-^{13}C]-glucose labeled (green) and [2-^{13}C]-glucose labeled (magenta) MxiH needle samples. Strips are extracted for three indicated resonance positions, corresponding to the assignments of ^{13}C nuclei T23Cγ_2, Q27Cβ and W10Cδ_1. Assigned cross-peak labels are colored black for intra-residue, dark red for medium-range and light red for long-range atom pair contacts. **(b, c)** Converged structural features of the T3SS needle highlighting the quality of ssNMR constraints used, for atoms in (b): Q27Cβ from subunit *i* (blue), T23Cγ2 from subunit *i* (pink), and Y60Cα from subunit *i* (green), and in (c) P44Cδ from subunit *i–11* (blue), W10Cδ1 from subunit *i* (green), and P6Cδ from subunit *i* (pink).

Due to the high spectral resolution and signal-to-noise ratio of the ssNMR data, a large number of distance constraints can be found for individual nuclei. Excerpts from PDSD spectra are shown in Fig. 10a for the resonances of atoms T23Cγ_2, Q27Cβ and W10Cδ_1 for which 16, 20 and 22 distance correlations are found. Those correlations are

highlighted in the final calculated structure in Fig. 10b along with distance correlations from atoms P6Cδ (12 correlations), P44Cδ (23) and Y60Cα (18).

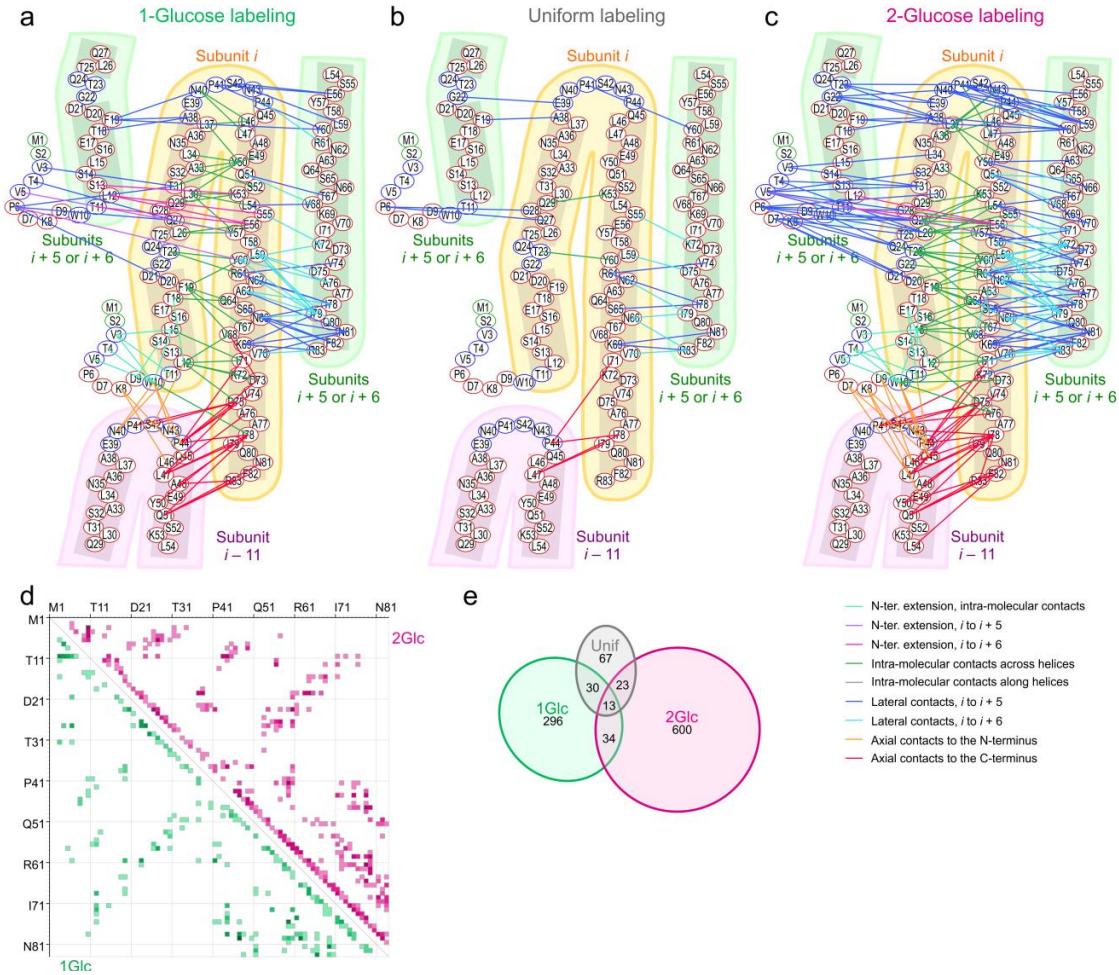

Figure 11: Long-range ssNMR constraints detected using complementary isotopic labeling schemes and used during the structure calculations. Chemical-shift unambiguous long-range constraints identified in **(a)** [1-^{13}C]-glucose, **(b)** [U-^{13}C]-glucose, and **(c)** [2-^{13}C]-glucose labeled samples. In (a–c) interactions are color-coded according to the connecting subunits as follows: Green, cyan: intrasubunit. Blue, light blue and magenta: interface *i*, *i*±*5* or *i*, *i*±*6*; Orange, red: interface *i*, *i*±*11*; **(d)** Venn partition diagram of the ssNMR constraints identified in this study considering the different ^{13}C-labeling schemes, as outlined in Table 2. **(e)** Residue-residue contact map of the ssNMR constraints, showing medium to long-range correlations (|*i*-*j*|>2) present in the data.

An analysis of the final list of constraints reveals that the distance correlations obtained from the two sparse ^{13}C labeling schemes are highly complementary, with <5% of constraints being shared between the 1-Glc and 2-Glc datasets (Fig. 11a,c). Although few common cross-peaks are shared between the two datasets (Fig. 11e), the amino acid pairs giving rise to long-range correlations are highly similar (Fig. 11d), providing an independent confirmation that the identified protein fold and inter-molecular interfaces are accurate (Fig. 11a and 11c).

10.5.3. Assignment of lateral interface ambiguities and iterative Rosetta Structure calculations

Macromolecular assemblies pose a significant challenge to conventional "stepwise" structural modeling approaches that involve docking semi-rigid monomeric domains into higher-order assemblies, due to the fact that these approaches may not capture important conformational changes needed to form the correct complex structure. Instead, we have implemented the Rosetta "fold-and-dock" approach[38] extended for helical symmetry[11] in which the internal backbone and sidechain degrees of freedom defining the subunit structure are sampled at the same time as the rigid-body degrees of freedom that define the helical subunit arrangement.

We performed iterative structure calculations to integrate ssNMR data and cryoEM data towards determining the final MxiH needle structure. We used a brute force approach that makes use of prior structural information alongside the structure determination process. We start by assigning all constraints from 2-Glc data into the 7 interface types based on the shortest distance in the published homology model of MxiH needles[13] and performing a first round of structure calculations. The first round lowest-energy models showed convergence to the known needle fold and subunit arrangements as established previously for PrgI[11]. However, the structural convergence

in this first-round ensemble was insufficient to yield a high-resolution structure (~5 Å backbone RMSD computed over the entire 29-subunit system).

The 10 lowest-energy models are then used as a basis to verify the chemical shift assignment of the NMR peak lists and to assign the proper subunit, (*i*) to (*i* + 5) or (*i* + 6), for lateral constraints. We performed two more iterations of structure calculations followed by peak list refinement until structural convergence to below 2.5 Å was reached in the low-energy ensemble. A final list of 996 intermediate- and long-range constraints was obtained from the 1-Glc and 2-Glc datasets, with the following distribution: 580 intra-subunit, 124 inter-subunit, axial and 292 inter-subunit, lateral.

In the final structure calculations, we used this refined dataset with an upper limit of 9 Å as a calculation bias. An EM density correlation term is applied in all structure calculation stages as described in methods. A total of 5,000 models were computed and ranked according to the weighted sum of Rosetta energy, EM correlation and NMR constraint score terms. The 10 top-ranking models of the final assignment round are converged to below 2.5 Å in backbone RMSD and show a minimal number of constraint violations (1.6-3.5% using an upper limit of 12 Å), while also showing good correlation to the EM density (0.62-0.67) and structural statistics according to Rosetta's Energy function.

Three models were further selected based on different criteria: 1) Rosetta Energy 2) Number of constraint violations and 3) Correlation to the EM density. Each of the 3 top-ranking models was further refined in full-atom mode 10 times by reducing to one-half the weights of both the EM density and NMR constraint score terms, while keeping the upper distance bounds and potential steepness the same. This step was done to evaluate how changes in sidechain packing and local backbone dihedrals (with 1.5 Å backbone RMSD) affect the energy of different starting models. The resulting models

show optimized Rosetta energies and EM density correlations (Supplementary **1** 1) while maintaining a very small number of constraint violations (less than 2%). A final refined ensemble of the top-10 ranking models according to Rosetta Energy was submitted in the PDB (PDB ID 2MME). The final ensemble is converged to below 1 Å in backbone RMSD (Table 5).

The final high-resolution structure determined here is consistent with the needle architecture established through our previous work[11,13] consisting of 5.6 subunits per turn of a 23.5 Å-pitch helix (Fig. 12). The radius of the needle is 23.5 Å, consistent with previous EM studies[39], and the tilt of the 11-start protofilament is -6.40°, positive in the counter-clockwise direction when viewed along the helical axis.

The structure of the N-terminus is now fully resolved in the final models, showing a short α-helical conformation involving residues P6 to D9 (PDKD), that occupies a "protrusion" region of the EM density (Fig. 10c, Fig. 12). The same density region was incorrectly attributed to an intra-subunit β-sheet in a previously published model using the cryoEM data alone[19]. The conformation of the N-terminus is supported by 132 intra-subunit constraints, including a cluster of constraints connecting V3, W10 and L15 (Fig. 10b). In addition, there are 46 inter-subunit constraints connecting the N-terminal residues V3-W10 of subunit (*i*) to residues D20-L34 at the N-terminal α-helix of subunit (*i* – 5) (Fig. 10c). Two correlations between subunits (*i*) and (*i* – 5), V5-Y57 and P6-Y60, indicate that the beginning of the PDKD motif points inside the needle assembly. Finally, a cluster of 3 constraints connects T11 of subunit (*i*) to E56 located in the C-terminal (inner) α-helix of subunit (*i* – 6).

Table 5: NMR and cryo-EM constraint and refinement statistics

NMR distance, dihedral angle & EM density constraints	
Distance constraints (Calculation set)	
Total	996
Intra-subunit, intermediate-range	391
Intra-subunit, long-range	189
Inter-subunit, lateral: (*i*) to (*i* ± 5)	188
Inter-subunit, lateral: (*i*) to (*i* ± 6)	104
Inter-subunit, axial: (*i*) to (*i* ± 11)	124
Hydrogen bonds	0
Distance constraints (Validation set)*	
Total	691
Uniform labeling	96
1-Glc ambiguous	230
2-Glc ambiguous	221
Uniform labeling ambiguous	144
Total dihedral angle constraints**	162
φ	81
ψ	81
EM density constraints	
Resolution (Å) ***	7.7/10.0
Grid spacing (Å)	5.0
Structural statistics	
Distance constraint violations	
Total violations per model	22.5/31.0
Average violation distance (Å)	0.9
EM density correlation	0.67
Ramachandran and rotamer quality	
Favored	81
Allowed	1
Outliers	1
Poor rotamers	0
Clashscore[++]	2.8 (98pc)
Average RMSD (Å) [+++]	
All heavy atom	0.7
Backbone	0.4

** Not used in the calculations, but reserved as a validation set.*

*** Used to bias the selection of 3mer and 9mer backbone fragments from the PDB, as outlined in methods.*

**** Estimated from a Fourier shell correlation analysis (Fuji et al.) / used in the calculations (this study).*

[++] Defined as the number of serious steric overlaps (> 0.4 Å) per 1000 atoms – pc: percentile.

[+++] Computed over all members of the NMR ensemble relative to the coordinates of the first model.

10.5.4. Cross-validation of the hybrid structural determination approach

Having obtained a well-converged ensemble of final structures, we carried out two important steps for the validation of our hybrid approach. First, the accuracy of the calculated structures was determined by cross-validation using a set of distance constraints not employed for structure calculation. Second, we verified and confirmed the compatibility of protein samples employed for cryo-EM and ssNMR.

For cross-validation, we collected distance constraints not used at any stage of the iterative calculations and assignment process from two sources (Table 5): ^{1}H-^{1}H correlations from the uniformly-labeled dataset obtained in ChhC and NhhC spectra (96 correlations) and ambiguous correlations from all three isotopic labeling schemes (595 correlations). Only cross-peaks with a signal-to-noise ratio higher than 6 and corresponding to intermediate- or long-range correlations were considered. In order to prevent introducing any bias in the analysis due to the prior constraint assignment, we systematically selected the chemical shift assignment and the subunit interface giving rise to the shortest inter-nuclear distance within all assignment possibilities contained in the chemical shift tolerance window. This procedure allows quantifying the agreement of a PDB structure with experimental ssNMR distance constraints in a completely unbiased and operator-free fashion.

The vast majority of the constraints are satisfied for the final ensemble (validation set: 660 / 691, 4.5 % violations; calculation set: 758 / 781, 3.0 % violations with an upper limit of 12 Å), therefore supporting the correctness of the proposed structure. The median ^{13}C-^{13}C distance detected in PDSD spectra is 6.10 Å and the 10th- and 90th-percentile distances are 4.37 Å and 10.08 Å, a range of distances which is expected for long mixing periods in PDSD spectra. The constraints detected in ChhC and NhhC spectra involve ^{1}H-^{1}H inter-nuclear distances and therefore offer a higher resolution

than the ^{13}C-^{13}C distances obtained from 1-Glc and 2-Glc datasets used in the structure determination process, with a median ^{1}H-^{1}H distance of 5.39 Å, and 10th- and 90th-percentile distances of 4.02 Å and 8.35 Å. The final models have a higher resolution than can be afforded by the used data, due largely to Rosetta energy function that determines the precise placement of hydrogen atoms.

Using the unbiased cross-validation approach, we tested whether the previously published PDB structure modeled on cryoEM data alone[19] was compatible with the experimental ssNMR distance constraints. The number of distance violations more than doubled (validation set: 615 / 682, 9.8 % violations; calculation set: 668 / 772, 13.5 % violations). A pairwise comparison of all distances in the validation dataset indicated that all PDB structures modeled using ssNMR and cryoEM have significantly shorter distances compared to the PDB structure modeled on cryoEM data alone, on average 1.22 Å shorter per distance constraint (paired difference Student t-test, 95 % confidence level), demonstrating the power of the hybrid structural determination approach. The median distance for the validation set and pairwise comparison of distances between successive rounds of hybrid modeling were also employed to monitor and guide the modeling progress, similar to the concept of R_{free} employed in crystallography[40].

10.5.5. Verification of atomic- and macroscopic-level sample compatibility

In our hybrid approach, structural constraints obtained from two experimental techniques were combined. The employed T3SS needle samples differ in their preparation: for the cryoEM density map, over-expressed MxiH serotype 2 needles are extracted by shearing from the bacterial surface; for ssNMR structural constraints, serotype 6 MxiH needles are polymerized *in vitro*. In the previous sections, it was demonstrated that the hybrid models satisfy all structural information from both sample preparations: all features of the cryoEM density map (correlation of 0.62 to 0.67)

including the protrusion region of electron density between subunits (*i*) and (*i* – 5), and independent ssNMR distance constraints.

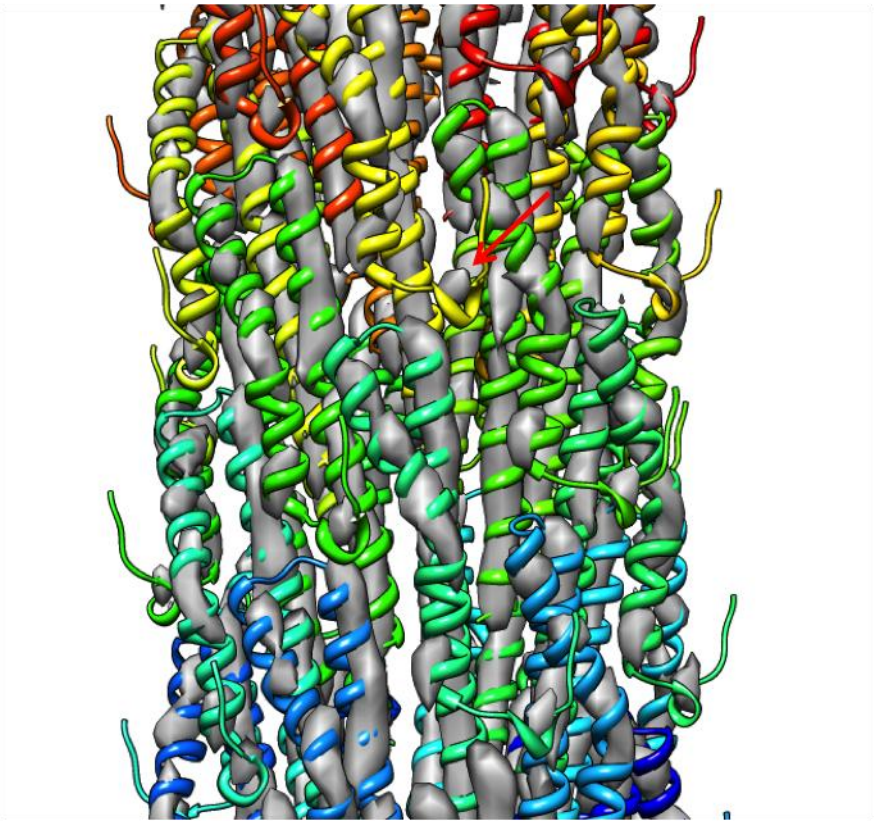

Figure 12: Fit to the high-resolution cryoEM density. Rigid-body fit of the final MxiH model on the 7.7-Å cryoEM density map[19]. A good overlap with the map is obtained (correlation of 0.67), while the individual map features overlap with structural features of the model. Notably, the "protrusion" region of the map (red arrow) is occupied by a short α-helical segment of the MxiH subunit N-terminus. The figure was generated using the program CHIMERA[41,42].

In order to confirm the compatibility of the two samples at the macroscopic level, we recorded scanning transmission electron microscopy (STEM) images of *in vitro* polymerized MxiH needles (Fig. 13). STEM images are recorded on three channels by scintillator-photomultiplier detectors with near-quantum efficiency. Electrons which are elastically scattered from the nucleus are collected by the Large Angle (LA) and Small

Angle (SA) dark-field annular detectors (Fig. 14a), with acceptance angles of 200-40 mRad and 40-15 mRad respectively. Unscattered electrons are collected by the Bright Field (BF) detector (15-0 mRad). The image most reliable for mass measurement is obtained on the Large Angle detector.

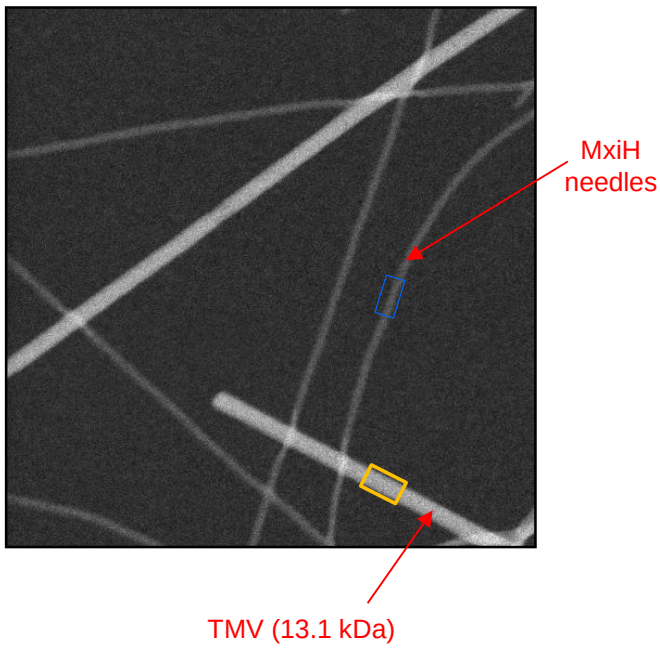

Figure 13: Dark-field STEM image of MxiH needles. The integration region for a MxiH needle is indicated (blue) as well as the region for a TMV particle (yellow).

For thin specimens, the signal intensity detected in the irradiated pixel in the LA and SA detectors are proportional to the number of atoms multiplied by their atomic number (Z, number of protons). As proteins show only minute differences in their atomic composition (Table 6), the pixel intensity can be directly related to the mass by calibrating the image using an object of known mass-per-length, usually tobacco mosaic virus (TMV) particles which have a standard mass-per-length of 13.1 kDa/Å. Indeed, the molecular mass of the MxiH protein per number of protons is very similar to that of the TMV coat protein; the two values differ by only 0.035%.

	TMV coat protein		MxiH protein	
Nb. Hydrogen	1197	(49.3%)	649	(49.5%)
Nb. Carbon	774	(31.9%)	410	(31.3%)
Nb. Nitrogen	211	(8.7%)	111	(8.5%)
Nb. Oxygen	244	(10.0%)	139	(10.6%)
Nb. Sulfur	3	(0.1%)	1	(0.1%)
Number of protons	9318		5014	
Molecular mass (Da), Theoretical	17458.3		9389.3	
Molecular mass (Da), Experiment	–		9391	
Mass/Proton (Da)	1.8736		1.8726 (theo.) 1.8730 (exp.)	

Table 6: Atomic composition of analyzed STEM samples

A total of 4079 image segments could be obtained for MxiH needles and 1173 image segments for TMV particles (Table 3). A global scaling factor was applied such that the average mass-per-length value for TMV particles is 13100 Da/Å. The scaling of each STEM image was adjusted by minimizing the RMSD of the particle used for calibration. TMV particles are usually used for this purpose; however, due to the lesser number of TMV image segment, there was concern that the under-sampling of TMV calibrating segments could be a source of uncertainty affecting the mass-per-length value of MxiH needles (Fig. 15a). A poor sampling of TMV results in a broadening of the MxiH distribution (Fig. 15b) but does not affect the TMV distribution since images are nevertheless re-scaled based on TMV segments. Indeed, it was observed that the distribution of mass-per-length values for TMV does not follow a normal distribution but that it has positive excess kurtosis (leptokurtic), e.g. with an acute central component but fatter tails. As a control, the calibration was repeated using needle segments as reference (Table 7). The uncertainty in needle mass-per-length is reduced and the TMV distribution then follows a normal distribution. The average needle mass-per-length only changes by 0.2%.

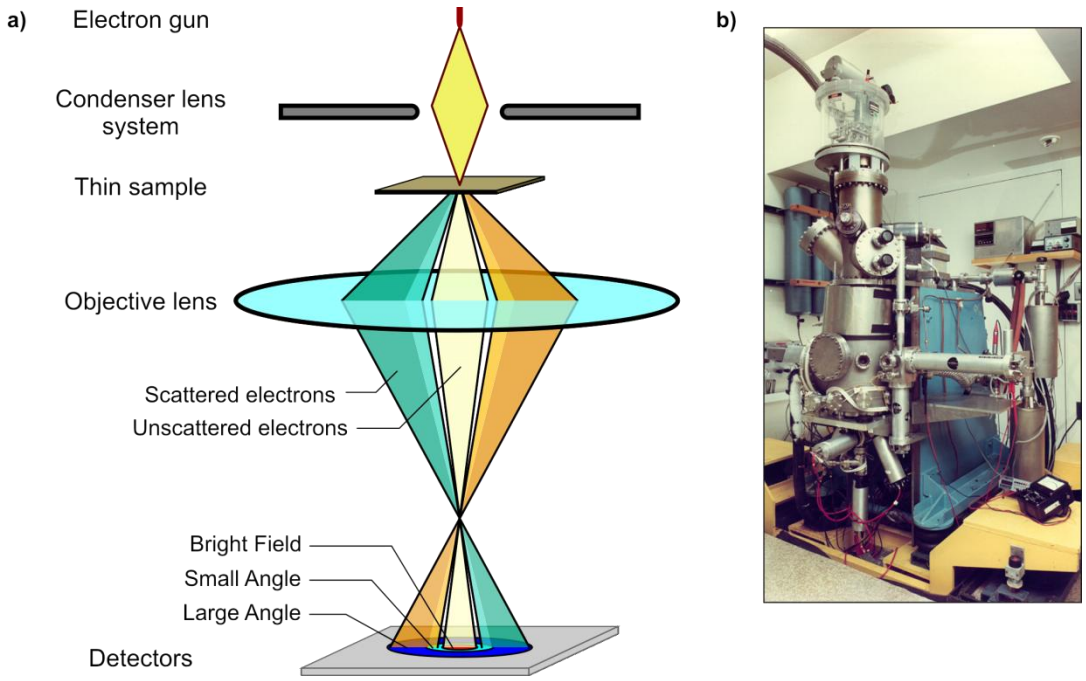

Figure 14: a) Operating principle of the STEM microscope: a low-dose electron beam (yellow) under a 40-kV voltage is focused on a condensed area of the frozen sample. Electrons are elastically scattered by nuclei encountered in the sample and can depart the sample at large angles (orange and green beams). The electron beams are refocused by an objective lens and detected by scintillator-photomultipliers. Electrons scattered at larger angles (dark green/orange) are collected by the Large Angle detector (outer disc, blue) while those scattered at smaller angles (light green/orange) are collected by the Small Angle detector (middle disc, cyan). Transmitted electrons (pale yellow) are collected by the Bright Field detector (central disc, red). Alternatively, the Bright Field detector can be replaced by a X-ray detector. b) The BNL STEM microscope.

Particle	**Avg. Mass-per-length** (Da/Å)	**Standard error** (Da/Å)	**Calibration**
TMV particle	13100.0	8.0	TMV particle
MxiH needle	2184.8	2.2	TMV particle
TMV particle	13100.0	12.5	MxiH needle
MxiH needle	2180.9	1.9	MxiH needle

Table 7: Extraction of average mass-per-length values from STEM measurements

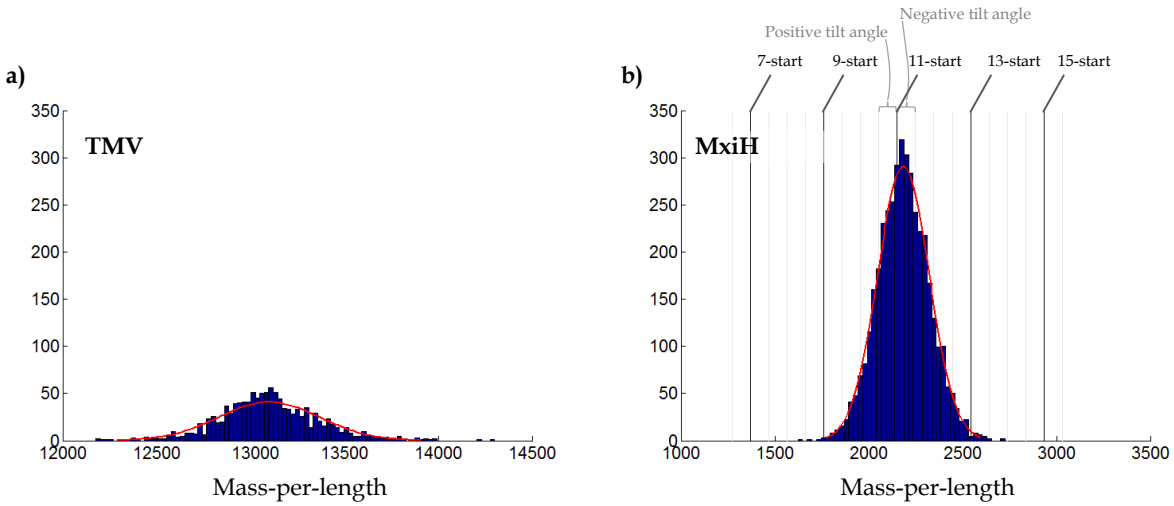

Figure 15: Histograms of STEM mass measurements

By integration of needle segments from calibrated images, we could thus determine the mass-per-length of the polymerized needle assemblies present in the ssNMR samples (Fig. 15). The mass-per-length of 2184±2 Da/Å indicates unambiguously that the MxiH *in vitro* polymerized needles have an 11-start helical assembly (Fig. 15b).

10.5.6. Determination of helical tilt angle

The needle filament consists of identical, helical repeats of the 83-residue monomeric subunit. The symmetry space group has a Hermann-Mauguin symbol $p11N_1$, where N is the number of monomers per unit turn, for instance N=5.5 for an 11-start helix. Six rigid-body degrees of freedom define the symmetric transformation of adjacent subunits along the helical axis. In addition to the three rotation angles that define the orientation of the starting subunit in the local Cartesian coordinate system, one rotation per subunit (φ) defines the number of subunits per unit turn (N=360°/φ), one axial translation defines the pitch of the helix (l), and one distance refines the radius of the helix (R).

In our previous work for the PrgI and MxiH needles that is consistent with earlier STEM and EM measurements[19], we have shown that the overall subunit arrangements and helical parameters are conserved across needles at values close to 5.6 subunits/turn (φ=64°), 4.2 Å/subunit axial translation (23.5 Å helical pitch) and 23.5 Å radius[13].

Focusing on the 11-start protofilament, a structural parameter that is very useful in describing the needle topology is the tilt angle relative to subunit (*i* + 11) (Fig. 16). If the number of subunits per turn is exactly N = 5.5, the subunit (*i* + 11) will be related to subunit (*i*) by a simple translation parallel to the helix axis as the super-helix completes a full 360° rotation. However, if this number is slightly inexact, the subunit (*i* + 11) will be slightly more rotated (N < 5.5) or less rotated (N > 5.5) than 360°. As a result, when linking all CoM of subunits related by an axial interface (subunits $i \pm n \cdot 11$), the super-helix will appear 'tilted', with a slight rotation in the counter-clockwise direction (N < 5.5) or in the clockwise direction (N > 5.5).

If L is the axial translation per two full turns, then $L = 2 \times l$. Thus, the number of subunits per two turns, $T = L \times m_L / MW$, where m_L is the mass-per-unit-length and MW is the molecular weight of the needle subunit. It then follows that the tilt angle is $\alpha = (360°/T) \times (11 - T)$, positive in the counter-clockwise direction.

The precise value of the subunits/turn in our final models (5.6), and subsequently the exact tilt value (-6.40°), is determined by the NMR constraints and Rosetta energy function, with a smaller contribution from the EM correlation term, as outlined in detail in the results section. We can estimate L = 24 Å from the offset in α-helix register between two adjacent subunits. The mass-per-length measured by STEM allows us to

independently obtain the tilt angle of the polymerized needles, -5.37°, which is compatible with the tilt of the hybrid models.

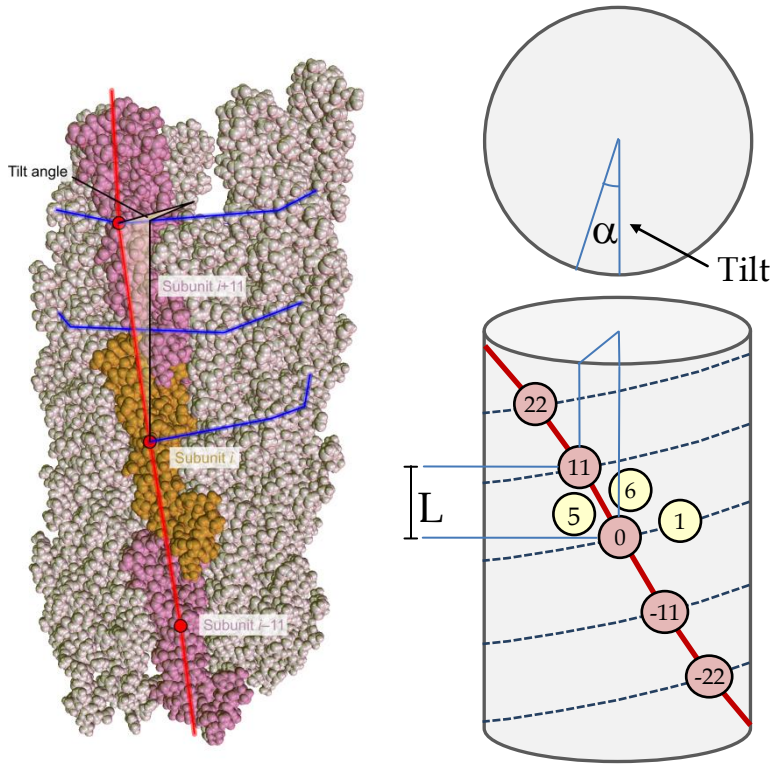

Figure 16: Relationship between STEM measurements and helical parameters. The tilt angle is positive in the counter-clockwise direction.

10.5.7. Determination of helical assembly handedness

The new structure determination approach presented here is able to further determine the handedness of the needle super-helix. The handedness is defined as right-handed when subsequent subunits [i.e. from (*i*) to (*i* + 1)] are arranged in counter-clockwise direction around the helical assembly (see top panels in Fig. 17). The subunit (*i*) is sandwiched between subunit (*i* + 5) on the left and subunit (i + 6) on the right in a right-handed helix (and vice-versa in a left-handed helix). By convention, the center of mass (CoM) of subunit (*i* + 5) and the CoM of subunit (*i*) have a shorter distance when

projected on the super-helix axis than the projected distance between the CoM of (*i* + 6) and the CoM of subunit (*i*).

In the previous PrgI needle calculations the handedness of the needle could not be defined on the basis of the experimental restraints alone, as both left- and right-handed geometries gave very similar restraint scores. The current MxiH dataset contains a much larger number of long-range ssNMR restraints (605 relative to 247 for PrgI, for roughly the same number of residues), confidently assigned to the lateral ±5,6 interfaces (Fig. 9b and Table 5) that should in principle enable to distinguish between the two alternative arrangements. Indeed, in a further structural study of the PrgI needle, it was possible to determine unambiguously the handedness of the helical assembly, benefitting from a large number of distance cross-peaks obtained in spectra of [2-^{13}C]-glycerol and [1,3-^{13}C]-glycerol labeled samples[12].

To address the question of the handedness in our system, we have repeated the calculations assuming a left-handed needle, by swapping the ±5 with ±6 restraint assignments, and vice versa. Notably, the right-handed calculations lead to significantly better optimization of the NMR restraints (average of 22.5 violations per model relative to 37 for the left-handed calculations) that can be attributed to fewer violations of lateral restraints. However, a more significant difference is obtained in the final Rosetta Energies, leading to an average of -176 relative to -238 units, for the left and right-handed low energy ensembles respectively, suggesting that the right-handed structures show more favorable inter-subunit packing and hydrogen-bonding terms.

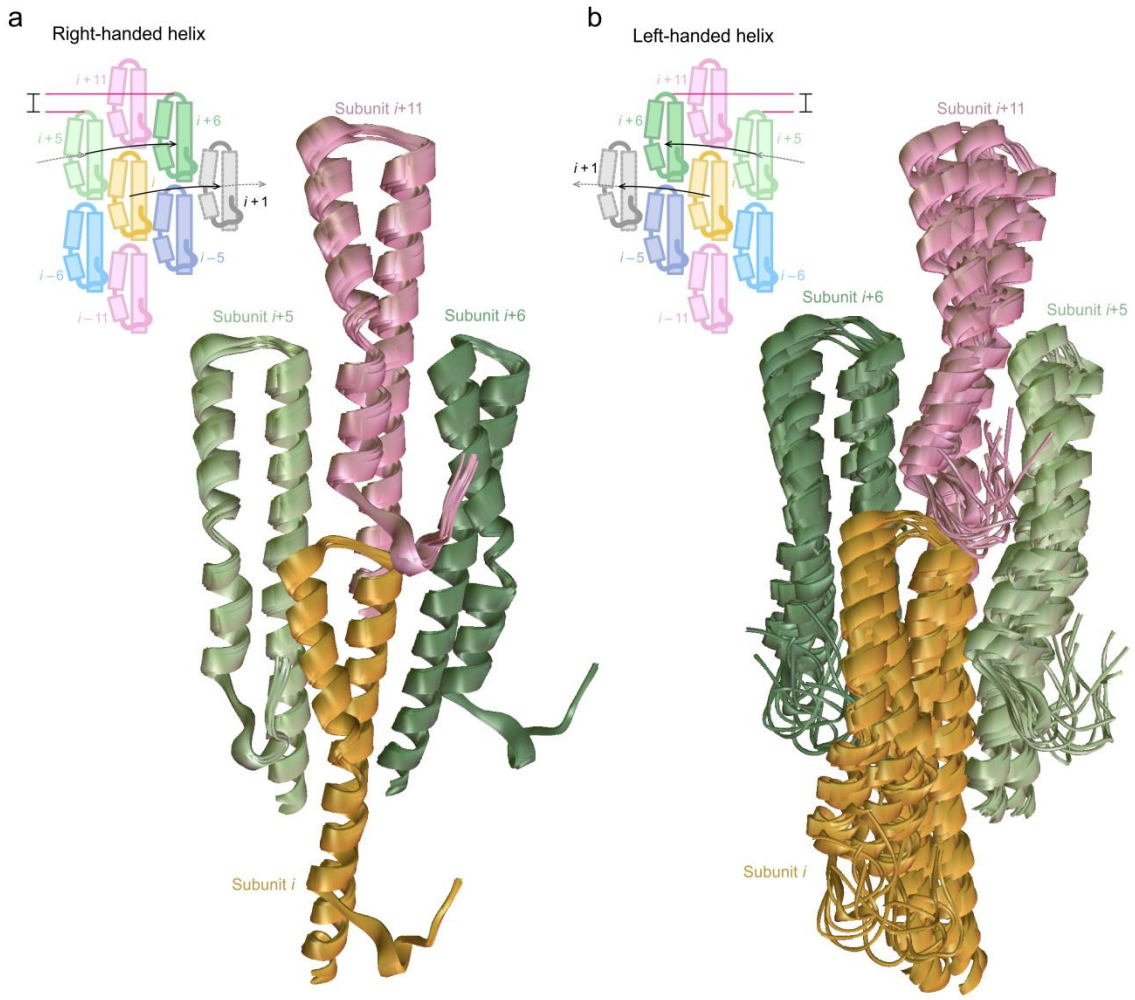

Figure 17: Comparison of right-handed and left-handed structural ensembles

10.6. Discussion

Many biologically relevant large supramolecular assemblies are not amenable to conventional atomic structure determination techniques. However, precise knowledge of the structure of biological assemblies is at the foundation of a mechanistic understanding of biological processes, such as bacterial infection. Here, we demonstrate that a hybrid approach can solve the structure of molecular assemblies at atomic

resolution with high accuracy, by integrating two complementary sources of experimental information, solid-state NMR and cryo-EM.

The new approach has several key advantages relative to the current state-of-the-art structure determination protocols based solely on solid-state NMR[43-45]:

1) The symmetry of the system is modeled explicitly using a generalized Rosetta framework[35] recently extended to include helical symmetries[11]. This allows for manipulating the internal backbone and side-chains together with the rigid-body degrees of freedom for more efficient sampling of conformational space by a) only considering conformations that are consistent with the symmetry type and b) performing a minimal degree of energy and derivative calculations that are propagated among the different subunits. This further allows us to model the long-range order of the needle filament, which is important for the use of the EM density as a calculation bias in addition to the NMR data.

2) We are using a brute-force, structure-guided approach to assign constraints into intra-subunit, and six types of inter-subunit interactions from uniform labeled samples. Although a homology-based template is used to initialize the assignment procedure, the structure calculations are done in a *de novo* manner, starting from completely extended polypeptide chains (the initial assignments can also be obtained manually, as we did originally for the PrgI needle structure[11]). This circumvents the need for expensive labeling schemes using uniform, diluted and mixed samples described in[43], and also allows for the use of prior knowledge from homologous structures in the PDB.

3) Because of the use of Rosetta's energy function to model hydrogen-bonding networks and sidechain packing interactions, our approach does not rely as heavily on the experimental constraints, which are used only as a minor calculation bias with minimal weighting. This approach also avoids the need for inferring additional H-bonding constraints not directly observed experimentally, as done in previous ssNMR

studies of similar systems[44,45], and is more robust to the exact parametrization of constraint upper limits, that can depend on both the system, type of experiment and labeling scheme, as shown extensively in [43]. Our approach is making use of only rough estimates of upper limits based on the analysis of distance histograms (as described previously in the Cross-validation section) which further simplifies the structure determination process.

The needle structure highlights key, conserved features involved in the translocation mechanism of substrate proteins. A recent functional and cryoEM analysis of functional MxiH needles using designed trapped substrates showed that effector proteins are translocated in an unfolded state directly through the needle pore in a directional manner[46]. Close inspection of the electrostatic potential on the structure itself reveals that, while the needle lumen presents several charged residues to interactions with the unfolded substrates, these are typically compensated by conserved opposite charges, resulting in an electrostatically balanced surface (Fig. 18b). Key conserved residues Lys69, Lys 72 and Asp 73 participate in symmetric electrostatic interactions resulting in a circular pattern along the lumen of the structure (Fig. 18d, inset).

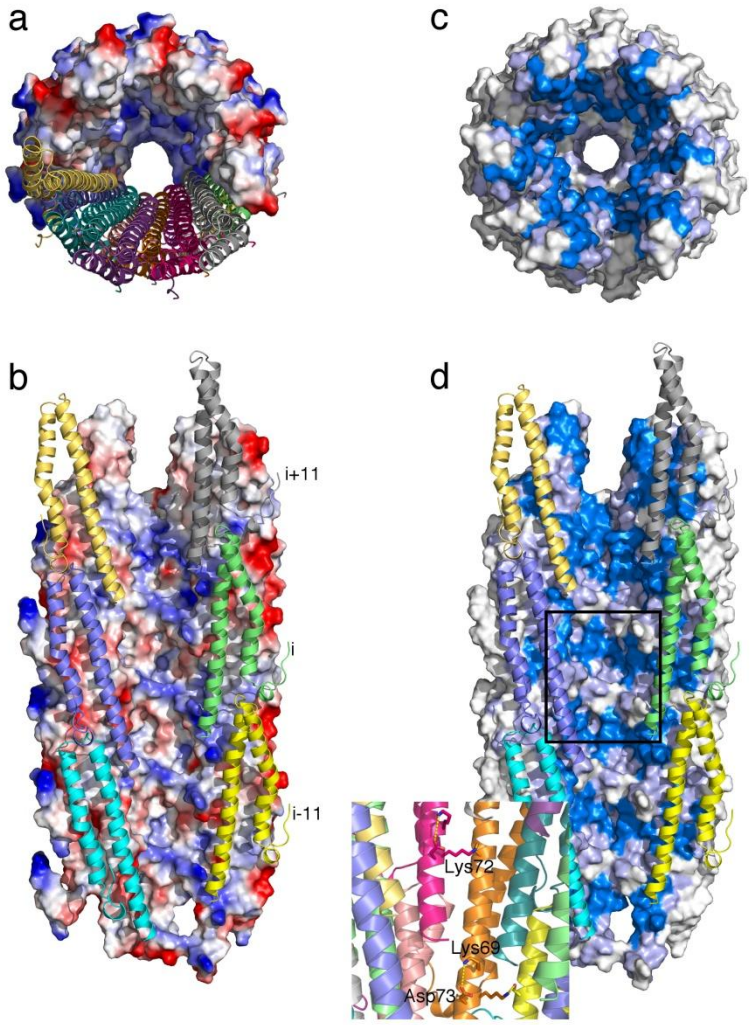

Figure 18: Conserved charged residues decorate the MxiH needle pore. **(a)** Top and **(b)** side view of the hybrid needle structure showing the surface electrostatic potential computed using APBS[47]. The helical arrangement of subunits is shown as cartoons for one-half of the full 29-subunit system as a guide. In (b, d) three 11-start protofilaments have been removed for simplicity. **(c, d)** Same view as in (a, b), with surface coloring according to the sequence conservation index calculated from the alignment of 102 unique needle sequences using Jalview[48], measured on a 1-10 scale. Marine color indicates high (7-10), light purple medium (4-6) and white low (1-3) sequence conservation index. The boxed region in (d) is enlarged in the inset, indicating the pattern of highly conserved charged residues on the helical structure, as discussed in the main text.

A previous systematic Alanine scanning mutagenesis study[49] has investigated sequence-function relationships in the MxiH needle. This study has shown that mutation of each of these three conserved residues to Alanine resulted in functionally defective mutants that cannot invade or lyse host cells, although they still show assembly of relatively intact needle structures that are secretion competent. While K69A and K72A resulted in altered secretion profiles of different substrates, the D73A mutant showed a constitutively on phenotype and secreted effector proteins in a de-regulated manner without sensing an inducing signal. These results are in agreement with the luminal localization of K69 and K72 allowing direct side chain interactions with the secreted proteins and further suggest a role of D73 in regulating substrate release from the needle. The availability of the MxiH structure enables the rational design of experiments towards further elucidating the mechanism of translocation trough the needle pore.

10.7. Conclusion

The hybrid approach presented here provides an avenue for structural characterization of supramolecular assemblies that, due to their difficulty in crystallization and their large size are hard to determine using crystallography and solution NMR, respectively. Taken together, our results show that the new, hybrid approach can conclusively define the long-range features of the structure, such as its handedness, in addition to the radius, tilt angle and helical pitch parameters. By combining two complementary sources of experimental information, the new approach extends the range of targets amenable to structure determination towards future structural biology applications.

10.8. References

1. Karaca, E., Bonvin, A. M. J. J. Advances in integrative modeling of biomolecular complexes. *Methods* **59**, 372-81 (2013).
2. Renault, M., Cukkemane, A., Baldus, M. Solid-State NMR Spectroscopy on Complex Biomolecules. *Angewandte Chemie-International Edition* **49**, 8346-57 (2010).
3. Goldbourt, A. Biomolecular magic-angle spinning solid-state NMR: recent methods and applications. *Current Opinion in Biotechnology* **24**, 705-15 (2013).
4. Muller, H., Etzkorn, M., Heise, H. in *Modern NMR Methodology* Vol. 335 *Topics in Current Chemistry* (eds H. Heise & S. Matthews) 121-56 (2013).
5. Loquet, A., Habenstein, B., Lange, A. Structural investigations of molecular machines by solid-state NMR. *Accounts of Chemical Research* **46**, 2070-9 (2013).
6. Zhou, Z. H. Towards atomic resolution structural determination by single-particle cryo-electron microscopy. *Current Opinion in Structural Biology* **18**, 218-28 (2008).
7. Baker, M. L., Zhang, J., Ludtke, S. J., Chiu, W. Cryo-EM of macromolecular assemblies at near-atomic resolution. *Nature Protocols* **5**, 1697-708 (2010).
8. Troisfontaines, P., Cornelis, G. R. Type III secretion: More systems than you think. *Physiology* **20**, 326-39 (2005).
9. Sansonetti, P. J. Rupture, invasion and inflammatory destruction of the intestinal barrier by Shigella, making sense of prokaryote-eukaryote cross-talks. *Fems Microbiology Reviews* **25**, 3-14 (2001).
10. Schroeder, G. N., Hilbi, H. Molecular pathogenesis of Shigella spp.: Controlling host cell signaling, invasion, and death by type III secretion. *Clinical Microbiology Reviews* **21**, 134-56 (2008).
11. Loquet, A., Sgourakis, N. G., Gupta, R., Giller, K., Riedel, D., Goosmann, C., Griesinger, C., Kolbe, M., Baker, D., Becker, S., Lange, A. Atomic model of the type III secretion system needle. *Nature* **486**, 276-9 (2012).
12. Loquet, A., Habenstein, B., Chevelkov, V., Vasa, S. K., Giller, K., Becker, S., Lange, A. Atomic structure and handedness of the building block of a biological assembly. *Journal of the American Chemical Society* **135**, 19135-8 (2013).
13. Demers, J.-P., Sgourakis, N. G., Gupta, R., Loquet, A., Giller, K., Riedel, D., Laube, B., Kolbe, M., Baker, D., Becker, S., Lange, A. The Common Structural Architecture of Shigella flexneri and Salmonella typhimurium Type Three Secretion Needles. *PLoS pathogens* **9**, e1003245 (2013).
14. Fricke, P., Demers, J.-P., Becker, S., Lange, A. Studies on the MxiH Protein in T3SS Needles Using DNP-Enhanced ssNMR Spectroscopy. *Chemphyschem : a European journal of chemical physics and physical chemistry* **15**, 57-60 (2014).
15. Loquet, A., Lv, G., Giller, K., Becker, S., Lange, A. C-13 Spin Dilution for Simplified and Complete Solid-State NMR Resonance Assignment of Insoluble Biological Assemblies. *Journal of the American Chemical Society* **133**, 4722-5 (2011).
16. Habenstein, B., Loquet, A., Giller, K., Becker, S., Lange, A. Structural characterization of supramolecular assemblies by 13C spin dilution and 3D solid-state NMR. *Journal of Biomolecular NMR* **55**, 1-9 (2012).
17. Lv, G., Fasshuber, H. K., Loquet, A., Demers, J.-P., Vijayan, V., Giller, K., Becker, S., Lange, A. A straightforward method for stereospecific assignment of val and leu prochiral methyl groups by solid-state NMR: Scrambling in the 2-C-13 Glucose labeling scheme. *Journal of Magnetic Resonance* **228**, 45-9 (2013).
18. Chevelkov, V., Giller, K., Becker, S., Lange, A. Efficient CO-CA transfer in highly deuterated proteins by band-selective homonuclear cross-polarization. *Journal of Magnetic Resonance* **230**, 205-11 (2013).
19. Fujii, T., Cheung, M., Blanco, A., Kato, T., Blocker, A. J., Namba, K. Structure of a type III secretion needle at 7-A resolution provides insights into its assembly and signaling mechanisms. *Proceedings of the National Academy of Sciences of the United States of America* **109**, 4461-6 (2012).

20. Szeverenyi, N. M., Sullivan, M. J., Maciel, G. E. Observation of spin exchange by two-dimensional fourier-transform ^{13}C cross-polarization magic-angle spinning. *Journal of Magnetic Resonance* **47**, 462-75 (1982).
21. Lange, A., Becker, S., Seidel, K., Giller, K., Pongs, O., Baldus, M. A concept for rapid protein-structure determination by solid-state NMR spectroscopy. *Angewandte Chemie-International Edition* **44**, 2089-92 (2005).
22. Lange, A., Luca, S., Baldus, M. Structural constraints from proton-mediated rare-spin correlation spectroscopy in rotating solids. *Journal of the American Chemical Society* **124**, 9704-5 (2002).
23. Bockmann, A., Gardiennet, C., Verel, R., Hunkeler, A., Loquet, A., Pintacuda, G., Emsley, L., Meier, B. H., Lesage, A. Characterization of different water pools in solid-state NMR protein samples. *Journal of Biomolecular NMR* **45**, 319-27 (2009).
24. Fung, B. M., Khitrin, A. K., Ermolaev, K. An improved broadband decoupling sequence for liquid crystals and solids. *Journal of Magnetic Resonance* **142**, 97-101 (2000).
25. Thakur, R. S., Kurur, N. D., Madhu, P. K. Swept-frequency two-pulse phase modulation for heteronuclear dipolar decoupling in solid-state NMR. *Chemical Physics Letters* **426**, 459-63 (2006).
26. Augustine, C., Kurur, N. D. Supercycled SWf-TPPM sequence for heteronuclear dipolar decoupling in solid-state nuclear magnetic resonance. *Journal of Magnetic Resonance* **209**, 156-60 (2011).
27. Chandran, C. V., Madhu, P. K., Kurur, N. D., Brauniger, T. Swept-frequency two-pulse phase modulation (SWf-TPPM) sequences with linear sweep profile for heteronuclear decoupling in solid-state NMR. *Magn Reson Chem* **46**, 943-7 (2008).
28. Shaka, A. J., Keeler, J., Frenkiel, T., Freeman, R. An Improved Sequence for Broad-Band Decoupling - WALTZ-16. *Journal of Magnetic Resonance* **52**, 335-8 (1983).
29. Delaglio, F., Grzesiek, S., Vuister, G. W., Zhu, G., Pfeifer, J., Bax, A. NMRPIPE: a multidimensional spectral processing system based on UNIX pipes. *Journal of Biomolecular NMR* **6**, 277-93 (1995).
30. SPARKY 3 v. 3.113 (2006).
31. Stevens, T. J., Fogh, R. H., Boucher, W., Higman, V. A., Eisenmenger, F., Bardiaux, B., van Rossum, B.-J., Oschkinat, H., Laue, E. D. A software framework for analysing solid-state MAS NMR data. *Journal of Biomolecular NMR* **51**, 437-47 (2011).
32. Vranken, W. F., Boucher, W., Stevens, T. J., Fogh, R. H., Pajon, A., Llinas, P., Ulrich, E. L., Markley, J. L., Ionides, J., Laue, E. D. The CCPN data model for NMR spectroscopy: Development of a software pipeline. *Proteins-Structure Function and Bioinformatics* **59**, 687-96 (2005).
33. Lundström, P., Teilum, K., Carstensen, T., Bezsonova, I., Wiesner, S., Hansen, D. F., Religa, T. L., Akke, M., Kay, L. E. Fractional C-13 enrichment of isolated carbons using [1-C-13]- or [2-C-13]-glucose facilitates the accurate measurement of dynamics at backbone C-alpha and side-chain methyl positions in proteins. *Journal of Biomolecular NMR* **38**, 199-212 (2007).
34. Hong, M. Determination of multiple phi-torsion angles in proteins by selective and extensive ^{13}C labeling and two-dimensional solid-state NMR. *Journal of Magnetic Resonance* **139**, 389-401 (1999).
35. DiMaio, F., Leaver-Fay, A., Bradley, P., Baker, D., Andre, I. Modeling symmetric macromolecular structures in Rosetta3. *PLOS One* **6**, e20450 (2011).
36. DiMaio, F., Tyka, M. D., Baker, M. L., Chiu, W., Baker, D. Refinement of Protein Structures into Low-Resolution Density Maps Using Rosetta. *Journal of molecular biology* **392**, 181-90 (2009).
37. Bloembergen, N. On the interaction of nuclear spins in a crystalline lattice. *Physica* **15**, 386-426 (1949).
38. Das, R., Andre, I., Shen, Y., Wu, Y., Lemak, A., Bansal, S., Arrowsmith, C. H., Szyperski, T., Baker, D. Simultaneous prediction of protein folding and docking at high resolution. *Proceedings of the National Academy of Sciences of the United States of America* **106**, 18978-83 (2009).
39. Cordes, F. S., Komoriya, K., Larquet, E., Yang, S. X., Egelman, E. H., Blocker, A., Lea, S. M. Helical structure of the needle of the type III secretion system of Shigella flexneri. *J Biol Chem* **278**, 17103-7 (2003).
40. Brunger, A. T. Free R-Value - A Novel Statistical Quantity for Assessing the Accuracy of Crystal-Structures. *Nature* **355**, 472-5 (1992).

41. Pettersen, E. F., Goddard, T. D., Huang, C. C., Couch, G. S., Greenblatt, D. M., Meng, E. C., Ferrin, T. E. UCSF Chimera—A visualization system for exploratory research and analysis. *Journal of Computational Chemistry* **25**, 1605-12 (2004).
42. Goddard, T. D., Huang, C. C., Ferrin, T. E. Visualizing density maps with UCSF Chimera. *Journal of structural biology* **157**, 281-7 (2007).
43. Van Melckebeke, H., Wasmer, C., Lange, A., Eiso, A. B., Loquet, A., Bockmann, A., Meier, B. H. Atomic-Resolution Three-Dimensional Structure of HET-s(218-289) Amyloid Fibrils by Solid-State NMR Spectroscopy. *Journal of the American Chemical Society* **132**, 13765-75 (2010).
44. Shahid, S. A., Bardiaux, B., Franks, W. T., Krabben, L., Habeck, M., van Rossum, B.-J., Linke, D. Membrane-protein structure determination by solid-state NMR spectroscopy of microcrystals. *Nature Methods* **9**, 1212-U119 (2012).
45. Wang, S., Munro, R. A., Shi, L., Kawamura, I., Okitsu, T., Wada, A., Kim, S.-Y., Jung, K.-H., Brown, L. S., Ladizhansky, V. Solid-state NMR spectroscopy structure determination of a lipid-embedded heptahelical membrane protein. *Nature Methods* **10**, 1007-12 (2013).
46. Radics, J., Königsmaier, L., Marlovits, T. C. Structure of a pathogenic type 3 secretion system in action. *Nat Struct Mol Biol* **21**, 82-7 (2014).
47. Baker, N. A., Sept, D., Joseph, S., Holst, M. J., McCammon, J. A. Electrostatics of nanosystems: Application to microtubules and the ribosome. *Proceedings of the National Academy of Sciences of the United States of America* **98**, 10037-41 (2001).
48. Waterhouse, A. M., Procter, J. B., Martin, D. M. A., Clamp, M., Barton, G. J. Jalview Version 2-a multiple sequence alignment editor and analysis workbench. *Bioinformatics* **25**, 1189-91 (2009).
49. Kenjale, R., Wilson, J., Zenk, S. F., Saurya, S., Picking, W. L., Picking, W. D., Blocker, A. The needle component of the type III secreton of Shigella regulates the activity of the secretion apparatus. *J Biol Chem* **280**, 42929-37 (2005).
50. Andronesi, O. C., von Bergen, M., Biernat, J., Seidel, K., Griesinger, C., Mandelkow, E., Baldus, M. Characterization of Alzheimer's-like paired helical filaments from the core domain of tau protein using solid-state NMR spectroscopy. *Journal of the American Chemical Society* **130**, 5922-8 (2008).

10.9. Appendix

The following Sparky extension module was used to display the resonance frequency of corresponding cross-peaks for intra-residue, sequential or all correlations as described in section 10.4.4.

1) To install, copy the following three files to your %SPARKY_HOME%\python\sparky\ directory

File jpde.py

```
# ------------------------------------------------------------------------------
#
# In the process of spectrum assignment, it is useful to verify the position of other
# assignment for a cross-peak. While Sparky has built-in indicator for the average
# position for all spectra (view Resonances, keyboard shortcut 'vR'), it is sometimes
# more useful to only know the average value within the same spectrum, as peak positions
# can systematically vary from one spectrum to another (e.g. due to different sample or
# recording conditions, different acquisition and processing parameters, ...).
#
# The necessary Python functions are coded in the 'jpde.py' source file.
# The optional 'jpde_groups.py' Python file specifies which spectra should be grouped together
#   as they have the same recording and processing conditions.
# The Sparky initialization script 'sparky_init.py' adds the following keyboard shortcuts:
#
#   Shortcuts starting with 'j' will display all assigned lines the selected peak(s).
#   Shortcuts starting with 'k' will display a box around the selected peak(s);
#     The position of the box correspond to the robust mean,
#     The width and height of the box correspond to the robust standard deviation.
#     Those robust estimates
#   'j0' and 'k0': Remove all lines
#   'j1' and 'k1': Only intra-residue assignments from same spectrum
#   'j2' and 'k2': Only intra-residue and sequential assignments from same spectrum
#   'j3' and 'k3': All assignments from same spectrum
#   'j4' and 'k4': Only intra-residue assignments from all spectra
#   'j5' and 'k5': Only intra-residue and sequential assignments from all spectra
#   'j6' and 'k6': All assignments from all spectra
#
# Additional information is printed in the Python console (Menu Extensions > Python console)
#   or keyboard shortcut 'py'
#
# To install this extension, add the three files in the %SPARKY_HOME%\python\sparky\ directory.
#
# Best regards, Jean-Philippe Demers (jpde@nmr.mpibpc.mpg.de)
#
# ------------------------------------------------------------------------------

import sparky, pyutil, sputil, re, math

def add_lines_intra(session,option=1,mode=0):
  """For each selected peak, add guiding lines corresponding to other intra found on the same axes of the spectrum."""
  spectrum = session.selected_spectrum()

  if spectrum:
    peaks = spectrum.selected_peaks()
    peakcount=0
    for peak in peaks:
      for axis in range(spectrum.dimension):
        resonance_addline(spectrum, peak, axis, peaks, option, peakcount, mode)
      peakcount=peakcount+1

# ------------------------------------------------------------------------------
#
def resonance_addline(spectrum, peak, axis, not_these_peaks, option, peakcount, mode):
  """Draws the guiding lines."""
  ppm_width=0.35
  tiny_width=0.0075
  color_list=['magenta',     'cyan',        'blue',\
              'purple',      'green',       'tomato',\
              'maroon',      'purple',      'pink',\
              'gold',        'red',         'yellow',\
              'orange',      'light green', 'maroon',\
              'coral',       'light blue',  'turquoise']
```

```
  freq = peak.frequency[1-axis] #Peak frequency in the other dimension, used later to define the line
  r = peak.resonances()[axis]
  if r:
    linecount=0
    opeaks = assigned_peaks(spectrum, r, axis, option)
    opeaks = pyutil.subtract_lists(opeaks, not_these_peaks)
    color_number=divmod(peakcount+3*(option-1),len(color_list))[1]
    line_color=color_list[color_number]
    if mode==0: # In mode 0, all lines are drawn on the spectrum.
      for opeak in opeaks:
        ofreq = opeak.frequency[axis]
        if axis == 0:
          line = sparky.Line(spectrum, (ofreq,freq-ppm_width), (ofreq,freq+ppm_width))
        else:
          line = sparky.Line(spectrum, (freq-ppm_width,ofreq), (freq+ppm_width,ofreq))
        linecount=linecount+1
        line.selected = 0
        line.color = line_color
      spectrum.session.stdout.write("%.0f lines added for resonance %s in w%.0f (%s)\n" % \
            (linecount,peak.resonances()[axis].name,axis+1,line_color))
    else: # In mode 1, only the confidence interval is drawn on the spectrum.
      opeak_l=[]
      for opeak in opeaks:
        opeak_l = opeak_l + [opeak.frequency[axis]]
      (opeak_mean,opeak_std)=robust_mean_and_std(opeak_l)
      opeak_std=min(opeak_std,ppm_width/3.)
      color_number=divmod(peakcount+3*(option-1),len(color_list))[1]
      opeak_lines=(opeak_mean-tiny_width/2.-opeak_std,\
                   opeak_mean+tiny_width/2.-opeak_std,\
                   opeak_mean-tiny_width/2.+opeak_std,\
                   opeak_mean+tiny_width/2.+opeak_std)
      for ff in opeak_lines:
        if axis == 0:
          line = sparky.Line(spectrum, (ff,freq-ppm_width),\
                                       (ff,freq+ppm_width))
        else:
          line = sparky.Line(spectrum, (freq-ppm_width,ff),\
                                       (freq+ppm_width,ff))
        line.selected = 0
        line.color = line_color

      spectrum.session.stdout.write("Resonance %s in w%.0f: Mean %.2f ppm, Std %.2f ppm  (%s)\n" % \
            (peak.resonances()[axis].name,axis+1,opeak_mean,opeak_std,line_color))


# ------------------------------------------------------------------------------
#
def assigned_peaks(spectrum, resonance, axis, option):
  """Returns the list of assigned resonances."""
  peaks = []
  resid_0=-9999
  resid_1= 9999
  for peak in resonance.peak_list():
    if peak.resonances()[0]:
      resid_0 =  int(re.findall(r'[-0-9]+', peak.resonances()[0].name)[0])
    if peak.resonances()[1]:
      resid_1 =  int(re.findall(r'[-0-9]+', peak.resonances()[1].name)[0])
    diff=abs(resid_0-resid_1)
    # Spectra recorded in similar conditions can be grouped together for
    # better precision of the mean and standard deviation.
    # Groups have to be defined in the optional file jpde_groups.py
    try:
      import jpde_groups
      reload(jpde_groups)
      spectrum_groups = jpde_groups.get_groups()
    except ImportError:
      spectrum_groups = 50
    if spectrum.name not in spectrum_groups:
      spectrum_yes = peak.spectrum == spectrum
    else:
      if peak.spectrum.name not in spectrum_groups:
        spectrum_yes = False
      else:
        spectrum_yes = spectrum_groups[peak.spectrum.name] == spectrum_groups[spectrum.name]
    if (peak.resonances()[axis] != resonance)     or \
       (option < 4 and not spectrum_yes) or \
       (divmod(option-1,3)[1] < 2 and diff > 1)       or \
       (divmod(option-1,3)[1] == 0 and diff > 0):
      continue
    peaks.append(peak)
  return tuple(peaks)
```

```
# ------------------------------------------------------------------------------
#
def delete_all_lines(session):
  """Deletes all lines (but not grids) from the currently selected spectrum."""
  spectrum = session.selected_spectrum()
  linecount=0

  for line in spectrum.line_list():
    sparky_del(session, line)
    linecount=linecount+1
  spectrum.session.stdout.write("%.0f lines deleted in spectrum %s\n" % \
                                (linecount,session.selected_spectrum().name))


#-----Robust Mean--------------
#
def robust_mean_and_std(y):
  """Calculates robust estimates for the mean and standard deviation."""
  n = len(y)
  if n < 1:
    return (0.,1.)
  if n == 1:
    return (mean(y),1.)
  if n == 2:
    return (mean(y),std(y))
  y.sort()
  n_mid=n/2
  y_lower=y[:(n_mid+n%2)]
  y_upper=y[(n_mid):]
  q_mid = len(y_lower)/2
  if q_mid % 2:
    QT1=y_lower[q_mid]
    QT3=y_upper[q_mid]
  else:
    QT1=(y_lower[q_mid]+y_lower[q_mid-1])/2.0
    QT3=(y_upper[q_mid]+y_upper[q_mid-1])/2.0

  IQR = QT3-QT1
  lowFense = QT1 - 1.5*IQR
  highFense = QT3 + 1.5*IQR
  y_ok=[]
  for yy in y:
    if (yy>lowFense) and (yy<highFense):
      y_ok = y_ok + [yy]
  return (mean(y_ok),std(y_ok))

def mean(l):
  """Arithmetic mean."""
  if len(l) < 1:
    return 0. #We return 0 in case of error.
  return float(sum(l))/len(l)

def std(l):
  """Sample standard deviation."""
  if len(l) < 2:
    return 1. #We return 1 in case of error.

  s0 = sum(1. for x in l)
  s1 = sum(float(x) for x in l)
  s2 = sum(float(x*x) for x in l)

  return math.sqrt((s0 * s2 - s1 * s1)/(s0 * (s0 - 1)))

# ==============================================================================
#
def sparky_del(session, object):
  """Deletes a sparky object (e.g. peak, line, label)."""
  if sparky.object_exists(session) and sparky.object_exists(object):

    selected_ornaments = session.selected_ornaments()

    session.unselect_all_ornaments()
    object.selected = 1
    session.command_characters(chr(127))

    for ornament in selected_ornaments:
      if sparky.object_exists(ornament):
        ornament.selected = 1
```

File jpde_groups.py

```
def get_groups():
  return { \
          'MXIH2GLC_PDSD850ms_850_P3'  : 1, \
          'MXIH2GLC_PDSD400ms_850_P3'  : 1, \
          'MXIH2GLC_PDSD50ms_850_P3'   : 1, \
          'MXIH2GLC_PDSD850ms_600_P'   : 2, \
          'MXIH2GLC_PDSD300ms_600'     : 2, \
          'MXIH1GLC_PDSD50ms_600'      : 3, \
          'MXIH1GLC_PDSD300ms_600'     : 3, \
          'MXIH1GLC_PDSD850ms_600'     : 3, \
          'MXIH1GLC_PDSD100ms_850_P3'  : 4, \
          'MXIH1GLC_PDSD400ms_850_P3'  : 4, \
          'MXIH1GLC_PDSD850ms_850_P3'  : 4, \
          'MXIH1GLC_PDSD700ms_800'     : 5, \
          'MXIH1GLC_PDSD700ms_800_B'   : 5, \
          'MXIH_NCA_850'               : 6, \
          'MXIH_NCACX_850'             : 6, \
          'MXIH_NCO_850'               : 6, \
          'MXIH_NCOCX_850'             : 6, \
          'MXIH_PDSD100ms_600_B3'      : 7, \
          'MXIH_PDSD200ms_600_B3'      : 7, \
          }
```

File sparky_init.py

```
def initialize_session(session):

  def Je_command(option=1,mode=0):
    import jpde
    reload(jpde)
    if option==0:
      jpde.delete_all_lines(session)
    else:
      jpde.add_lines_intra(session,option,mode)

  session.add_command('j0', "", lambda:Je_command(0))
  session.add_command('j1', "", lambda:Je_command(1))
  session.add_command('j2', "", lambda:Je_command(2))
  session.add_command('j3', "", lambda:Je_command(3))
  session.add_command('j4', "", lambda:Je_command(4))
  session.add_command('j5', "", lambda:Je_command(5))
  session.add_command('j6', "", lambda:Je_command(6))

  session.add_command('k0', "", lambda:Je_command(0,1))
  session.add_command('k1', "", lambda:Je_command(1,1))
  session.add_command('k2', "", lambda:Je_command(2,1))
  session.add_command('k3', "", lambda:Je_command(3,1))
  session.add_command('k4', "", lambda:Je_command(4,1))
  session.add_command('k5', "", lambda:Je_command(5,1))
  session.add_command('k6', "", lambda:Je_command(6,1))

  pass
```